



**HAL**  
open science

# Novel electrode and photoelectrode materials for hydrogen production based on molecular catalysts

Andrew Joshua Bagnall

► **To cite this version:**

Andrew Joshua Bagnall. Novel electrode and photoelectrode materials for hydrogen production based on molecular catalysts. Catalysis. Université Grenoble Alpes [2020-..]; Uppsala universitet, 2022. English. NNT : 2022GRALV088 . tel-04076051

**HAL Id: tel-04076051**

**<https://theses.hal.science/tel-04076051>**

Submitted on 20 Apr 2023

**HAL** is a multi-disciplinary open access archive for the deposit and dissemination of scientific research documents, whether they are published or not. The documents may come from teaching and research institutions in France or abroad, or from public or private research centers.

L'archive ouverte pluridisciplinaire **HAL**, est destinée au dépôt et à la diffusion de documents scientifiques de niveau recherche, publiés ou non, émanant des établissements d'enseignement et de recherche français ou étrangers, des laboratoires publics ou privés.



UPPSALA  
UNIVERSITET

THÈSE

Pour obtenir le grade de

**DOCTEUR DE L'UNIVERSITÉ GRENOBLE ALPES  
et de l'UNIVERSITÉ D'UPPSALA**

École doctorale : École Doctorale de Chimie et Sciences du Vivant  
Spécialité : Chimie inorganique et bio-inorganique  
Unité de recherche : Laboratoire de Chimie et Biologie des Métaux

**UGA**  
Université  
Grenoble Alpes

# **Nouveaux matériaux d'électrodes et de photoélectrodes à base de catalyseurs moléculaires pour la production d'hydrogène**

## **Novel electrode and photoelectrode materials for hydrogen production based on molecular catalysts**

Présentée par :

**Andrew Joshua BAGNALL**

Direction de thèse :

**M. Vincent ARTERO**

Directeur de recherche, CEA

Directeur de thèse

**M. Leif HAMMARSTRÖM**

Professeur, Uppsala Universitet

Co-Directeur de thèse

Rapporteurs :

**M. Alexander COWAN**

Professeur, University of Liverpool

**Mme. Élodie ANXOLABÉHÈRE-**

**MALLART**

Directrice de recherche, CNRS

Thèse soutenue publiquement le **13 décembre 2022**, devant le jury composé de :

**M. Alexander COWAN**

Professeur, University of Liverpool

Rapporteur

**Mme. Élodie ANXOLABÉHÈRE-**

**MALLART**

Directrice de recherche, CNRS

Rapporteuse

**M. James GARDNER**

Professeur Associé, KTH

Examineur

**M. Andreas ORTHABER**

Professeur Associé, Uppsala Universitet

Président du jury



**Titre :** Nouveaux matériaux d'électrodes et de photoélectrodes à base de catalyseurs moléculaires pour la production d'hydrogène

**Mots clés :** mécanisme électrochimique, hydrogène, photosynthèse artificielle, catalyseur moléculaire, dégagement d'hydrogène, cobalt

**Résumé :** L'hydrogène peut être un carburant de l'avenir et est une matière première chimique importante. Dans le cadre du projet eSCALED sur la photosynthèse artificielle, cette thèse porte sur l'utilisation de catalyseurs moléculaires sans métaux nobles, en particulier un complexe de coordination de cobalt, pour faciliter et accélérer la production d'hydrogène à partir de protons, l'une des demi-réactions du craquage de l'eau, en liant les protons et en leur transférant des électrons à la bonne phase. Le milieu chimique du complexe sert à optimiser la chimie du centre métallique de cobalt pour la réaction et à lier efficacement le cobalt et stabiliser ainsi le système.

Comment le complexe accomplit cela (le mécanisme catalytique), comment le complexe est incorporé sur des électrodes des électrolyseurs, et comment le complexe produit de l'hydrogène par photocatalyse directe lorsqu'il est mélangé avec des boîtes quantiques qui absorbent la lumière sont les projets phares de ce travail.

**Title:** Novel electrode and photoelectrode materials for hydrogen production based on molecular catalysts

**Keywords:** electrochemical mechanism, hydrogen, artificial photosynthesis, molecular catalyst, hydrogen evolution, cobalt

**Abstract:** Hydrogen is a promising green fuel and an important chemical feedstock. As part of the larger eSCALED project on artificial photosynthesis, this thesis focuses on the use of noble metal-free molecular catalysts, in particular a cobalt coordination complex, to facilitate – speed up and reduce the energy barrier for – the production of hydrogen from protons (one of the half-reactions of water-splitting), by binding the protons and transferring electrons to them at the right time. The chemical environment of the coordination complex serves to optimise the chemistry of the cobalt metal centre for the reaction and bind the cobalt effectively to stabilise the system.

How the complex does this (the catalytic mechanism), how the complex can be incorporated onto electrodes for water-splitting devices (electrolysers) by chemical modification, and how the complex can produce hydrogen by direct photocatalysis when mixed with light-absorbing quantum dots were the key projects of this work.

*“To achieve great things, two things are needed;  
a plan, and not quite enough time.”*

Leonard Bernstein



# List of Papers

This thesis is based on the following papers, which are referred to in the text by their Roman numerals.

- I. **Electrocatalytic Reduction of Protons to Dihydrogen by the Cobalt Tetraazamacrocyclic Complex [Co(N<sub>4</sub>H)Cl<sub>2</sub>]<sup>+</sup>: Mechanism and Benchmarking of Performances.**  
Li, C.-B.<sup>§</sup>, Bagnall, A. J.<sup>§</sup>, Sun, D., Rendon, J., Koepf, M., Gambarelli, S., Mouesca, J.-M., Chavarot-Kerlidou, M., Artero, V. *Sustainable Energy Fuels*, 2022, **6**, 143.
- II. **Molecular Engineering of Electrocatalytic Nanomaterials for Hydrogen Evolution Based on a Cobalt Tetraazamacrocyclic Catalyst.**  
Bagnall, A. J., Haake, M., Grau-Abarca, S., Moghaddam, N. J., Straistari, T., Koepf, M., Gimbert-Suriñach, C., Llobet, A., Hammarström, L., Chavarot-Kerlidou, Reuillard, B., M., Artero, V. *Manuscript in preparation*.
- III. **Ultrafast Electron Transfer from CuInS<sub>2</sub> Quantum Dots to a Molecular Catalyst for Hydrogen Production: Rethinking the Binding Models**  
Bagnall, A. J.<sup>§</sup>, Eliasson, N.<sup>§</sup>, Chavarot-Kerlidou, M., Artero, V., Hammarström, L. *Manuscript in preparation*.

Reprints were made with permission from the respective publishers.

Review papers not included in this thesis:

- IV. **Heterogenised Molecular Catalysts for Sustainable Electrochemical CO<sub>2</sub> Reduction.**  
Grammatico, D., Bagnall, A. J., Riccardi, L., Fontecave, M., Su, B.-S., Billon, L. *Angew. Chem. Int. Ed.*, 2022, **61**, e202206399.

# Contribution Report

- I. (Co-first author) Planned and interpreted EPR experiments with coworkers. Prepared all samples for the extensive EPR studies. Performed a large part of the electrochemical experiments (high scan rate experiments, controls, repeats, re-analysis of the data and calculations). Assisted in interpretation and structure modelling for the complete mechanism. Supported in the writing of the manuscript. Major role in the extensive final revision and corrections.
- II. Optimised the synthesis of the intermediate CAT1-CO<sub>2</sub>H. Carried out the first syntheses of the novel pyrene-functionalised catalyst (CAT2). Performed the initial homogeneous and heterogeneous electrochemical characterisations of CAT2 and the initial tests of CAT2 and CAT3 on multi-walled carbon nanotubes. Contributed to the interpretation of results and hypotheses. Ran the first bulk electrolysis-H<sub>2</sub> gas measurement test of CAT2. Carried out preliminary tests of CAT2 on screen-printed electrodes. Wrote the initial draft of the manuscript. Supported in corrections for the attached version.
- III. Synthesised the CAT1-CO<sub>2</sub>H derivative and the CIS quantum dot batches. Carried out the steady-state spectroscopy and TCSPC characterisation of the quantum dots, the photocatalytic H<sub>2</sub> measurements and the PL quenching experiments. Processed the modelling of PL quenching with feedback from coauthors. Did preliminary tests on NiO compatibility. Co-wrote the initial draft of the manuscript and supported in corrections for the attached version.





# Contents

1	Introduction .....	9
1.1	Hydrogen & the Green Energy Transition .....	10
1.2	Natural and Artificial Photosynthesis .....	12
1.3	Hydrogen-Evolving Catalysts .....	15
1.3.1	Solid-state Material Catalysts .....	15
1.3.2	Bioinspiration from Enzymes .....	15
1.3.3	Molecular Catalysts and the State of the Art .....	17
1.3.4	Immobilisation Strategies .....	18
1.4	The Molecular Catalyst ‘CAT1’ .....	20
2	Key Experimental Techniques.....	22
3	Mechanistic Studies on CAT1 for the Hydrogen Evolution Reaction ( <b>Paper I</b> ) .....	26
3.1	Motivations and Background .....	26
3.2	Previous Mechanistic Understanding.....	27
3.3	New Studies in <b>Paper I</b> .....	27
	Electrochemical Characterisation .....	27
	Spectroscopic Characterisation.....	31
3.4	Overall Proposed Mechanism and Benchmarking .....	32
4	Electrocatalytic Hydrogen Evolution from Novel Anchorable Derivatives of CAT1 ( <b>Paper II</b> ).....	35
4.1	Motivations and Background .....	35
4.2	Synthesis of a Pyrene-Containing Derivative .....	36
4.3	Surface Immobilisation of Derivatives .....	38
4.4	Electrochemical Behaviour .....	39
4.5	Outlook and Perspective for Device Integration .....	44
5	Ultrafast Electron Transfer from CuInS <sub>2</sub> Quantum Dots to CAT1 and CAT1-CO <sub>2</sub> H for Hydrogen Production: <i>Rethinking the Binding Models</i> ( <b>Paper III</b> ).....	46
5.1	Motivations and Background .....	46
5.2	Photocatalysis Performance .....	48
5.3	Spectroscopic Characterisation and PL Quenching .....	49
5.4	Transient Absorption Spectroscopy for ET Rates.....	52
5.5	Modelling the System .....	54
5.6	Outlook and Implications.....	56
	Appendix: Extracted $\lambda$ and [QD] values .....	57
6	Summary and Outlook.....	58
7	Brief Synopsis of Other Projects .....	60
7.1	MWCNT-Based Inks .....	60
7.2	Polymer End-Functionalised with Catalyst.....	62
8	Résumé en Français .....	64
9	Popular Scientific Summary .....	67
10	Populärvetenskaplig Sammanfattning .....	68
11	Acknowledgements .....	69
	References.....	71

# Abbreviations

AEM	Anion Exchange Membrane
AWE	Alkaline Water Electrolysis
BPM	Bipolar Membrane
CA	ChronoAmperometry
CAT1	[Co <sup>III</sup> (N <sub>4</sub> H)Cl <sub>2</sub> ] <sup>+</sup> a.k.a. [Co <sup>III</sup> (CR)Cl <sub>2</sub> ] <sup>+</sup>
CB	Conduction Band
CEPT	Concerted Electron-Proton Transfer
CFE	Capillary-Fed Electrolysis
CO <sub>2</sub> RR	CO <sub>2</sub> Reduction Reaction
CPE	Controlled Potential Electrolysis
CV(s)	Cyclic Voltammetry/Voltammogram(s)
DFT	Density Functional Theory
DHA	DeHydroAscorbic acid
DMF	<i>N,N</i> -DiMethylFormamide
$E_{1/2}$	half-wave potential
EC	Electrolyser Cell
EC	Electrochemical step, then Chemical step (mechanism)
EDL	Electrical Double Layer
EI	Electronic Ionisation
EnT	Energy Transfer
EPR	Electron Paramagnetic Resonance (spectroscopy)
ESI	Electrospray Ionisation
ET	Electron Transfer
F4TCNQ	2,3,5,6-tetrafluoro-7,7,8,8-tetracyanoquinodimethane
Fc	Ferrocene
FE	Faradaic Efficiency
FOWA	Foot-Of-the-Wave Analysis
fs-TA(S)	femtosecond Transient Absorption (Spectroscopy)
GC	Gas Chromatography
GC	Glassy Carbon
HER	Hydrogen Evolution Reaction
ICP	Inductively Coupled Plasma (atomic emission spectroscopy)
IR	InfraRed (spectroscopy)
ISET	Inner-Sphere Electron Transfer
KD	negligible substrate consumption (Kinetic zone)
KS	S-shaped (Kinetic zone)
KT2	Total catalysis 2 (Kinetic zone)
LED	Light-Emitting Diode
MBM	poly(methyl methacrylate)- <i>b</i> -poly( <i>n</i> -butyl acrylate)- <i>b</i> -poly(methyl methacrylate)
MIR	Mid-InfraRed
MS	Mass Spectrometry
MWCNT(s)	Multi-Walled Carbon NanoTube(s)
NHE	Normal Hydrogen Electrode
NMR	Nuclear Magnetic Resonance (spectroscopy)
OSET	Outer-Sphere Electron Transfer
P3HT	poly(3-hexylthiophene)
PC	Photocatalytic

PCET	Proton-Coupled Electron Transfer
pCNA	para-cyanoaniline
pCNAH.BF <sub>4</sub>	para-cyanoanilinium tetrafluoroborate
PEC	Photoelectrochemical
PEM	Proton Exchange Membrane
PGM	Platinum Group Metals
PIA	Photo-Induced Absorption
PL	Photoluminescence
PT	Proton Transfer
PV	Photovoltaic(s)
PVC	poly(vinyl chloride)
PV-EC	Photovoltaic-electrochemical
Q	Quencher
QD(s)	Quantum Dot(s)
RHE	Reversible Hydrogen Electrode
SAC	Single Atom Catalyst
SI	Supporting Information
SOE	Solid Oxide Electrolysis
TBABF <sub>4</sub>	TetraButylAmmonium tetrafluoroborate
TCSPC	Time-Correlated Single Photon Counting
THF	TetraHydroFuran
TOF	TurnOver Frequency
TON	TurnOver Number
UV-Vis	UltraViolet-Visible (spectroscopy)
VB	Valence Band
WOR	Water Oxidation Reaction
$\Delta E$	peak potential separation

# 1 Introduction

*“Everything in life is somewhere else, and you get there in a car.”*

– E. B. White

Modern civilisation has largely been built on the basis of fossil fuel consumption, and remains heavily dependent to the present day.

However, in the face of society’s ever increasing demand for energy, the environmental impacts resulting from the emissions given off by the combustion of hydrocarbons – including both toxic air pollutants<sup>1</sup> and greenhouse gasses<sup>2</sup> – and the inherently finite nature of fossil fuel reserves – which take millions of years to form – are issues with which we shall have to reckon sooner rather than later.

*“The 21st century will be largely defined by the way we face and resolve the energy crisis.”*

– Armaroli and Balzani<sup>3</sup>

Decarbonisation (more specifically, defossilisation) of the of the economy – i.e. reaching carbon neutrality and closing the carbon cycle (**Figure 1.1**) – is therefore a major global priority.<sup>3</sup>

Renewable sources of electricity have seen rapid growth in recent years, especially solar and wind energy (wind in fact being an indirect form of solar energy), but the intermittent nature of these weather-dependent sources and the impracticality of connecting all vehicles and remote settlements to the electrical grid will necessitate the development of medium- to long-term energy storage solutions.<sup>4</sup>

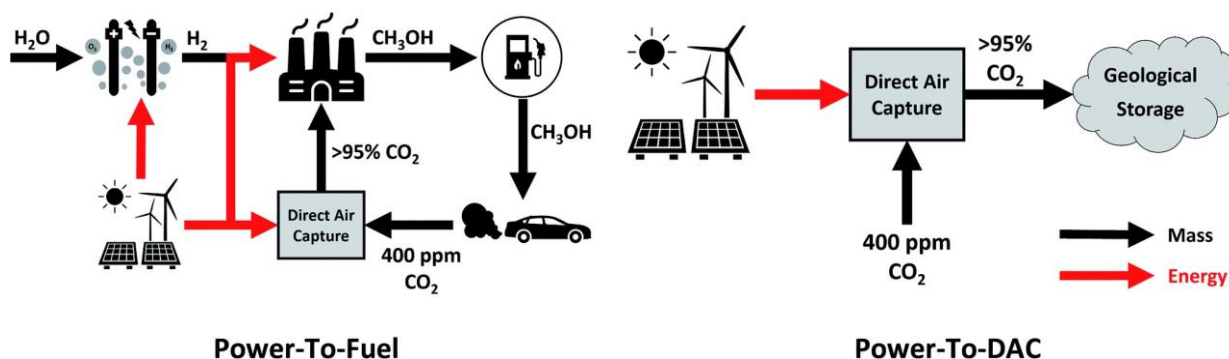


**Figure 1.1:** Illustration of strategies towards achieving a circular economy and closing the carbon cycle, evaluated by Daggash *et al.*, showing the roles which renewable energy sources (represented by wind and solar) and hydrogen generated from them would play. Reproduced from Ref. 5 with permission from the Royal Society of Chemistry.

Solar fuels represent one of the most promising strategies in this regard, efficiently storing captured solar energy in chemical bonds, which represent the most versatile and highest energy density storage mechanism that is technologically accessible to society (**Figure 1.2**).<sup>4\*</sup>

<sup>6</sup>Nuclear or antimatter-based energy storage is unlikely to be practical in the foreseeable future.

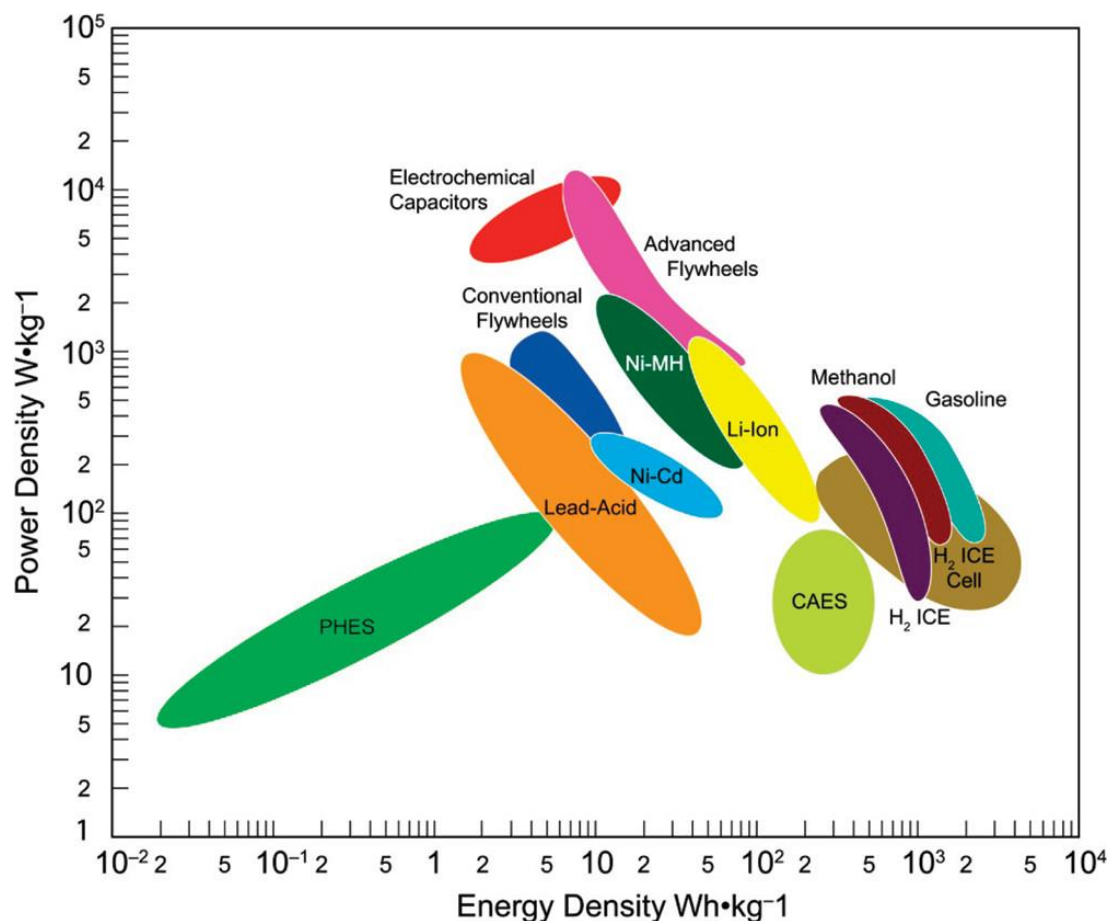


**Figure 1.2:** Ragone plot of specific power density versus energy density of various storage methods assessed by Cook *et al.* Chemical fuels sit on the far right side, having the highest energy densities of practical storage methods.<sup>4</sup> Reprinted with permission from *Chem. Rev.* 2010, 110, 11, 6474–6502. Copyright 2010 American Chemical Society.

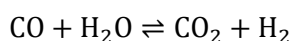
## 1.1 Hydrogen & the Green Energy Transition

Among potential solar fuels, hydrogen shows a lot of promise because it has the highest energy density per mass, is relatively simple to produce, and reacts efficiently with oxygen in fuel cells, giving off only non-toxic water as a by-product,<sup>7</sup> and is indeed already used as a motor fuel in some limited areas.

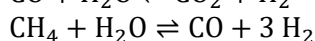
Although, pending further advances to enable a widespread infrastructure for hydrogen transport and storage, other solar fuels based on reduced carbon dioxide are likely to predominate, due to their easier storage and greater compatibility with current systems,<sup>8</sup> hydrogen nonetheless remains a critical chemical feedstock for the Haber–Bosch, Fischer–Tropsch and chemical hydrogenation processes, among others, ensuring its high demand (**Figure 1.3**).<sup>4</sup>

However, most hydrogen (around 96%) is currently produced from fossil fuel sources, such as via the water-gas shift reaction, which consumes carbon monoxide and releases carbon dioxide.<sup>9,10</sup> The carbon monoxide is generally produced from steam reforming, for example from methane in natural gas. This hydrogen is classified as ‘grey’ and is not compatible with the end goal of total decarbonisation.<sup>9,11</sup>

*Water-gas shift reaction:*



*Steam reforming of methane:*



The majority of the remaining hydrogen (around 4%) is produced by water-splitting in electrolyzers powered from the electrical grid. If (and only if) the electrical power is renewably sourced, this hydrogen may be classified as ‘green’.<sup>9,11,12</sup> However, the economic viability of this strategy is restricted by current

technology: current commercial electrolyzers are generally based on either Alkaline Water Electrolysis (AWE) or Proton Exchange Membrane (PEM, a.k.a. Polymer Electrolyte Membrane) electrolysis.<sup>13–15</sup>

AWE is the most mature technology, but suffers from issues of corrosion and complicated maintenance and construction. PEM electrolysis is a newer technology, relying on milder (normally acidic) conditions and a proton-conducting membrane which shows a lot of promise to pave the way towards a green hydrogen economy, but is held back by high manufacturing costs, in part due to the per-area cost of the membranes and in part due to dependence on rare Platinum Group Metals (PGMs). In particular, iridium oxide is usually employed as the catalyst for the water-oxidising anode and platinum as the catalyst for the hydrogen-evolving cathode. As such, these have been identified as a potential barriers to current PEM electrolyzers becoming economically competitive and upscalable.<sup>4,13</sup>

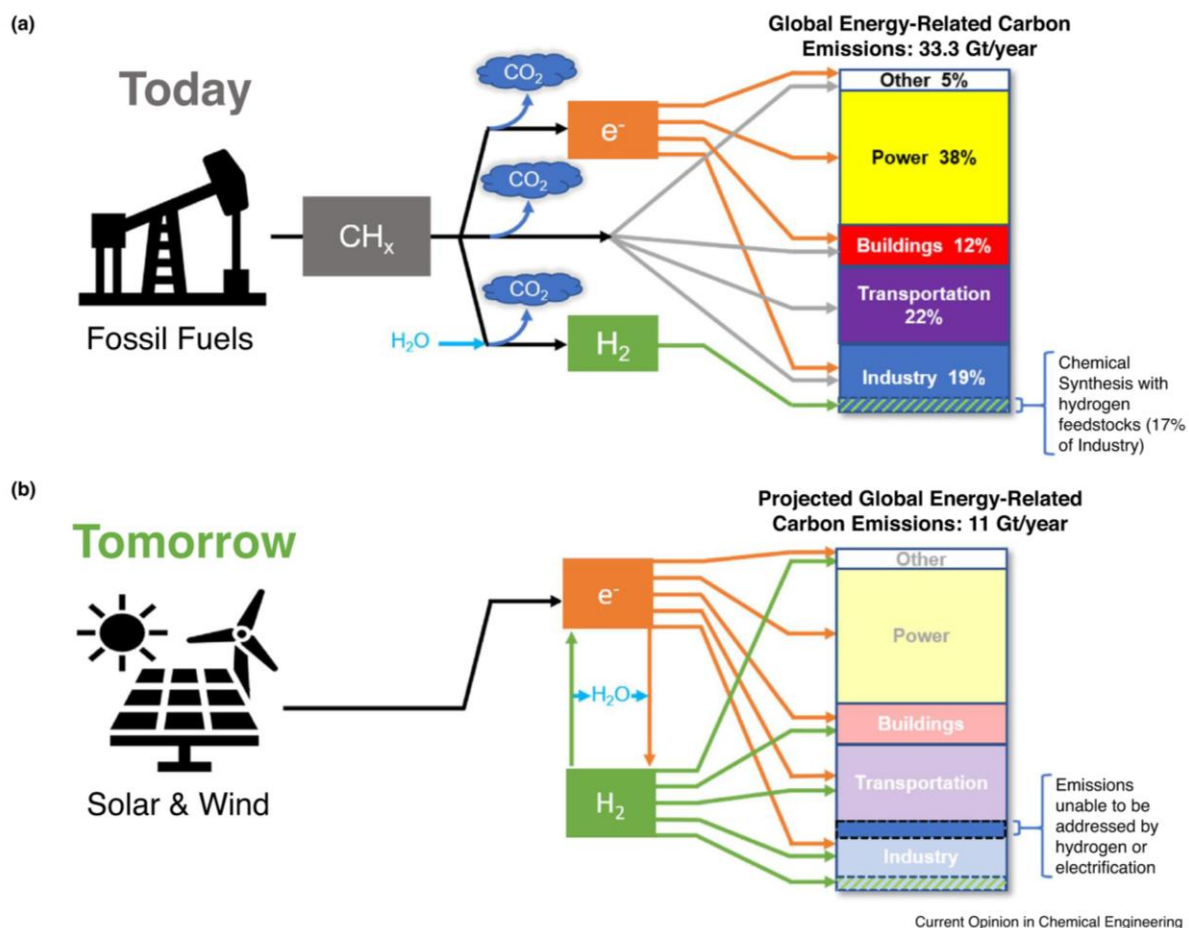


**Figure 1.3:** The potential role of hydrogen in the energy sectors of today and tomorrow envisaged by Yan and coworkers.<sup>9</sup> Reprinted from *Current Opinion in Chemical Engineering*, Volume 33, Oliveira *et al.*, A green hydrogen economy for a renewable energy society, 100701, Copyright (2021), with permission from Elsevier.

Note that other, less mature systems also exist which may become commercially relevant in the near future, such as: (i) Anion Exchange Membrane (AEM) electrolysis, which is similar to AWE with improved efficiency, but still requires corrosive alkaline conditions which can destabilise the membrane, and also typically has lower current densities than PEM,<sup>14</sup> (ii) Solid Oxide Electrolysis (SOE) technology, which uses a solid oxide electrolyte and requires high operating temperatures,<sup>14,15</sup> (iii) Bipolar Membrane (BPM) electrolysis, which combines the advantages of PEM and AEM, but is still a relatively new and under-explored approach,<sup>16,17</sup> and (iv) Capillary-Fed Electrolysis (CFE), which is a very recent advance in AEM technology, where the electrolyte is supplied to the electrodes by capillary action and gasses are evolved directly into the collection chambers.<sup>18</sup>

## 1.2 Natural and Artificial Photosynthesis

Clearly, in order to realise decarbonisation, a revolutionary approach is called for to sustainably produce and store the energy, fuels and chemical feedstocks demanded by society.

The ideal strategy would be to directly harness the energy that is continuously provided (and expected to continue reliably for billions of years) as a result of nuclear fusion occurring in the sun's core, arriving at Earth in the form of electromagnetic radiation, mainly as light, ultraviolet, and infrared radiation. It is often mentioned that the amount of solar energy that reaches the Earth *per hour and a half* exceeds the amount consumed by society *per year*.<sup>19,20</sup>

Harvesting solar energy directly into solar fuels with devices or systems that are composed of optimised, highly-effective and stable materials, made up of only abundant elements, would represent a huge leap forwards towards sustainability in the energy and chemical industries. The key sought-after properties can be expressed as a trifecta of *efficiency*, *robustness* and *scalability* (**Figure 1.4**). However, it is not enough for each material employed to individually meet these demands under different, incompatible conditions – the ultimate challenge is to develop and combine compatible materials which function simultaneously under the same conditions to complete the device or system.<sup>20–22</sup>

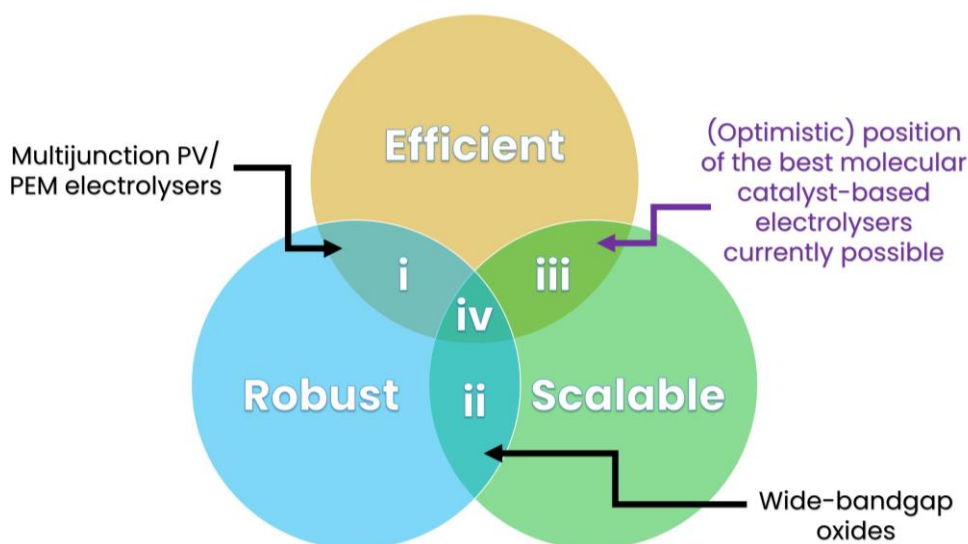


**Figure 1.4:** The trifecta of requirements for an artificial photosynthetic system to become economically viable, discussed by Gray and coworkers.<sup>21</sup> They point out that current multijunction PV/PEM electrolyser technology may be considered both robust and efficient, but ultimately not currently scalable due to membrane and component repair costs (*zone i*), while wide-bandgap oxides may be considered robust and scalable, but not sufficiently efficient (*zone ii*). The ultimate aim – *Holy Grail* – of artificial photosynthesis research is to develop complete systems that meet all requirements (*zone iv*). With further development, nascent molecular catalyst-based systems might be considered efficient and in principle scalable, but with poor robustness as their current major weakness, they would sit in *zone iii*.

Of course, in nature, autotrophic biological organisms (aside from extremophiles relying on geothermal vents) have long met their energy needs by converting sunlight, carbon dioxide and water into organic molecules through natural photosynthesis (illustrated in **Figure 1.5**). Millions of years of evolution have resulted in optimisation of many of the photosynthetic steps using only abundant elements available to biology, but organisms have the aim of producing biomass for their own survival, not economically desired fuels. As a consequence, generally their overall efficiency of solar energy conversion does not exceed 1%.<sup>23</sup>

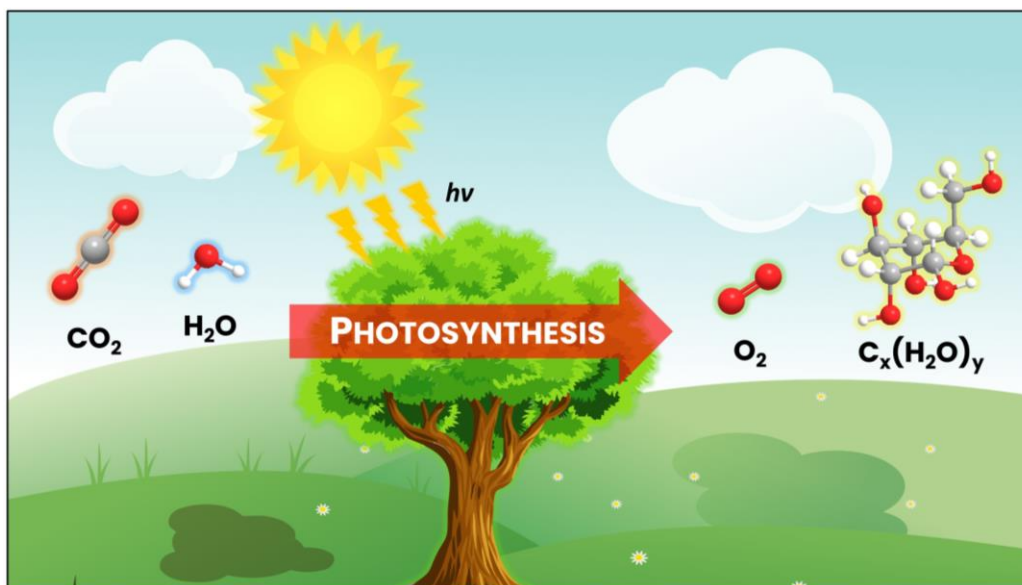
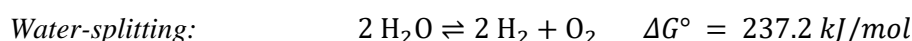


**Figure 1.5:** Illustration of natural photosynthesis, as carried out in plants, to convert carbon dioxide and water into carbohydrates (represented here by glucose) and oxygen using solar energy. (Weather not necessarily an accurate depiction of Sweden.)

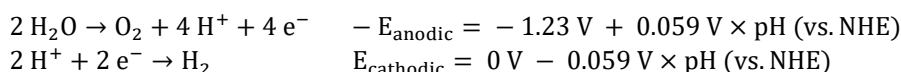
This means that, although *biomimicry* – copying natural systems directly – can lead to rapid progress in some facets of light-harvesting and water-splitting technology, fundamental optimisations with non-biological materials based on *bioinspiration* – understanding the principles behind natural systems and improving on them – can be exploited in designing artificial light-harvesting and water-splitting devices in order to cater far more efficiently to society’s needs than traditional agriculture or biofuel production, which rely on the natural photosynthesis in leaves. Indeed, there exists a spectrum of strategies between purely biological and purely artificial systems that can be created to try to reach the best of both worlds, but it is likely that purely biological systems will be incapable of reaching the efficiencies ultimately necessary.<sup>20</sup>

On this basis, artificial photosynthesis has been described as one of the Holy Grails of Chemistry.<sup>8,24</sup> The final aim would be the construction of an economically-viable artificial leaf<sup>25</sup> – a device which would produce hydrogen directly from water-splitting using captured sunlight:



More complex reactions to produce hydrocarbons or carbohydrates by the carbon dioxide reduction reaction (CO<sub>2</sub>RR) are also possible. This may simultaneously help in capturing CO<sub>2</sub> to close the carbon cycle, but technology is not advanced enough yet to do this directly with atmospheric CO<sub>2</sub> concentrations.

For natural photosystems H<sub>2</sub>O is used as the electron donor and the oxidative side of water-splitting is carried out by photosystem II and the reductive side by photosystem I,<sup>26</sup> but in artificial photosynthetic systems the half-reactions can be studied separately so they can be decoupled and each half optimised separately. This can be expressed as two half-reactions, for the water oxidation reaction (WOR) and the hydrogen evolution reaction (HER):



Alongside thermally-driven pathways,<sup>27</sup> the photon-based strategies to drive these half reactions with energy from absorbed sunlight can be classified by a few fundamental approaches (**Figure 1.6**):<sup>21,28–31</sup>

- (i) Photovoltaic-electrochemical (PV-EC),<sup>32</sup> connecting an electrolytic cell electrically to a solar cell. This has the advantages of exploiting a lot of already-existing technology and being compatible with the electrical grid, but suffers from the weaknesses of electrolysis cells discussed



previously and, for a complete integrated device, may represent a relatively complex system, due to the many different components.

- (ii) Photoelectrochemical (PEC),<sup>32</sup> an intermediate approach, consisting of an electrolysis cell where one or both of the electrodes is a photoelectrode based on a semiconductor capable of absorbing light both to generate photo-excited charge carriers to carry out one of the half-reactions, while also generating an electrical potential across the cell to enable the other electrode to perform the other half-reaction, which can eliminate the need for the external photovoltaic unit, or complement it in a PEC-PV tandem cell setup.
- (iii) Photocatalytic (PC),<sup>33</sup> involving only photosensitisers, typically connected directly to co-catalysts for one or both of the half-reactions, and dissolved directly in solution. This is therefore the simplest approach, but at the cost of lower efficiencies and there being no way to apply a bias or directly separate produced gasses by compartmentalisation of each half-reaction.

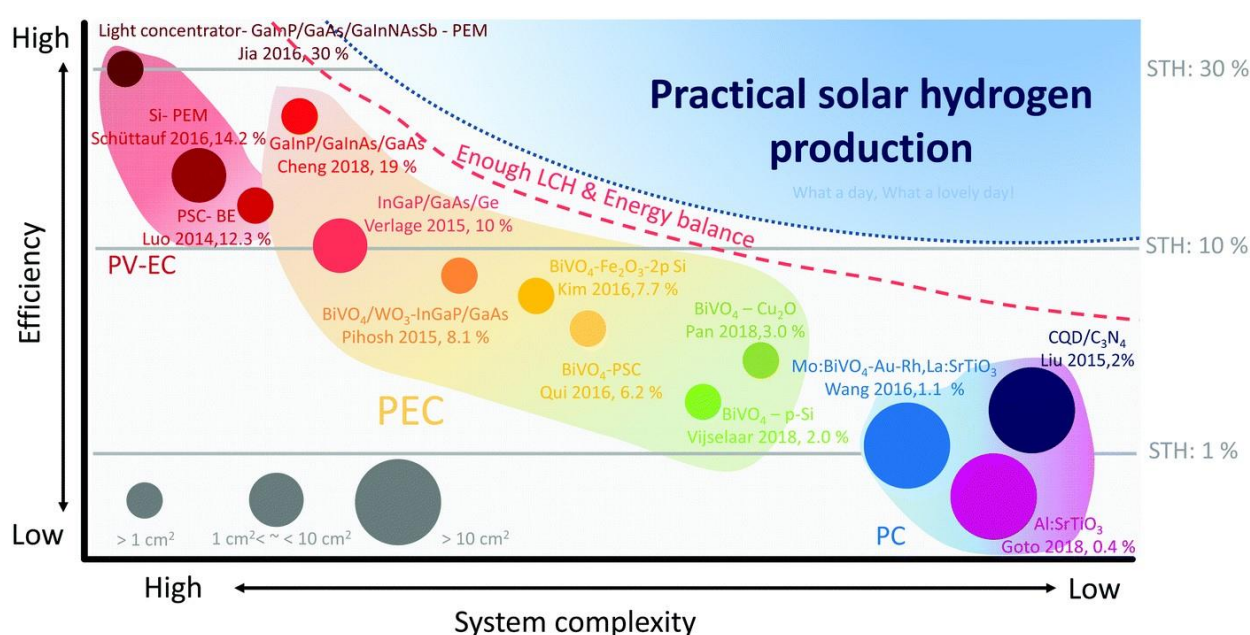


**Figure 1.6:** Overview of reported efficiencies for systems from each of the fundamental approaches, compared by Kim *et al.* Reproduced from Ref. 28 with permission from the Royal Society of Chemistry.

The larger eSCALED project (funded by the European Union's Horizon 2020 research and innovation programme under the Marie Skłodowska-Curie grant agreement No. 765376), of which this PhD project was a part, aimed to elaborate artificial leaf designs and focused on advancing the technological readiness and understanding of PV-EC designs, in particular of PEM electrolyzers, and developing scalable materials for the components of such a device, following the principles of bio-inspiration and bio-mimicry (**Figure 1.7**).

However, for performing each half-reaction a specific catalyst is typically employed in most strategies.<sup>34</sup> This is necessary to lower the reaction barriers and maximise efficiency and selectivity for the desired processes. Within this context, this work focuses on studying *molecular catalysts* for the HER, where the catalyst combines two protons and two electrons to release hydrogen.

These catalysts can be applied in cathodic materials for the reductive half reaction of water-splitting and integrated into electrolyser cells as part of a PV-EC approach, but also be used directly with photosensitisers in solution as part of a direct PC approach, from which a PEC approach can also be developed by immobilising the photosensitiser and catalyst together onto an appropriate semiconductor electrode.

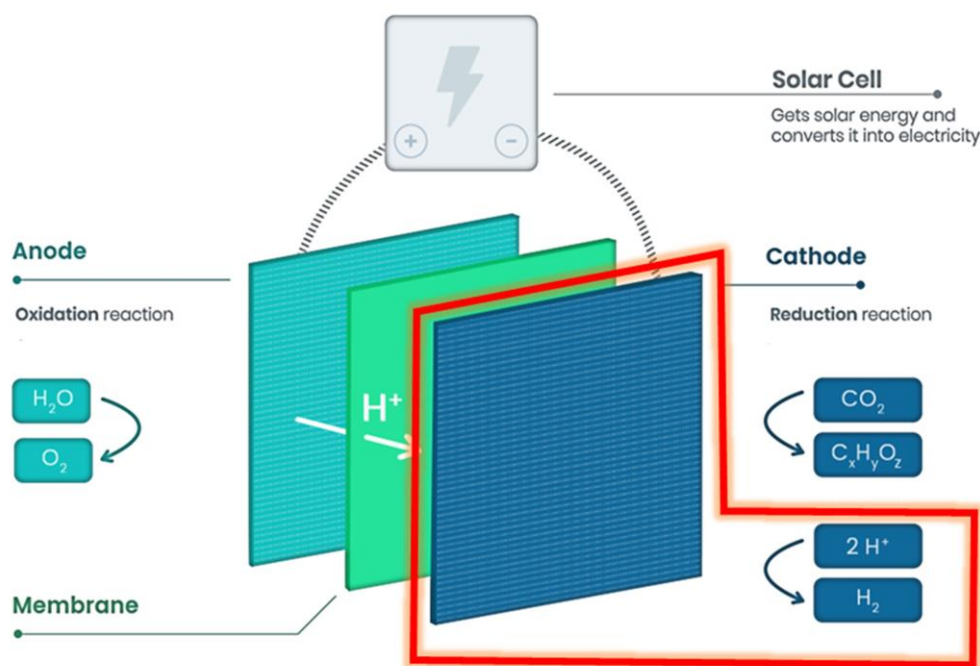


**Figure 1.7:** Schematic illustration of the eSCALED project artificial leaf design, with the cathode component for the electrocatalytic HER highlighted. Copyright (2018) ESCALED.

## 1.3 Hydrogen-Evolving Catalysts

### 1.3.1 Solid-state Material Catalysts

In terms of HER catalysts, aside from rare noble metals such as platinum, many of the more widely known and commonly studied catalysts are solid-state compound materials, MoS<sub>2</sub>-based catalysts being prime examples.<sup>34,35</sup>

Typically, the best solid-state material catalysts have good stability and can be nanostructured for high surface area. However, they also have a number of common issues: their active sites are often ill-defined and difficult to quantify, surface restructuring often occurs during catalytic turnover, selectivity for a specific reaction can be limited. Additionally, as is the case at all electrode surfaces, interface charge issues from double layer capacitance may hinder performance. The difficulty in understanding a specific process or mechanism responsible for catalysis in particular can make rational optimisation difficult. Furthermore, the large number of metal sites which are inactive or under the surface undermines the metal-atom economy.<sup>36</sup>

Therefore, there are advantages to moving towards catalysts that have well-defined active sites, in order to be able to apply rational design principles to improve the performance in multiple ways and achieve an efficient use of the metal, especially vital when scarce metals are employed. In this regard, single-atom catalysts (SACs) are one step towards improving the metal-atom economy, but still lack well-defined active sites.<sup>36,37</sup>

### 1.3.2 Bioinspiration from Enzymes

Nature provides a great example for optimising and controlling the catalytic activity of abundant metals in the form of enzymes. Through specifically evolved protein scaffolds, enzymes generally possess extremely well-defined active sites, resulting in very high selectivities and turnover frequencies (TOFs) of up to 10<sup>4</sup> s<sup>-1</sup> with high energetic efficiency, demonstrated by low required overpotentials in electrocatalysis. For the

HER, the prime examples are the [FeFe] and [NiFe]-hydrogenases (**Figure 1.8**).<sup>38</sup> In fact, in biology many of these enzymes are bidirectional, but the [NiFe]-hydrogenases are more active for the hydrogen oxidation reaction (HOR), whereas the [FeFe]-hydrogenases are more active for the HER. Thanks to their highly optimised mechanism, many operate electrochemically reversibly.<sup>39</sup>

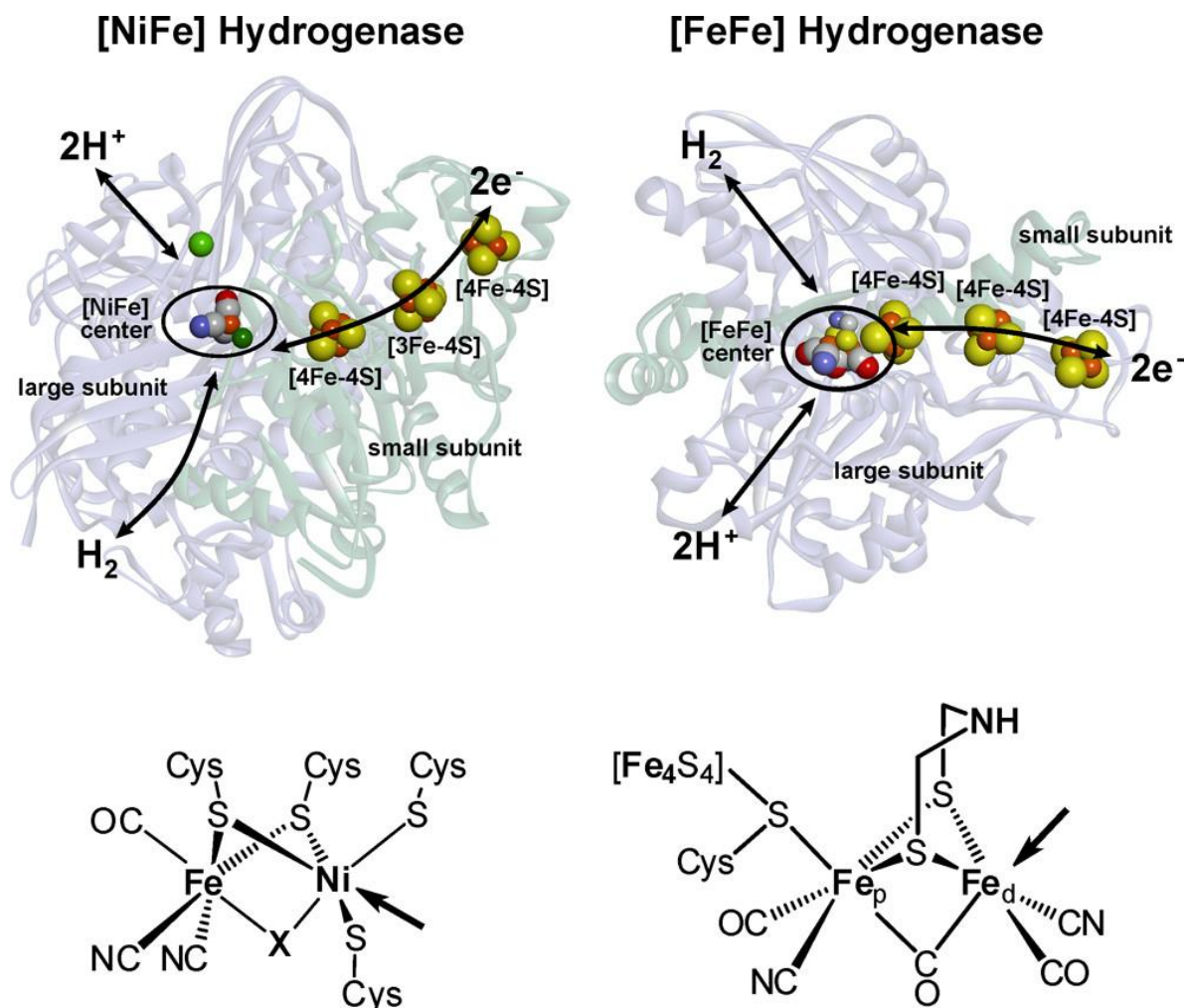


**Figure 1.8:** Above: Example structures of a [NiFe] and an [FeFe] hydrogenase with electron transfer chains and proton transfer pathways illustrated. Below: Cofactors with arrows indicating the open metal coordination sites.<sup>38</sup> Reprinted with permission from Chem. Rev. 2014, 114, 8, 4081–4148. Copyright 2014 American Chemical Society.

However, as touched on previously, using natural systems outside of their natural environment may render them ineffective and they are difficult to adapt without extensive biological or chemical engineering, which represent issues for scaling.<sup>40</sup> Hence, enzymatic catalysts typically display limited tunability, limited stability outside natural conditions, and prove difficult to connect to other materials due to their bulky size. Therefore, with inspiration from biology, developing catalysts on the molecular level – *molecular catalysts* – that can function outside of a tightly-controlled protein scaffold and have a much smaller footprint has emerged as an exciting and promising strategy (**Figure 1.9**).<sup>41,42</sup>

### 1.3.3 Molecular Catalysts and the State of the Art

Molecular catalysts for the HER typically consist of a metal centre or centres within a specific coordination sphere, normally exploiting the chelate and/or macrocycle effect to bind the metal tightly, although metal-free organic molecular catalysts for the HER are also known.<sup>43</sup>

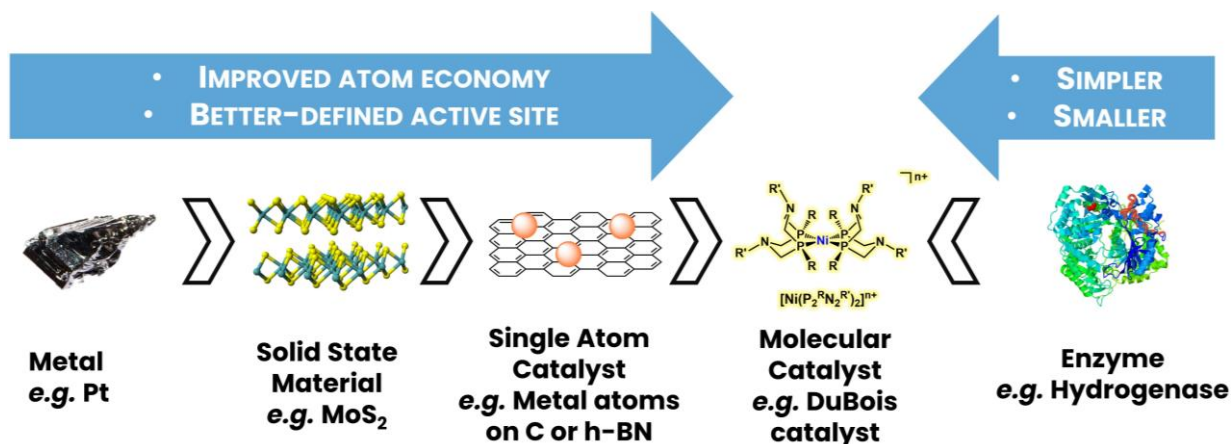


**Figure 1.9:** Rough illustration of the relative position of molecular catalysts compared to other catalytic materials, and the general advantages of molecular catalysts. A DuBois-type nickel bisdiphosphine HER catalyst is shown here as a representative molecular catalyst.<sup>44,45</sup>

For a well-designed molecular catalyst, the well-defined active site and coordination environment imparts a high selectivity, high catalytic activity high efficiency in terms of TOF and a low required overpotential, respectively. Furthermore, through tuning the critical steric and electronic effects from the inner and outer coordination spheres, it can be possible to optimise these properties. Elucidating key parts of the catalytic mechanism is imperative for rational tuning, but this is also typically possible thanks to the well-defined active site. Critically, such optimisations are the key to making Earth-abundant first-row transition metals sufficiently active and efficient for economically competitive catalysis to replace non-scalable rare metals like platinum. For this reason, there is significant interest in researching molecular catalysts for the future production of solar fuels.<sup>31,36,46</sup>

It has been deduced from studying natural and artificial systems that good molecular HER catalysts typically include certain features:<sup>42,46</sup> a metal centre which has its redox couples at moderate potentials, a clear coordination position on the metal for binding a hydride ligand (either vacant or with a labile ligand) and one or more basic sites which can receive and transfer protons to the active site and may facilitate highly-efficient proton-coupled electron transfer (PCET) steps (see **Figure 1.10**).<sup>47,48</sup> These groups are often termed proton relays.<sup>49</sup>

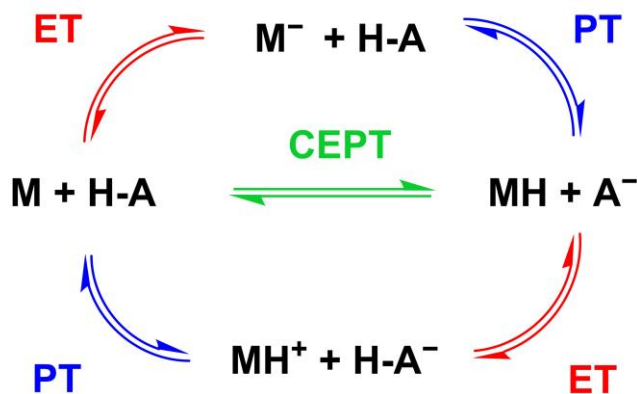


**Figure 1.10:** Scheme of possible proton-coupled electron transfer (PCET) mechanisms for the proton transfer (PT) from acid H-A and electron transfer (ET) to a species M. Top: Electron transfer followed by proton transfer (ETPT). Bottom: Proton transfer followed by electron transfer (PTET). Middle: Concerted electron-proton transfer (CEPT), where both the proton and electron are transferred in a single kinetic step, both passing through the same transition state via quantum tunnelling.<sup>47,48</sup>

There are numerous examples of such catalysts which are well-studied in the literature, most prominently the DuBois nickel bisdiphosphine catalysts,<sup>44,45</sup> [FeFe]-hydrogenase mimics,<sup>50</sup> cobaloximes,<sup>51,52</sup> and cobalt diimine-dioximes (**Figure 1.11**),<sup>53,54</sup> as well as phthalocyanines,<sup>55</sup> corroles,<sup>56</sup> porphyrins,<sup>57</sup> polypyridines<sup>58,59</sup> and bisthiosemicarbazones.<sup>60</sup>

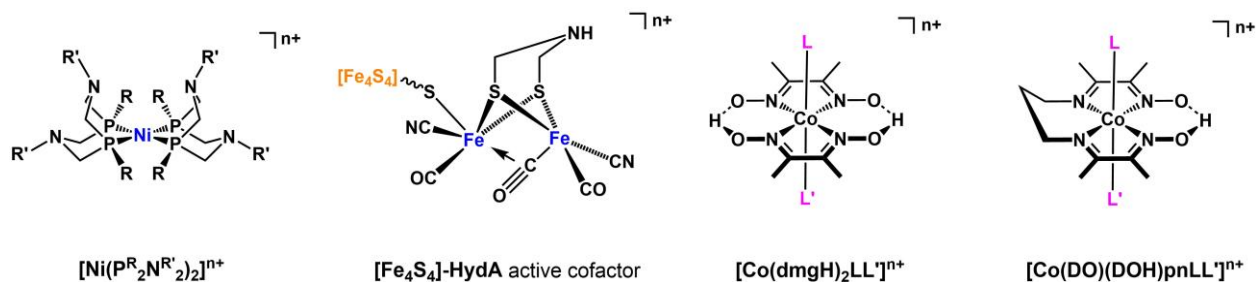


**Figure 1.11:** Scheme of the structures of the most prominent HER molecular catalysts,<sup>46</sup> from left to right: the DuBois nickel bisdiphosphine catalysts  $[\text{Ni}(\text{P}^{\text{R}_2}\text{N}^{\text{R}'_2})_2]^{n+}$ , where R and R' can be alkyl or aryl groups; the active cofactor of [FeFe]-hydrogenases, on which their mimics are based; cobaloximes  $[\text{Co}(\text{dmgH})_2\text{LL}']^{n+}$ ; and cobalt diimine-dioximes  $[\text{Co}(\text{DO})(\text{DOH})\text{pnLL}']^{n+}$ . L and L' can be solvent molecules, halides, a hydride or other ligands. Overall charges depend on metal oxidation state and ligands.

Nonetheless, the perceived major weakness of molecular catalysts is their limited stability.<sup>36,46</sup> This is an issue that cannot be overlooked: thinking back to the trifecta of *efficiency*, *robustness* and *scalability*, it is necessary to meet all three of these demands for commercial viability.<sup>21,42</sup> Thus developing and utilising ever more stable molecular catalysts is a priority for the field. In biological systems, enzymes overcome this issue by being constantly regenerated, but for molecular catalysts this is not yet possible, although a reserve of excess catalyst may be included in some systems to replace that which degrades.<sup>61</sup>

### 1.3.4 Immobilisation Strategies

Beyond this, for incorporation into PV-EC or PEC devices, it is critical to stably heterogenise the catalyst onto the electrode or photoelectrode. Unless the unmodified catalyst naturally adsorbs strongly on the surface, appropriate modification of the catalyst's molecular structure is required to add 'anchoring' functional groups, which immobilise the active site on the specified material through covalent bonds or intermolecular forces. Which anchoring groups will be effective depends on the material in question and what reaction the catalyst is carrying out. For the HER in water, the anchoring group must be water-tolerant under the reducing conditions applied.<sup>29,31,46</sup>

In the research setting, electrolyser cathodes for PV-EC are commonly built from  $\text{sp}^2$  carbon materials, such as glassy carbon, carbon fibre-based gas diffusion layers, multi-walled carbon nanotubes (MWCNTs) and graphite-based carbon pastes. To bind onto these materials, on the one hand covalent binding can be achieved by modifying the carbon surface through diazonium reduction reactions (**Figure 1.12**).<sup>62</sup> On the other hand, intermolecular forces such as  $\pi$ - $\pi$  interactions can be exploited by incorporating a polyaromatic group on the catalyst, such as pyrene (**Figure 1.13**).<sup>63</sup>

For photoelectrodes based on semiconductors for PEC, typical anchoring groups for ionic binding include carboxylic acids, phosphonic acid, hydroxamic acids and silatranes (**Figure 1.14**).<sup>64,65</sup> An additional strategy for either case is to entrap the catalyst in a polymeric layer at the electrode or photoelectrode surface.<sup>66</sup>

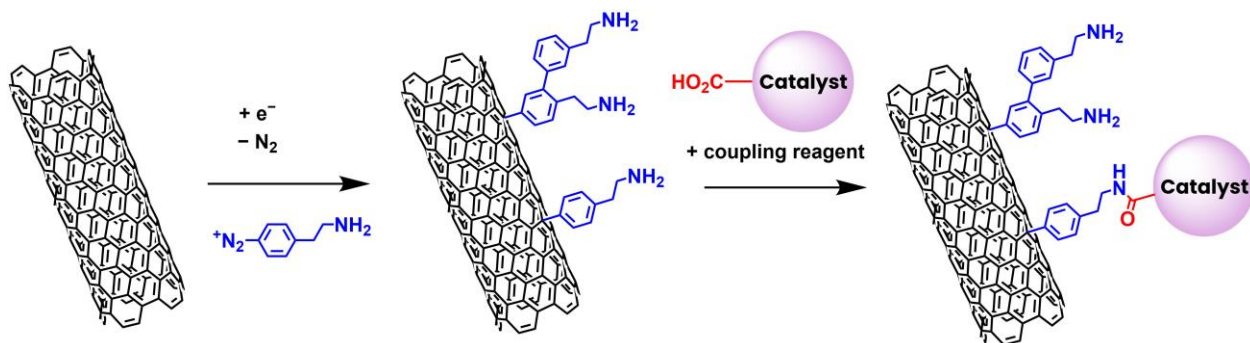


**Figure 1.12:** Example scheme of covalent immobilisation of a catalyst on carbon nanotubes by first modifying the surface through a diazonium reduction reaction, then performing an amide coupling reaction.<sup>46</sup>

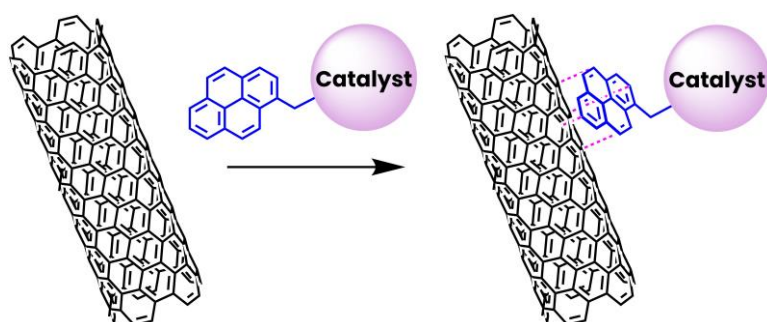


**Figure 1.13:** Example scheme of non-covalent immobilisation of a catalyst on carbon nanotubes by  $\pi$ - $\pi$  interactions with a pyrene anchoring group.<sup>46</sup>

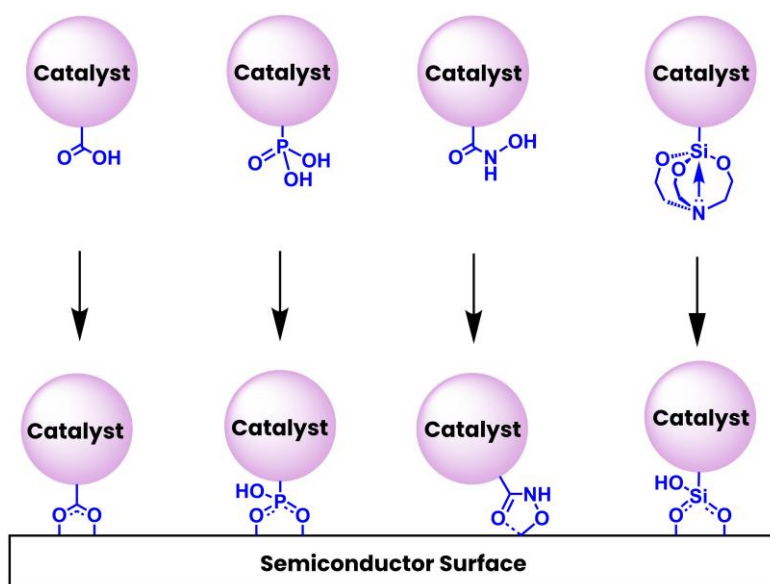


**Figure 1.14:** Example scheme of anchoring groups for semiconductor materials and their normally most favoured binding modes are shown. From left to right: carboxylic acid, phosphonic acid, silatrane and hydroxamic acid.<sup>64,65</sup>

## 1.4 The Molecular Catalyst ‘CAT1’

The cobalt complex commonly referred to in the literature either as  $[\text{Co}^{\text{III}}(\text{N}_4\text{H})\text{Cl}_2]^+$  or  $[\text{Co}^{\text{III}}(\text{CR})\text{Cl}_2]^+$  (where CR = 2,12-dimethyl-3,7,11,17-tetra-azabicyclo[11.3.1]-heptadeca-1(17),2,11,13,15-pentaene), was first synthesised half a century ago by Long and Busch.<sup>67,68</sup> In this thesis and the appended papers, it is abbreviated as ‘CAT1’ or ‘1’.

Like other related cobalt tetraazamacrocyclic complexes, such as cobaloximes and diimine-dioximes, it bears some structural resemblance to vitamin B12,<sup>69–71</sup> which is a vital redox-active cofactor for certain isomerases, methyltransferases and dehalogenases (Figure 1.15).<sup>72</sup>

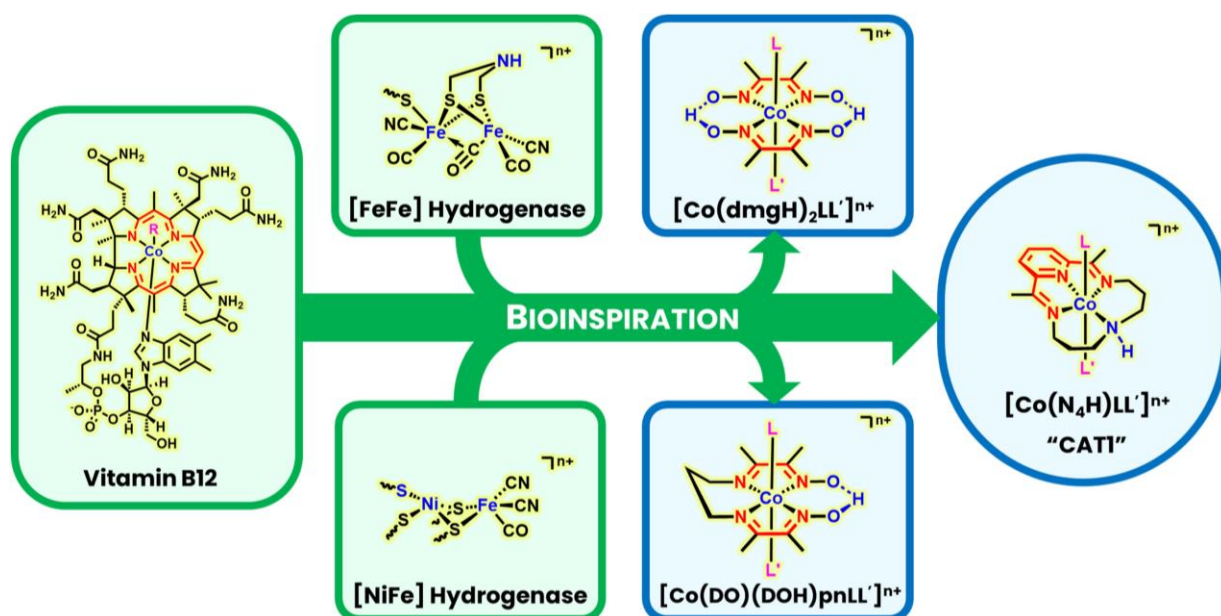


**Figure 1.15:** Illustration of vitamin B12 (for which R = Me<sup>-</sup>, H<sub>2</sub>O, CN<sup>-</sup>, adenosyl, etc. in nature) and natural hydrogenases as the key sources of bioinspiration for cobalt tetraazamacrocyclic molecular catalysts, including CAT1 on the right. L and L' can be solvent molecules, halides, a hydride or other ligands. Overall charges depend on metal oxidation state and ligands. Chelating nitrogen atoms and associated extended conjugated systems coloured red to highlight structural similarity. Metal centres and nearby basic groups which may act as proton relays coloured blue.<sup>71</sup>

One decade ago, CAT1 was discovered by Leung *et al.* to be an effective molecular catalyst for the HER in organic and aqueous conditions.<sup>73</sup> Subsequent studies into its mechanism and performance have shown that it has excellent properties for the HER under various conditions.<sup>74–79</sup> Under homogeneous electrocatalytic conditions, it displays a high maximal turnover frequency (indicating a high catalytic activity), retains a low overpotential requirement (meaning a high energy efficiency for catalysis) and achieves a faradaic yield of H<sub>2</sub> of over 90% (meaning efficient transfer of the electrons to the protons without loss of electrons to other undesired processes).

The structure of the macrocyclic ligand is believed to stabilise the complex against decomposition by tightly binding the cobalt centre and also by the extended conjugation of the diiminopyridine core playing a role in resisting hydrolysis and stabilising the various oxidation states while modulating the redox potentials, possibly involving non-innocent behaviour.<sup>78</sup> The axial ligands become labile in the Co(I) to provide the site for binding a hydride, while the amine group has been identified as a probable proton relay.<sup>75</sup> Incidentally, probably for similar reasons, CAT1 is also a significantly active catalyst for the CO<sub>2</sub>RR.<sup>80,81</sup>

**Paper I** covers our studies into the HER catalytic mechanism in organic conditions, using electrochemical and spectroscopic techniques to elucidate the structures of intermediates, the mechanistic steps, and the rates of those steps. Such studies serve to evaluate and explain the reasons behind the catalyst's effectiveness and also to inform us as to which parts of the molecular structure are critical for catalytic function – such as proton relays. These points are important in the rational design of novel derivatives, either for the sake of improving the catalytic properties or of introducing anchoring groups for device compatibility.

Additionally, CAT1 is known for its tolerance to O<sub>2</sub> and stability.<sup>76,77,82</sup> This robustness makes it an interesting candidate for testing integration onto electrolyser cathodes for PV-EC water-splitting, since the typically poor robustness of molecular catalysts is normally the limiting factor in the efficiency and longevity of systems that rely upon them. **Paper II** covers our work into developing novel derivatives of CAT1 which can be immobilised on electrodes and then studying the performance of the heterogenised catalyst under these conditions for the electrocatalytic HER, paying particular attention to the effects of the modification with an anchoring group at different positions to highlight rational design principles.

Meanwhile, under PC water-splitting conditions, relatively high turnover numbers (TONs) are reported at both high and low concentrations of catalyst with a variety of photosensitisers,<sup>75,76,83-85</sup> most notably reaching TONs of up to 7700 per catalyst with CuInS/ZnS core-shell quantum dots (QDs),<sup>86,87</sup> illustrating the versatility of the catalyst. **Paper III** covers our studies into the causes for the remarkable photocatalytic performances of CAT1 with CuInS QDs, but using shell-less 'hybrid passivated'<sup>88</sup> CuInS QDs which were adapted for compatibility with mesoporous NiO thin films. This paves the way for the future incorporation of this system onto photoelectrodes for PEC water-splitting. Comparing the electron transfer rates and quenching efficiency of CAT1 and a derivative with an intended anchoring group, a binding model for static quenching was developed to account for the reliably ultrafast electron transfer.



## 2 Key Experimental Techniques

In order to analyse the processes, species and products related to catalysis, a number of analytical techniques are extremely useful. Among others, these include:

### Nuclear Magnetic Resonance Spectroscopy

In brief, nuclear magnetic resonance spectroscopy (NMR) is a technique which uses radio frequency electromagnetic pulses to probe samples within a strong magnetic field. This excites the spin states of a specific isotope of atomic nuclei in the sample for which the pulse frequency corresponds to the energy gap between the nuclear spin states of the nucleus. The resulting signals are used for determining the number of different chemical environments that nucleus exists in within the sample (from how many separate peaks appear), as well as certain details about these environments, such as the number and identity of certain neighbouring nuclei (based on peak-splitting from *J-coupling* effects), and the probable surrounding functional groups (based on the *chemical shift*,  $\delta$ , affected by ‘shielding’ and ‘deshielding’ inductive effects, as well as anisotropic effects in e.g. aromatic systems).

Altogether, the information provided by NMR make it an extremely powerful technique for identifying chemical structures – both of synthesised species and isolated catalytic intermediates. However, NMR can only provide information for nuclear isotopes with a non-zero spin quantum number,  $I$ . Some of the most commonly studied nuclei are  $^1\text{H}$ ,  $^{13}\text{C}$ ,  $^{19}\text{F}$  and  $^{31}\text{P}$ , for all of which  $I = \frac{1}{2}$ . For isotopes where  $I > \frac{1}{2}$ , termed quadrupolar nuclei, additional effects make interpretation more complicated. Additionally, the presence of paramagnetic species (species with unpaired electrons) similarly can make interpretation difficult.

### Electron Paramagnetic Resonance Spectroscopy

On the other hand, electron paramagnetic resonance spectroscopy (EPR) is an analogous technique that probes paramagnetic samples by exciting the spin states of unpaired electrons to determine details about their environment. The main details are the *g-factor* (roughly equivalent to the chemical shift in NMR), the *zero field splitting* and *exchange coupling* effects in systems with multiple unpaired electrons, the *hyperfine* and *superhyperfine coupling* (analogous to NMR *J-coupling*) effects arising from the interaction with the nuclei on which the electrons are localised and nearby ones, and the line shape of the spectrum. From these details, a lot of information can be extracted about the parts of the structure of the sample species that affect the unpaired electrons.

### Mass Spectrometry

Mass spectrometry (MS) is another analytical technique which is useful for determining the structure of chemical species. In chemical synthesis, MS helpfully complements NMR because it generally identifies which species are present more directly, while NMR excels at revealing the structure of those species.

Typically, samples are first ionised – this can be either by a ‘hard’ ionisation method, such as electron ionisation (EI), or a ‘soft’ ionisation method, such as electrospray ionisation (ESI). The generated ions are then separated by their mass-to-charge ( $m/z$ ) ratio before reaching the detector. Once ionised, fragmentation processes can occur, which can indicate which groups are present in the structure after interpretation of the differences in  $m/z$  between the product peaks of charged fragment ions and the parent peak, corresponding to the unfragmented species. Hard ionisation methods result in a lot of fragmentation, whereas soft ionisation methods discourage fragmentation and often allow the observation of the parent peak.

## Electrochemical Techniques

Most analytical electrochemical techniques involve either recording the current (flow of electrons) that passes through a solution when a fixed electric potential is applied (*potentiostatic* conditions) or, *vice versa*, recording the potential across a sample when a fixed current is maintained (*galvanostatic* conditions).<sup>89</sup>

To do this, a device known as a *potentiostat* is typically connected to a three-electrode setup, including (i) a *working electrode*, at which the electrochemical event of interest occurs, (ii) a *reference electrode*, which should have a reliable and known electrode potential, against which the potential applied by the potentiostat is controlled, but through which no current should flow, and (iii) a *counter electrode*, through which current flows to complete the electrical circuit, but which should be inert and highly conductive to not interfere with measurements at the working electrode.

The electrochemical cell is filled with an *electrolyte solution*, usually containing an inert ionic species, known as *supporting electrolyte*, to make it highly conductive. Soluble chemical species can be studied by being dissolved directly in this solution (homogeneous conditions), while materials can be studied by being used directly as the working electrode, or by being immobilised on the surface of a standard working electrode.

Most electrochemical cells (electrolysers, fuel cells, batteries etc.) operate with just two electrodes – a designated anode and cathode, since the current is expected to flow in only one direction. The current response to an applied potential across the entire device can still be recorded to measure the performance, but without the third electrode, it is not possible to accurately control the precise conditions (such as potential) at the electrode surfaces, which is important for analytical studies.

Two of the most commonly used electrochemical analytical techniques are *chronoamperometry* (CA) and *cyclic voltammetry* (CV).<sup>89-91</sup> In chronoamperometry, a constant potential is applied across the cell (*controlled potential electrolysis*, CPE) and the current response over time is measured. This can be used to measure *e.g.* the rate of redox catalysis at the working electrode, as well as stability over time.

In cyclic voltammetry, the applied potential starts at an initial potential and is first swept at a constant scan rate,  $v$ , in one direction (either to more negative, reducing potentials, or to more positive, oxidising potentials) up to a certain bound, then swept back in the opposite direction to another bound and back, cycling for one or more scans. The current response is measured over the course of this potential cycling.

The constant change in applied potential combined with sweeping back in the reverse direction means that cyclic voltammetry, performed under appropriate conditions, can confer a remarkable amount of information for redox processes and chemical reactions that are connected to them, including: chemical reversibility (if the product of an electrochemical reaction can be converted back into the starting reactant), electrochemical reversibility (related to the rate of electron transfer), reaction rates for connected reactions, and whether the redox active species adsorbs on the electrode surface or diffuses freely, as well as the rate of that diffusion.

## Gas Chromatography

Gas chromatography (GC) is a chromatographic method for separating and analysing gaseous or volatile substances. The sample is injected into a carrier gas as the mobile phase and passes through a stationary phase column (often based on a polysiloxane). When fitted with a thermal conductivity detector (TCD),  $H_2$  gas can be quantified from injected samples taken from the headspace of an electrochemical cell or photocatalysis reaction vial.<sup>92</sup>

## Steady-State Absorption and Fluorescence Spectroscopy

Absorption spectroscopy measures the absorbance of radiation by a sample across a frequency range of electromagnetic radiation. Aside from NMR and EPR discussed above, which cover the radio wave range, two of the most common ranges for absorption spectroscopy are the ultraviolet-visible (UV-Vis) and infrared (IR) ranges.

UV-Vis spectroscopy is commonly used to determine the concentration of a species in solution using its known molar extinction coefficient at a specific wavelength using the Beer-Lambert law, which relates the absorbance,  $A$ , to the pathlength of the sample holder,  $l$ , and the molar extinction coefficient,  $\epsilon$ , and concentration of the absorbing species,  $c$ :

$$A = \epsilon lc$$

More fundamentally, the wavelengths and intensities of absorption can give information about the electronic excitations that occur in the molecular or material, since the wavelength,  $\lambda$ , is the inverse of the frequency,  $\nu$ , and related to the energy of the absorbed photon by the Planck relation (below) and therefore to the difference between the ground and excited state energy levels of the electron. The absorption intensity indicates the ‘allowedness’ of that transition, based on quantum mechanical selection rules.

$$E = h\nu = \frac{hc}{\lambda}$$

Fluorescence spectroscopy is a complementary technique which records the emission of light by a sample. If the sample is initially excited by absorbing photons provided through irradiation with a beam of ultraviolet or visible light, this emission is referred to as photoluminescence. Once electrons are in an excited state, they may fall back to the ground state over time, emitting photons of the corresponding energy difference, if the decay is radiative. The relative intensity of the emitted light over a range of wavelengths is recorded. For an emissive species, there are many factors involved in the intensity of emission, relating to the rate of emission versus the rates of other decay pathways available for the excited state (determining its lifetime), as well as the *Stokes shift* – the difference between the emission maximum and the corresponding absorption maximum. Fluorescence spectroscopy can be used to deduce the nature of excited state energy or electron transfer (EnT or ET) processes and their rates and efficiencies.<sup>93</sup>

## Time-Resolved Spectroscopy

Beyond the steady-state spectroscopy techniques discussed above, time-resolved spectroscopy techniques measure the change in absorbance or fluorescence of a sample over time, to follow dynamic processes. Typically, the process is initiated by illumination of the sample by a light source. For following processes on very short time scales, the photons of light need to be sent in ultrafast pulses: for this purpose, ultrafast laser spectroscopy techniques are used.

Time-correlated single photon counting (TCSPC) is a technique which records a decay profile for the emission of a species over time after its excitation by photons. This is achieved by exciting the sample with a mode-locked pulsed laser with a high repetition rate (number of pulses sent per second) and recording the emission of single photons from the sample, correlating their time of arrival after the time of the laser pulse,  $\Delta t$ . This is measured by the detection signal being sent to a series of electronics components: a constant function discriminator (CFD) receives the signal, transfers it to a time-to-amplitude converter (TAC), which generates a voltage ramp – a voltage that increases linearly with time on the nanosecond timescale – so that the voltage is proportional to  $\Delta t$ . The voltage is amplified by a programmable gain amplifier (PGA) and converted into a numerical value by an analogue-to-digital converter (ADC). This setup allows the minimisation of false readings by accepting only signals within a certain range of voltages. The recorded signals are used to plot a histogram for the decay profile. From interpreting this plot and fitting it as a multi-exponential decay, lifetimes and relative contributions of multiple different decay processes can be extracted, something which is not possible in steady-state spectroscopy techniques. This is also especially useful in distinguishing between static and dynamic quenching processes where the excited state transfers

its energy or an electron (or hole) to a 'quencher' species, since excited state lifetimes are reduced in dynamic quenching scenarios, but not in static quenching ones.<sup>93</sup>

Femtosecond transient absorption spectroscopy (fs-TAS) is a pump-probe technique. The sample is excited using a short pulse laser (the pump), while the changes in absorption at certain time points after this excitation are measured using another, less intense pulse (the probe). There are multiple processes which contribute to the observed signal: the loss of the absorption by the initial ground state species (*ground state bleach*), the growth of new absorption by the excited state species and products of the resulting photo-induced reactions (*induced absorption*), and also emission processes from the excited state which are stimulated by the photons of the probe pulse (*stimulated emission*). From this, a lot of information can be gleaned regarding the dynamics of the excited state and the rates of the various induced chemical processes.<sup>94</sup>

### 3 Mechanistic Studies on CAT1 for the Hydrogen Evolution Reaction (Paper I)

#### 3.1 Motivations and Background

As discussed in **Section 1.4**, CAT1 displays a number of favourable properties for the catalysis of the HER, most notably its high robustness and resistance to oxygen, combined with its high efficiency in terms of  $\text{TOF}_{\text{max}}$ . Thus, although relatively under-explored compared to the more prominent HER molecular catalysts (DuBois, hydrogenase mimics, cobaloximes etc.), CAT1 was evaluated favourably, often in comparison to selected competing catalysts, in many previous publications that either studied its catalytic processes<sup>77,95</sup> or applied it directly in PEC dyad or PC systems,<sup>81,84,86,87,96,97</sup> or did both.<sup>75,76,78,85</sup>

In particular, compared against a series of other catalysts, it was noted by Roy *et al.* to stand out in terms of its total TON for hydrogen evolution when mixed with a few different standard chemical/photochemical reducing agents, and, interestingly, to retain HER activity under a range of acidic to neutral conditions and with most of the reducing agents tested at pH 7.<sup>79</sup> As discussed before, these are interesting key properties for PEM applications.

However, before our studies, precise metrics to benchmark the performance of CAT1 for comparison with other state-of-the-art HER catalysts were limited and not all of the specifics of the mechanism were firmly established. Understanding, for example, which parts of the macrocycle could be acting as a beneficial proton relay<sup>49</sup> would be important for informing rational design of derivatives of CAT1, which would pave the way for device integration or optimisation. Such a behaviour of the ligand system was previously postulated because of the reported pH dependence of the Co(III/II) redox couple.<sup>77</sup> This indicates the binding of a proton to the complex at the Co(II) oxidation state, even though formation of a cobalt-hydride from the Co(II) state is very improbable.

In terms of modifying the structure for whatever purpose, two sites emerge as the first choices in terms of simplifying the synthesis and maintaining maximal symmetry of the complex (which typically reduces complications that can arise from structural alterations). These are the pyridine's *para*-position and the amine on the macrocycle (**Figure 3.1**). If the amine, however, is critically involved as a proton relay in the HER catalytic mechanism, then it might be less appealing as a position for modification of the structure for catalytic optimisation, unless an alternative proton relay can be provided.

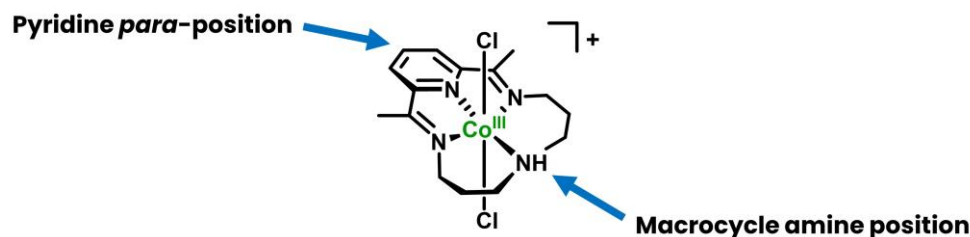


**Figure 3.1:** CAT1 in its air-stable Co(III) state with two chloride axial ligand. The most obvious positions for simpler structural modification are indicated by arrows.

The effects of substituting a methyl or hydroxymethyl group on the amine were recently studied in detail by Grau *et al.*<sup>75</sup> and, indeed, there were significant differences in the cyclic voltammetry profile of the Co(II/I) reduction and associated HER catalytic wave, which indicated a slower formation of Co(III)-hydride from the Co(I) state for both amine-modified derivatives, attributed by the authors to changes in geometry and electronic density at the cobalt centre. Nevertheless, the activation energies in both catalytic

pathways were reported not to significantly differ between the derivatives and CAT1, and, in fact, faster initial catalysis under photocatalytic conditions was reported. Altogether, this may imply that there is a negative effect on the kinetics of the step that is rate-limiting under electrocatalytic conditions, but this is not rate-limiting under those photocatalytic conditions. Therefore, the authors befittingly describe the role of the macrocycle ligand in the HER catalysis as ‘intricate’ – warranting further studies.

## 3.2 Previous Mechanistic Understanding

A heterolytic (i.e., relying on only a single catalyst site by itself to turnover, as opposed to homolytic, where two need to come into contact),<sup>98</sup> and most likely ECEC mechanism (E = single-electron reduction ‘electrochemical’ step; C = protonation ‘chemical’ step) had previously been proposed and supported by X-ray absorption spectroscopy,<sup>95</sup> and DFT calculations.<sup>75</sup> However, these previous studies focused mostly on photocatalytic conditions. Additionally, multiple groups had already noted that the protonation of the Co(I) state is unambiguously the rate-determining step for the overall HER under all electrocatalytic and photocatalytic conditions tested.<sup>75-77</sup>

## 3.3 New Studies in Paper I

To explore beyond previous work, new electrochemical investigations were carried out within the Artero group in organic conditions, using acetonitrile as the main solvent, since CAT1 is noted to display especially complicated behaviour in water, particularly regarding the relation of the onset of the HER catalytic wave to the Co(II/I) redox couple.<sup>77</sup> These investigations were supported by NMR and EPR spectroscopy to elucidate details about the structure and interaction or non-interaction with acid, as well as to identify possible ligands at the cobalt for each step.

The perchlorate salt of a Co(III) sample of CAT1 was used as the starting materials in the studies (the air-stable form, with an inert counter-anion).

### Electrochemical Characterisation

For homogeneous redox catalysis of electrochemical reactions, the waveform (shape of the response) from a CV experiment is determined by a number of conditions of the system (i.e. the concentrations of catalyst,  $C_P^0$  and substrate,  $C_A^0$ , the scan rate,  $\nu$ , and the homogeneous electron transfer rate constant,  $k_e$ ), analysed as the kinetic ( $\lambda$ ) and excess ( $\gamma$ ) dimensionless parameters.<sup>99</sup>

For identifying the nature of the waveform for an obtained cyclic voltammogram, *kinetic zone diagrams* are used. The kinetic zone diagram for a simple one-electron, one-substrate electrocatalytic is shown in **Figure 3.2**. The application of zone diagrams has however been extended to multi-electron, multi-substrate process by Dempsey and coworkers.<sup>100</sup> It is important to identify to which zone an obtained voltammogram belongs, so that the system can be adjusted to the desired behaviour by changing the conditions listed above. This is necessary because practical equations for accurately extracting the electron transfer rate,  $k_e$ , only exist for certain zones. Generally, KT2, KS and KD zones are the desired zones for this purpose.

For CAT1 dissolved in acetonitrile with an inert electrolyte salt (tetrabutylammonium tetrafluoroborate, TBABF<sub>4</sub>) under typical electrochemical conditions (catalyst concentration of 0.5 mM, standard three-electrode cell setup, glassy carbon working electrode, scan rate of 100 mV s<sup>-1</sup>), with gradual addition of the acid *para*-cyanoanilinium tetrafluoroborate (pCNAH.BF<sub>4</sub>) the voltammograms displayed in **Figure 3.3** were obtained. Of note are the usual redox responses of CAT1: the Co(III/II) redox couple at  $E_{1/2} = -0.47$  V ( $\Delta E_p = 92$  mV) and the Co(II/I) redox couple at  $E_{1/2} = -0.96$  V ( $\Delta E_p = 86$  mV) vs. Fc<sup>+</sup>/Fc. Both are quasi-reversible under these conditions. As the concentration of pCNAH.BF<sub>4</sub> was increased, clear changes occurred: a dramatic shift of the Co(III/II) couple to more positive potentials and a milder shift of the Co(II/I)

couple, matching previous observations by McCrory *et al.* in aqueous conditions.<sup>77</sup> Associated with the Co(II/I) couple was a growing catalytic wave, reaching a plateau at around 30 equivalents of acid.

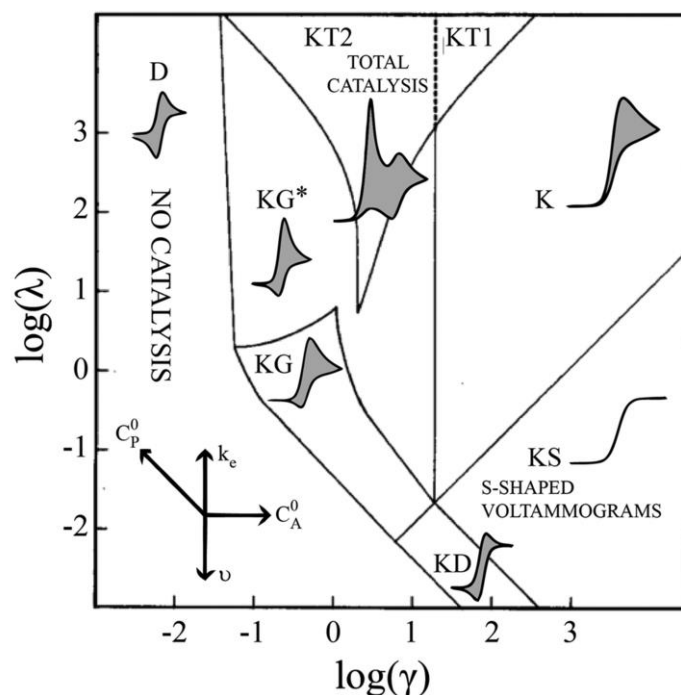


**Figure 3.2:** Example illustrated kinetic zone diagram for the one-electron, one-substrate electrocatalytic (EC') mechanism. Reproduced from Ref. 100 with permission from the Royal Society of Chemistry.

Note that pCNAH.BF<sub>4</sub> was chosen as the main acid because of its relatively moderate acidity (pK<sub>a</sub> = 7.0 in MeCN),<sup>101</sup> sufficient to elicit a good catalytic response but not destabilise the complex, and its previous use by Lau and coworkers.<sup>73</sup> It was additionally noted that the presence of its conjugate base, *para*-cyanoaniline (pCNA) did not produce any change in the CV of CAT1 in the absence of acid (**Paper I**, SI).

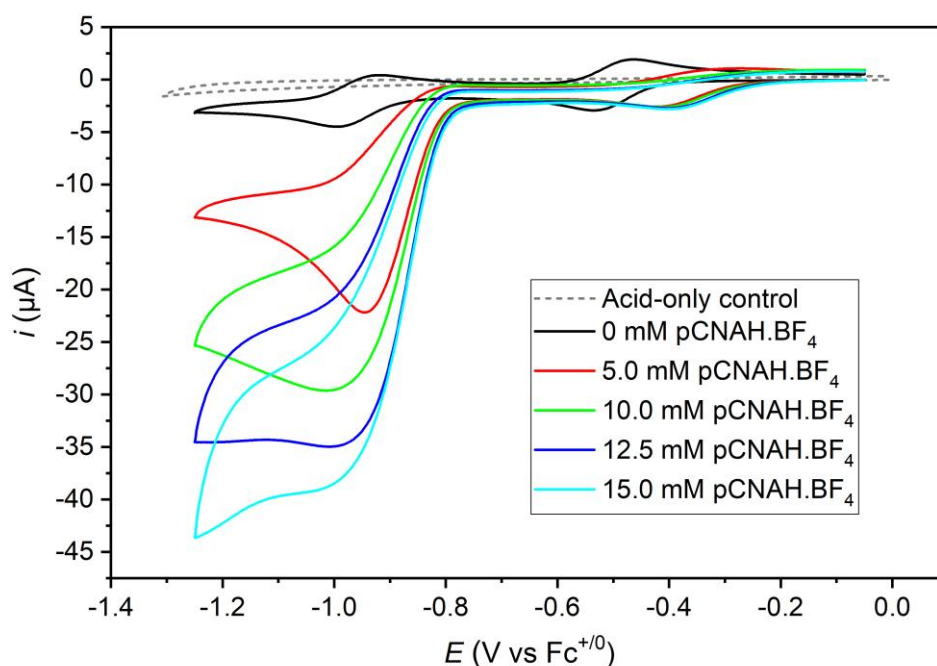


**Figure 3.3:** Cyclic voltammogram of CAT1 (0.5 mM) in MeCN (0.1 M TBABF<sub>4</sub>) with increasing concentration of pCNAH.BF<sub>4</sub> acid. Scan rate: 100 mV s<sup>-1</sup>. Working electrode: Polished glassy carbon, diameter: 1.6 mm. Reference electrode: Ag/AgCl (KCl, 3 M). Counter electrode: Pt wire. Acid-only control was 15 mM pCNAH.BF<sub>4</sub> without catalyst. Reproduced from **Paper I** with permission from the Royal Society of Chemistry.

To extract information about rates, further CV experiments were carried out, modifying the conditions to adjust the behaviour according to the zone diagrams discussed above. Firstly, the position of the Co(II/I) redox couple  $E_{1/2}$  under conditions of high acid concentration was determined to be  $-0.89$  V vs.  $\text{Fc}^+/\text{Fc}$  by running CV with a high scan rate of  $10 \text{ V s}^{-1}$ , at which the catalytic processes were outrun and did not obscure the redox peaks (**Figure 3.4**).

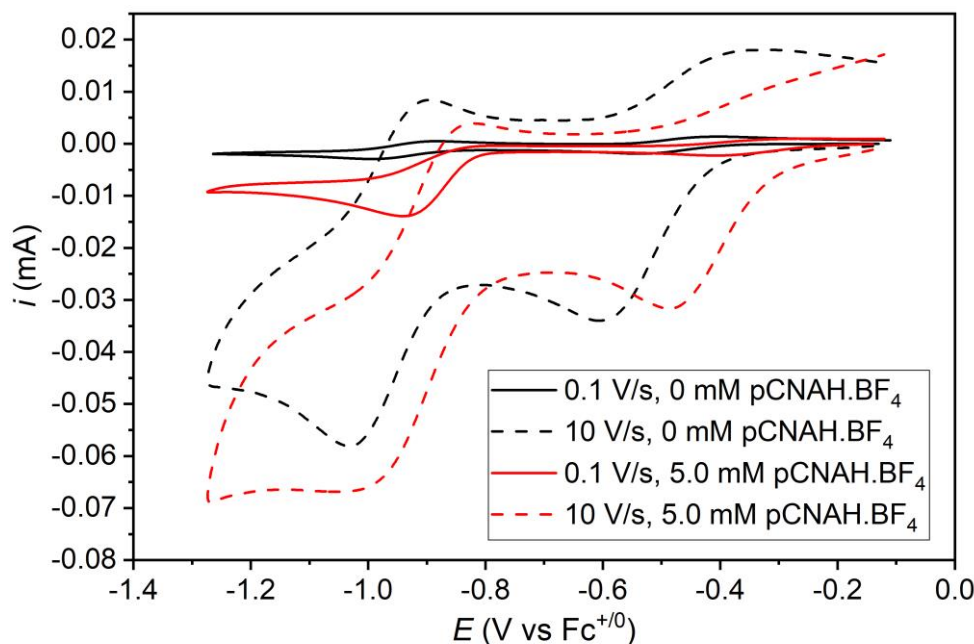


**Figure 3.4:** Cyclic voltammogram of CAT1 (0.5 mM) in MeCN (0.1 M TBABF<sub>4</sub>) without acid (black) or with 5.0 mM pCNAH.BF<sub>4</sub> (red). Scan rate:  $0.1 \text{ V s}^{-1}$  (solid line) or  $10 \text{ V s}^{-1}$  (dashed line). Working electrode: Polished glassy carbon, diameter: 1.6 mm. Reference electrode: Ag/AgCl (KCl, 3 M). Counter electrode: Pt wire. Reproduced from **Paper I** with permission from the Royal Society of Chemistry.

### Determining $k_2$ for the Second Protonation Step

It was determined that there was a consistent plateau of the catalytic wave for 1.6 mM CAT1 with 60 mM of pCNAH.BF<sub>4</sub>, independent of scan rate across a range of  $\nu = 200 \text{ mV s}^{-1}$  to  $500 \text{ mV s}^{-1}$  (pure kinetic conditions), with a mid-wave potential of  $-0.87$  V vs.  $\text{Fc}^+/\text{Fc}$ . Furthermore, a linear dependence of the catalytic plateau current to the concentration of catalyst (0.8 – 2.0 mM) was observed for a fixed concentration of acid (60 mM) when adjusting the scan rate to stay within a pure kinetic regime (**Figure 3.5 Left**), and a linear dependence of the plateau current on the square root of acid concentration (40 – 60 mM) was observed for a fixed concentration of catalyst (1 mM) and scan rate (**Figure 3.5 Right**).

These observations are consistent with an ECEC mechanism with a thermodynamically easier second reduction step, starting from the Co(II) state (elaborated in mechanism section). Since the second protonation step is also known to be the rate-determining one from previous studies (supported by FOWA for  $k_1$ , discussed next), assuming the overall catalytic cycle requires two electrons, the equation for the relating the plateau current to the second protonation step,  $k_2$ , is the following:<sup>102</sup>

$$i_{\text{pl}} = 2FS C_{\text{cat}}^0 \sqrt{k_2 D_{\text{cat}} C_{\text{AH}}^0}$$

where  $i_{\text{pl}}$  is plateau current,  $F$  is the Faraday constant,  $S$  is the electrode surface area,  $C_{\text{cat}}^0$  is the catalyst concentration,  $D_{\text{cat}}$  is its diffusion coefficient, and  $C_{\text{AH}}^0$  is the concentration of acid.  $D_{\text{cat}}$  was obtained as  $10^{-5} \text{ cm}^2 \text{ s}^{-1}$  from applying the Randles-Ševčík equation<sup>90</sup> to CVs of the catalyst without acid at different scan rates, and plotting the peak currents of the redox couples against the square root of the scan rate. Through this method, the second-order rate constant for the rate-determining second protonation step,  $k_2$ , was determined to be  $5.3 \pm 0.1 \times 10^3 \text{ M}^{-1} \text{ s}^{-1}$ .



The fact that this rate constant for the second protonation step (or overall chemical step) is first-order with respect to the concentration of acid implies the H<sub>2</sub> formation and release is coupled with immediate reprotonation of the amine, considering that there are no more positions available for another protonation to occur until the H-H bond is formed. Otherwise, the reprotonation and H<sub>2</sub> formation and release rates of these steps may be expected to be independent of the proton concentration, i.e. if the H<sub>2</sub> formation and release steps were uncoupled and rate-determining.<sup>100</sup> This coupling may be either in a concerted manner or through kinetic coupling.

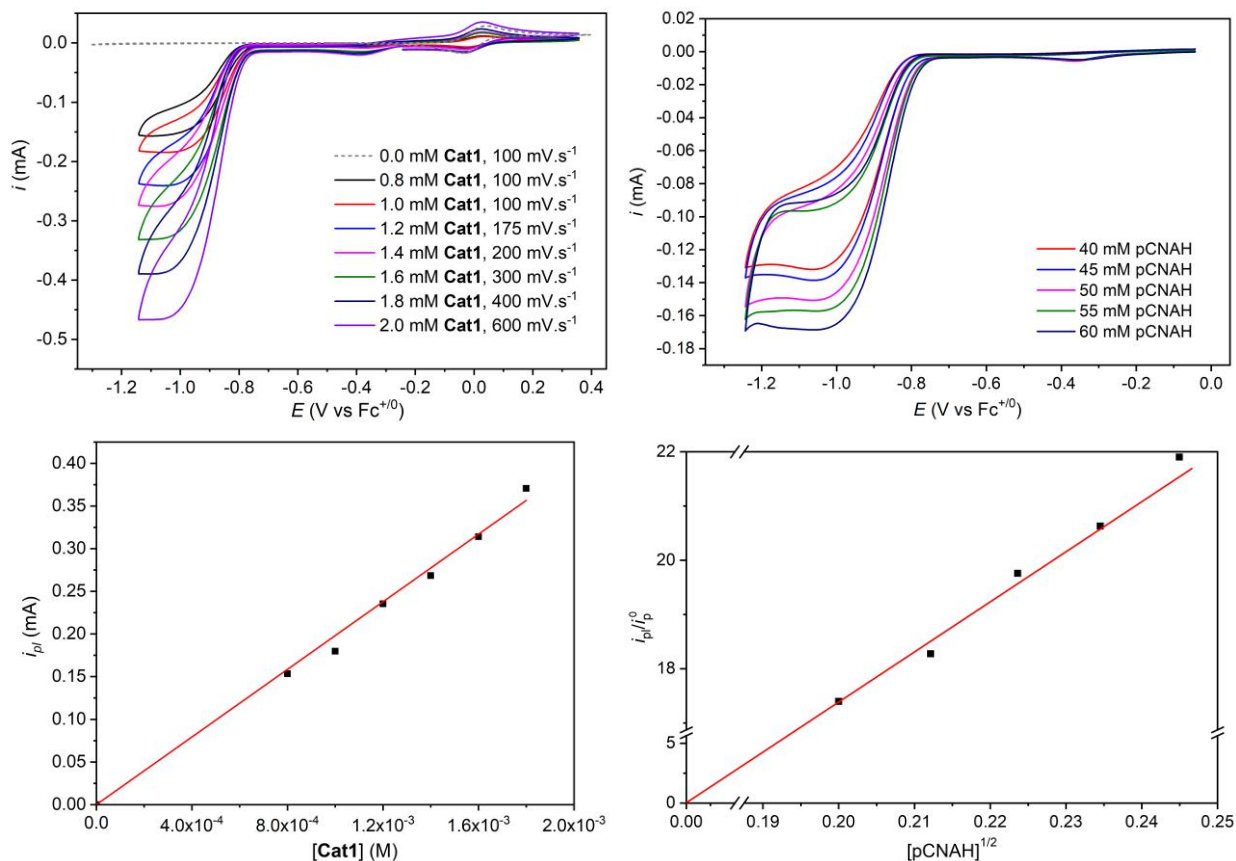


**Figure 3.5:** CVs for calculating the second protonation rate constant,  $k_2$ . **Left:** CVs varying catalyst concentration (top) and linear fit of plateau current to catalyst concentration (bottom). **Right:** CVs varying acid concentration (top) and linear fit of plateau current to the square root of acid concentration (below). Reproduced from **Paper I** with permission from the Royal Society of Chemistry.

### Determining $k_1$ for the First Protonation Step

To determine  $k_1$ , *foot-of-the-wave analysis* (FOWA)<sup>102–104</sup> was used as the primary method. Applying scan rates of 100, 400 and 1000  $\text{mV s}^{-1}$  for samples with 5 and 25 mM pCNAH.BF<sub>4</sub>. In brief, FOWA extracts kinetic information from the onset of a catalytic wave (i.e. the ‘foot’). This region is suitable for the analysis because the current-potential response is largely ‘idealised’ due to the general lack of side phenomena (catalyst degradation, substrate consumption, etc.) at that point impacting the waveform.

For the first protonation step in this ECEC mechanism,  $k_1$  is derived by plotting the ratio of the catalytic current over the peak current in the absence of acid against a linearizing expression derived from the difference between the applied potential ( $E$ ) for each datapoint at the foot of the wave and the standard potential of the protonated Co(II/I) couple, which was already obtained from the high scan rate voltammograms in **Figure 3.4**. The linear region of these plots was fitted (**Paper I**, SI)<sup>74</sup> and used to derive a value for the second order rate constant for the first protonation,  $k_1$ , of  $2.5 \pm 0.4 \times 10^4 \text{ M}^{-1} \text{ s}^{-1}$ .

This was backed up by (i) analysis of the shift of the catalytic mid-wave potential shifting to more positive potentials with increasing acid concentration to yield the same value but with greater uncertainty, and (ii) by using a method proposed by Dempsey and coworkers for the analysis of the variation of the catalytic peak

potential in voltammograms in the total catalysis (KT2) zone, reached by having low acid concentration.<sup>104</sup> Although the condition that both rate constants ( $k_1$  and  $k_2$ ) be greater than  $10^7 \text{ M}^{-1} \text{ s}^{-1}$ , which is required for the empirical basis of their method, was not met, this still yielded a value of  $2.1 \pm 0.3 \times 10^4 \text{ M}^{-1} \text{ s}^{-1}$ , which is very close to the FOWA-derived value.

From determining the protonation rate constants and behaviour consistent with the proposed ECEC mechanism, the catalytic cycle could be put together. However, electrochemical data requires careful analysis because many factors can be at play and assumptions have to be rigorous, otherwise the conclusions that are drawn may be incorrect. Additional evidence was required to support the idea that a Co(II) state with protonation on the macrocycle could be generated by the second protonation step (coupled with  $\text{H}_2$  release), and to confirm that this protonation did not occur at Co(III) state, to explain the strong shift of the Co(III/II) redox couple with addition of only low concentrations acid.

## Spectroscopic Characterisation

Firstly,  $^1\text{H}$  NMR spectroscopy was employed to verify that the Co(III) state of CAT1 is not protonated in the presence of the acid pCNAH.BF<sub>4</sub>, which supports that the shift of the Co(III/II) couple with the addition of acid is due to protonation of the Co(II) state. However, for revealing information about the paramagnetic  $d^7$  low-spin Co(II) state (overall spin =  $1/2$ ), NMR is not an effective technique. Isolating the square-planar Co(I) intermediates that are relevant in the catalytic cycle is also impractical, since in the presence of acid the Co(I) state will simply turnover and regenerate Co(III) or (II).

Therefore, EPR spectroscopy was employed to study the effect of the introduction of acid or conjugate base on the Co(II) state (**Paper I**, SI). To prepare the Co(II) samples, 0.5 mM CAT1 dissolved in MeCN was reduced in inert atmosphere conditions, before adding a fraction of THF as a glassing cosolvent to facilitate amorphous freezing of the samples. To control for the possible effects of the electrolyte salt which has to be present in electrochemical reduction via controlled potential electrolysis, samples were also prepared by chemical reduction with one equivalent of cobaltocene and compared with and without the salts. UV-Vis spectroscopy was used to monitor the reduction of CAT1 based on reported spectra.<sup>76</sup>

The EPR studies corroborated the voltammograms that showed addition of only the conjugate base pCNA did not affect the catalyst (**Paper I**, SI). However, significant disruption of the Co(II) coordination system in the presence of acids is indicated by major changes in the profile of the spectra. In fact, the addition of acid resulted in much better resolved spectra which could clearly be identified as fitting  $d^7$  low-spin cobalt, showing a clear hyperfine octet splitting from the  $^{59}\text{Co}$  nuclei (caused by its nuclear spin,  $I = 7/2^-$ ). The lone unpaired electron should localise in the  $d_z^2$  orbital, interacting with the axial ligands. Moreover, when the added acid was pCNAH.BF<sub>4</sub>, a super-hyperfine splitting of those peaks into five each was observed with a 1:2:3:2:1 intensity ratio, corresponding to two identical overlapping 1:1:1 triplet splittings, with a coupling constant of 45 Hz. This fits to the coordination of two axial nitrogen ligands ( $^{14}\text{N}$ ,  $I = 1+$ ). On the other hand, when the added acid was tetrafluoroboric acid etherate (HBF<sub>4</sub>·OEt<sub>2</sub>), very similar spectra were seen except with only splitting into three 1:1:1 peaks each with a coupling constant of 40 Hz, implying the coordination of only one axial nitrogen (**Figure 3.6**). Both electrochemical and chemical reduction methods resulted in the same responses.

From this EPR data, it is concluded that with addition of pCNAH.BF<sub>4</sub>, Co(II) takes two axial ligands binding via nitrogen. It is not possible to distinguish whether these are the conjugate base, pCNA, or solvent, MeCN, binding through their respective nitrile groups, since they would be indistinguishable by EPR. However, the fact that only one nitrogen ligand binds when HBF<sub>4</sub> is the acid (which must be acetonitrile), implies that the nature of the acid and the binding ability of nucleophiles in solution can affect the coordination system the Co(II) state takes. Furthermore, the displacement of the chloride ligands shows that the axial ligands become very labile already at the Co(II) state when acid is present. A 19-electron six-coordinate Co(II) state being expected to be unfavoured, it is strongly implied that one part of the macrocycle is de-coordinating in response to the added acid – this would support the amine being protonated and detaching.

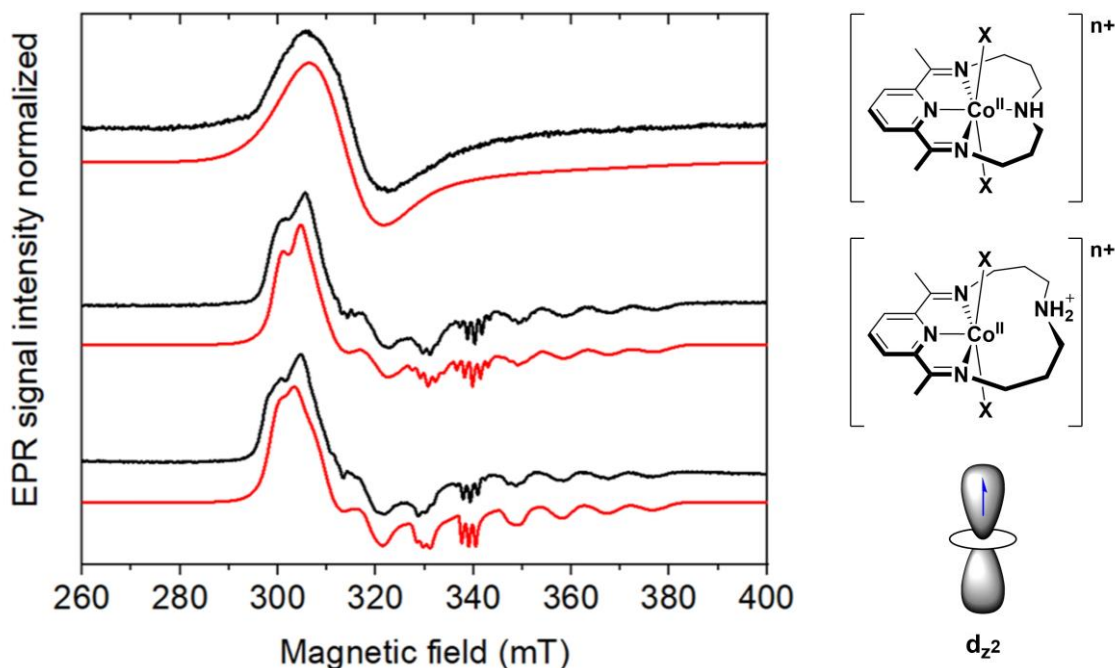


**Figure 3.6:** EPR spectra of electrochemically reduced CAT1 (CW X-band, 9.65 GHz, 30 K, 1 mW microwave power, 1600 G field sweep). **Top:** With no other added species. **Middle:** With 5 eq. of the acid pCNAH.BF<sub>4</sub>. **Bottom:** With 5 eq. of the acid HBF<sub>4</sub>. Recorded spectra in black versus simulations in red. Reproduced from **Paper I** with permission from the Royal Society of Chemistry. To the right: illustration of CAT1 and the orientation of the singly-occupied  $d_{z^2}$  orbital into the axial ligands.

### 3.4 Overall Proposed Mechanism and Benchmarking

From the experiments carried out, an overall mechanism could be proposed for CAT1's catalysis of the HER in organic conditions (**Figure 3.7**). Relying on extensive electrocatalytic studies and spectroscopy characterisation of intermediates instead of photocatalytic experiments, it has the following properties: It is heterolytic, ECEC-type, and has a rate-determining second protonation step.

This disagrees partially with that proposed by Grau *et al.*,<sup>75</sup> due to the assertion in **Paper I** of a protonation of the Co(II) state. However, electrochemically, in acetonitrile, some kind of rapid protonation event upon reduction to Co(II) is clearly evidenced by the observed Co(III/II) shift. Additionally, in the mechanisms proposed by Grau *et al.* they considered the possibility of protonation and de-coordination of the amine for the Co(II)-hydride state, *after* both the formation of the Co(III)-hydride and its subsequent reduction. Although the energy barrier to H<sub>2</sub> formation from a close intramolecular interaction between the hydride and the ammonium – which may operate as a proton relay – was calculated by DFT to be low ( $\Delta G^\ddagger = 5$  kcal/mol, assuming a penta-coordinated intermediate), the formation of the ammonium itself was calculated to be significantly endergonic, due to the required de-coordination of the amine ( $\Delta G = 27$  kcal/mol, implying  $\Delta G^\ddagger$  must be even greater). On the other hand, the kinetic barrier for direct protonation of the hydride from solution was reported to be below that value ( $\Delta G^\ddagger = 19$  kcal/mol), and thus expected to be the favoured route.

This contrasts with the proposed mechanism of **Paper I**, where the amine has already been protonated and de-coordinated from the start of the cycle at the Co(II) state. In fact, the protonated amine is expected to remain protonated and de-coordinated over the course of the mechanistic cycle, assuming a sufficient acid concentration, since the release of H<sub>2</sub> is apparently coupled with immediate reprotonation of this amine. The labilisation of macrocycle amine groups is not unknown for related complexes, such as the penta-coordinate analogues of CAT1 with two amines, where a de-coordinated amine is thought to function as a proton relay,<sup>82,83</sup> so it may well be possible that CAT1 shares similar behaviour. Software simulations (DigiElch) reproduced the potential shifts shown in **Figure 3.4** for an equilibrium constant of protonation above 10<sup>4</sup> and a bimolecular protonation rate of 10<sup>7</sup> M<sup>-1</sup> s<sup>-1</sup>. Altogether with the DFT modelling by Grau

*et al.*, this would imply that the amine group has the capability of act as a proton relay during catalysis, to form the H-H bond with the metal hydride, as it holds a proton close to the reactive centre – otherwise the alternative possibility is that protonated Co(II) hydride has to find and react directly with a free proton in solution to turn over, in which case the protonated amine only serves to modulate the potentials, but does not shuttle protons. An alternative pathway for the surmised relay mechanism, where the ammonium provides the proton to form the hydride with the Co(I) centre, and is then reprotonated to facilitate the H-H bond formation, was considered less likely, because of the probably insufficient, weaker acidity of the ammonium group than of the pCNAH.BF<sub>4</sub> species used.

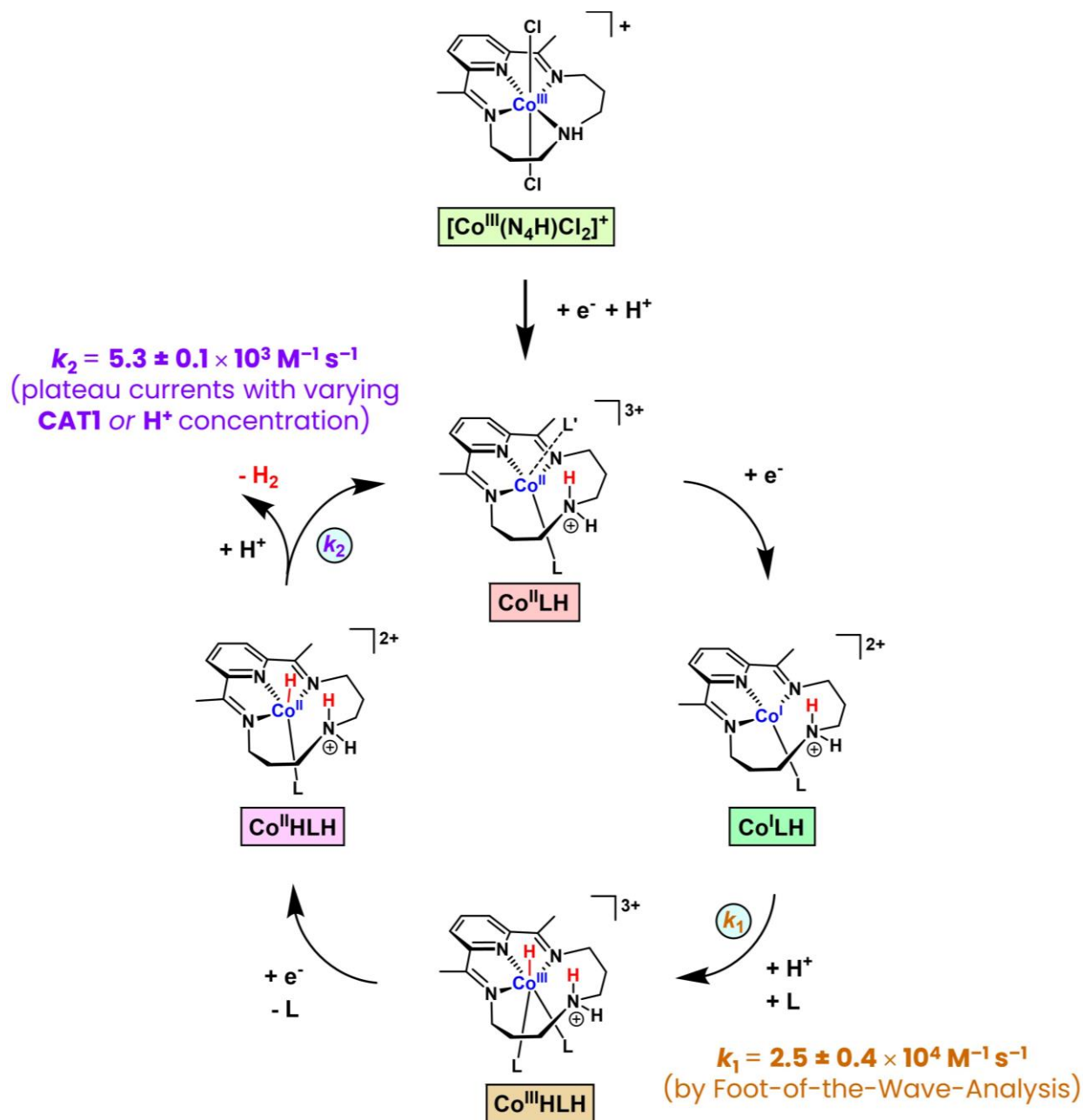


**Figure 3.7:** Proposed ECEC catalytic mechanism and protonation rate constants for HER catalysis by CAT1 in MeCN. L and L' are MeCN or pCNA in this case.

In any case, there were some critical differences in the conditions used to arrive at the different proposed mechanisms, and there remain some ambiguities in a number of regards: The effectiveness of the amine group as a proton relay, the effect of different methods of reduction of the catalyst, the effect of solvent on the mechanism, and the exact relationship between the HER reduction wave and the Co(II/I) redox couple in water. Therefore, further work towards resolving the remaining questions is still immensely interesting.

For finalising the mechanism proposed in **Paper I**, the additional assumption was made that the protonated Co(III)-hydride state does not evolve hydrogen due to the low polarity of the Co-H bond in that state (hydricity considerations). Reduction first to Co(II) would be expected to expedite the release of H<sub>2</sub> and associated immediate protonation of the resulting Co(II) state complex. This is also supported by DFT.<sup>75</sup> Additionally, the hydrogen-evolution step is first-order with respect to acid concentration and occurs alongside rapid reprotonation, so it is considered that these two processes are coupled in the mechanism under typical conditions. The reduction of the Co(III)-hydride to Co(II)-hydride, followed by spontaneous release of H<sub>2</sub> and rapid reprotonation may be considered to belong within the proton-coupled electron transfer classification.

As a final point, the fact that the proposed rate determining step is still relatively fast in terms of its rate constant, and has been calculated as thermoneutral by previous DFT calculations,<sup>75</sup> goes some way to explaining the effectiveness of CAT1 as a catalyst for the HER. From CV with 1 M pCNAH.BF<sub>4</sub>, a TOF<sub>max</sub> value of  $5.3 \times 10^3 \text{ s}^{-1}$  was reported and, with additional considerations (**Paper I**), was used to plot a catalytic Tafel plot<sup>105</sup> to evaluate CAT1's intrinsic catalytic activity (**Figure 3.8**). CAT1's high TOF<sub>max</sub> value sets it in a position between the highly-active, but generally unstable, cobaloximes and the slightly less active, but often extremely efficient, DuBois catalysts. Of note, regarding considerations for use in devices, CAT1 has an overpotential requirement of about 400 mV for approaching its maximum rate in organic homogeneous conditions, although it does display some activity at low overpotentials.

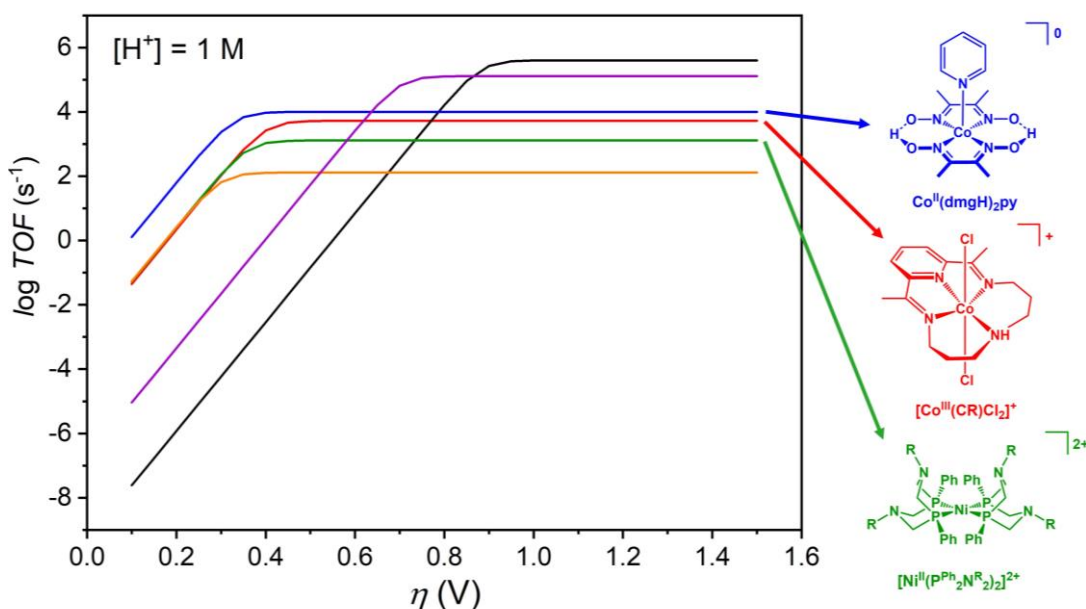


**Figure 3.8:** Catalytic Tafel plots of CAT1 (i.e. [Co<sup>III</sup>(CR)Cl<sub>2</sub>]<sup>+</sup>) in MeCN with pCNAH.BF<sub>4</sub> (red) against other competitor molecular catalysts: Iron tetraphenylporphyrin, Fe<sup>II</sup>TPP in DMF with Et<sub>3</sub>NH<sup>+</sup> (black), pyridine-cobaloxime, Co<sup>II</sup>(dmgH)<sub>2</sub>py in DMF with Et<sub>3</sub>NH<sup>+</sup> (blue), phenylphosphine DuBois catalyst with phosphonate ester groups, [Ni<sup>II</sup>(P<sup>Ph</sup><sub>2</sub>NR<sub>2</sub>)<sub>2</sub>]<sup>2+</sup>, R = *p*-C<sub>6</sub>H<sub>4</sub>-CH<sub>2</sub>P(O)(OEt)<sub>2</sub> in MeCN with DMFH<sup>+</sup> (green), a cobalt bithiosemicarbazone in DMF with Et<sub>3</sub>NH<sup>+</sup> (orange), and a cobalt polypyridine complex, [Co<sup>II</sup>(bapbpy)Cl]<sup>+</sup> in DMF with Et<sub>3</sub>NH<sup>+</sup> (purple).  $\eta$  = applied overpotential for the HER. Reproduced from **Paper I** with permission from the Royal Society of Chemistry. Note the position of the red line for CAT1 with TOF<sub>max</sub> between the green (DuBois) and blue (cobaloxime).

It is concluded from the studies in **Paper I** that CAT1 is a promising molecular catalyst for further applications, not least because of its versatility in a variety of conditions and robustness observed in previous reports, but also its intrinsic activity for the HER is competitive with other state-of-the-art molecular catalysts. The reasons for this seem to be linked to the high rates of each protonation step in its ECEC mechanism, which is also conclusively demonstrated to be heterolytic rather than homolytic, another positive factor for the suitability of CAT1 for immobilisation in device applications. Finally, a supportive proton relay action of the amine group is surmised from the investigated organic conditions, which may inform and underline the importance of the rational design principles for future molecular modification, as discussed in the introduction, which may open many possibilities for optimisations or applications through ‘molecular-engineering’.

## 4 Electrocatalytic Hydrogen Evolution from Novel Anchorable Derivatives of CAT1 (**Paper II**)

### 4.1 Motivations and Background

On the basis of the encouraging conclusions in **Paper I** and other literature regarding CAT1's catalytic properties for the HER,<sup>75–78,85,95</sup> CAT1 was selected as an interesting molecular catalyst to investigate for structural modification for solar fuel production applications, in particular towards immobilising it on conductive carbon surfaces for the cathodes of PV-driven electrolyzers. Like for studies into its catalytic mechanism, studies into synthesising derivatives of CAT1 and analysing their catalytic behaviours were relatively few at the time of investigation, especially when compared with other prominent HER catalysts, highlighted in the introduction (**Figures 1.11** and **1.15**).

Out of these catalysts, the DuBois catalysts are well known for their versatility in terms of derivatisation<sup>44,46</sup> and have been successfully incorporated as the immobilised catalysts on hydrogen-evolving cathodes with increasing effectiveness as new innovations in immobilisation strategy are made.<sup>63,106–109</sup> However, due to the vulnerability of the reduced form of the catalyst' phosphine groups to oxidation by O<sub>2</sub>, which leads to the deactivation of the catalyst, it would be necessary to develop ways of either making an O<sub>2</sub> tolerant derivative of the catalyst which still retains sufficient activity for the HER or to exclude O<sub>2</sub> by encapsulation under an O<sub>2</sub>-impermeable polymer or coating.<sup>110,111</sup>

On the other hand, for cobaloximes, reasonable O<sub>2</sub>-tolerance is reported<sup>110,111</sup> and substitution of the neutral axial ligand provides an effective way of optimising the catalytic performance in solution.<sup>51,112</sup> However, using this strategy for anchoring the catalyst is not practical because the axial positions become labile over the catalytic cycle.<sup>64,112</sup> Alternative anchoring strategies using the macrocycle are synthetically difficult.<sup>113</sup> Cobalt diimine-dioximes share the O<sub>2</sub>-tolerance reported for cobaloximes, but can be conveniently be modified with anchoring groups via the propylene bridge for immobilisation on electrodes, and operate effectively for the HER at around pH 4.5.<sup>62,114</sup> However, under strongly acidic conditions or neutral conditions they are known to degrade into metastable nanoparticles<sup>115,116</sup> and under neutral conditions are notably less active than cobaloximes.<sup>79</sup>

In this context, applying anchorable derivatives of CAT1 on hydrogen-evolving cathodes appears as an exciting next step, particularly because of its superior robustness and activity versus cobalt diimine-dioximes,<sup>79</sup> while still retaining good O<sub>2</sub>-tolerance: CAT1's faradaic efficiency decreases from about 100% to about 70% in presence of atmosphere O<sub>2</sub> concentration but it is not deactivated.<sup>82</sup>

However, at the start of the project, structural modification of CAT1, either for the sake of catalytic optimisation or for adding anchoring groups was still relatively under-explored. Pioneering work by Lee *et al.* in 2013 produced a derivative functionalised with a 2,4-bis(trifluoromethyl)phenyl substituent at the *para*-position of the pyridine (see **Figure 3.1**) and then pacman and hangman derivatives by the same method.<sup>117</sup> Since then, other *para*-position functionalised derivatives have been reported only recently: Wang and coworkers reported a (2,6-dicarboxypyridin-4-yl) derivative designed for immobilisation onto semiconductor quantum dots<sup>87</sup> and photocathodes,<sup>118</sup> and Bold *et al.* attached the active site as part of a molecular dyad system onto dye-sensitized photocathodes,<sup>96,97</sup> while McCrory and coworkers reported a series of derivatives with stepwise optimisation for the homogeneous CO<sub>2</sub>RR.<sup>81</sup>

On the other hand, Grau *et al.* recently prepared the CAT1 derivatives functionalised with either a methyl or hydroxymethyl group at the macrocycle amine position in order to investigate the effect of such substitutions on the homogeneous HER. As discussed in the previous section, the effects of modifications at the

amine position are complicated, which is tentatively attributed to the mechanistic importance of the amine, acting either as a proton relay or otherwise modifying the redox potentials of the cobalt centre in a beneficial way for HER catalysis.

Therefore, at the start of this project, although CAT1 derivatives were beginning to receive significant interest, no anchorable direct derivatives of CAT1 for heterogeneous electrocatalysis of the HER were reported in literature. Only for the penta-coordinate analogue of CAT1 was a *para*-position derivative functionalised with a pyrene moiety for  $\pi$ - $\pi$  and CH- $\pi$  interactions reported recently.<sup>119,120</sup> Hence, it was decided to prepare novel derivatives of CAT1 which could be anchored to sp<sup>2</sup> carbon materials through the macrocycle pyridine, since in the literature similar modifications were not reported to interfere with the catalytic activity, while the possible effects of modification at the amine seemed more unpredictable based on the work by Grau *et al.* and in **Paper I**. Anchoring via  $\pi$ - $\pi$  interactions was the prioritised strategy, since it does not require chemical modification of the carbon surface, which should make the application to device scale electrodes for PV-EC simpler and more readily scalable compared with covalent anchoring strategies.

## 4.2 Synthesis of a Pyrene-Containing Derivative

Based on a synthetic strategy previously developed in the Artero group to produce a derivative of CAT1 with a benzoic acid moiety (abbreviated as **CAT1-CO<sub>2</sub>H**) added at the *para*-position of the pyridine, a couple of pathways (shown in **Figure 4.1**) were devised to produce a novel derivative with a pyrene moiety for  $\pi$ - $\pi$  interactions (shown in **Figure 4.2**, abbreviated as **CAT2**, or **2** in **Paper II**). The first pathway involved preparing the modified diacetylpyridine ligand precursor first, and then performing the templated macrocyclisation with the triamine and the cobalt salt in an appropriate solvent system. This was the default strategy for synthesis of derivatives of CAT1, and the only one that had been successfully carried out previously in literature.

The major challenge with this strategy is that the solvent system has to be adjusted to deal with the modifications made either to the modified diacetylpyridine or the triamine. The solvent system needs to dissolve all of the three reagents well for the macrocyclisation to occur. This is an issue, as the cobalt salt is typically very hydrophilic and requires a polar solvent to dissolve, while the triamine typically needs an alcohol to dissolve it (for norspermidine, ethanol or methanol work) and the modified diacetylpyridine's solubility will depend on any extra moieties attached to it. It is possible to replace the default cobalt(II) halide salts with alternatives that dissolve better in organic solvents, e.g. cobalt(II) nitrate<sup>75</sup> or trifluoromethanesulfonate.<sup>119</sup> This was used by Grau *et al.* in order to use methanol as the sole solvent for macrocyclisation with their substituted triamines.

However, if the modifications made cause one of the ligand precursors to be insoluble in all solvent mixtures that can dissolve the cobalt salts, then this strategy may not work. For example, adding polyaromatic groups such as pyrene can greatly increase the hydrophobicity of a species. In the case of the first devised pathway for CAT2, the insolubility of pyrene-functionalised diacetylpyridine (i.e. 4-(2,6-diacetyl-pyridin-4-yl)-*N*-(pyren-1-ylmethyl)benzamide) either in a mixture of water, ethanol and 1,4-dioxane or in anhydrous methanol with 1,4-dioxane meant that this pathway was not successfully applied. Therefore, a new pathway was developed to prepare CAT2 by attaching the pyrene anchoring group with an amide coupling reaction after the macrocyclisation. This route goes via the synthesis of CAT1-CO<sub>2</sub>H itself, whose synthesis was first optimised by modifying the solvent system for macrocyclisation with 1,4-dioxane to improve the solubility of the reagents.

To couple CAT1-CO<sub>2</sub>H with 1-pyrenemethylamine, several amide coupling reagents were tested, however the reaction was only found to work under these conditions with the especially effective coupling reagents HATU and BOP. Use of DMF as solvent dissolved all the reagents effectively, and allowed the product CAT2 to be precipitated by addition of Et<sub>2</sub>O. CAT2 was purified effectively and simply by redissolution in MeOH and reprecipitation by addition of ethyl acetate. This method opens up the path to the synthesis of other derivatives of CAT1, with different anchoring groups or linker lengths, which may be used in the future to tune the performance of immobilised active site.

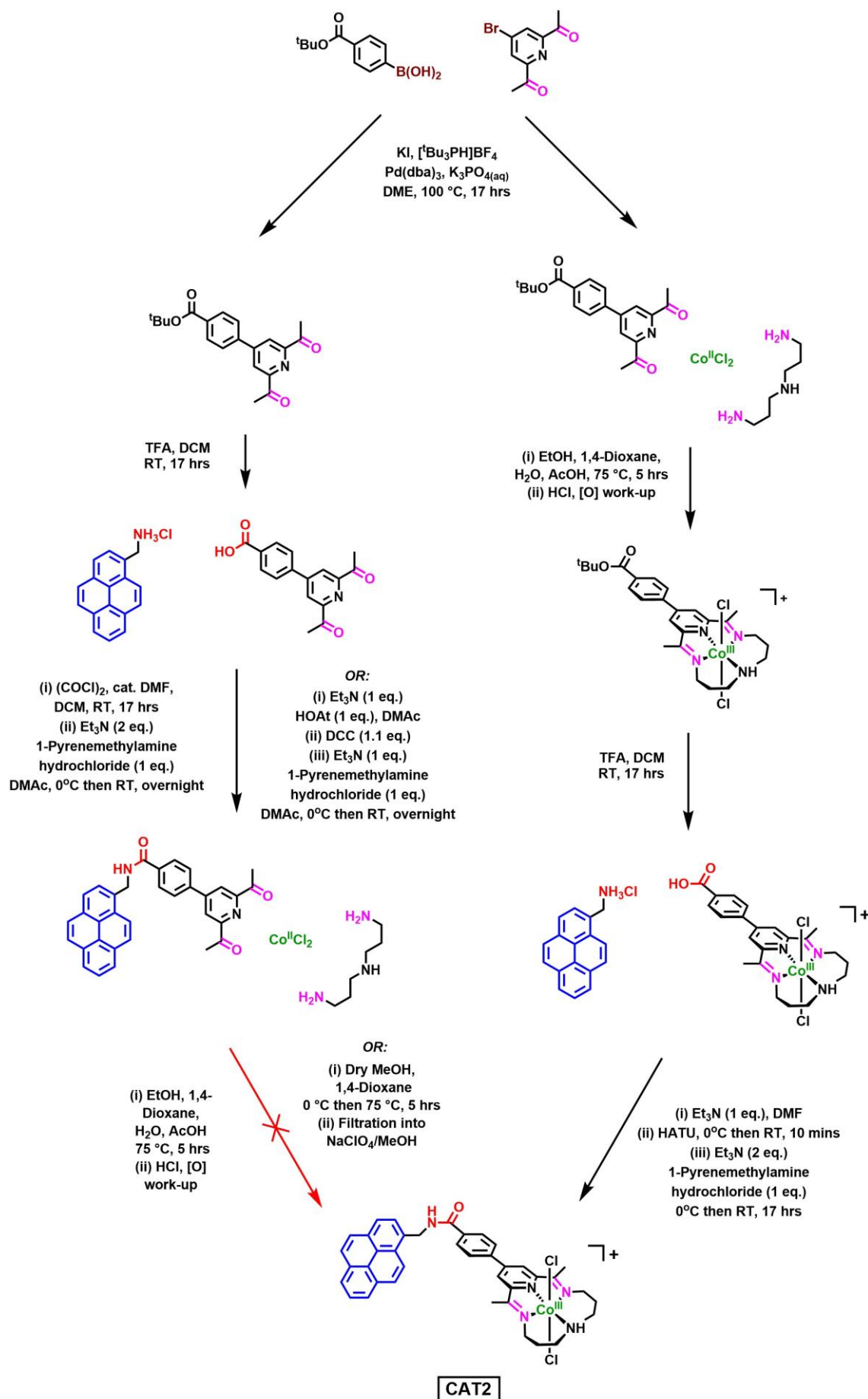


**Figure 4.1:** Overview of the two synthetic pathways towards **CAT2**: a pyrene-functionalised **CAT1** at the *para*-pyridine position. **Left:** Amide coupling to attach the anchoring group first, then macrocyclisation. **Right:** Macrocyclisation first to form **CAT1-CO<sub>2</sub>H**, then amide coupling to attach the anchoring group.



As an additional note, CAT1-CO<sub>2</sub>H has the possibility to be used itself as an anchorable derivative onto polar surfaces, such as semiconductors (in **Paper III**), via its carboxylic acid group. Moreover, the carboxylic acid group may also be used in future work to covalently anchor the active site onto e.g. amine-functionalised carbon surfaces via similar coupling reactions.

### 4.3 Surface Immobilisation of Derivatives

An analogous novel derivative of CAT1, modified with a pyrene attached by a methylene linker at the macrocycle's amine position, abbreviated here to **CAT3**, or **3** in **Paper II** (see **Figure 4.2**), was also prepared and provided by collaborators at ICIQ for comparison with **CAT2**.

To immobilise these catalysts onto electrode surfaces, it is first necessary to choose an appropriate sp<sup>2</sup> carbon material to attach them onto. Multi-walled carbon nanotubes (MWCNTs) represent an auspicious material for positioning the catalytic sites to be both electrically connected and accessible to the substrate. MWCNTs are highly conductive and have large, generally well-defined surface areas, allowing high areal loading densities of molecular catalysts, while also being amenable to either covalent or non-covalent anchoring strategies, such as  $\pi$ - $\pi$  interactions.<sup>46</sup>

In order to investigate the electrocatalytic behaviour and performance of the immobilised catalysts, analytical-scale electrodes were prepared by dropcasting a standard 3 mg/mL dispersion of MWCNTs in EtOH onto a 1.6 mm diameter glassy carbon (GC) disc and immersing it in 10 mM DMF solutions of the catalysts, before rinsing in DMF, then H<sub>2</sub>O (**Figure 4.3**). Both pyrene-functionalised derivatives CAT2 and CAT3 were demonstrated to bind to the MWCNTs on the electrode in aqueous solutions by cyclic voltammetry, showing a linear dependence of redox peak heights to scan rate in acidic conditions (pH 2) and neutral conditions (pH 7) (**Figure 4.4**).

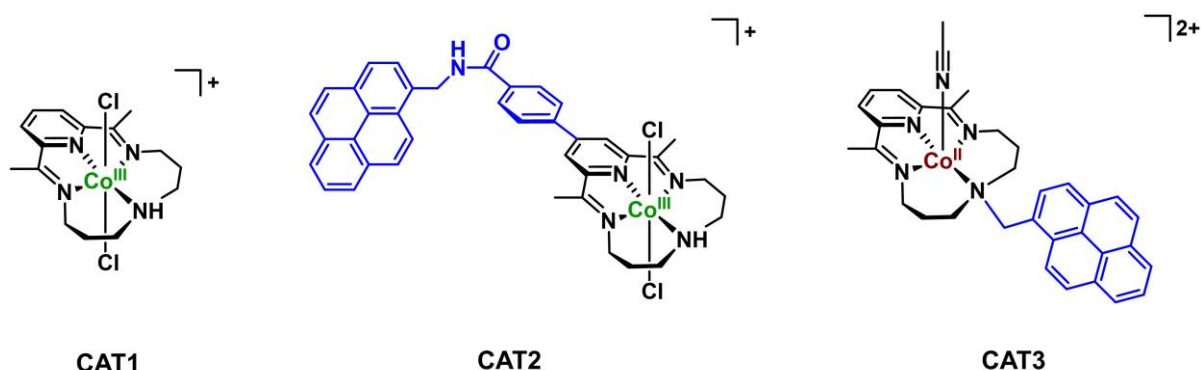


**Figure 4.2:** Chemical structures of CAT1 and its pyrene-functionalised derivatives, CAT2 and CAT3, in their air-stable oxidation states when isolated as solids. CAT2 was prepared as its chloride salt, CAT3 as its diperchlorate salt. Adapted from **Paper II**.

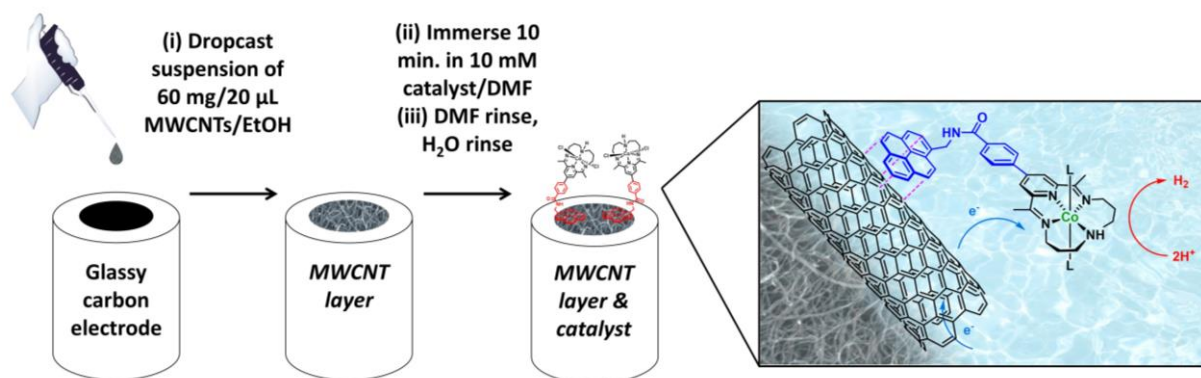


**Figure 4.3:** Diagram of the method for dropcasting MWCNTs onto a glassy carbon electrode and immobilising pyrene-functionalised molecular catalysts. Here, for illustration, CAT2/MWCNTs is shown. Adapted from **Paper II**.

## 4.4 Electrochemical Behaviour

First, the CV responses of the derivatives CAT2 and CAT3 were recorded under homogeneous conditions in DMF to compare with CAT1 (in **Paper II**). The expected Co(II/I) and formally Co(I/0) (attributed to a reduction on the ligand system) redox couples were observed for both, however the Co(III/II) couple was only observed clearly for CAT2. For CAT3 at the same concentration, the redox signals appear universally weaker. Additionally, for CAT3 the substitution at the macrocycle amine can cause the Co(III/II) couple to become highly irreversible and hard to observe under certain conditions. This is explained by Grau *et al.* for the related complexes with a square mechanism, considering the de-/re-coordination of a ligand associated with this redox couple.<sup>75</sup> However, it was observed that, overall, the addition of the anchoring group had only a moderate impact on the electrocatalytic behaviour, as similar redox couple potentials and plateau currents were recorded in the presence of strong acid.

Next, the CV responses of the immobilised derivatives were investigated for the catalyst/MWCNTs/GC electrodes to determine the conditions under which they act as effective electrocatalysts for the HER (**Figure 4.4, Table 4.1**). Some significant differences were observed compared with homogeneous conditions. For both derivatives, a clear redox couple attributed to Co(III/II) was now observed, with interpeak separations in the ranges of 100–200 mV for CAT2 and 50–100 mV for CAT3. This means that the Co(III/II) redox couple loses reversibility for CAT2, but, contrariwise, becomes more reversible and distinct for CAT3 with immobilisation, although CAT3's current signals are still much smaller, despite immobilisation via the same conditions.

The amount of electrochemically active complex immobilised on the electrode surfaces could be quantified through integration of the Co(III/II) redox peaks:

$$\Gamma_{\text{Co}} = \frac{q}{nFS}$$

where  $\Gamma_{\text{Co}}$  is the surface concentration of immobilised catalyst (cobalt centres),  $q$  is the charge passed over the redox process,  $n$  is the number of electrons for the process,  $F$  is the Faraday constant and  $S$  is the electrode's geometric surface area.

**Table 4.1:** Summary of electrochemical potentials extracted from the voltammograms at 100 mV s<sup>-1</sup> in **Figure 4.4** for the CAT2/MWCNTs/GC and CAT3/MWCNTs/GC electrodes (Potentials in V vs. NHE).

Electrode	Solution	Redox Event	E <sub>pc</sub>	E <sub>pa</sub>	E <sub>1/2</sub>	ΔE
CAT2/ MWCNTs	pH 2	Co(III/II)	0.39	0.52	0.46	0.12
		Co(II/I)	-	-0.29*	-	-
CAT2/ MWCNTs	pH 7	Co(III/II)	0.31	0.47	0.39	0.16
		Co(II/I)	-0.42	-0.28	-0.35	0.14
CAT3/ MWCNTs	pH 2	Co(III/II)	0.65	0.69	0.67	0.04
		Co(II/I)	-	-0.31*	-	-
CAT3/ MWCNTs	pH 7	Co(III/II)	0.34	0.43	0.38	0.09
		Co(II/I)	-0.46	-0.38	-0.42	0.07

\*Co(II/I) couple not observed clearly under high [H<sup>+</sup>] conditions due to the HER catalytic response. The nature of the return oxidation signal is complicated by the catalytic wave.

Further CV experiments (**Paper II**) gave values for typical surface concentrations of CAT2 and CAT3 on MWCNTs of 17 ± 1 nmol cm<sup>-2</sup> and 1.2 ± 0.4 nmol cm<sup>-2</sup>, respectively. These values are within the expected range for immobilised molecular catalysts.<sup>31,108</sup> However, assuming that the peak integrals directly give the surface concentrations of catalyst these values are accurate, this means that CAT3 loads less densely on the MWCNTs surface by an order of magnitude. It is possible that the behaviour of the Co(III/II) couple of CAT3 is still somewhat complicated once heterogenised, with its reversibility depending on the situation, like seen in solution for itself and related complexes.

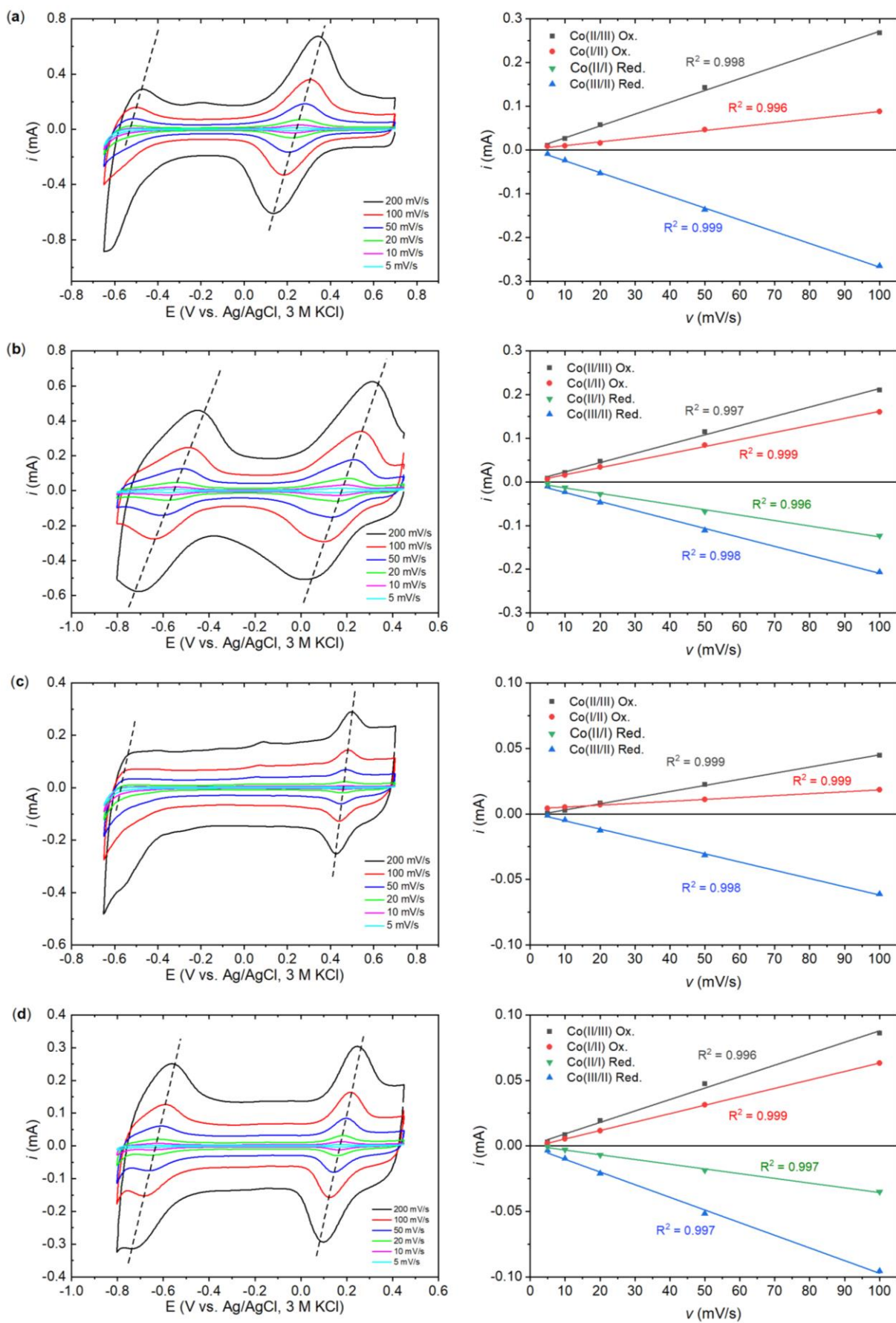


**Figure 4.4:** Cyclic voltammograms for the scan rate dependence of peak currents of CAT2 and CAT3 immobilised onto MWCNTs on a glassy carbon working electrode. Linear correlations of peak currents to scan rates up to 100  $\text{mV s}^{-1}$  are shown on the right with  $R^2$  values: (a) CAT2 on MWCNTs in pH 2 buffer (0.1 M chloride), (b) CAT2 on MWCNTs in pH 7 buffer (0.1 M phosphate), (c) CAT3 on MWCNTs in pH 2 buffer (0.1 M chloride), (d) CAT3 on MWCNTs in pH 7 buffer (0.1 M phosphate).

However, another possible factor is that the assumption relating surface concentration to peak integrals (the above equation) relies on electron transfer to the catalyst occurring through an outer-sphere electron transfer (OSET) mechanism, for which a current peak is recorded in CV at the appropriate potentials. If the active site has the ability to bind close enough to the electrode surface, within the electronic double layer (EDL), so that it becomes electronically coupled to the electrode, it may be only receiving electrons through an inner-sphere electron transfer (ISET) mechanism, for which it is possible that no peak is observed in CV, unless the process is coupled to the reversible binding of an ion from solution.<sup>121–123</sup> ICP experiments are planned to investigate further. In any case, for interpreting the behaviours, it should be important to consider the effects of local chemical environment at the nanotubes-solvent interface on the effective pH and local ion concentrations that the catalysts experience.<sup>124</sup>

To briefly look at the pH-dependence of the two redox processes for immobilised CAT2 and CAT3, the peak and half-wave potentials of the redox couples for each are plotted against pH in **Figure 4.5**,<sup>125</sup> extracted from 100 mV voltammograms once stabilised (5<sup>th</sup> cycles, from **Figure 4.7**). The shifts in  $E_{1/2}$  for the Co(III/II) couple for CAT2/MWCNTs and CAT3/MWCNTs give gradients of  $-49$  mV per pH unit and  $-58$  mV per pH unit, respectively, close to the theoretical  $-59$  mV per pH unit that indicates an equilibrium protonation, reported previously for dissolved CAT1.<sup>74,77</sup> As discussed in **Paper I**, this indicates that the Co(II) state is protonated after a one-electron reduction from the Co(III) state.

However, the shift in  $E_{1/2}$  for the Co(II/I) couple for both systems gives much smaller gradients of  $-12$  mV and  $-3$  mV per pH unit respectively. For CAT2, this is notably less than the  $-24$  mV per pH unit previously reported for CAT1.<sup>77</sup> For CAT3, this behaviour appears similar to that reported for other amine-functionalised derivatives of CAT1, for which the Co(II/I) couple also does not change noticeably with pH.<sup>75</sup> This may mean that for both immobilised catalysts, the Co(II/I) redox couple is effectively pH-independent and does not involve a major change in the coordination sphere, as proposed in **Paper I**.

Plotted against the HER thermodynamic equilibrium line, the stronger association of the catalytic current responses to the Co(II/I) reduction in acidic conditions compared with neutral conditions can be rationalised: it is apparent that the Co(I) state is sufficiently reducing to catalyse the HER at low pHs, but may be expected to struggle at pH 7, unless there is some beneficial effect from the electrode's electronic or polarising effects, or the formal Co(0) state becomes involved.

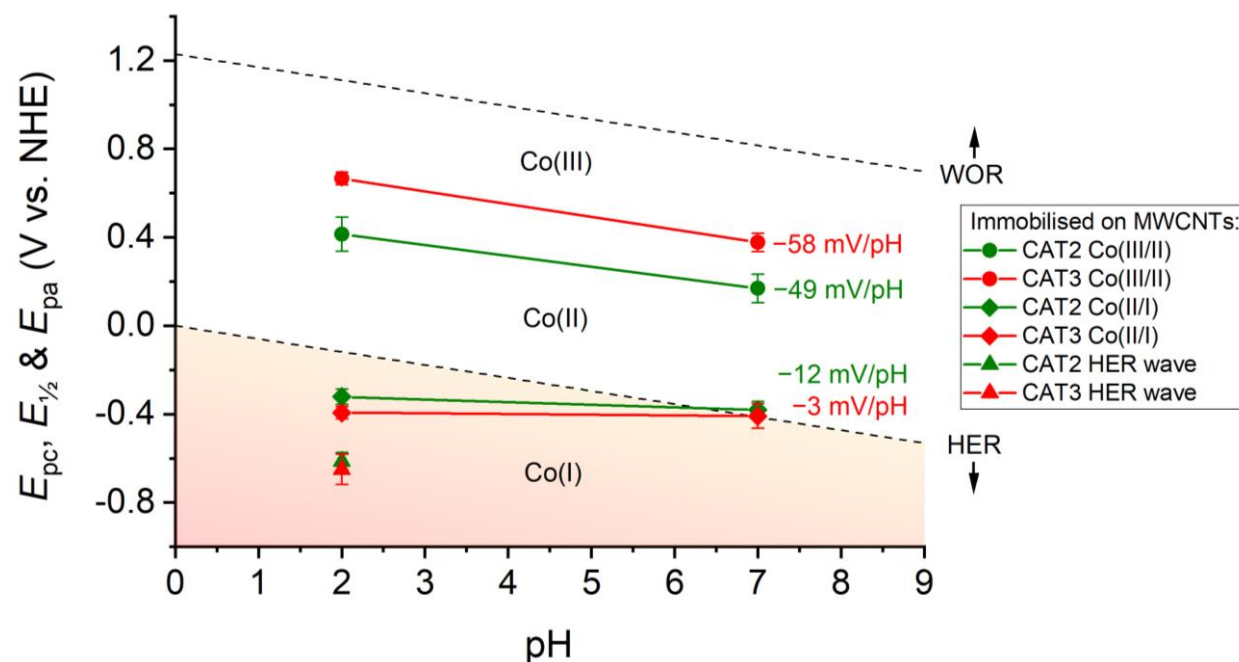


**Figure 4.5:** Outline Pourbaix diagram of the redox behaviour of CAT2/MWCNTs and CAT3/MWCNTs from the CV data recorded at pH 2 and pH 7 (0.1 M chloride and 0.1 M phosphate respectively). Redox potentials plotted from CV 5<sup>th</sup> cycles (after stabilisation) at 100 mV s<sup>-1</sup> with lower scan bound of  $-0.99$  V vs. NHE. Bottom bars:  $E_{pc}$ , central points:  $E_{1/2}$ , top bars:  $E_{pa}$ .

The performance and behaviour of the catalyst/MWCNT electrodes under controlled potential electrolysis (CPE) in a nitrogen-purged gas-tight two-compartment cell was followed by chronoamperometry (CA) in order to study the magnitude and stability of the catalytic currents for the HER, while the evolved H<sub>2</sub> was measured by gas chromatography of headspace samples (**Figure 4.6**).

For simplicity, in calculated current densities, the MWCNT layer is always assumed to be circular with a diameter of 0.60 cm, for an estimated geometric area of 0.28 cm<sup>2</sup> (the maximum size possible on the top of the glassy carbon electrodes). The modification with either catalyst results in a marked increase in catalytic current densities over those of the MWCNT control, which had a current density of 0.17 mA cm<sup>-2</sup> after 1 hour at pH 2. The CAT2/MWCNTs system exhibits the higher catalytic current densities of the two derivatives: after 1 hour of CPE at pH 2 the current density remained above **1 mA cm<sup>-2</sup>** and 23.9 ± 5.3 μmol cm<sup>-2</sup> of H<sub>2</sub> had been produced with a faradaic efficiency (FE) of **97.7 ± 2.1%**. The CAT3/MWCNTs system exhibited lower HER catalytic current densities which decayed more rapidly: after 1 hour of CPE, the current density was just above **0.17 mA cm<sup>-2</sup>** and 5.3 ± 1.0 μmol cm<sup>-2</sup> of H<sub>2</sub> had been produced with FE of **90.4 ± 3.3%**. The more rapid drop-off of current density, even within limited time periods at catalytic conditions, implies that the CAT3/MWCNTs system begins to lose HER catalytic activity already after few turnovers in acid. In pH 7, higher current densities for the same overpotential vs. RHE were observed and both systems had largely stabilised after one hour of electrolysis: CAT2/MWCNTs at **1.6 mA cm<sup>-2</sup>** after producing 35.0 ± 5.0 μmol cm<sup>-2</sup> H<sub>2</sub>; CAT3/MWCNTs at **0.9 mA cm<sup>-2</sup>** after producing 23.2 ± 0.9 μmol cm<sup>-2</sup> of H<sub>2</sub>. Remarkably, in neutral conditions, both systems operated with faradaic efficiencies of about **100%** over one hour.

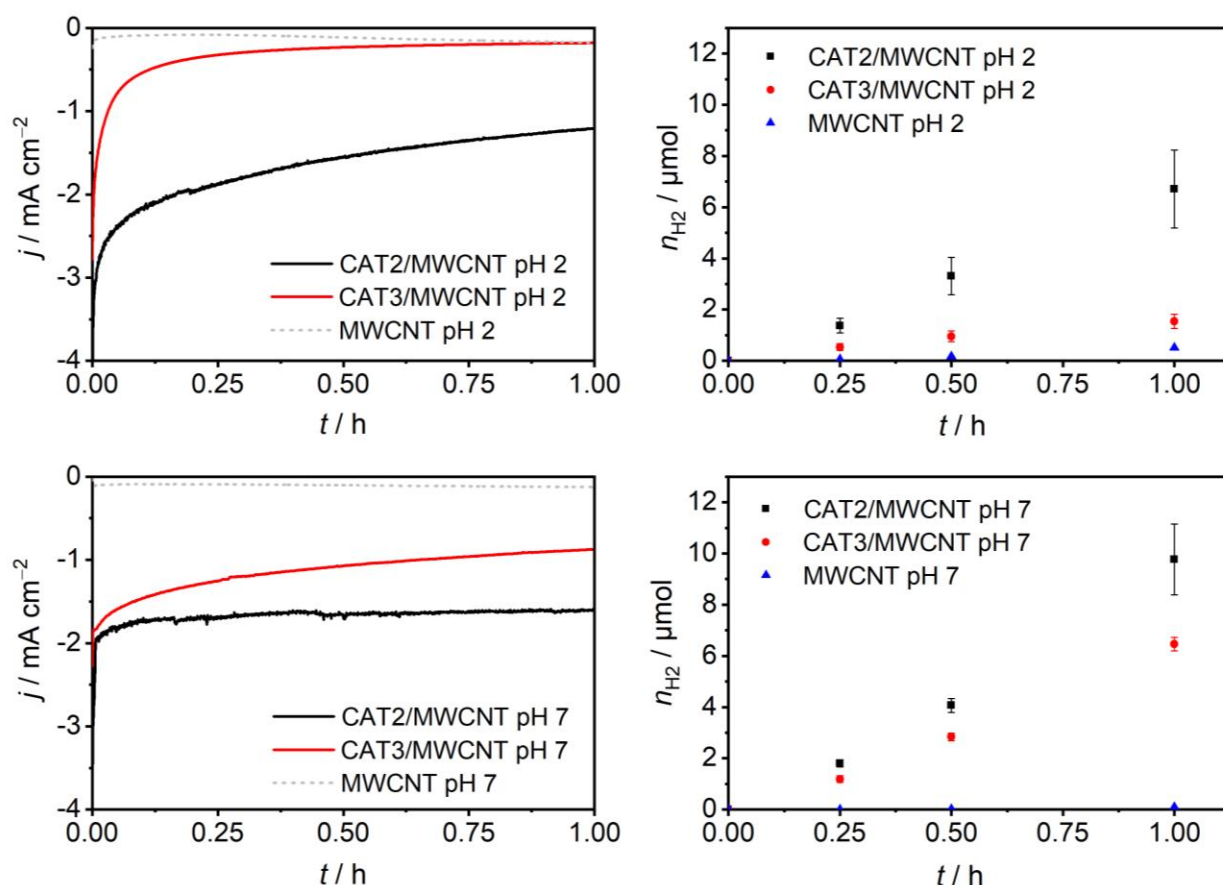


**Figure 4.6:** Chronoamperometry traces (**Left**) and hydrogen measurements (**Right**) with error bars from triplicate experiments for the modified electrodes: CAT2/MWCNT (black traces), CAT3/MWCNT (red traces) and MWCNT-only controls (dotted traces/blue points). Applied potentials:  $-0.60$  V vs. NHE in pH 2, 0.1 M chloride buffer and  $-0.90$  V vs. NHE in pH 7, 0.1 M phosphate buffer, so that both conditions have the same applied overpotential ( $-0.48$  V vs. RHE). Reprinted from **Paper II**.

CV over many cycles was carried out on the catalyst-modified electrodes to gauge preliminarily what kind of processes might occur to the catalysts from the applied potentials and continuous cycling at the electrode interface (**Figure 4.7**). It is noteworthy that the catalytic enhancement provided by the immobilised catalysts versus unmodified MWCNTs, seen in CA and H<sub>2</sub> measurements to be more significant and more stable at pH 7 than at pH 2, is less obvious in CV measurements, even at a lower scan rate, since the catalytic wave currents do not appear to grow much, so CV may not be a clear indicator of catalyst effectiveness for this system.

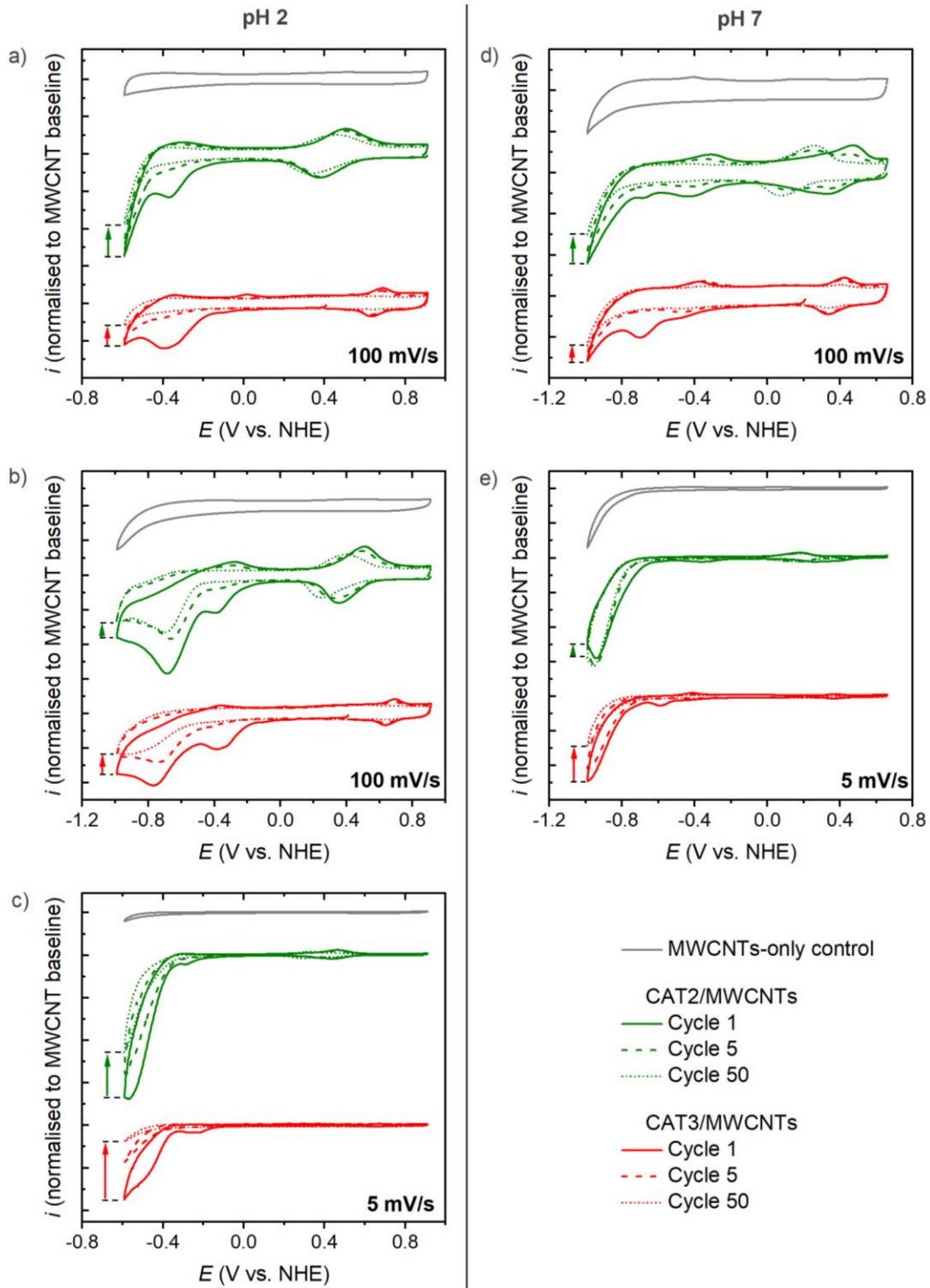


**Figure 4.7:** Cyclic voltammograms of CAT2/MWCNTs and CAT3/MWCNTs on a glassy carbon working electrode, against a MWCNT-only control. First, fifth and fiftieth scans are shown. (a) 100 mV s<sup>-1</sup>, at pH 2, lower scan bound: -0.59 V vs. NHE. (b) 100 mV s<sup>-1</sup>, at pH 2, lower scan bound: -0.99 V vs. NHE. (c) 5 mV s<sup>-1</sup>, at pH 2, lower scan bound: -0.59 V vs. NHE. (d) 100 mV s<sup>-1</sup>, at pH 7, lower scan bound: -0.99 V vs. NHE. (e) 5 mV s<sup>-1</sup>, at pH 7, lower scan bound: -0.99 V vs. NHE. pH 2 buffer: 0.1 M chloride. pH 7 buffer: 0.1 M phosphate.

Furthermore, it is noted that under practically all conditions and for both CAT2 and CAT3, after only a few cycles the separate Co(II/I) reduction peak (which normally is less than stoichiometric to the Co(III/II) couple) disappears to leave only the HER catalytic wave. The Co(III/II) couple however remains visible for longer and is especially stable for CAT2. However, for CAT2 the Co(III/II) couple always shifts slightly to more negative potentials, broadens and then stabilises over the first few cycles. This potential shift does not seem to be explainable by the expected effect of displacing the chloride axial ligands with water upon turnover, and the preservation of the clear apparent Co(III/II) couple would imply that the molecular structure of the catalyst is maintained.

Moreover, for CAT3, the redox couples' peaks can shrink entirely, yet still a mild HER catalytic enhancement is observed, although the speed of the peak shrinking may also corroborate CAT3's quicker diminishing currents in CA. Thus, it appears that upon initiating cycling to catalytically active potentials, some changes happen that affect the catalysts' responses, and the surface rapidly re-equilibrates and stabilises, before slower degradation processes over long-term cycling. The cause for the disappearance of redox peaks is not clear, but it might be postulated that after being reduced during the catalytic cycle to states where the axial ligands are labilised, it may be possible for the metal centres' surroundings to be changed such that they can become trapped closer to the surface and begin to engage in ISET processes for the HER instead of the initial OSET processes, if the active sites penetrate the EDL.<sup>121-123</sup> The relative rigidity and length of the anchor's linker in CAT2 compared to in CAT3 could hypothetically play a role in this kind of effect.

## 4.5 Outlook and Perspective for Device Integration

On the basis of the chronoamperometry and hydrogen gas measurements under CPE at sufficient overpotentials, both derivatives of CAT1 function as effective heterogenised electrocatalysts for the HER, with especially notable faradaic efficiencies in neutral conditions. In terms of applications for hydrogen-evolving cathodes for a PEM cell, these materials are therefore promising and testing on larger electrodes is warranted.

CAT2 operates with the higher current densities and stability, and was successfully immobilised in initial tests onto small printed graphite-based electrodes, both with and without MWCNTs as a support. It was therefore selected as one of the molecular catalysts to be tested in small PV-EC device-scale electrodes in further studies, in collaboration with other groups within the eSCALED project. To incorporate the molecular catalyst with or without supporting MWCNTs, an appropriate base material for the underlying electrode is also important. For PV-EC device engineering, the end criteria would be scalability and mass production. Two options are the often-used carbon fibre-based gas diffusion layers, which have been industrially developed for PEM technologies,<sup>46</sup> and printed electrodes typically made from graphite-based carbon pastes, which are a particular focus of the eSCALED project because they can be produced using printing techniques which can be adapted for upscaling, eventually maybe even with roll-to-roll processing, etc.<sup>126</sup> Samples of CAT2 have been supplied to collaborating groups for testing with these materials.

Of note, although the two derivatives share the same core CAT1 active site, CAT2 performed better than CAT3 under all conditions tested, in terms of current densities, stabilities and faradaic efficiency. Hence there is a clear effect from the different modification strategies. For informing rational design principles it would be useful to understand the reasons behind this, however a more systematic and extensive study would be needed for this purpose for the specifics of this system.

It might be hypothesised that the modification at the macrocycle amine could be interrupting a proton relay or otherwise mechanistically important part of the active site. However, CAT3 still operates comparably effectively under neutral conditions for many cycles. An alternative explanation could arise from the difference in the rigidity, nature and length of the linkers to the anchoring groups on each derivative. Compared to the long, conjugated and rigid benzamide linker in CAT2, the shorter and more flexible methylene linker in CAT3 may reduce the distance to the electrode surface to potentially facilitate the ET processes,

but may also leave it vulnerable to deactivation processes if the anchoring group blocks or interacts with the active site.

Ideally, when appending anchoring groups, any negative impact on the active site's efficiency or ability to access substrate and turn over should be avoided or minimised, and surface conductivity must be maintained or ET from the electrode otherwise facilitated.<sup>31</sup> Therefore, there may ultimately be multiple factors and principles determining the optimum linker design and anchoring strategy for the system, which would require further investigation to understand and take advantage of for developing future derivatives and improving the CAT1-based system, as has occurred over the past decade for the DuBois catalyst.<sup>63,106-109</sup>



# 5 Ultrafast Electron Transfer from CuInS<sub>2</sub> Quantum Dots to CAT1 and CAT1-CO<sub>2</sub>H for Hydrogen Production: *Rethinking the Binding Models (Paper III)*

## 5.1 Motivations and Background

On the opposite side of the spectrum for photon-based strategies for solar-driven water-splitting, direct photocatalysis is also an interesting approach. When done directly in a solution (ideally water, for hydrogen evolution), the system for study can be constructed as simply as by just dissolving a photosensitiser and a catalyst in water. When not studying a complete system with a complementary water oxidation catalyst, it is necessary to also provide a buffer to maintain the proton concentration and a sacrificial electron donor to regenerate the ground state of the photosensitiser to study the catalytic performance over time.

Furthermore, effective photosensitiser-catalyst combinations studied under (typically homogeneous) PC conditions can often be adapted to PEC setups by heterogenising the species through immobilisation onto a suitable solid semiconductor material to construct catalytically active photoelectrodes. The PEC approach would generally be considered more readily applicable to device construction than PC. PEC has certain advantages: the spatial organisation of the PEC components as separated (photo)electrodes enables the automatic separation of the production gases and prevents certain recombination pathways that can arise from the proximity of components in PC water-splitting. Additionally, the (photo)electrodes are electronically connectable, giving the possibility to apply a potential bias to increase efficiency versus a pure PC system. This bias can often be substantially smaller than the required applied potential across an electrolyser cell without any photosensitisers.<sup>28,29</sup>

CAT1 has previously proven effective for the photocatalytic HER with a fairly diverse range of photosensitisers. These include [Ru<sup>II</sup>(bpy)<sub>3</sub>]<sup>2+</sup>,<sup>75,78,83,95</sup> triazatriangulenium organic dyes,<sup>84,127</sup> and CdTe quantum dots,<sup>85</sup> as well as within dye-catalyst ‘dyad’ assemblies.<sup>96,97</sup> Again, this showcases the versatility of CAT1. Of particular note was the performance of CAT1 with copper indium sulfide-zinc sulfide core-shell quantum dots (CIS/ZnS QDs), reported by the Wang and Collomb groups.<sup>86,87,118</sup> Impressive per-catalyst turnover numbers (TON) of up to 7700 were reported in mildly acidic conditions, while ET rates on the nano-second scale or below were claimed. The derivative of CAT1 functionalised with a 2,6-dicarboxypyridin-4-yl anchoring group, mentioned in the previous section, was compared to the unmodified CAT1. Some substantial, though not immense, improvements in terms of photocatalytic H<sub>2</sub> production (of about 3.5-times) and quantum dot-to-catalyst ET rates (approximately double) were reported for the anchorable derivative.<sup>87</sup>

However, the reasons for the very high reported TONs and ultrafast electron transfer rates – with or without designated anchoring group – are still under-explored, and the unexpectedly small improvements achieved by incorporating a sophisticated anchoring group seemed somewhat mysterious. The aim of this project was to investigate and explain these observations by clarifying the mechanism of quantum dot-to-catalyst electron transfer and the effects on the photocatalytic behaviour from varying certain system parameters.

## Quantum Dots

Quantum dots (QDs) are nanocrystals (approximately spherical, crystalline structures on the nanometer-scale in all three dimensions) made up of a semiconductor material. QDs can be prepared through a bottom-up wet chemical synthesis procedure and are often referred to as ‘colloidal’ when dispersed in a solution. When they absorb light radiation of an appropriate energy, an exciton (a bound excited electron-hole pair) is generated.

The specific defining characteristic of QDs is that they exhibit a strong *quantum confinement* effect due to their particularly small size,<sup>128</sup> which reaches the exciton Bohr radius (the characteristic delocalisation length between an excited electron and its associated hole for the macroscopic semiconductor) or below. At this point, the electronic wavefunctions become spatially confined, which significantly affects the electronic energy levels. Therefore, by adjusting the size of the particles through controlled chemical synthesis and purification, it is possible to tune the energy gap of the QDs, thereby also tuning the frequency of absorbed or emitted light and the valence band (VB) and conduction band (CB) potentials.<sup>129,130</sup> In fact, other parameters, such as composition<sup>131,132</sup> and the nature of capping ligands<sup>130,133</sup> can also be used to tune the QDs’ properties.

When employed as photosensitisers for driving electrons to or from molecular catalysts, QDs have some distinct advantages when compared to molecular photosensitisers. Firstly, the aforementioned tunability of their photophysical and electronic properties. Secondly, their relatively large size compared to molecules gives them a relatively large surface area, since this scales to the square of the particle’s diameter (typically QDs have diameters of between 2 and 10 nm, molecular catalysts will typically have diameters below about 1 nm). This larger surface area, typically providing various different possible binding modes involving the surface atoms/ions of the QD,<sup>134</sup> may help to encourage the attraction of species such as molecular catalysts onto the QD surface, allowing for faster and more efficient electron transfer.<sup>135</sup> Thirdly, as a result of this surface area onto which a catalyst can connect, it can be possible to template and form a catalyst active site structure around labile metal ions,<sup>136</sup> or stabilise catalysts that are vulnerable to deactivation via dimerisation,<sup>137</sup> which is one proposed deactivation pathway of cobalt tetraazamacrocyclic catalysts. Finally, QDs typically are highly photostable and have long excited state lifetimes, and may be able to act as electron reservoirs to facilitate the transfer of multiple electrons over multiple steps, which is a major challenge in catalytic processes for solar fuels production.<sup>138–141</sup>

Furthermore, it is noted that electron transfer from QDs to molecular catalysts is often reported to be very efficient and very rapid, perhaps beyond even what would be expected with the known advantages listed above.<sup>86,87,135,142,143</sup> For example, Jian *et al.* noted two orders of magnitude improvement in terms of both TONs and TOFs for a pair of [FeFe]-hydrogenase mimics when combined with CdSe QDs instead of [Ru(bpy)<sub>3</sub>]Cl<sub>2</sub>.<sup>144</sup>

In recent times, the semiconductor ternary alloy, copper indium sulfide (CIS) has become a popular choice as a material for QDs, particularly with the push towards Pb- and Cd-free QDs for lower toxicity. CIS has interesting properties for tunability based on size,<sup>145</sup> stoichiometry<sup>146–148</sup> and the nature of the shell (typically ZnS) and ligand sphere.<sup>147</sup> A purportedly green synthesis of CIS/ZnS core-shell quantum dots was reported by Chen *et al.* in 2013.<sup>147</sup> Conveniently, the method was water-based, air-tolerant, relatively low-temperature (95 °C) and produced water-soluble quantum dots – an important factor for water-splitting PC. Additionally, the number of ZnS shell monolayers could be controlled, and glutathione and citrate were used as the default stabilising agents. This method therefore proved practical and adjustable.

Building upon this, at UU a new, similar type of CIS QDs was developed by Huang *et al.* These CIS QDs differed from the common core-shell types in the literature by the substitution of the ZnS shell with a *hybrid-passivating*<sup>88</sup> ligand sphere, consisting of cysteine and iodide.<sup>149</sup> This hybrid-passivating ligand system was designed to enable compatibility with meso-porous NiO thin-films printed on fluorine-doped tin oxide glass plates: firstly, by shrinking the overall size of the QDs, since the ZnS shell greatly increased their radii, and, secondly, by avoiding destabilisation of the NiO layer, which some species (such as glutathione) had been reported to do.<sup>149</sup> This would enable future adaptation towards a PEC system, as discussed

above, which had been previously tested for a Re-based CO<sub>2</sub>RR molecular catalyst.<sup>149</sup> The reducing potential of the photoexcited hybrid-passivated CIS QDs was estimated to be  $-1.3$  V vs. NHE from their conduction band, providing ample overpotential for the HER, as well as the CO<sub>2</sub>RR with the efficient catalyst they employed.

However, in order to provide a comparison with the results from the Wang and Collomb groups, the effects of replacing the typical ZnS shell with the *hybrid passivation* ligand system had to first be studied to verify that the QD-to-CAT1 ET was still effective, since the removal of the ZnS shell would be anticipated to have significant effects on the properties of photogenerated excitons, the ET processes from the QDs to any recipient species, and the recombination processes that the charge-separated states could undergo. Finally, the benzoic acid-functionalised derivative, CAT-CO<sub>2</sub>H was also employed as a catalyst with the CIS QDs to compare with CAT1. It was supposed that the *para*-pyridine position benzoic acid moiety on CAT1-CO<sub>2</sub>H would function as an anchoring group to attach onto the semiconductor QDs. This would provide some comparison of the behaviour of the system with an intended anchoring group on the catalyst versus without.

## 5.2 Photocatalysis Performance

First, to check that the CIS QD-CAT1 photocatalytic system (illustrated in **Figure 5.1**) still functioned effectively for the HER for the new hybrid-passivated QDs without the ZnS shell, photocatalytic experiments were carried out, measuring evolved H<sub>2</sub> by gas chromatography and illuminating with constant visible light irradiation. Sodium ascorbate/ascorbic acid was used both as the buffer and the sacrificial electron donor. A total buffer concentration of 0.5 M and pH 4.5 were set as conditions that had previously been optimised by Collomb and coworkers.<sup>86</sup> A light intensity of 57 mW cm<sup>-2</sup> from an LED light source (420–750 nm) was used for illumination (estimated to be roughly one sun).

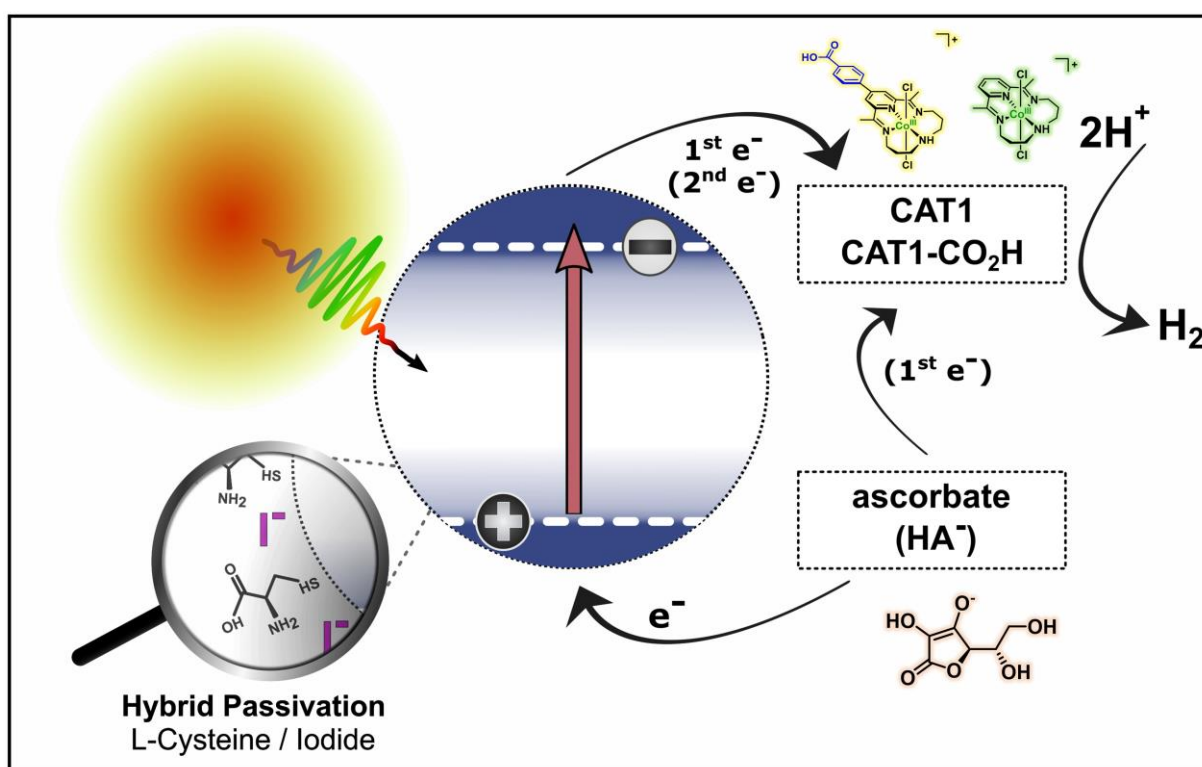


**Figure 5.1:** Illustrative overview of the photocatalytic system under investigation, with hybrid-passivated copper indium sulfide quantum dots as photosensitiser, ascorbate (highlighted orange) as sacrificial electron donor, and the two HER catalysts, CAT1 (highlighted green) and CAT1-CO<sub>2</sub>H (highlighted yellow). Adapted from **Paper III**.

H<sub>2</sub> gas injection measurements were taken up to 24 hours after the start of illumination: it had been previously shown for other systems that after this time the system's performance would become limited by the

build-up of dehydroascorbic acid (DHA), generated from the disproportionation of the ascorbyl radical (formed by oxidised ascorbate). DHA ‘short-circuits’ such systems and eventually prevents QD-to-catalyst ET at high enough concentrations.<sup>86,150</sup> In system using a sacrificial donor without this behaviour, or a heterogenised PEC system, this would not be the limiting factor.

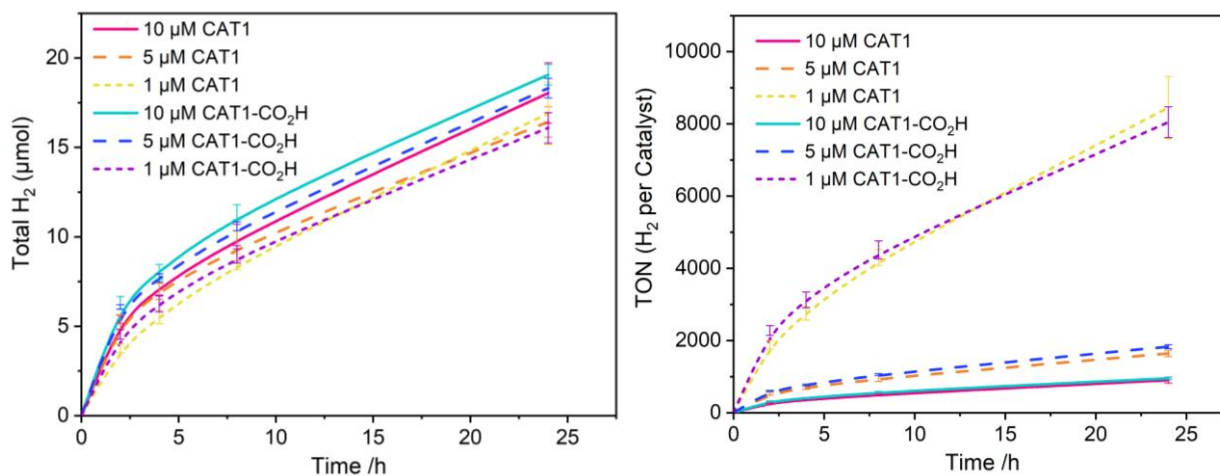


**Figure 5.2:** Produced H<sub>2</sub> (Left) and TON per catalyst (Right), measured by gas chromatography against time of irradiation, varying concentration of CAT1 and CAT1-CO<sub>2</sub>H (2 mL solution, 7 mL headspace). Visible light irradiation intensity (57 mW cm<sup>-2</sup>) and CIS QD concentration were kept constant. (QD absorbance at 405 nm: 0.35 for a 1 cm pathlength. Estimated QD concentration: 5 μM QDs, estimated from quenching studies and modelling discussed later). Buffer solution: 0.5 M H<sub>2</sub>Asc/NaHAsc, pH 4.5. Reprinted from **Paper III**.

From these photocatalytic H<sub>2</sub> measurements, where the concentration of each catalyst was varied between 1–10 μM for an estimated 5 μM concentration of QDs (**Figure 5.2**), it is immediately apparent that (a) the concentration of catalyst across this range is having little effect upon the H<sub>2</sub> production of the system over one day (only around 10% increase for a tenfold increase in [CAT]), meaning that the TON per catalyst is effectively scaling inversely with [CAT], and (b) the presence of the designated anchoring group on CAT1-CO<sub>2</sub>H also has little effect upon H<sub>2</sub> production.

This implies that the system is limited by another factor under these conditions – probably the rate of absorption of photons to photoexcite the QDs and the rates of competing charge recombination reactions – rather than the availability of catalyst or the intrinsic ET rate from excited QDs to catalyst. Additional photocatalytic experiments to control for varying the QD concentration and light intensity are planned. Nonetheless, the TON per catalyst for about 5 μM of QDs 8000 is close to the maximum value reported by Sandroni *et al.*<sup>86</sup> for their CIS/ZnS system, but, in their case, higher concentrations of photosensitiser were used and increasing [CAT] still improved H<sub>2</sub> production almost quantitatively. It may be roughly assumed from this that the hybrid-passivated CIS QDs are the more efficient system in terms of quantum yield of H<sub>2</sub>, but without strictly comparable illumination conditions, a direct comparison is not possible.

### 5.3 Spectroscopic Characterisation and PL Quenching

Spectroscopic studies were carried out to investigate the causes and possible mechanisms of the CIS-CAT1 system’s behaviour. Firstly, the hybrid-passivated CIS QDs were characterised (**Figure 5.3**). QD physical and structural characterisation details and interpretation are described in **Paper III**. The CIS QDs absorb over a wide range of wavelengths and re-emit with a large Stokes shift. Absorption at around 515 nm is assigned to the band-edge excitons; the shoulder around 430 nm is assigned to a higher excitonic state involving a deep hole state; the tail of lower energy absorbances is assigned to sub-bandgap transitions. The photoluminescence (PL) spectrum is interpreted as a main, broad band centred around 715 nm, involving trapped charge carriers, and a higher-energy tail below 600 nm.

Following analysis of the QDs alone, PL quenching studies were carried out with the molecular catalysts. The molecular catalysts act as oxidative quenchers, by receiving electrons from the photoexcited quantum dots. After this process, the oxidised QDs no longer have an excited state that can decay radiatively, so they are non-emissive, and wait for a sacrificial electron donor to reduce them back to their ground state. This is observed in fluorescence spectroscopy as a decrease in intensity of the photoluminescence peak associated with the radiative emission from de-excitation of the electrons (example in **Figure 5.4**), as these electrons have instead been transferred to the quencher. The broad PL band centred around 715 nm is the one predominantly quenched by the catalysts. A small blueshift of the PL peak is observed simultaneously.

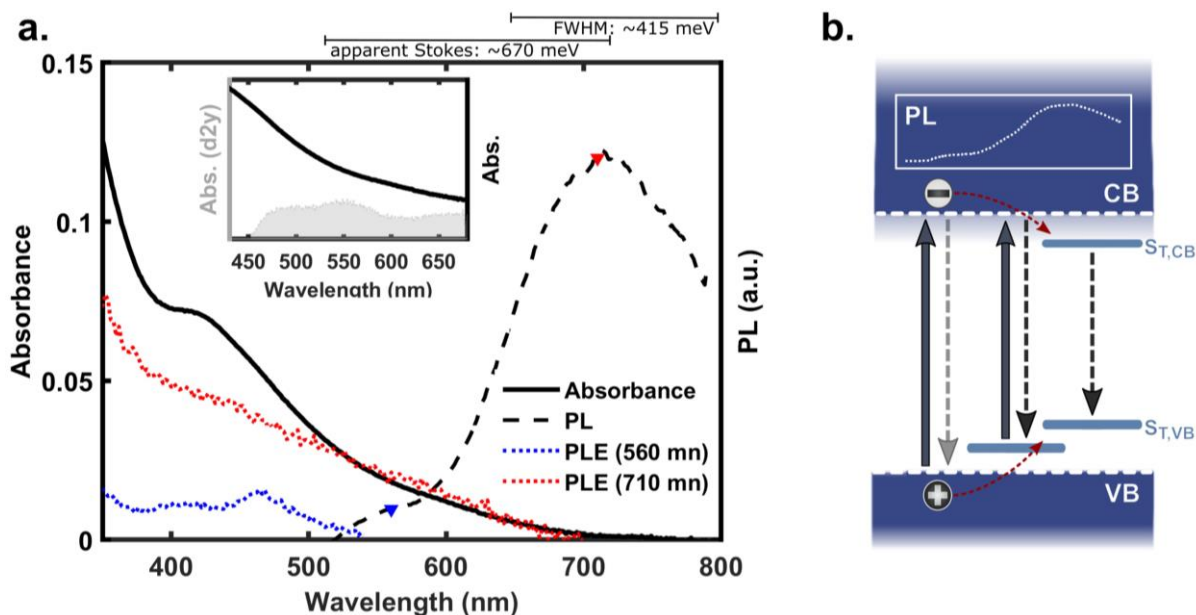


**Figure 5.3.** **Left:** Absorbance, photoluminescence (PL) and photoluminescence excitation (PLE) spectra for approximately 1  $\mu\text{M}$  CIS QDs dispersed in water. Monitored wavelengths marked with triangles. PLE at 560 nm emission is scaled up by 5 times. Inset: zoomed around 550 nm with smoothed second derivative plot. **Right:** Diagram of the energy level transitions that can occur in the QDs and their tentative assignments, including trap states, ‘ $S_T$ ’. Solid arrows: absorption. Dashed arrows: PL.

The quenching experiments were done for a range of QD concentrations, and also with and without ascorbate at 0.1 M or 0.5 M concentrations for specific QD concentrations. It was noted that the presence of ascorbate also had a quenching effect by itself, and amplified the quenching effect of the catalysts (discussed later). In any case, when plotting the ratio of the PL intensity without quencher over the PL intensity with quencher,  $F_0/F$ , against the concentration of quencher,  $[Q]$ , the linear trend expected for a classic Stern-Volmer relationship was not observed for either CAT1 or CAT1- $\text{CO}_2\text{H}$ .<sup>93</sup> A linear trend would correspond to dynamic (a.k.a. collisional) quenching or pure static quenching with a weak association. However, the  $F_0/F$  ratio instead appeared to increase exponentially with quencher concentration: plotting  $F_0/F$  on a logarithmic scale yielded strongly linear plots, implying a form of static quenching with very high QD-catalyst binding affinities. Therefore, an alternative model had to be applied to account for the observations (discussed in 5.5 *Modelling of the System*, **Figure 5.9**), since forcing a Stern-Volmer analysis would be inappropriate and lead to misinterpretation of the quenching mechanism.<sup>151</sup>

In order to first determine whether the oxidative quenching by the catalysts was static in nature, TCSPC experiments were carried out alongside the PL quenching experiments. Observing the decay profiles and applying triexponential fits, it was noted that there is little change in the plots or fitted lifetimes with increasing concentration of either catalyst, even up to over 80% quenching (**Figure 5.5**; details in **Paper III**). This lack of change in the lifetimes with the increased quencher concentrations supports a static quenching mechanism for the catalysts.

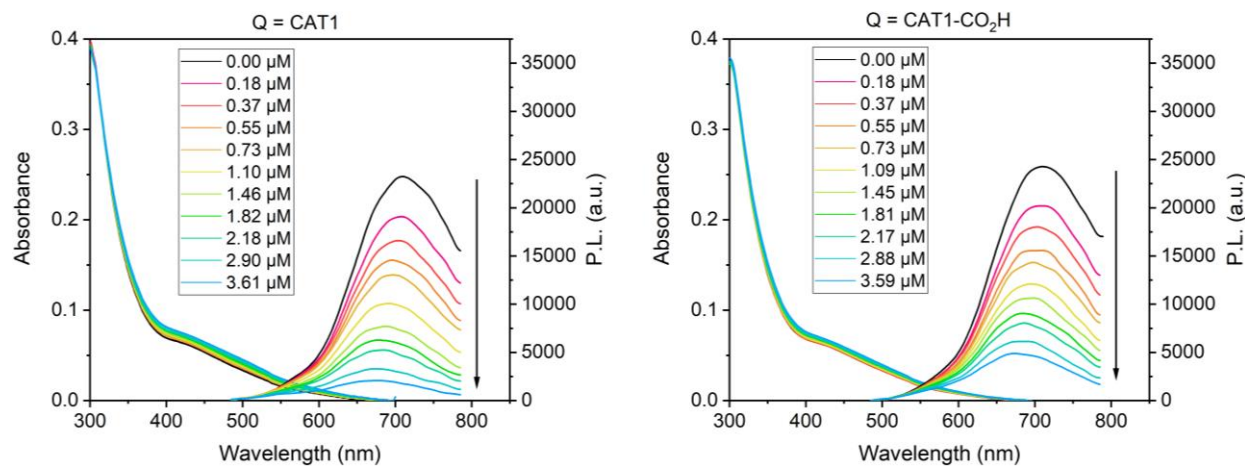


**Figure 5.4:** Example PL quenching spectra (with corresponding absorbance spectra overlapped for each) of a CIS QD sample diluted to have an absorbance of 0.07 at 405 nm (estimated [QD]: approximately 1  $\mu\text{M}$ ) with increasing concentration of either CAT1 (**Left**) or CAT1-CO<sub>2</sub>H (**Right**). PL excitation wavelength: 405 nm. Cuvette pathlength: 1 cm. Solvent: deionised water.

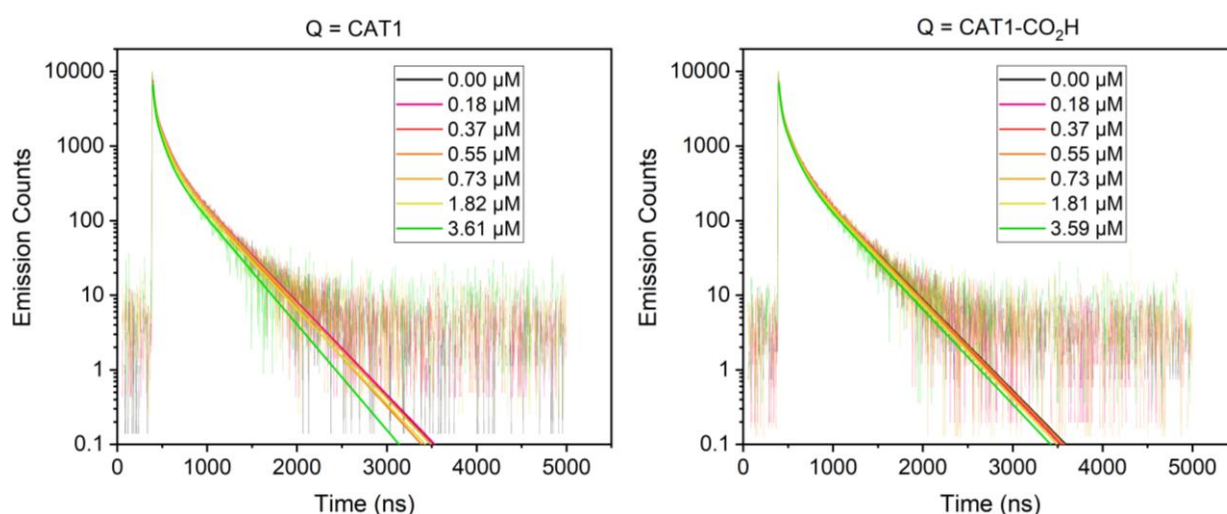


**Figure 5.5:** Example TCSPC traces and rough triexponential fits for the same samples as in **Figure 5.4**: A CIS QD sample diluted to have an absorbance of 0.07 at 405 nm (estimated [QD]: approximately 1  $\mu\text{M}$ ) with increasing concentration of either CAT1 (**Left**) or CAT1-CO<sub>2</sub>H (**Right**). PL excitation wavelength for TCSPC: 470 nm. Cuvette pathlength: 1 cm. Solvent: deionised water.

Additionally, it is known from literature that ascorbate rapidly reduces CAT1 from its air-stable Co(III) state to its Co(II) state. However, atmospheric O<sub>2</sub> dissolved in water will also re-oxidize CAT1 to its Co(III) state.<sup>76</sup> Therefore, for these unpurged experiments, both with and without ascorbate, the observed oxidative quenching process is assigned to an ET which reduces the catalyst from Co(III) to Co(II); this is supported by the fs-TA experiments in the following section. The Co(II/I) reduction is thermodynamically more demanding but is expected to have a similar lifetime and efficiency.<sup>87</sup> Furthermore, as ascorbate acts as a reductive quencher for the CIS QDs, the quenching effect of ascorbate on its own was also investigated and modelled.

From PL quenching and TCSPC experiments with ascorbate as the sole quencher (**Figure 5.6**, and, from TCSPC in **Paper III**, the overall  $\tau_0/\tau$  ratio closely follows the  $F_0/F$  ratio), it is apparent that, up to 0.5 M ascorbic acid/ascorbate total concentration, it behaves as a dynamic reductive quencher. Additionally, a significant redshift of the emission peak reaching up to 50 nm at 1.0 M ascorbic acid/ascorbate concentration was noted. A cooperative quenching effect of ascorbate with catalyst, causing the catalysts to quench twice as effectively or more in the presence of ascorbate is not accounted for by their separate quenching effects combined; it is possible that ascorbate can act as a ligand within the QDs' ligand sphere and affect their surface properties (more details in **Paper III**). Possible explanations for these observations are still being considered.

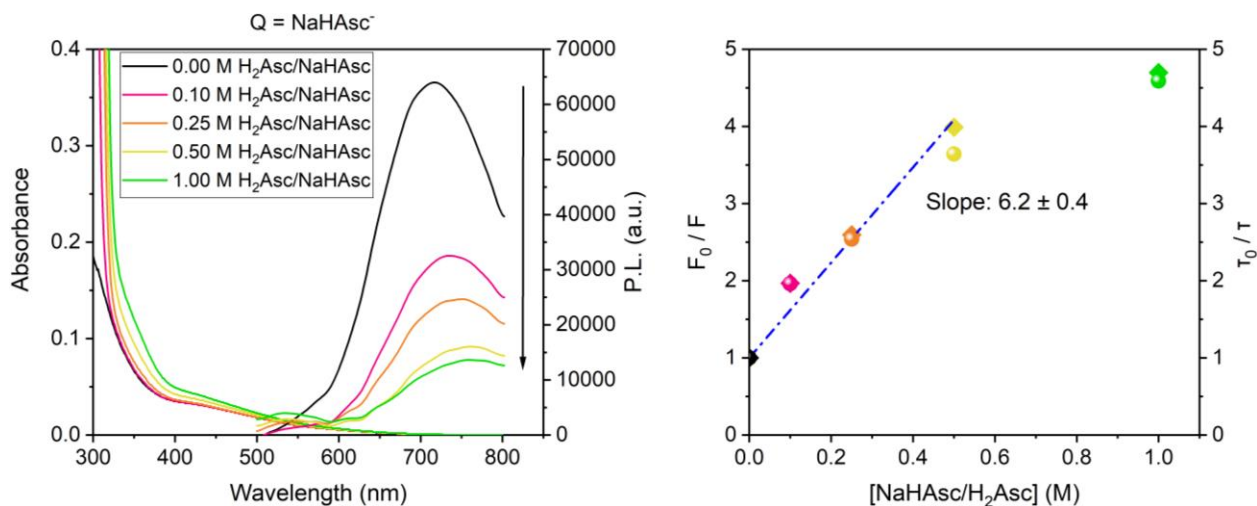


**Figure 5.6.** Left: Example PL quenching spectra (with corresponding absorbance spectra overlapped for each) of a CIS QD sample diluted to have an absorbance in a 1 cm cuvette of 0.36 at 405 nm (estimated [QD]: approximately 5  $\mu$ M) with increasing concentration of ascorbate buffer at pH 4.5. Note that the concentration of the ascorbate conjugate base is about 70% of the total buffer concentration ( $pK_{a1} \sim 4.2$ ). PL excitation wavelength: 405 nm. Experiment cuvette pathlength: 1 mm. Solvent: deionised water. Right: Stern-Volmer plot of quenching by ascorbate. Diamonds:  $F_0/F$ ; circles: overall  $\tau_0/\tau$ . Linear region fitted for  $F_0/F$  values to obtain a Stern-Volmer quenching constant of  $K_{SV} = 6.2 \pm 0.4 \text{ M}^{-1}$ .<sup>93</sup>

## 5.4 Transient Absorption Spectroscopy for ET Rates

Additionally, femtosecond transient absorption spectroscopy was employed to study the electronic processes within and ET rates from the CIS QDs. Exciting the samples with 400 nm light, long lived negative bands are observed at approximately 430 nm (B0), 520 nm (B1) and 610 nm (B2). These are assigned to transitions with corresponding excitation energies at or above the optical bandgap (B0 & B1) and to sub-bandgap transitions (B2) (**Figure 5.7a**). On the basis of previous work with closely related CIS QDs,<sup>143</sup> the bands B1 and B2 are attributed to the bleaching of two separate optical transitions which primarily correspond to optical transitions from the VB to the CB (B1) and from hole trap states above the VB to the CB (B2), shown in **Figure 5.7b**. Additionally, broad positive signals below 400 nm and above 525 nm are observed which extend into the IR region.

The effects of the presence of 0.1 M ascorbate buffer at pH 4.5 versus no buffer were noted in the form of static and dynamic changes (**Figure 5.7a** versus **5.7c**), however, these effects were attributed to the difference in pH by control experiments in acetate buffer, indicating that pH has some significant effects on the QD optical responses in TAS and must be accounted for or controlled for interpretation (**Figure 5.7d**).

The presence of either CAT1 or CAT1-CO<sub>2</sub>H causes significant changes in the recorded spectra in both the mid-IR (MIR) and UV-visible regions (**Figure 5.8a** & **c**, respectively). On the one hand, the decay of the broad positive QD feature in the mid-IR range is accelerated by the addition of either catalyst. This is interpreted as CB electrons (generated by photo-excitation from the pump laser) being depleted through ET events to the catalysts (illustrated in **Figure 5.8b**). Notably, the timescale for this is 1 ps and above. On the other hand, the addition of either catalyst results in an enhanced recovery of the B1 bleach band and the appearance of a superimposed positive transient corresponding to a long-lived charge-transfer product – the Co(II) form of the catalyst – while little change to the B2 band is observed (**Figure 5.8d**).

The spectral profile of the reduced catalysts (assumed to be reduced to their Co(II) state for the reasons discussed before regarding the effect of ascorbate in unpurged solution) is noted to be redshifted compared with their typical solution absorption spectra. A similar effect was observed for the bound Co(III) states, extracted from the difference between absorption spectra for the CIS QDs with and without catalyst (**Paper III**, SI), implying that the dielectric environment at the QD surface has an effect on the optical transitions.

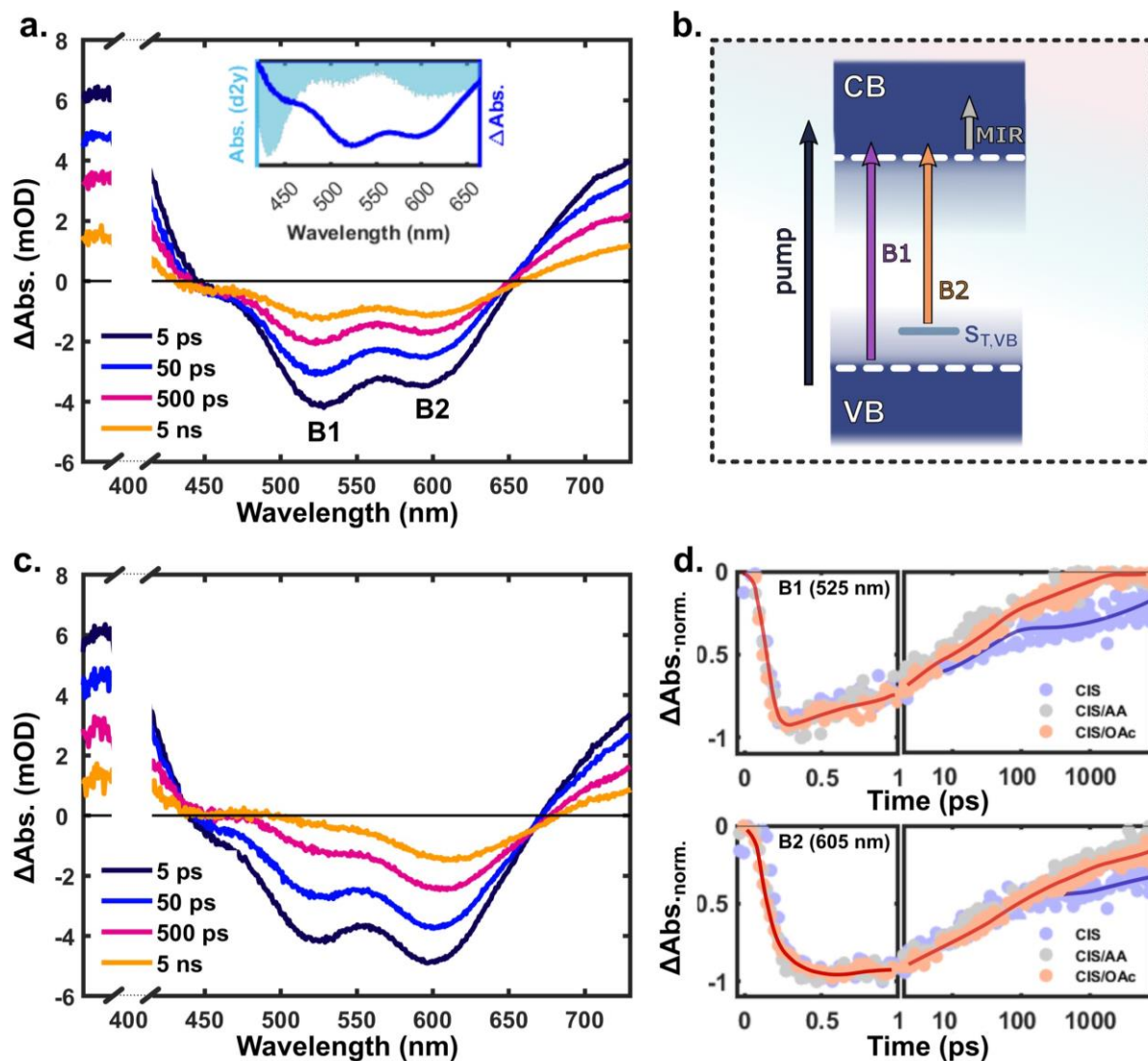


**Figure 5.7:** fs-TA measurements using a 400 nm pump. **a)** fs-TA spectra of CIS QDs in H<sub>2</sub>O at indicated time-delays. The inset shows the second derivative of the QD ground state absorption spectrum (light blue) together with the fs-TA spectrum at 50 ps pump-probe time delay (dark blue). **b)** Schematic of the pump-induced optical transitions monitored in the UV-Vis (B1/B2 bleach bands) and mid-IR (MIR), assigned to photo-induced absorption (PIA). **c)** fs-TA spectra of CIS QDs in H<sub>2</sub>Asc/NaHAsc buffer (pH 4.5, 0.1 M). **d)** Normalised fs-TA kinetics comparing CIS QDs in H<sub>2</sub>O at neutral pH (CIS, blue) with CIS in H<sub>2</sub>Asc/NaHAsc (grey) and NaOAc/HAc (red) buffer at a pH of 4.5. Reprinted from **Paper III**.

In any case, the formation of the reduced catalysts was fitted to lifetimes of electron transfer,  $\tau_{ET}$ , of approximately 3.5 ps and 4.8 ps for CAT1 and CAT1-CO<sub>2</sub>H, respectively, notably faster by almost three orders of magnitude than those reported by Nie *et al.* for ZnS-shell CIS QDs.<sup>87</sup> Again, in this case, the anchoring group is not fundamentally changing the behaviour or significantly improving the performance parameters, but also not disabling the system. To either catalyst, the rate of electron transfer from the hybrid-passivated CIS QDs is faster than the diffusion limit, reinforcing that the mechanism of quenching is static.



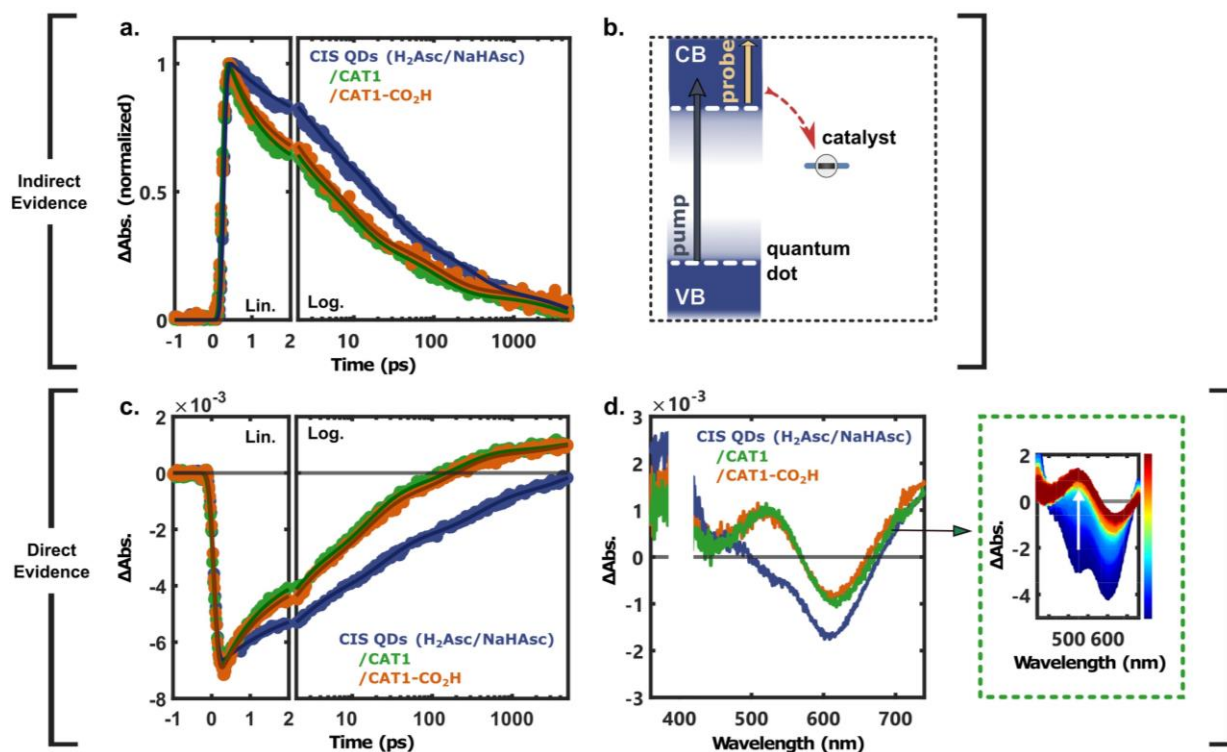


**Figure 5.8:** fs-TA spectra of CIS QDs (blue) mixed with CAT1 (green) or CAT1-CO<sub>2</sub>H (orange) in 0.1 M H<sub>2</sub>Asc/NaHAsc buffer (pH 4.5), excited by a 400 nm wavelength pump. **a)** MIR kinetics averaged between 3600–4000 nm and normalized. **b)** Schematic representation of pump and probe in the MIR together with the transfer of electrons from the CB of photoexcited QDs to the catalysts. **c)** UV-Vis kinetics extracted at 530 nm corresponding to the photo-induced absorption of the reduced catalysts (attributed to their Co(II) states). **d)** Transient spectra at  $t = 2$  ns, zooming in on the CIS/CAT1 spectral evolution from 3 ps (dark blue) to 8 ns (dark red). Reprinted from **Paper III**.

## 5.5 Modelling the System

Since the PL quenching data universally showed strong linear correlations between  $\ln(F_0/F)$  and concentration of either catalyst, it was apparent that the relationship was exponential, while also the mechanism of quenching was demonstrated to be static in nature by TCSPC and fs-TAS. Therefore, a Poissonian distribution model of adsorbed catalyst over the QDs was applied, making the assumption that the presence of even a single catalyst adsorbed at the surface of a QD would be sufficient to guarantee quenching of the PL of that QD (i.e., extremely efficient and rapid ET), and that the association constant of binding for catalyst molecules with QDs is very high, so that practically no added catalyst remains free in solution. This is analogous to a *quenching sphere of action* model for high quencher concentrations,<sup>93</sup> among other models for e.g. micellar systems.<sup>152</sup>

On the basis of the assumptions laid out, the  $F_0/F$  ratio for the quenched PL band would be determined by the ratio of the concentration of all quantum dots in solution over the concentration of quantum dots with zero catalyst molecular adsorbed (i.e., those that are unquenched):

$$F_0/F = [\text{QD}]_{\text{total}}/[\text{QD}]_{n=0}$$

where  $n$  is the number of catalyst molecules adsorbed to the surface of a QD.

Assuming a random distribution of the catalyst molecules across the QDs (implicitly assuming that all consecutive binding equilibria for one more catalyst to bind to a QD are equivalent and each catalyst binds independently), the Poisson distribution applies. The probability of a quantum dot having zero catalyst molecules adsorbed is  $P(0)$  (and thus not being quenched), defined as:

$$P(0) = e^{-\lambda}$$

where  $\lambda$  is the mean number of quenchers per QD in the solution. Therefore:

$$F_0/F = e^{-\lambda}$$

So, the probability of a QD having no catalyst adsorbed on its surface and thereby remaining photoluminescent decreases exponentially with the concentration of added catalyst. This can account for why plotting  $F_0/F$  on a logarithmic scale yields linear plots. From fitting lines of best fit, values for  $\lambda$  can be extracted from the gradients and used to estimate the concentration of QDs in each sample (**Figure 5.9** and **Table 5.1**, details and possible caveats are discussed in **Paper III**).

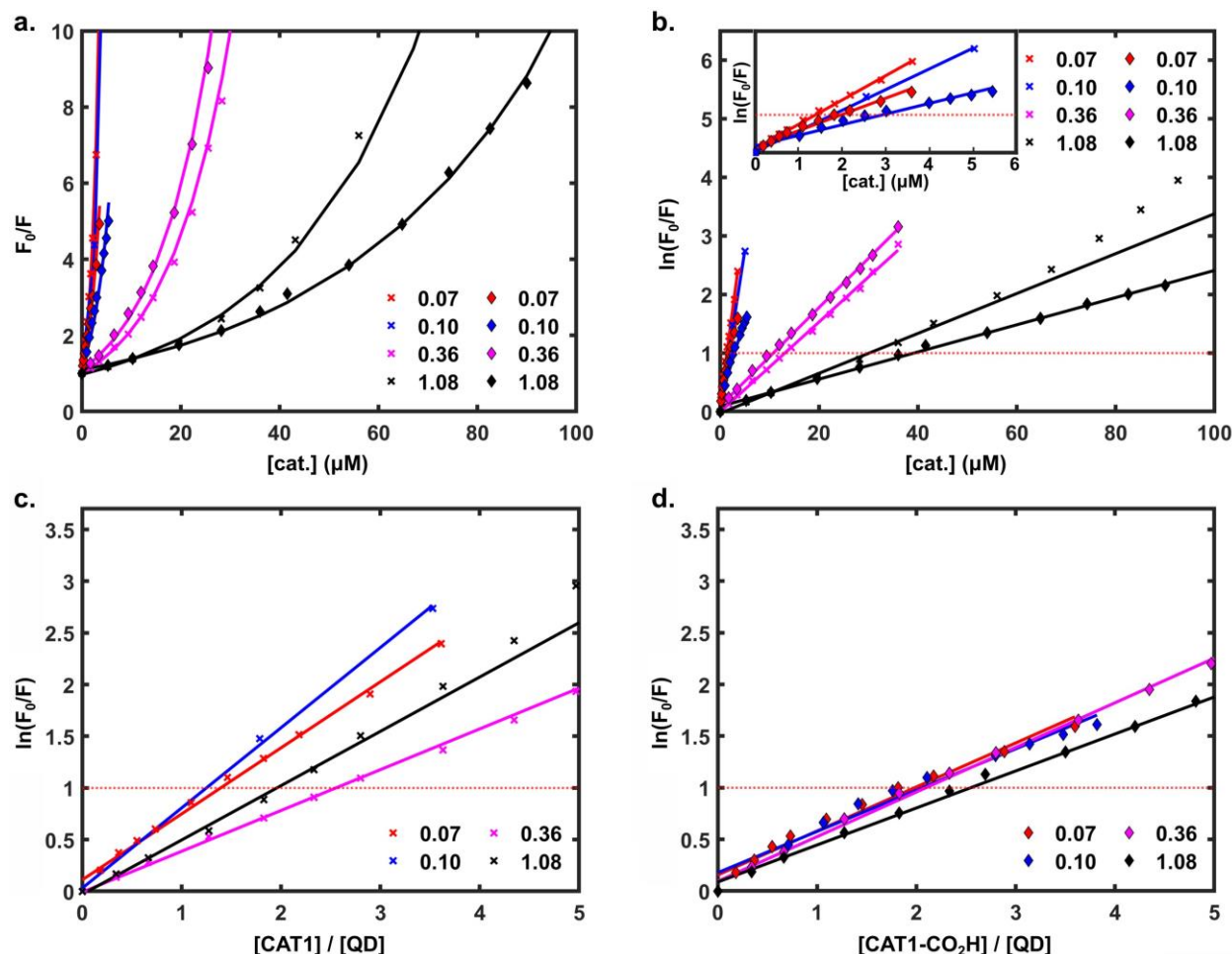


**Figure 5.9:** Plots derived from PL quenching experiments for modelling the quenching mechanism. Different concentrations of CIS QDs in different colours, labelled by their absorbance at 405 nm in a 1 cm cuvette. Only experiments without ascorbate shown for clarity; solvent: deionised water. Datasets with CAT1 as the quencher marked with crosses ( $\times$ ), those with CAT1-CO<sub>2</sub>H marked with diamonds ( $\blacklozenge$ ). Solid lines represent lines of best fit over the linear regions (exponential fit in **a**). Dashed red line:  $\lambda = 1$ . **a**) Direct plots of  $F_0/F$  against catalyst concentration. **b**) Plots of  $\ln(F_0/F)$  against catalyst concentration. Inset: zoomed in for lower concentrations. **c**) Plots of  $\ln(F_0/F)$  against catalyst concentration divided by estimated QD concentration for CAT1 (see text). **d**) Plots of  $\ln(F_0/F)$  against catalyst concentration divided by estimated QD concentration for CAT1-CO<sub>2</sub>H (see text). The estimated QD concentrations are based on the assumption that the dataset with the highest slope (CAT1, 0.10) represents a perfect estimate of QD concentration, and that the values for QD concentration for all other samples scale linearly with relative absorbance, as per the Beer-Lambert law. Reprinted from **Paper III**.

The lines of best fit, calculated by the least-squares method, fitted the datasets with a logarithm applied to the y-axis ( $F_0/F$ ) remarkably well, reflected by  $R^2$  values in **Table 5.1**, supporting the Poissonian binding model. In addition, when the x-axis for the concentration of catalyst is dividing by the relative concentration of quantum dots (as judged by from the relative absorbance at 405 nm), in order to normalise it across all datasets, the datasets and their lines of best fit appear to be in fairly good agreement (**Figure 5.9c & d**). Theoretically, all lines should ideally pass through  $\ln(F_0/F) = 1$  at  $[CAT]/[QD] = 1$ . The lower gradients (down to half the expected value) may be attributed to less than 100% of catalyst binding to the quantum

dots. Nonetheless, especially for CAT1-CO<sub>2</sub>H, the lines of best fit overlap quite well, although for CAT1 there is more random spread between them. Complete overlap should be expected if the binding affinities and ET efficiencies etc. are not affected by the changes in absolute QD concentrations, since the gradient, assumed to be simply  $\lambda$ , represents the ratio of quenchers to QD: when the  $x$ -axis is normalised for different QD concentrations for different datasets, they should share the same gradient.

## 5.6 Outlook and Implications

From these studies, a binding and quenching model has been devised and applied to the CIS-CAT1 and CIS-CAT1-CO<sub>2</sub>H systems with satisfactory fitting of the PL quenching data. Alongside photocatalysis experiments, TCSPC and fs-TAS, it has been shown that hybrid-passivated CIS QDs are quenched by CAT1 through a static quenching mechanism with a strong binding affinity and extremely rapid ET processes.

Although these features of the systems are probably to some extent particular to hybrid-passivated CIS QDs (judging by the differences in ET rates and the TON-[CAT1] relationship against systems with ZnS shells<sup>86,87</sup>), it may also be the case that many other QD-molecular catalyst combinations have remarkably strong binding affinities and efficient ET processes that lead to remarkable photocatalytic performances. In any case, this work and previous reports may demonstrate that quantum dots, with the appropriate structure, are remarkably effective photosensitisers and perhaps uniquely well-suited for photocatalysis of certain small molecule activation reactions with molecular catalysts, for the reasons elaborated here and discussed in the introduction. The fact that the performances are in a number of cases roughly equivalent with or without anchoring groups<sup>143</sup> implies that QDs' surfaces often provide a welcoming and stabilising platform for the adsorption of molecular catalysts, regardless.

Furthermore, using hybrid-passivated quantum dots that are compatible with thin-film semiconductor materials of interest (e.g. NiO) may pave the way for the heterogenisation and adaptation of such systems to photoelectrodes for PEC for H<sub>2</sub> production, though so far only preliminary tests for this system were carried out around this project. Nonetheless, even with highly favoured binding equilibria, it is important for heterogenised systems to have irreversibly immobilised components. For this reason, it is important that the photosensitiser and catalysts not only have a high affinity for each other in terms of equilibrium binding constants, but also are not kinetically labile either from the surface or from each other (depending on the immobilisation architecture), because otherwise they may still leach into solution and be lost. Therefore, the results of **Paper III**'s binding model do not at all necessarily rule out the importance or benefits of well-designed anchoring groups for constructing photoelectrodes, nor for photocatalytic systems when there is not a natural affinity between QD and catalyst.

In addition, the observation of effective natural QD-catalyst association, very fast ET processes and largely catalyst concentration-independent H<sub>2</sub> production implies that, for this system, the limiting factors are not the efficiency of electron transfer or the availability of catalyst. The high concentration of the sacrificial electron donor and the high mobility of protons in acidic water would also imply that these factors cannot be limiting, so the absorption of photons and competing recombination processes after photoexcitation of the QDs would be expected to be the major limits. In this context, which may be shared for many PC systems, it does not make sense to further optimise the QD and catalyst interactions to speed up ET or to choose a catalyst with an extremely high intrinsic activity (i.e. TOF<sub>0</sub> value<sup>103</sup>). Rather, the priority would be to make sure that all components resist both recombination and decomposition for the entire timescale of the catalytic cycle.<sup>153–155</sup> Decomposition may occur due to instability from the stepwise transfer of charge carriers; i.e., as discussed in the **Section 1.2**, improving the robustness of the molecular catalyst perhaps should be the primary focus. This point of view may explain why CAT1 performs well in PC systems compared to other related catalysts (which may be more intrinsically active and efficient, but less stable) under photocatalytic conditions, given CAT1's relative stability with a variety of reducing agents.<sup>79</sup>

Appendix: Extracted  $\lambda$  and [QD] values

**Table 5.1:** Estimated concentrations of CIS QDs from extracted  $\lambda$  values from PL quenching plots and fits.

Abs. at 405nm (rel. [QD])	Catalyst	$\lambda / 10^3$	R <sup>2</sup>	[QD] ( $\mu\text{M}$ )	Avg. [QD] ( $\mu\text{M}$ )
0.07	CAT1	690	0.991	1.4	1.7
0.07	CAT1-CO <sub>2</sub> H	496	0.938	2.0	
0.1	CAT1	539	0.994	1.9	2.5
0.1	CAT1-CO <sub>2</sub> H	325	0.935	3.1	
0.36	CAT1	76	0.998	13.1	12.2
0.36	CAT1-CO <sub>2</sub> H	88	0.995	11.4	
1.08	CAT1	35	0.994	28.7	34.9
1.08	CAT1-CO <sub>2</sub> H	24	0.995	41.1	
0.07	CAT1 (0.1 M Asc)	928	0.988	1.1	1.1
0.07	CAT1-CO <sub>2</sub> H (0.1 M Asc)	898	0.976	1.1	
0.36	CAT1 (0.5 M Asc)	295	0.988	3.4	5.5
0.36	CAT1-CO <sub>2</sub> H (0.5 M Asc)	132	0.976	7.6	

## 6 Summary and Outlook

Within the context of the global social and economic transition towards green, renewable energy sources, the drive to develop new materials and strategies for producing solar fuels through artificial photosynthesis will continue. In particular, across all the strategies and device architectures, the major challenge for economic viability and societal relevance is finding mutually compatible materials that meet all three requirements of *efficiency*, *robustness* and *scalability*.

Alongside light-harvesting materials, catalysts for each desired reaction are typically employed to speed up reaction rates and improve efficiencies and selectivity. For the production of hydrogen by light-driven water-splitting, current commercial technologies are generally considered inadequately scalable for meet all potential demand for hydrogen as a fuel and feedstock. In state-of-the-art proton exchange membrane (PEM) electrolysis technology, this is in part due to reliance on rare platinum group metal-based catalysts.

To provide alternative catalytic materials, based on more abundant elements, molecular catalysts show a lot of promise in terms of their versatility, selectivity and modifiability to optimise the catalytic properties of more common metals. Their specific, well-defined active sites in particular allow for deeper mechanistic understandings that can rationally guide optimisation through molecular engineering. Currently, however, their key weakness for practical applications is generally insufficient robustness, which is a critical issue to be addressed in applied molecular catalyst research. An additional issue for most water-splitting strategies is the need to immobilise the molecular catalysts to integrate them into device components without deactivating them.

**CAT1** (a.k.a.  $[\text{Co}^{\text{III}}(\text{N}_4\text{H})\text{Cl}_2]^+$ ) is a cobalt tetraazamacrocyclic complex which acts as an effective molecular catalyst for the hydrogen-evolution reaction (HER), and, interestingly, also the carbon dioxide reduction reaction ( $\text{CO}_2\text{RR}$ ). This catalyst is most noted for its relatively high robustness under a range of electrocatalytic and photocatalytic conditions for the HER when compared with related catalytically active complexes.

In **Paper I**, the performance of CAT1 under homogeneous organic electrocatalytic conditions was benchmarked against other catalysts and it was found that CAT1 has intrinsic activity for the HER (in terms of  $\text{TOF}_{\text{max}}$ ) comparable to the DuBois catalyst and cobaloximes. Furthermore, mechanistic studies on CAT1 under the conditions investigated in this paper revealed an ECEC mechanism with rate-determining second protonation step and detailed the protonation of the macrocycle amine group, implicating this group as a possible proton relay. If indeed so, this may play a role in explaining the efficacy of the catalyst, but also implies that chemical modifications at the amine position may result in significant changes to catalytic mechanism and/or performance: this may be informative for applying rational design principles to modifications.

In **Paper II**, a new synthetic pathway to *para*-pyridine position functionalised derivatives of CAT1 is presented; this is hoped to facilitate future preparation of new derivatives. A pyrene-functionalised derivative prepared by this route and an analogous derivative functionalised at the amine position were shown to anchor onto multi-walled carbon nanotubes (MWCNTs). The electrocatalytic activity of both derivatives for the HER was confirmed in both neutral (pH 7) and acidic (pH 2) aqueous conditions at 480 mV applied overpotential. Remarkably, faradaic efficiencies of approximately 100% were obtained in neutral conditions for both derivatives. However, the overall current density and its stability were notably higher for the derivative modified at the *para*-pyridine position, implying that this derivative was more stable under turnover conditions. The MWCNTs modified with anchored catalyst can be added to the cathode of a PEM electrolyser cell to test their performance at the level of a device; this is the next step.

Additionally, the electrochemical responses of the immobilised catalysts in cyclic voltammetry showed some familiar similarities in redox behaviour to CAT1 dissolved in solution, but there were also some noted differences and changes that occurred over time. Further studies would be required to understand all the effects at play, but it may be assumed that the length, nature and rigidity of the linker can play a role (possibly affecting the nature of electron transfer from the electrode to the catalyst), as can the position on the catalyst to which the linker is attached. This highlights the importance of mechanistic insight for rational design principles when modifying molecular catalysts.

In **Paper III**, the photocatalytic activity of CAT1 with copper indium sulfide quantum dots (CIS QDs) as the photosensitiser for the HER was re-investigated, on the basis of previous positive reports for similar systems.<sup>86,87</sup> A different type of *hybrid-passivated* CIS QDs without a ZnS shell were used. This type of CIS QDs was designed to be compatible with NiO films for constructing photocathodes, so that the system could be adapted in the future for photoelectrocatalysis. A derivative of CAT1 with a carboxylic acid anchoring group (CAT1-CO<sub>2</sub>H) was also used to compare with CAT1.

From photocatalytic hydrogen measurements in water with ascorbate as sacrificial electron donor, it was noted that H<sub>2</sub> production was almost independent of catalyst concentration for the conditions tested. Photoluminescence quenching experiments indicated remarkably effective quenching by even low concentrations of either catalyst, the presence of the anchoring group making no significant difference. Furthermore, TCSPC and fs-TAS experiments confirmed that the mechanism of quenching was static, with ultrafast QD-to-catalyst electron transfer processes. Deducing that the affinity of either catalyst to the QDs was very high and that the donation of electrons from photoexcited QDs to any catalyst molecules adsorbed at their surface was efficient, the effectiveness of the quenching against concentration of catalyst could be satisfactorily modelled with a Poissonian (random) distribution of bound quenchers over QDs, accounting for the exponential trend in the datasets of photoluminescence intensity ratio versus concentration of catalyst.

Therefore, it was concluded that the molecular catalyst tightly adsorbs to the CIS QDs, even without the intended anchoring group. This behaviour can partly explain the particular effectiveness of QDs as photosensitisers for molecular catalysts, and may be true for many studied QD-molecular catalyst combinations. Moreover, the limiting factors in the system are most likely the absorption of light and the recombination processes, rather than the electron transfer from excited QDs to catalyst or the catalyst's intrinsic turnover frequencies. In such cases, modifying the catalyst to bind more effectively to the QDs or to have a higher intrinsic activity would not lead to significant improvements in system performance. Instead it would make more sense to expend effort into improving the robustness of the catalyst and reducing recombination processes. This may also explain why the combination of CIS and CAT1 is particularly effective: even if CAT1 turns over more slowly, its superior stability leads to an overall improvement in the photocatalysis.

To conclude, it is hoped that the improved understanding of CAT1's catalytic properties and mechanism for the HER, along with the development of new synthetic pathways towards new derivatives, will facilitate the future development and application of this family of catalysts in solar fuels research and test devices.

### Keypoints:

- The importance of mechanistic insights for rational design principles regarding chemical modification of molecular catalysts.
- The importance of the careful design of anchoring groups and linkers with consideration of surface environments, catalytic conditions and electron transfer processes.
- The importance of focusing on improving the robustness of molecular catalysts over improving their intrinsic activities, if they are not a limiting factor.

## 7 Brief Synopsis of Other Projects

### 7.1 MWCNT-Based Inks

For screen-printing electrodes, the most common inks are commercial graphite-based carbon pastes.<sup>126</sup> However, in general, graphite has a relatively amorphous and poorly characterised surface. As discussed in **Paper II**, MWCNTs provide an excellent support material for anchoring molecular catalysts onto, due to their large surface areas with well-defined surfaces and high intrinsic conductivities. Furthermore, it has been reported that the local environment at the surface of carbon nanotubes can modulate the selectivity of molecular catalysts, depending on the number of nanotube layers and their curvature.<sup>156</sup> For catalysing the CO<sub>2</sub>RR in particular, this may be advantageous. Therefore, producing printable inks that also used MWCNTs as the primary conductive ‘active’ component was an interesting topic to investigate, in case this could confer advantages over e.g. carbon-paste printed electrodes with MWCNT layers dropcast on top.<sup>126</sup>

There are examples in the literature of carbon nanotube-based inks for printable electronics for use on fabrics, paper or other substrates.<sup>157–161</sup> However, for printing electrodes for electrocatalytic devices, it would be interesting to minimise any additives in the ink (such as surfactants), and include only the conductive active component, the binder and the solvent. This would minimise the amount of non-conductive material remaining once the ink dries, and also minimise the number of components that could interact non-desirably with any immobilised catalysts or affect the EDL at the electrodes.

As the concentration of MWCNTs in the ink increases, so does its viscosity and conductivity. The main challenge is to maximise the concentration of MWCNTs to maximise conductivity, while keeping the viscosity low enough for screen-printing (aiming for a viscosity below 100 Pa·s for shear rates around 1 s<sup>-1</sup>, measured by rheometry). Often, these carbon-based inks designed for screen-printing are rheologically non-Newtonian fluids, displaying shear-thinning (pseudoplastic) and mildly thixotropic behaviour.

A series of ink compositions were prepared similarly to graphite inks previously utilised within the eSCALED project.<sup>126</sup> A commercial triblock copolymer poly(methyl methacrylate)-*b*-poly(*n*-butyl acrylate)-*b*-poly(methyl methacrylate) (MBM, LA series, Kuraray) was used as the matrix to bind either a graphite powder or the MWCNTs with *p*-xylene as solvent, and no other additives. Single-layer squares were screen-printed with the inks on a PVC substrate to measure the conductivities (**Figure 7.1**). It was noted that annealing improved the conductivity for the graphite ink, but had little noticeable effect on the MWCNT inks.

Although it was possible to reach a conductivity of almost 0.6 S cm<sup>-1</sup> for an ink with only a 23% weight-for-weight dry concentration of MWCNTs (about one fifth of that for the analogous 70% w/w graphite-based ink), increasing the concentration of MWCNTs further while maintaining a printable ink is complicated because the concentration of binder must be reduced, but sufficient binder is required to disperse the MWCNTs in the ink and stabilise them in the print, while ensuring they spread out evenly enough to maintain bulk conductivity. An insufficient binder concentration may lead to inhomogeneity in prints, due to the nanotubes preferring to aggregate if inadequately dispersed in the ink, which would harm bulk conductivity and the electrochemically active surface area of the printed electrodes (**Figure 7.2**).

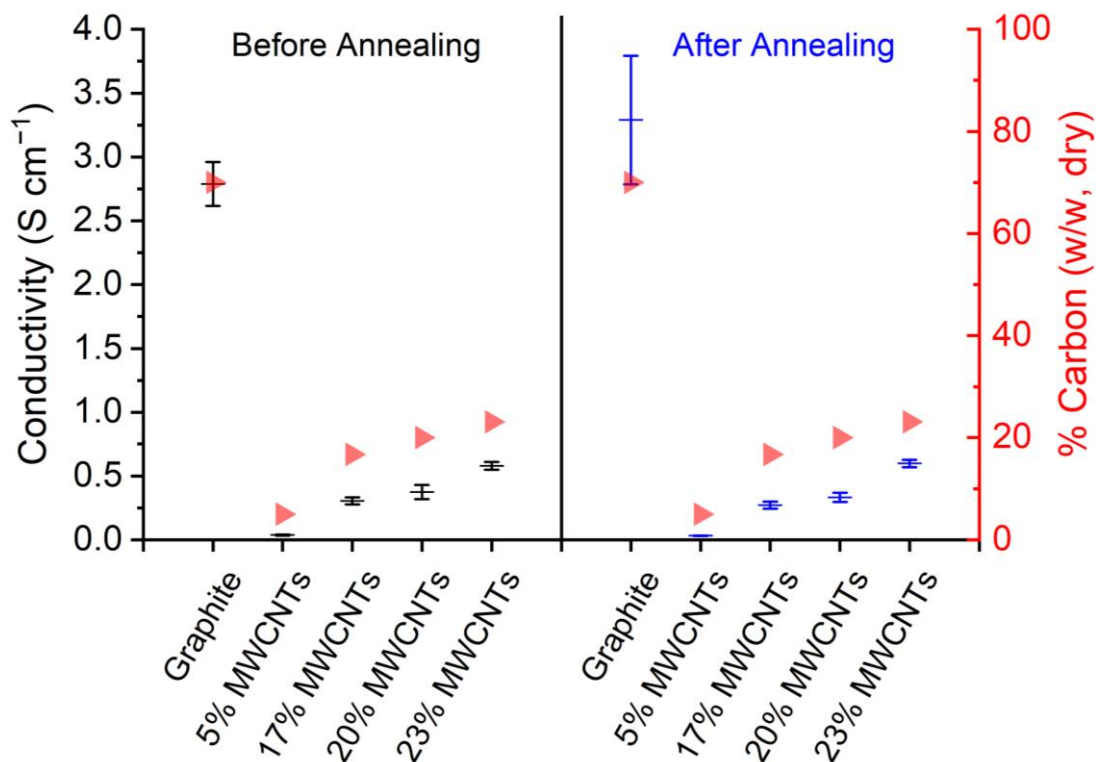


**Figure 7.1:** Plot of measured conductivities (black or blue, standard deviation represented by error bars) versus active carbon component content (red, % w/w upon drying) for prints of the series of MWCNT-based inks and a graphite ink control (70% w/w graphite). Binder: Commercial MBM triblock copolymer; Solvent: *p*-xylene. **Left:** Before annealing. **Right:** After annealing at 85 °C for 30 minutes.

Since the bulk conductivity of printed electrodes is a major issue in their application for electrolysis,<sup>126</sup> this would be an important issue to overcome for a useful application of MWCNT-based inks. Possible steps forward may be the use of inert surfactants to improve maximum ink concentration of MWCNTs,<sup>158</sup> investigating alternative solvents, and blending a mixture of MWCNTs and other carbon materials (graphite, carbon black, etc.) to investigate possible synergistic effects on conductivity (if it is acceptable to have other forms of carbon present).<sup>162</sup> Further studies are required to determine the viability of these kinds of inks for electrocatalytic water-splitting purposes.

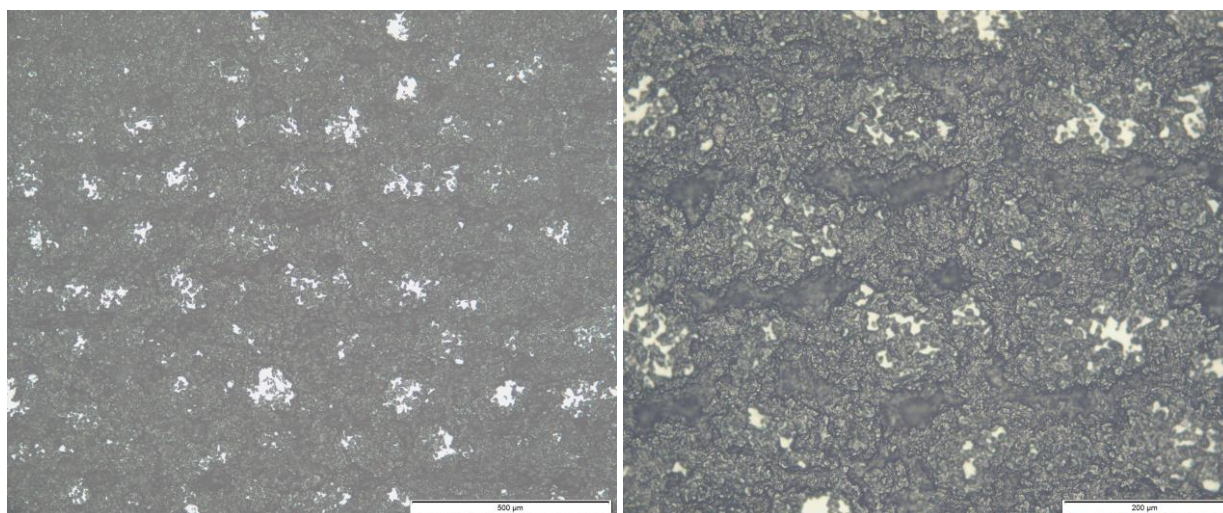


**Figure 7.2:** Optical microscopy images of screen-printed squares made from 23% w/w MWCNT ink. Some inhomogeneity and unconducting ‘gaps’ without MWCNTs are apparent (lighter regions).



## 7.2 Polymer End-Functionalised with Catalyst

From collaboration with coworkers at UPPA, a poly(3-hexylthiophene) polymer (P3HT) was prepared and end-functionalised with a cobalt diimine-dioxime HER catalyst via a metal-free Huisgen cycloaddition ‘click’ reaction (**Figure 7.3**). As a well-studied conjugated semiconducting polymer, P3HT may make an interesting model scaffold for molecular catalysts.

This polymer was dissolved in THF and dropcast onto a glassy carbon electrode for electrochemical analysis in MeCN (0.1 M TBABF<sub>4</sub>). However, apart from characteristic P3HT oxidation and reduction responses at more positive/negative potentials, only a very weak current (sub- $\mu$ A) was seen in the expected region for the cobalt catalyst. It was concluded that the limited conductivity of undoped P3HT meant that the electrode surface was effectively insulated. To try to enhance the current signals to combat this, the *p*-type dopant, F4TCNQ (2,3,5,6-tetrafluoro-7,7,8,8-tetracyanoquinodimethane) was mixed with the polymer in a 17% molar ratio of dopant molecule to monomer, as had previously been found in literature to maximise conductivity,<sup>163</sup> and the mixture was dropcast onto a layer of MWCNTs on a glassy carbon electrode.

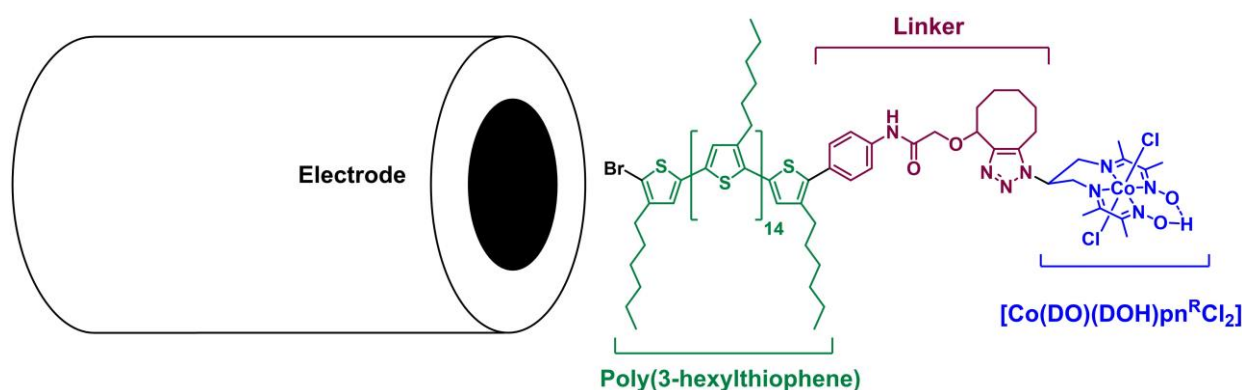


**Figure 7.3:** Illustration of the P3HT polymer end-functionalised with a cobalt diimine-dioxime catalyst. The dropcast polymer film sticks on the electrode surface: it is surmised that P3HT anchors itself onto  $sp^2$  carbon surfaces, such as glassy carbon or MWCNTs, via  $\pi$ - $\pi$  interactions.

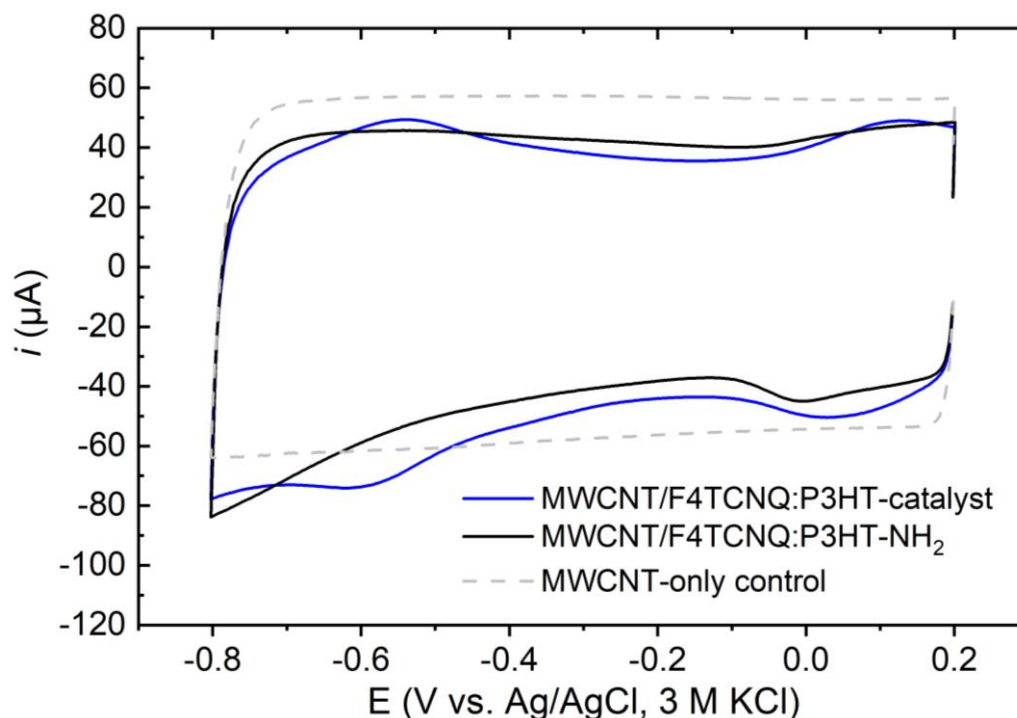


**Figure 7.4:** Cyclic voltammograms of doped P3HT end-functionalised with catalyst (blue) and without (amine end group, black), dropcast onto MWCNTs on a glassy carbon electrode (first cycles). Dashed grey: MWCNTs-only blank. Solution: MeCN (0.1 M TBABF<sub>4</sub>). Scan rate:  $\nu = 100 \text{ mV s}^{-1}$ .

In **Figure 7.4**, for the doped P3HT-catalyst layer on MWCNTs, a few redox features were found that were not seen in the control containing only the polymer without end-functionalised with the catalyst (end group: -NH<sub>2</sub>). Two redox couples appear to be observable at  $E_{1/2} = 0.06$  V and  $-0.57$  V vs. Ag/AgCl (KCl, 3 M), which may be attributed to Co(III/II) and Co(II/I), respectively. This appears to show some resemblance to cobalt diimine-dioxime anchored directly onto MWCNTs, reported in the literature as having those redox couples at  $E_{1/2} = -0.11$  and  $-0.67$  V vs. Ag/AgCl (KCl, 3 M), respectively,<sup>62,71,114</sup> which would mean positive shifts of 150 mV and 100 mV for the P3HT-based system. However, on the basis of the “Co(III/II)” peak integrals, the apparent loading of electronically connected, active catalyst centres attached to P3HT is approximately  $0.3 \text{ nmol cm}^{-2}$ , two orders of magnitude lower than for the MWCNT-anchored systems.<sup>114</sup> It is noted that the background currents with the polymer layers are still lower than from the MWCNT-only blank, implying that conductivity is still hindered. Therefore, further studies are required to ascertain whether these truly are the cobalt redox couples and whether the system is catalytically active for the HER, as well as to improve the conductivity of electrons to the active site through the polymer film.

For more advanced polymer-supported molecular catalyst systems in the future, other strategies may yield improved results: Binding catalysts to the sides of polymers to have a greater number of active sites for a greater total mass density of catalyst may greatly improve electrocatalytic response.<sup>164</sup> Additionally, the development and use of more conductive polymers may improve performance for electrocatalytic water-splitting, while the use of ever more sophisticated light-harvesting donor-acceptor polymers can be applied for photoelectrocatalytic or photocatalytic water splitting with molecular catalysts.

## 8 Résumé en Français

La thèse s'est concentrée sur l'application d'un complexe tétraazamacrocyclique de cobalt, nommé  $[\text{Co}(\text{CR})\text{Cl}_2]^+$  dans la littérature, comme catalyseur moléculaire pour la production d'hydrogène. Cette étude s'inscrit dans le cadre du projet EU MSCA H2020 ITN eSCALED, avec comme principal objectif la création d'une feuille artificielle pour stocker l'énergie solaire dans des combustibles chimiques. Les recherches entreprises visaient à développer de nouveaux matériaux bio-inspirés, adaptables et utilisables comme composant dans des électrolyseurs à membrane électrolytique polymère (PEM) : recherche de catalyseurs moléculaires basés sur des métaux de transition de la première série et abondants sur terre afin de remplacer les métaux rares et nobles actuellement utilisés dans ces technologies.

Dans le contexte de la transition sociale et économique mondiale vers des sources d'énergie vertes et renouvelables, la volonté de développer de nouveaux matériaux et des stratégies de production de carburants solaires par photosynthèse artificielle se poursuit. En particulier, dans toutes les stratégies et architectures de dispositifs, le défi majeur pour la viabilité économique et la pertinence sociétale est de trouver des matériaux mutuellement compatibles qui répondent aux trois exigences efficacité, robustesse et évolutivité.

Parallèlement aux matériaux collectant la lumière, des catalyseurs pour chaque réaction souhaitée sont généralement utilisés pour accélérer les vitesses de réaction et améliorer les efficacités et la sélectivité. Pour la production d'hydrogène par fractionnement de l'eau par la lumière, les technologies commerciales actuelles sont généralement considérées comme insuffisamment évolutives pour répondre à toute la demande potentielle d'hydrogène en tant que carburant et matière première. Dans la technologie d'électrolyse à membrane échangeuse de protons (PEM) de pointe, cela est en partie dû à la dépendance à l'égard de rares catalyseurs à base de métaux du groupe du platine.

Pour fournir des matériaux catalytiques alternatifs, basés sur des éléments plus abondants, les catalyseurs moléculaires sont très prometteurs en termes de polyvalence, de sélectivité et de possibilité de modification pour optimiser les propriétés catalytiques de métaux plus courants. Leurs sites actifs spécifiques et bien définis permettent en particulier une compréhension mécanistique plus approfondie qui peut guider à l'optimisation rationnelle par l'ingénierie moléculaire. Actuellement, cependant, leur principale faiblesse pour des applications pratiques est généralement leur robustesse insuffisante, qui est un problème critique à résoudre dans la recherche appliquée sur les catalyseurs moléculaires. De plus, la plupart des stratégies de fractionnement de l'eau nécessitent de modifier les catalyseurs moléculaires pour les intégrer dans les composants du dispositif sans les désactiver, ce qui représente un autre problème.

CAT1 (alias  $[\text{Co}^{\text{III}}(\text{N}_4\text{H})\text{Cl}_2]^+$  ou  $[\text{Co}(\text{CR})\text{Cl}_2]^+$ ) est un complexe tétraazamacrocyclique de cobalt qui agit comme un catalyseur moléculaire efficace pour la réaction de dégagement d'hydrogène (HER) et, fait intéressant, également pour la réaction de réduction du dioxyde de carbone ( $\text{CO}_2\text{RR}$ ). Ce catalyseur est surtout connu pour sa robustesse relativement élevée dans une gamme de conditions électrocatalytiques et photocatalytiques pour le HER par rapport aux complexes catalytiquement actifs apparentés.

Dans l'article I, les performances de CAT1 dans des conditions électrocatalytiques organiques homogènes ont été comparées à d'autres catalyseurs et il a été constaté que CAT1 a une activité intrinsèque pour le HER (en termes de  $\text{TOF}_{\text{max}}$ ) comparable au catalyseur DuBois et aux cobaloximes. De plus, des études mécanistiques sur CAT1 dans les conditions étudiées de cet article ont révélé un mécanisme ECEC avec une deuxième étape de protonation déterminant la vitesse. Les travaux ont également montré la protonation du groupe amine macrocycle, qui implique donc que ce groupe fonctionne comme un possible relais de protons. Si tel est le cas, cela peut jouer un rôle dans l'explication de l'efficacité du catalyseur, mais implique également que des modifications chimiques en position amine peuvent entraîner des changements

significatifs du mécanisme catalytique et / ou des performances: cela peut être instructif pour appliquer des principes de conception rationnelle lors de modifications.

Dans l'article II, une nouvelle voie de synthèse des dérivés fonctionnalisés en position *para*-pyridine de CAT1 est présentée ; Nous espérons que cela facilitera la préparation future de nouveaux dérivés. Un dérivé fonctionnalisé pyrène préparé par cette voie et un dérivé analogue fonctionnalisé en position amine se sont avérés capable de s'ancrer sur des nanotubes de carbone à parois multiples (MWCNT). L'activité électrocatalytique des deux dérivés pour le HER a été confirmée dans des conditions aqueuses neutres (pH 7) et acides (pH 2) pour une surtension appliquée de 480 mV. Remarquablement, des efficacités faradiques d'environ 100% ont été obtenues dans des conditions neutres pour les deux dérivés. Cependant, la densité de courant globale et sa stabilité étaient nettement plus élevées pour le dérivé modifié en position *para*-pyridine, ce qui implique que ce dérivé était plus stable dans des conditions de renouvellement. Les MWCNT modifiés avec catalyseur ancré peuvent être ajoutés à la cathode d'une cellule d'électrolyseur PEM pour tester leurs performances au niveau d'un dispositif ; c'est la prochaine étape.

De plus, les réponses électrochimiques des catalyseurs immobilisés en voltampérométrie cyclique ont montré certaines similitudes familières dans le comportement redox avec CAT1 dissous en solution, mais des différences et des changements notables se sont également produits au fil du temps. D'autres études seraient nécessaires pour comprendre tous les effets en jeu, mais nous pouvons supposer que la longueur, la nature et la rigidité du ligand peuvent jouer un rôle (affectant éventuellement la nature du transfert d'électrons de l'électrode au catalyseur), tout comme la position sur le catalyseur à laquelle le ligand est attaché. Cela met en évidence l'importance de la compréhension mécanistique pour les principes de conception rationnelle lors de la modification des catalyseurs moléculaires.

Dans l'article III, l'activité photocatalytique de CAT1 avec des points quantiques de sulfure de cuivre-indium (CIS QD) comme photosensibilisateur pour le HER a été réexaminée, sur la base de rapports positifs antérieurs pour des systèmes similaires.<sup>86,87</sup> Un type différent des QD CIS « hybride-passivés » sans coque ZnS a été utilisé. Ce type de QD CIS a été conçu pour être compatible avec les films NiO pour la construction de photocathodes, afin que le système puisse être adapté à l'avenir pour la photoélectrocatalyse. Un dérivé de CAT1 avec un groupe d'ancrage acide carboxylique (CAT1-CO<sub>2</sub>H) a également été utilisé pour comparer avec CAT1.

À partir de mesures d'hydrogène photocatalytique dans l'eau avec de l'ascorbate comme donneur d'électrons sacrificiel, il a été noté que la production de H<sub>2</sub> était presque indépendante de la concentration du catalyseur pour les conditions testées. Des expériences d'extinction de photoluminescence ont indiqué une extinction remarquablement efficace même à de faibles concentrations de l'un ou l'autre des catalyseurs, la présence du groupe d'ancrage ne faisant aucune différence significative. De plus, les expériences TCSPC et fs-TAS ont confirmé que le mécanisme d'extinction était statique, avec des processus de transfert d'électrons QD-catalyseur ultra-rapides. En déduisant que l'affinité de l'un ou l'autre des catalyseurs pour les QD était très élevée et que le don d'électrons des QD photoexcités à toute molécule de catalyseur adsorbée à leur surface était efficace, l'efficacité de la trempage par rapport à la concentration de catalyseur pourrait être modélisée de manière satisfaisante avec une distribution (aléatoire) de Poisson des extincteurs liés sur les QD, ce qui explique la tendance exponentielle dans les ensembles de données du rapport d'intensité de photoluminescence par rapport à la concentration de catalyseur.

Par conséquent, il a été conclu que le catalyseur moléculaire s'adsorbe étroitement aux QD CIS, même sans le groupe d'ancrage prévu. Ce comportement peut expliquer en partie l'efficacité particulière des QD en tant que photosensibilisateurs pour les catalyseurs moléculaires, et peut être vrai pour de nombreuses combinaisons de catalyseurs moléculaires-QD étudiées. De plus, les facteurs limitants du système sont très probablement l'absorption de la lumière et les processus de recombinaison, plutôt que le transfert d'électrons des QD excités vers le catalyseur ou les fréquences de renouvellement intrinsèques du catalyseur. Dans de tels cas, la modification du catalyseur pour se lier plus efficacement aux QD ou pour avoir une activité intrinsèque plus élevée ne conduirait pas à des améliorations significatives des performances du système. Au lieu de cela, il serait plus logique de déployer des efforts pour améliorer la robustesse du catalyseur et réduire les processus de recombinaison. Cela peut aussi expliquer pourquoi la combinaison de CIS et de

CAT1 est particulièrement efficace : même si CAT1 se retourne plus lentement, sa stabilité supérieure conduit à une amélioration globale de la photocatalyse.

Pour conclure, nous espérons que l'amélioration de la compréhension des propriétés catalytiques et du mécanisme de CAT1 pour le HER, ainsi que le développement de nouvelles voies de synthèse vers de nouveaux dérivés faciliteront le développement et l'application futurs de cette famille de catalyseurs dans la recherche et les tests sur les carburants solaires.

**Points clés :**

- L'importance des connaissances mécanistes pour les principes de conception rationnelle concernant la modification chimique des catalyseurs moléculaires.
- L'importance d'une conception soignée des groupes d'ancrage et des lieux en tenant compte des environnements de surface, des conditions catalytiques et des processus de transfert d'électrons.
- L'importance de privilégier l'amélioration de la robustesse des catalyseurs moléculaires à l'amélioration de leurs activités intrinsèques, si elles ne sont pas un facteur limitant.

## 9 Popular Scientific Summary

As of 2022, climate change is widely regarded as a major threat to the global ecosystem and human society. Anthropogenic (man-made) emissions of greenhouse gases have been identified as a key factor behind climate change. These gases trap heat that arrives at the Earth from the Sun by reducing the amount that escapes back into space, causing the planet to warm up.

One of the most important greenhouse gases in this context is carbon dioxide ( $\text{CO}_2$ ), which is widely emitted by human society from the burning of fossil fuels in transportation, electricity generation and industrial processes such as the production of concrete and steel. Although  $\text{CO}_2$  exists naturally and is constantly being cycled by living organisms, human activity breaks the natural balance in the carbon cycle, resulting in an increasing concentration of  $\text{CO}_2$  in the atmosphere.

In order to stop anthropogenic emissions of  $\text{CO}_2$ , it is necessary to decouple society and the economy from fossil fuels. To do this, an alternative source of energy must be found. Sunlight represents an abundant source of energy: the amount of solar energy that arrives at the Earth over one hour is estimated to be close to the consumption of society over one year. However, capturing this energy is complicated. In nature, photosynthesis is the process widely carried out by plants and many microorganisms to store energy from sunlight in chemical bonds, primarily by converting  $\text{CO}_2$  and water into sugars. Although nature has optimised many parts of this process, this is not directly scalable to meet all of society's needs: plants require a lot of land, fertile soil and the correct climate to thrive, and did not evolve to directly produce useful fuels efficiently.

Photovoltaics in solar panels work well to convert solar energy into electricity, but not everything can be connected to the grid, and there is the problem of intermittency – this means enough sunlight is not reliably always available when energy is needed, for example, at night or when it is cloudy. Therefore, as part of the eSCALED project, we are trying to develop strategies for artificial photosynthesis – inspired by natural organisms but overcoming their limitations – in order to directly convert sunlight into useful fuels. One strategy is to connect photovoltaics to electrolyzers which split water ( $\text{H}_2\text{O}$ ) into hydrogen and oxygen by applying a voltage across two electrodes.

Hydrogen is a promising fuel due to its high energy per mass density and clean and efficient release of energy when converted back into water in fuel cells, but, perhaps more importantly, it is also a critical chemical feedstock, notably in the production of fertilisers. Most hydrogen is currently produced from fossil fuel sources. Although commercial technologies exist to produce hydrogen efficiently and greenly through water-splitting without fossil fuels, for now they generally either rely on rare (and non-scalable) noble metals or strong alkaline conditions which degrade the components. Thus, developing novel materials based on more abundant materials for the electrodes which catalyse the two half-reactions behind water-splitting is anticipated to be necessary for scaling green water-splitting processes up.

This thesis focuses on the use of noble metal-free molecular catalysts, in particular a cobalt coordination complex, to facilitate – speed up and reduce the energy barrier for – the production of hydrogen from protons (one of the half-reactions), by binding the protons and transferring electrons to them at the right time. The chemical environment of the coordination complex serves to optimise the chemistry of the cobalt metal centre for the reaction and hold the cobalt tightly so that the system can last a long time. How the complex does this (the catalytic mechanism), how the complex can be incorporated into devices by chemical modification, and how the complex can produce hydrogen directly when mixed with light-absorbing quantum dots were the key projects of this work.

## 10 Populärvetenskaplig Sammanfattning

Från och med 2022 anses klimatförändringar allmänt vara ett stort hot mot det globala ekosystemet och det mänskliga samhället. Antropogena (orsakade av människan) utsläpp av växthusgaser har identifierats som en nyckelfaktor bakom klimatförändringarna. Dessa gaser fångar upp värme som kommer till jorden från solen genom att minska mängden som förs tillbaka ut i rymden, vilket får planeten att värmas upp.

En av de viktigaste växthusgaserna i detta sammanhang är koldioxid ( $\text{CO}_2$ ), som släpps ut i stor utsträckning av det mänskliga samhället från förbränning av fossila bränslen i transporter, elproduktion, samt i industriella processer, till exempel produktion av betong och stål. Även om  $\text{CO}_2$  finns naturligt och ständigt cirkuleras av levande organismer, bryter mänsklig aktivitet den naturliga balansen i kolcykeln, vilket resulterar i en ökande koncentration av  $\text{CO}_2$  i atmosfären.

För att stoppa antropogena utsläpp av  $\text{CO}_2$  är det nödvändigt att frikoppla samhället och ekonomin från fossila bränslen. För att göra detta måste en alternativ energikälla hittas. Solljus representerar en riklig energikälla: mängden solenergi som anländer till jorden under en timme uppskattas vara nära samhällets konsumtion under ett år. Men att fånga denna energi är komplicerat. I naturen är fotosyntes den process som i stor utsträckning utförs av växter och många mikroorganismer för att lagra energi från solljus i kemiska bindningar, främst genom att omvandla  $\text{CO}_2$  och vatten till sockerarter. Även om naturen har optimerat många delar av denna process, är denna inte direkt skalbar för att möta alla samhällets behov: växter kräver mycket mark, bördig jord och rätt klimat för att trivas, och har inte utvecklats för att direkt producera användbara bränslen effektivt.

Solceller i solpaneler fungerar bra för att omvandla solenergi till elektricitet, men allt kan inte anslutas till nätet, och det finns ett problem med intermittens – det betyder att tillräckligt med solljus inte alltid är tillgängligt när energi behövs, till exempel på natten eller när det är molnigt. Därför, som en del av eSCALED-projektet, försöker vi utveckla strategier för artificiell fotosyntes – inspirerad av naturliga organismer men med målet att övervinna deras begränsningar – för att direkt omvandla solljus till användbara bränslen. En strategi är att koppla solceller till elektrolysörer som delar vatten ( $\text{H}_2\text{O}$ ) till vätgas och syrgas genom att applicera en spänning över två elektroder.

Vätgas är ett lovande bränsle på grund av sin höga energi per kilogram och sitt rena och effektiva frigörande av energi när det omvandlas tillbaka till vatten i bränsleceller. Kanske ännu viktigare är att vätgas också är ett kritiskt kemiskt råmaterial, särskilt vid produktion av gödningsmedel. Det mesta av väte produceras för närvarande från fossila bränslen. Även om kommersiell teknik finns för att producera vätgas effektivt och grönt genom vattenuppsplidning utan fossila bränslen, förlitar den sig för närvarande i allmänhet antingen på sällsynta (och icke-skalbara) ädelmetaller eller starka alkaliska förhållanden som bryter ned komponenterna. Utveckling av nya material baserade på mer vanligt förekommande grundämnen för elektroderna som katalyserar de två halvreaktionerna bakom vattenuppsplidning förväntas således vara nödvändigt för att skala upp gröna vattenuppsplidningsprocesser.

Denna avhandling fokuserar på användningen av ädelmetallfria molekylära katalysatorer, särskilt ett koordinationskomplex av metallen kobolt, för att underlätta – påskynda och minska energibarriären för – produktionen av väte från protoner (en av halvreaktionerna), genom att binda protonerna och överföra elektroner till dem vid rätt tidpunkt. Den kemiska miljön i koordinationskomplexet tjänar till att optimera kemin i koboltmetallcentret för reaktionen och hålla kobolten tätt så att systemet kan hålla länge. Hur komplexet gör detta (den katalytiska mekanismen), hur komplexet kan inkorporeras i enheter genom kemisk modifiering och hur komplexet kan producera vätgas direkt när det blandas med ljusabsorberande kvantprickar var nyckelprojekten i detta arbete.

# 11 Acknowledgements

I would like to thank everyone I met, all the friends I made, and especially everyone who supported me along the way and helped me write this (especially **Edgar**, **Louis** and **Leif** for checking the translations).

To my family and friends back home, thanks for putting up with me being abroad for another four years.

To **Fabio**, thank you so much for recommending me this project and for always being happy to catch up and discuss.

To all the other students in the eSCALED project, **Ludo**, **Dome**, **Silvia**, **Diogo**, **Saeed**, **Karell**, (the other) **Andy**, **Robin**, **Van**, **Olivera**, **Bruno** and **Ignasi**. I wish you all the best for the future, I will miss you guys. Especially thanks to everyone who was in Pau, without you (and Jurançon) the pandemic would have been a lot grimmer, and to **Dome** for being an amazing lead author. And especially, especially thanks to my eSCALED twin **Afridi**, I would write something in Bangla, but then they wouldn't let me print this thesis.

Gràcies **Laia** per tot, sense tu, no hi ha eSCALED. Gràcies a tu i a la teva família, Nicolas, Mateu, Leanne i Baldufa, sense vosaltres, la pandèmia hauria estat molt més dura.

From CEA, thank you **Nathan** for your genius and crazy humour, **Tim** for your fan (saved us during the heatwaves), **Nick** for all your absolutely solid advice, **Cristina** for all your help (I wish your family and Django all the best), **Adina** for writing the most useful electrochemistry guide ever, **Jennifer** for holding the lab together, **Tanya** for your brilliant skills in synthesis. Thank you, **Umberto**, **Seb** and **Manos** for always being super helpful and super cool to hang out with, I miss you guys. Special thanks to the elusive 'TTeam', **Kun**, **Duc** "Pro", **Ghislain** "Big G", **Louis** "Lou-tea" and **Afridi** (again), you guys are awesome and probably the most formidable amateur photography squad Grenoble has ever seen. To **Mariam**, **Antonin**, and **Angelica**, I'm sorry we only met a few times, but I hope to see you round and I wish you all the best.

To **Matthieu H.** and **Bertrand**, thank you so much for your work on **Paper II**, and also for being awesome, without you this wouldn't have come together. Thank you, **Murielle**, for your giant role in my PhD and always being supportive, and helping me not get deported. And a million times thank you to my (even better-than-Best-Office) officemate, Monsieur **Matthieu K.**, you are one of the most amazing scientists/gardeners/wine connoisseurs I know and an absolute legend in every regard. Also, thank you to the amazing **Rainbow Swingers** (that's not what you think it is: l'Ensemble Vocal de l'Université Grenoble-Alpes), I wish I could have stayed longer.

From ICIQ, thank you to the whole Llobet group of 2019: **Jan H.**, **Jan O.**, **Marta**, **Nataliia**, **Navid**, **Sergi**, **Prima**, **Abi**, **Victor**, **Florian**, **Tingting** and **Doro**. Thanks also to **Laura** and **Ansgar** for your sailing skills (seriously that was an amazing feat) and great taste in boardgames. Especially thanks to **Marcos** for all your support to everyone and contributions to eSCALED, to **Carolina** for hosting me and always having incredible scientific ideas and insight into our projects, and to **Toni** for letting me work in his group, following our projects the whole way, and always being super positive and supportive.

Thank you, **Claudia** and **Ana**, at Eurecat, I am sorry I didn't get the chance to work with you, but thank you so much for being so welcoming and for the collaboration.



From UPPA, thank you **Guillaume, Thibault, Chris, Hisham, Aurelien, Fabio** and everyone else. Thank you, **Pierre**, for your epic and unrelenting Béarnais dad jokes. Especially thank you **Tik** for everything you taught me and for the collaboration, and to **Antoine** and **Laurent** for hosting me at UPPA, guiding the projects there and leading the eSCALED project through the toughest of times.

From UU, thank you to everyone from all of Hus 7. Thank you, **Holly, Nina, Salauat, Edgar, Ashleigh, Amol, Sagar, Hemlata, Sergii, Orkun, Princess, Michael, Gustav** and **Stefano** for all the great discussions and advice, **Anders** for the synthetic lab training, **Fatemeh, Mira** and **Larissa** for helping me with the GC, **Mariia** for all the photocatalysis training, **Fiona** and **Aneta** for the help and expertise in quantum dots issues, and **Javi** for being so enthusiastic about them. Thanks **Ignacio**, for organising loads of cool stuff and being hilarious and fellow European fundee **Moritz** for his impressive fire-making skills.

Thank you, fellow physical chemistry members, **Martin** (for having maybe the best taste in music ever), **Sina, Belinda, Astrid, Rima, Sigrid, Clara, Minli, Alenka, Bin,** and **Gaurav**. Huge thanks to my waste disposal partner, **Xinjian**. Thank you, boss **Sicong**, for being so helpful in ordering equipment, and **Andrea** for your ever-insightful advice and indisputable magical wizard powers. Thank you, fellow Best Office members, **Andela, Samir, Nidhi**, distinguished researcher **Hongwei, Leigh Anna**, and honorary members **João** and **Victor**, for always being there. Almost literally never leaving the office. You guys get an extra <3 because **Nidhi** insisted.

Thank you **Sascha** for being my co-supervisor and always being interested in our projects, **Haining** and **Jing** for all your feedback and help in the **Paper III** project. Thank you an infinite number of times and for an infinite number of things, **Nora**. Without you, **Paper III** would never have come together.

... the planet Saturn, and, of course, all of its rings...

And, of course, a huge thank you to my supervisors, **Vincent** and **Leif**, especially for providing absolutely excellent feedback at such short notice.

# References

1. J. Lelieveld, A. Pozzer, U. Pöschl, M. Fnais, A. Haines and T. Münzel, *Cardiovascular Research*, 2020, **116**, 1910–1917.
2. R. K. Pachauri, M. R. Allen, V. R. Barros, J. Broome, W. Cramer, R. Christ, J. A. Church, L. Clarke, Q. Dahe, P. Dasgupta, N. K. Dubash, O. Edenhofer, I. Elgizouli, C. B. Field, P. Forster, P. Friedlingstein, J. Fuglestvedt, L. Gomez-Echeverri, S. Hallegatte, G. Hegerl, M. Howden, K. Jiang, B. J. Cisneroz, V. Kattsov, H. Lee, K. J. Mach, J. Marotzke, M. D. Mastrandrea, L. Meyer, J. Minx, Y. Mulugetta, K. O'Brien, M. Oppenheimer, J. J. Pereira, R. Pichs-Madruga, G.-K. Plattner, H.-O. Pörtner, S. B. Power, B. Preston, N. H. Ravindranath, A. Reisinger, K. Riahi, M. Rusticucci, R. Scholes, K. Seyboth, Y. Sokona, R. Stavins, T. F. Stocker, P. Tschakert, D. van Vuuren and J.-P. van Ypserle, *Climate Change 2014: Synthesis Report. Contribution of Working Groups I, II and III to the Fifth Assessment Report of the Intergovernmental Panel on Climate Change*, IPCC, Geneva, Switzerland, 2014.
3. N. Armaroli and V. Balzani, *Angew. Chem. Int. Ed.*, 2007, **46**, 52–66.
4. T. R. Cook, D. K. Dogutan, S. Y. Reece, Y. Surendranath, T. S. Teets and D. G. Nocera, *Chem. Rev.*, 2010, **110**, 6474–6502.
5. H. A. Daggash, C. F. Patzschke, C. F. Heuberger, L. Zhu, K. Hellgardt, P. S. Fennell, A. N. Bhave, A. Bardow and N. Mac Dowell, *Sustainable Energy Fuels*, 2018, **2**, 1153–1169.
6. P. Walker and G. Dracoulis, *Nature*, 1999, **399**, 35–40.
7. T. Faunce, S. Styring, M. R. Wasielewski, G. W. Brudvig, A. W. Rutherford, J. Messinger, A. F. Lee, C. L. Hill, H. deGroot, M. Fontecave, D. R. MacFarlane, B. Hankamer, D. G. Nocera, D. M. Tiede, H. Dau, W. Hillier, L. Wang and R. Amal, *Energy Environ. Sci.*, 2013, **6**, 1074.
8. D. G. Nocera, *Acc. Chem. Res.*, 2017, **50**, 616–619.
9. A. M. Oliveira, R. R. Beswick and Y. Yan, *Current Opinion in Chemical Engineering*, 2021, **33**, 100701.
10. P. Nikolaidis and A. Poulikkas, *Renewable and Sustainable Energy Reviews*, 2017, **67**, 597–611.
11. M. Noussan, P. P. Raimondi, R. Scita and M. Hafner, *Sustainability*, 2020, **13**, 298.
12. A. Velazquez Abad and P. E. Dodds, *Energy Policy*, 2020, **138**, 111300.
13. Y. Guo, G. Li, J. Zhou and Y. Liu, *IOP Conf. Ser.: Earth Environ. Sci.*, 2019, **371**, 042022.
14. R. Gao, L. Zhang, L. Wang, X. Zhang, C. Zhang, K.-W. Jun, S. Ki Kim, H.-G. Park, Y. Gao, Y. Zhu, T. Zhao, H. Wan and G. Guan, *Energy Conversion and Management*, 2022, **263**, 115671.
15. C. Xiang, K. M. Papadantonakis and N. S. Lewis, *Mater. Horiz.*, 2016, **3**, 169–173.
16. B. Mayerhöfer, D. McLaughlin, T. Böhm, M. Hegelheimer, D. Seeberger and S. Thiele, *ACS Appl. Energy Mater.*, 2020, **3**, 9635–9644.
17. B. Siritanaratkul, M. Forster, F. Greenwell, P. K. Sharma, E. H. Yu and A. J. Cowan, *J. Am. Chem. Soc.*, 2022, **144**, 7551–7556.
18. A. Hodges, A. L. Hoang, G. Tsekouras, K. Wagner, C.-Y. Lee, G. F. Swiegers and G. G. Wallace, *Nat Commun*, 2022, **13**, 1304.
19. L. Hammarström and S. Hammes-Schiffer, *Acc. Chem. Res.*, 2009, **42**, 1859–1860.
20. S. Styring, *Faraday Discuss.*, 2012, **155**, 357–376.
21. J. R. McKone, N. S. Lewis and H. B. Gray, *Chem. Mater.*, 2014, **26**, 407–414.
22. J. H. Montoya, L. C. Seitz, P. Chakthranont, A. Vojvodic, T. F. Jaramillo and J. K. Nørskov, *Nature Mater*, 2017, **16**, 70–81.
23. J. Barber, *Chem. Soc. Rev.*, 2009, **38**, 185–196.
24. A. J. Bard, G. M. Whitesides, R. N. Zare and F. W. (Eds. ) McLafferty, *Acc. Chem. Res.*, , DOI:10.1021/ar00051a001.
25. D. G. Nocera, *Acc. Chem. Res.*, 2012, **45**, 767–776.
26. N. Nelson and A. Ben-Shem, *Nat Rev Mol Cell Biol*, 2004, **5**, 971–982.
27. S. Haussener, *Solar Energy*, 2022, **246**, 294–300.
28. J. H. Kim, D. Hansora, P. Sharma, J.-W. Jang and J. S. Lee, *Chem. Soc. Rev.*, 2019, **48**, 1908–1971.
29. N. Queyriaux, N. Kaefffer, A. Morozan, M. Chavarot-Kerlidou and V. Artero, *Journal of Photochemistry and Photobiology C: Photochemistry Reviews*, 2015, **25**, 90–105.
30. S. Ardo, D. Fernandez Rivas, M. A. Modestino, V. Schulze Greiving, F. F. Abdi, E. Alarcon Llado, V. Artero, K. Ayers, C. Battaglia, J.-P. Becker, D. Bederak, A. Berger, F. Buda, E. Chinello, B. Dam, V. Di Palma, T.

- Edvinsson, K. Fujii, H. Gardeniers, H. Geerlings, S. M. H. Hashemi, S. Haussener, F. Houle, J. Huskens, B. D. James, K. Konrad, A. Kudo, P. P. Kunturu, D. Lohse, B. Mei, E. L. Miller, G. F. Moore, J. Muller, K. L. Orchard, T. E. Rosser, F. H. Saadi, J.-W. Schüttauf, B. Seger, S. W. Sheehan, W. A. Smith, J. Spurgeon, M. H. Tang, R. van de Krol, P. C. K. Vesborg and P. Westerik, *Energy Environ. Sci.*, 2018, **11**, 2768–2783.
31. K. E. Dalle, J. Warnan, J. J. Leung, B. Reuillard, I. S. Karmel and E. Reisner, *Chem. Rev.*, 2019, **119**, 2752–2875.
  32. J. W. Ager, M. R. Shaner, K. A. Walczak, I. D. Sharp and S. Ardo, *Energy Environ. Sci.*, 2015, **8**, 2811–2824.
  33. D. M. Fabian, S. Hu, N. Singh, F. A. Houle, T. Hisatomi, K. Domen, F. E. Osterloh and S. Ardo, *Energy Environ. Sci.*, 2015, **8**, 2825–2850.
  34. C. C. L. McCrory, S. Jung, I. M. Ferrer, S. M. Chatman, J. C. Peters and T. F. Jaramillo, *J. Am. Chem. Soc.*, 2015, **137**, 4347–4357.
  35. J. D. Benck, T. R. Hellstern, J. Kibsgaard, P. Chakhranont and T. F. Jaramillo, *ACS Catal.*, 2014, **4**, 3957–3971.
  36. B. Zhang and L. Sun, *Chem. Soc. Rev.*, 2019, **48**, 2216–2264.
  37. G. Segev, J. Kibsgaard, C. Hahn, Z. J. Xu, W.-H. (Sophia) Cheng, T. G. Deutsch, C. Xiang, J. Z. Zhang, L. Hammarström, D. G. Nocera, A. Z. Weber, P. Agbo, T. Hisatomi, F. E. Osterloh, K. Domen, F. F. Abdi, S. Haussener, D. J. Miller, S. Ardo, P. C. McIntyre, T. Hannappel, S. Hu, H. Atwater, J. M. Gregoire, M. Z. Ertem, I. D. Sharp, K.-S. Choi, J. S. Lee, O. Ishitani, J. W. Ager, R. R. Prabhakar, A. T. Bell, S. W. Boettcher, K. Vincent, K. Takanaabe, V. Artero, R. Napier, B. R. Cuenya, M. T. M. Koper, R. Van De Krol and F. Houle, *J. Phys. D: Appl. Phys.*, 2022, **55**, 323003.
  38. W. Lubitz, H. Ogata, O. Rüdiger and E. Reijerse, *Chem. Rev.*, 2014, **114**, 4081–4148.
  39. V. Fourmond, E. S. Wiedner, W. J. Shaw and C. Léger, *J. Am. Chem. Soc.*, 2019, **141**, 11269–11285.
  40. X. Fang, S. Kalathil and E. Reisner, *Chem. Soc. Rev.*, 2020, **49**, 4926–4952.
  41. V. Artero, *Nat Energy*, 2017, **2**, 17131.
  42. V. Artero and M. Fontecave, *Coordination Chemistry Reviews*, 2005, **249**, 1518–1535.
  43. M. Axelsson, C. F. N. Marchiori, P. Huang, C. M. Araujo and H. Tian, *J. Am. Chem. Soc.*, 2021, **143**, 21229–21233.
  44. U. J. Kilgore, J. A. S. Roberts, D. H. Pool, A. M. Appel, M. P. Stewart, M. R. DuBois, W. G. Dougherty, W. S. Kassel, R. M. Bullock and D. L. DuBois, *J. Am. Chem. Soc.*, 2011, **133**, 5861–5872.
  45. M. L. Helm, M. P. Stewart, R. M. Bullock, M. R. DuBois and D. L. DuBois, *Science*, 2011, **333**, 863–866.
  46. N. Coutard, N. Kauffer and V. Artero, *Chem. Commun.*, 2016, **52**, 13728–13748.
  47. N. Elgrishi, B. D. McCarthy, E. S. Rountree and J. L. Dempsey, *ACS Catal.*, 2016, **6**, 3644–3659.
  48. R. Tyburski, T. Liu, S. D. Glover and L. Hammarström, *J. Am. Chem. Soc.*, 2021, **143**, 560–576.
  49. J. Savéant, *Angew. Chem. Int. Ed.*, 2019, **58**, 2125–2128.
  50. A. C. Ghosh, C. Duboc and M. Gennari, *Coordination Chemistry Reviews*, 2021, **428**, 213606.
  51. D. W. Wakerley and E. Reisner, *Phys. Chem. Chem. Phys.*, 2014, **16**, 5739–5746.
  52. J. L. Dempsey, B. S. Brunshwig, J. R. Winkler and H. B. Gray, *Acc. Chem. Res.*, 2009, **42**, 1995–2004.
  53. P.-A. Jacques, V. Artero, J. Pécaut and M. Fontecave, *Proc. Natl. Acad. Sci. U.S.A.*, 2009, **106**, 20627–20632.
  54. D. Sun, A. Karippara Harshan, J. Pécaut, S. Hammes-Schiffer, C. Costentin and V. Artero, *ChemElectroChem*, 2021, **8**, 2671–2679.
  55. L. Chen, R. U. R. Sagar, J. Chen, J. Liu, S. Aslam, F. Nosheen, T. Anwar, N. Hussain, X. Hou and T. Liang, *International Journal of Hydrogen Energy*, 2021, **46**, 19338–19346.
  56. B. Mondal, K. Sengupta, A. Rana, A. Mahammed, M. Botoshansky, S. G. Dey, Z. Gross and A. Dey, *Inorg. Chem.*, 2013, **52**, 3381–3387.
  57. R. M. Kellett and T. G. Spiro, *Inorg. Chem.*, 1985, **24**, 2373–2377.
  58. L. Tong, L. Duan, A. Zhou and R. P. Thummel, *Coordination Chemistry Reviews*, 2020, **402**, 213079.
  59. F. Lucarini, D. Bongni, P. Schiel, G. Bevini, E. Benazzi, E. Solari, F. Fadaei-Tirani, R. Scopelliti, M. Marazzi, M. Natali, M. Pastore and A. Ruggi, *ChemSusChem*, 2021, **14**, 1874–1885.
  60. T. Straistari, R. Hardré, J. Fize, S. Shova, M. Giorgi, M. Réglie, V. Artero and M. Orto, *Chem. Eur. J.*, 2018, **24**, 8779–8786.
  61. A. C. Benniston and A. Harriman, *Materials Today*, 2008, **11**, 26–34.
  62. E. S. Andreiadis, P.-A. Jacques, P. D. Tran, A. Leyris, M. Chavarot-Kerlidou, B. Jusselme, M. Matheron, J. Pécaut, S. Palacin, M. Fontecave and V. Artero, *Nature Chem*, 2013, **5**, 48–53.
  63. P. D. Tran, A. Le Goff, J. Heidkamp, B. Jusselme, N. Guillet, S. Palacin, H. Dau, M. Fontecave and V. Artero, *Angew. Chem. Int. Ed.*, 2011, **50**, 1371–1374.
  64. J. Willkomm, N. M. Muresan and E. Reisner, *Chem. Sci.*, 2015, **6**, 2727–2736.
  65. K. L. Materna, R. H. Crabtree and G. W. Brudvig, *Chem. Soc. Rev.*, 2017, **46**, 6099–6110.
  66. B. L. Wadsworth, D. Khusnutdinova, J. M. Urbine, A. S. Reyes and G. F. Moore, *ACS Appl. Mater. Interfaces*, 2020, **12**, 3903–3911.
  67. K. M. Long and D. H. Busch, *Inorg. Chem.*, 1970, **9**, 505–512.
  68. K. M. Long and D. H. Busch, *Journal of Coordination Chemistry*, 1974, **4**, 113–123.

69. G. N. Schrauzer, *Acc. Chem. Res.*, 1968, **1**, 97–103.
70. G. Costa, G. Mestroni and E. de Savognani, *Inorganica Chimica Acta*, 1969, **3**, 323–328.
71. N. Kaeffer, M. Chavarot-Kerlidou and V. Artero, *Acc. Chem. Res.*, 2015, **48**, 1286–1295.
72. M. Giedyk, K. Goliszewska and D. Gryko, *Chem. Soc. Rev.*, 2015, **44**, 3391–3404.
73. C.-F. Leung, Y.-Z. Chen, H.-Q. Yu, S.-M. Yiu, C.-C. Ko and T.-C. Lau, *Int. J. Hydrog. Energy*, 2011, **36**, 11640–11645.
74. C.-B. Li, A. J. Bagnall, D. Sun, J. Rendon, M. Koepf, S. Gambarelli, J.-M. Mouesca, M. Chavarot-Kerlidou and V. Artero, *Sustainable Energy Fuels*, 2022, **6**, 143–149.
75. S. Grau Abarca, M. Schilling, D. Moonshiram, J. Benet-Buchholz, S. Lubner, A. Llobet and C. Gimbert-Suriñach, *ChemSusChem*, 2020, **13**, 2745–2752.
76. S. Varma, C. E. Castillo, T. Stoll, J. Fortage, A. G. Blackman, F. Molton, A. Deronzier and M.-N. Collomb, *Phys. Chem. Chem. Phys.*, 2013, **15**, 17544.
77. C. C. L. McCrory, C. Uyeda and J. C. Peters, *J. Am. Chem. Soc.*, 2012, **134**, 3164–3170.
78. R. Gueret, C. E. Castillo, M. Rebarz, F. Thomas, A.-A. Hargrove, J. Pécaut, M. Sliwa, J. Fortage and M.-N. Collomb, *Journal of Photochemistry and Photobiology B: Biology*, 2015, **152**, 82–94.
79. S. Roy, M. Bacchi, G. Berggren and V. Artero, *ChemSusChem*, 2015, **8**, 3632–3638.
80. D. C. Lacy, C. C. L. McCrory and J. C. Peters, *Inorg. Chem.*, 2014, **53**, 4980–4988.
81. W. Nie, D. E. Tarnopol and C. C. L. McCrory, *J. Am. Chem. Soc.*, 2021, **143**, 3764–3778.
82. J. Wang, K. Yamauchi, H. Huang, J. Sun, Z. Luo, D. Zhong, T. Lu and K. Sakai, *Angew. Chem. Int. Ed.*, 2019, **58**, 10923–10927.
83. R. Gueret, C. E. Castillo, M. Rebarz, F. Thomas, M. Sliwa, J. Chauvin, B. Dautreppe, J. Pécaut, J. Fortage and M.-N. Collomb, *Inorg. Chem.*, 2019, **58**, 9043–9056.
84. R. Gueret, L. Poulard, M. Oshinowo, J. Chauvin, M. Dahmane, G. Dupeyre, P. P. Lainé, J. Fortage and M.-N. Collomb, *ACS Catal.*, 2018, **8**, 3792–3802.
85. C. Gimbert-Suriñach, J. Albero, T. Stoll, J. Fortage, M.-N. Collomb, A. Deronzier, E. Palomares and A. Llobet, *J. Am. Chem. Soc.*, 2014, **136**, 7655–7661.
86. M. Sandroni, R. Gueret, K. D. Wegner, P. Reiss, J. Fortage, D. Aldakov and M.-N. Collomb, *Energy Environ. Sci.*, 2018, **11**, 1752–1761.
87. C. Nie, W. Ni, L. Gong, J. Jiang, J. Wang and M. Wang, *J. Mater. Chem. A*, 2019, **7**, 27432–27440.
88. A. H. Ip, S. M. Thon, S. Hoogland, O. Voznyy, D. Zhitomirsky, R. Debnath, L. Levina, L. R. Rollny, G. H. Carey, A. Fischer, K. W. Kemp, I. J. Kramer, Z. Ning, A. J. Labelle, K. W. Chou, A. Amassian and E. H. Sargent, *Nature Nanotech.*, 2012, **7**, 577–582.
89. A. J. Bard and L. R. Faulkner, *Electrochemical methods: fundamentals and applications*, Wiley, New York, 2nd ed., 2001.
90. N. Elgrishi, K. J. Rountree, B. D. McCarthy, E. S. Rountree, T. T. Eisenhart and J. L. Dempsey, *J. Chem. Educ.*, 2018, **95**, 197–206.
91. J.-M. Savéant, *Chem. Rev.*, 2008, **108**, 2348–2378.
92. V. Varlet, F. Smith and M. Augsburger, *J. Mass Spectrom.*, 2013, **48**, 914–918.
93. J. R. Lakowicz, *Principles of fluorescence spectroscopy*, Springer, New York, 3rd ed., 2006.
94. R. Berera, R. van Grondelle and J. T. M. Kennis, *Photosynth Res.*, 2009, **101**, 105–118.
95. D. Moonshiram, C. Gimbert-Suriñach, A. Guda, A. Picon, C. S. Lehmann, X. Zhang, G. Doumy, A. M. March, J. Benet-Buchholz, A. Soldatov, A. Llobet and S. H. Southworth, *J. Am. Chem. Soc.*, 2016, **138**, 10586–10596.
96. S. Bold, T. Straistari, A. B. Muñoz-García, M. Pavone, V. Artero, M. Chavarot-Kerlidou and B. Dietzek, *Catalysts*, 2020, **10**, 1340.
97. S. Bold, J. Massin, E. Giannoudis, M. Koepf, V. Artero, B. Dietzek and M. Chavarot-Kerlidou, *ACS Catal.*, 2021, **11**, 3662–3678.
98. C. Costentin, H. Dridi and J.-M. Savéant, *J. Am. Chem. Soc.*, 2014, **136**, 13727–13734.
99. J. M. Savéant and K. B. Su, *Journal of Electroanalytical Chemistry and Interfacial Electrochemistry*, 1984, **171**, 341–349.
100. D. J. Martin, B. D. McCarthy, E. S. Rountree and J. L. Dempsey, *Dalton Trans.*, 2016, **45**, 9970–9976.
101. A. M. Appel, S.-J. Lee, J. A. Franz, D. L. DuBois, M. Rakowski DuBois and B. Twamley, *Organometallics*, 2009, **28**, 749–754.
102. C. Costentin and J.-M. Savéant, *ChemElectroChem*, 2014, **1**, 1226–1236.
103. C. Costentin, S. Drouet, M. Robert and J.-M. Savéant, *J. Am. Chem. Soc.*, 2012, **134**, 11235–11242.
104. E. S. Rountree, D. J. Martin, B. D. McCarthy and J. L. Dempsey, *ACS Catal.*, 2016, **6**, 3326–3335.
105. V. Artero and J.-M. Savéant, *Energy Environ. Sci.*, 2014, **7**, 3808–3814.
106. A. Le Goff, V. Artero, B. Jusselme, P. D. Tran, N. Guillet, R. Metaye, A. Fihri, S. Palacin and M. Fontecave, *Science*, 2009, **326**, 1384–1387.
107. T. N. Huan, R. T. Jane, A. Benayad, L. Guetaz, P. D. Tran and V. Artero, *Energy Environ. Sci.*, 2016, **9**, 940–947.

108. B. Reuillard, M. Blanco, L. Calvillo, N. Coutard, A. Ghedjatti, P. Chenevier, S. Agnoli, M. Otyepka, G. Granozzi and V. Artero, *ACS Appl. Mater. Interfaces*, 2020, **12**, 5805–5811.
109. J. Schild, B. Reuillard, A. Morozan, P. Chenevier, E. Gravel, E. Doris and V. Artero, *J. Am. Chem. Soc.*, 2021, jacs.1c07093.
110. D. W. Wakerley and E. Reisner, *Energy Environ. Sci.*, 2015, **8**, 2283–2295.
111. D. W. Wakerley, M. A. Gross and E. Reisner, *Chem. Commun.*, 2014, **50**, 15995–15998.
112. D. Dolui, S. Khandelwal, P. Majumder and A. Dutta, *Chem. Commun.*, 2020, **56**, 8166–8181.
113. S. Roy, Z. Huang, A. Bhunia, A. Castner, A. K. Gupta, X. Zou and S. Ott, *J. Am. Chem. Soc.*, 2019, **141**, 15942–15950.
114. N. Kaeffer, A. Morozan and V. Artero, *J. Phys. Chem. B*, 2015, **119**, 13707–13713.
115. N. Kaeffer, A. Morozan, J. Fize, E. Martinez, L. Guetaz and V. Artero, *ACS Catal.*, 2016, **6**, 3727–3737.
116. S. Cobo, J. Heidkamp, P.-A. Jacques, J. Fize, V. Fourmond, L. Guetaz, B. Jusselme, V. Ivanova, H. Dau, S. Palacin, M. Fontecave and V. Artero, *Nature Mater*, 2012, **11**, 802–807.
117. C. H. Lee, D. Villágran, T. R. Cook, J. C. Peters and D. G. Nocera, *ChemSusChem*, 2013, **6**, 1541–1544.
118. C. Nie, C. Liu, L. Gong and M. Wang, *J. Mater. Chem. A*, 2021, **9**, 234–238.
119. J.-W. Wang, M. Gil-Sepulcre, H.-H. Huang, E. Solano, Y.-F. Mu, A. Llobet and G. Ouyang, *Cell Reports Physical Science*, 2021, **2**, 100681.
120. J.-W. Wang, H.-H. Huang, P. Wang, G. Yang, S. Kupfer, Y. Huang, Z. Li, Z. Ke and G. Ouyang, *JACS Au*, 2022, jacsau.2c00073.
121. M. N. Jackson and Y. Surendranath, *Acc. Chem. Res.*, 2019, **52**, 3432–3441.
122. C. J. Kaminsky, S. Weng, J. Wright and Y. Surendranath, *Nat Catal*, 2022, **5**, 430–442.
123. A. J. Bard, *J. Am. Chem. Soc.*, 2010, **132**, 7559–7567.
124. A. Wagner, C. D. Sahn and E. Reisner, *Nat Catal*, 2020, **3**, 775–786.
125. B. D. McCarthy and J. L. Dempsey, *Inorg. Chem.*, 2017, **56**, 1225–1231.
126. R. N. Dürr, S. Chasvised, M. Gil-Sepulcre, A. Howe, M. A. Hoque, V. N’Guyen, S. Sadeghi, S. Reynaud, C. Cugnet, L. Authier, C. Gimbert-Suriñach, A. Bousquet, A. Llobet and L. Billon, *ACS Appl. Energy Mater.*, 2021, **4**, 10534–10541.
127. C. Costentin, F. Camara, J. Fortage and M.-N. Collomb, *ACS Catal.*, 2022, 6246–6254.
128. P. Kambhampati, *J. Phys. Chem. Lett.*, 2021, **12**, 4769–4779.
129. V. I. Klimov, *Annu. Rev. Phys. Chem.*, 2007, **58**, 635–673.
130. R. D. Harris, S. Bettis Homan, M. Kodaimati, C. He, A. B. Nepomnyashchii, N. K. Swenson, S. Lian, R. Calzada and E. A. Weiss, *Chem. Rev.*, 2016, **116**, 12865–12919.
131. W. Hu, S. Yang and J. Huang, *J. Chem. Phys.*, 2019, **151**, 214705.
132. M. D. Regulacio and M.-Y. Han, *Acc. Chem. Res.*, 2010, **43**, 621–630.
133. M. A. Boles, D. Ling, T. Hyeon and D. V. Talapin, *Nature Mater*, 2016, **15**, 141–153.
134. N. C. Anderson, M. P. Hendricks, J. J. Choi and J. S. Owen, *J. Am. Chem. Soc.*, 2013, **135**, 18536–18548.
135. F. Arcudi, L. Đorđević, B. Nagasing, S. I. Stupp and E. A. Weiss, *J. Am. Chem. Soc.*, 2021, **143**, 18131–18138.
136. X.-B. Fan, S. Yu, F. Zhan, Z.-J. Li, Y.-J. Gao, X.-B. Li, L.-P. Zhang, Y. Tao, C.-H. Tung and L.-Z. Wu, *ChemSusChem*, 2017, **10**, 4833–4838.
137. C. D. Windle, E. Pastor, A. Reynal, A. C. Whitwood, Y. Vaynzof, J. R. Durrant, R. N. Perutz and E. Reisner, *Chem. Eur. J.*, 2015, **21**, 3746–3754.
138. M. Abdellah, A. M. El-Zohry, L. J. Antila, C. D. Windle, E. Reisner and L. Hammarström, *J. Am. Chem. Soc.*, 2017, **139**, 1226–1232.
139. L. Hammarström, *Acc. Chem. Res.*, 2015, **48**, 840–850.
140. S. Karlsson, J. Boixel, Y. Pellegrin, E. Blart, H.-C. Becker, F. Odobel and L. Hammarström, *Faraday Discuss.*, 2012, **155**, 233–252.
141. C. Bozal-Ginesta, C. A. Mesa, A. Eisenschmidt, L. Francàs, R. B. Shankar, D. Antón-García, J. Warnan, J. Willkomm, A. Reynal, E. Reisner and J. R. Durrant, *Chem. Sci.*, 2021, **12**, 946–959.
142. J. Huang, M. G. Gatty, B. Xu, P. B. Pati, A. S. Etman, L. Tian, J. Sun, L. Hammarström and H. Tian, *Dalton Trans.*, 2018, **47**, 10775–10783.
143. N. Eliasson, B. P. Rimgard, A. Castner, C.-W. Tai, S. Ott, H. Tian and L. Hammarström, *J. Phys. Chem. C*, 2021, **125**, 14751–14764.
144. J.-X. Jian, C. Ye, X.-Z. Wang, M. Wen, Z.-J. Li, X.-B. Li, B. Chen, C.-H. Tung and L.-Z. Wu, *Energy Environ. Sci.*, 2016, **9**, 2083–2089.
145. D. H. Jara, S. J. Yoon, K. G. Stamplecoskie and P. V. Kamat, *Chem. Mater.*, 2014, **26**, 7221–7228.
146. B. Chen, H. Zhong, W. Zhang, Z. Tan, Y. Li, C. Yu, T. Zhai, Y. Bando, S. Yang and B. Zou, *Adv. Funct. Mater.*, 2012, **22**, 2081–2088.
147. Y. Chen, S. Li, L. Huang and D. Pan, *Inorg. Chem.*, 2013, **52**, 7819–7821.
148. D. H. Jara, K. G. Stamplecoskie and P. V. Kamat, *J. Phys. Chem. Lett.*, 2016, **7**, 1452–1459.

149. J. Huang, B. Xu, L. Tian, P. B. Pati, A. S. Etman, J. Sun, L. Hammarström and H. Tian, *Chem. Commun.*, 2019, **55**, 7918–7921.
150. E. Deponi, A. Luisa, M. Natali, E. Iengo and F. Scandola, *Dalton Trans.*, 2014, **43**, 16345–16353.
151. D. Genovese, M. Cingolani, E. Rampazzo, L. Prodi and N. Zaccheroni, *Chem. Soc. Rev.*, 2021, **50**, 8414–8427.
152. P. P. Infelta, M. Gratzel and J. K. Thomas, *J. Phys. Chem.*, 1974, **78**, 190–195.
153. A. J. Cowan and J. R. Durrant, *Chem. Soc. Rev.*, 2013, **42**, 2281–2293.
154. Y. Wang, A. Vogel, M. Sachs, R. S. Sprick, L. Wilbraham, S. J. A. Moniz, R. Godin, M. A. Zwijnenburg, J. R. Durrant, A. I. Cooper and J. Tang, *Nat Energy*, 2019, **4**, 746–760.
155. Z. Han, F. Qiu, R. Eisenberg, P. L. Holland and T. D. Krauss, *Science*, 2012, **338**, 1321–1324.
156. D. Grammatico, A. J. Bagnall, L. Riccardi, M. Fontecave, B.-L. Su and L. Billon, *Angew Chem Int Ed*, 2022, anie.202206399.
157. M. Dragoman, E. Flahaut, D. Dragoman, M. Al Ahmad and R. Plana, *Nanotechnology*, 2009, **20**, 375203.
158. R. Tortorich and J.-W. Choi, *Nanomaterials*, 2013, **3**, 453–468.
159. J.-W. Han, B. Kim, J. Li and M. Meyyappan, *Materials Research Bulletin*, 2014, **50**, 249–253.
160. X. Liang, H. Li, J. Dou, Q. Wang, W. He, C. Wang, D. Li, J. Lin and Y. Zhang, *Adv. Mater.*, 2020, **32**, 2000165.
161. H. Menon, R. Aiswarya and K. P. Surendran, *RSC Adv.*, 2017, **7**, 44076–44081.
162. C. Phillips, A. Al-Ahmadi, S.-J. Potts, T. Claypole and D. Deganello, *J Mater Sci*, 2017, **52**, 9520–9530.
163. D. T. Duong, C. Wang, E. Antono, M. F. Toney and A. Salleo, *Organic Electronics*, 2013, **14**, 1330–1336.
164. B. Reuillard, J. Warnan, J. J. Leung, D. W. Wakerley and E. Reisner, *Angew. Chem. Int. Ed.*, 2016, **55**, 3952–3957.



Cite this: *Sustainable Energy Fuels*,  
2022, 6, 143

# Electrocatalytic reduction of protons to dihydrogen by the cobalt tetraazamacrocyclic complex $[\text{Co}(\text{N}_4\text{H})\text{Cl}_2]^+$ : mechanism and benchmarking of performances†‡

Cheng-Bo Li,<sup>§ab</sup> Andrew J. Bagnall,<sup>§bc</sup> Dongyue Sun,<sup>b</sup> Julia Rendon,<sup>bd</sup> Matthieu Koepf,<sup>§b</sup> Serge Gambarelli,<sup>d</sup> Jean-Marie Mouesca,<sup>d</sup> Murielle Chavarot-Kerlidou,<sup>§b</sup> and Vincent Artero,<sup>§\*b</sup>

The cobalt tetraazamacrocyclic  $[\text{Co}(\text{N}_4\text{H})\text{Cl}_2]^+$  complex is becoming a popular and versatile catalyst for the electrocatalytic evolution of hydrogen, because of its stability and superior activity in aqueous conditions. We present here a benchmarking of its performances based on the thorough analysis of cyclic voltammograms recorded under various catalytic regimes in non-aqueous conditions allowing control of the proton concentration. This allowed a detailed mechanism to be proposed with quantitative determination of the rate-constants for the various protonation steps, as well as identification of the amine function of the tetraazamacrocyclic ligand to act as a proton relay during  $\text{H}_2$  evolution.

Received 19th August 2021

Accepted 4th November 2021

DOI: 10.1039/d1se01267c

rsc.li/sustainable-energy

Molecular cobalt complexes are popular and versatile catalysts for the electrocatalytic evolution of hydrogen.<sup>1–5</sup> Recently, the cobalt complex  $[\text{Co}(\text{N}_4\text{H})\text{Cl}_2]^+$  (**Cat1**, Fig. 1) based on the tetraazamacrocyclic 2,12-dimethyl-3,7,11,17-tetraazabicyclo[11.3.1]heptadeca-1(17),2,11,13,15-pentaene ligand,<sup>6</sup> described by Karn and Busch in 1966, has received increased interest<sup>7–9</sup> namely because this catalyst proves active and stable for the evolution of  $\text{H}_2$  from fully aqueous solutions.<sup>7–17</sup> A study carried out under homogeneous conditions using chemical reductants or photochemical activation confirmed the superior activity of **Cat1** in fully aqueous media,<sup>18</sup> and X-ray absorption spectroscopic monitoring of a homogeneous photocatalytic system for  $\text{H}_2$  evolution based on **Cat1** indicated an ECEC mechanism (E = monoelectronic electrochemical reduction, C = protonation step) starting from the bis-aqua  $\text{Co}(\text{II})$  complex.<sup>13,14</sup> However, very few metrics are currently available to benchmark the catalytic

activity of this compound. **Cat1** was included in a benchmarking study for  $\text{H}_2$ -evolving electrocatalysts carried out in aqueous electrolyte<sup>19</sup> but under quite acidic conditions likely to induce reductive degradation of the ligand during the test and formation of metallic particles responsible for the observed HER activity.<sup>20,21</sup> To gain quantitative information on the  $\text{H}_2$  evolution mechanism mediated by **Cat1**, we therefore revisited the non-aqueous conditions investigated by Lau and coworkers,<sup>22</sup> where it is easier to control the concentration and chemical potential of protons.<sup>23</sup>

The cyclic voltammogram of **Cat1** (perchlorate salt) in  $\text{CH}_3\text{CN}$  (with 0.1 M  $n\text{Bu}_4\text{NBF}_4$ , Fig. 2 and S1†) displays two quasi-reversible systems at  $-0.47$  V ( $\Delta E_p = 92$  mV) and  $-0.96$  V ( $\Delta E_p = 86$  mV) vs.  $\text{Fc}^+/\text{Fc}$ , corresponding to the  $\text{Co}^{\text{III/II}}$  and  $\text{Co}^{\text{III/I}}$  redox processes, respectively, based on previous literature. Of note, we will formally use the  $\text{Co}^{\text{I}}$  notation throughout this article, while the electronic state could also correspond to a reduced  $\text{N}_4\text{H}$  ligand ( $\pi$ -radical anion) antiferromagnetically

<sup>a</sup>Key Laboratory of Synthetic and Natural Functional Molecule of the Ministry of Education, The Energy and Catalysis Hub, College of Chemistry and Materials Science, Northwest University, Xi'an 710127, China

<sup>b</sup>Univ. Grenoble Alpes, CNRS, CEA, IRIG, Laboratoire de Chimie et Biologie des Métaux, 17 Rue des Martyrs, F-38054 Grenoble, Cedex, France. E-mail: vincent.artero@cea.fr

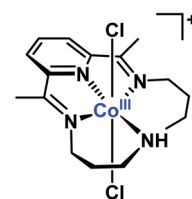
<sup>c</sup>Ångström Laboratory, Department of Chemistry, Uppsala University, SE75120 Uppsala, Sweden

<sup>d</sup>Univ. Grenoble Alpes, CNRS, CEA/IRIG-SyMMES, 17 Rue des Martyrs, F-38054 Grenoble, Cedex, France

† In memory of Dr Jean-Michel Savéant.

‡ Electronic supplementary information (ESI) available. See DOI: 10.1039/d1se01267c

§ Equal contribution.



$[\text{Co}(\text{N}_4\text{H})\text{Cl}_2]^+$  (**Cat1**)

Fig. 1 Structure of **Cat1**.



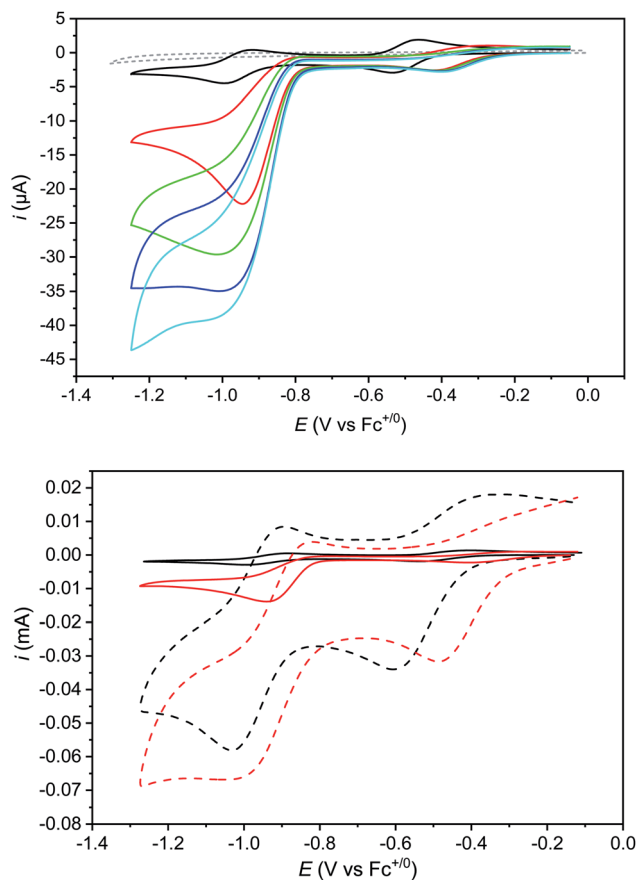


**Fig. 2** Top: cyclic voltammograms of **Cat1** (0.5 mM) in  $\text{CH}_3\text{CN}$  (+0.1 M  $n\text{Bu}_4\text{NBF}_4$ ) recorded at a glassy carbon electrode (1.6 mm diameter) in the absence (black trace) and in the presence of 5.0 (red trace), 10.0 (green trace), 12.5 (navy trace) and 15.0 mM (cyan trace) *p*-cyanoanilinium tetrafluoroborate; scan rate:  $100 \text{ mV s}^{-1}$ . A control voltammogram of 15 mM *p*-cyanoanilinium tetrafluoroborate without **Cat1** (gray dashed trace) is shown for comparison; bottom: cyclic voltammograms of **Cat1** (0.5 mM) in  $\text{CH}_3\text{CN}$  (+0.1 M  $n\text{Bu}_4\text{NBF}_4$ ) recorded at a glassy carbon electrode in the absence (black) and in the presence (red) of 5 mM *p*-cyanoanilinium tetrafluoroborate; scan rate: 0.1 (solid) and  $10 \text{ V s}^{-1}$  (dashed). See Fig. S5 $\ddagger$  for control voltammograms without catalyst under similar conditions.

coupled to a low-spin  $\text{Co(II)}$  ion.<sup>24</sup> A third ligand-centered process is observed at  $-1.89 \text{ V}$  ( $\Delta E_p = 69 \text{ mV}$ ) vs.  $\text{Fc}^+/\text{Fc}$ .<sup>22</sup> Upon addition of *p*-cyanoanilinium tetrafluoroborate ( $\text{p}K_a = 7.0$  in  $\text{CH}_3\text{CN}$ )<sup>25</sup> acting as a proton source, a catalytic wave develops on the top of the  $\text{Co}^{\text{II/I}}$  wave as previously described.<sup>22</sup> This electrocatalytic behavior corresponds to  $\text{H}_2$  evolution with  $>90\%$  faradaic yield<sup>22</sup> and nicely mirrors the one observed for **Cat1** in mildly acidic aqueous solution.<sup>11,13,22</sup> The addition of stronger acids such as  $\text{HBF}_4 \cdot \text{Et}_2\text{O}$  or  $\text{CF}_3\text{SO}_3\text{H}$  also triggers  $\text{H}_2$  evolution catalysis but is detrimental to the stability of **Cat1** at high concentration. **Cat1** is unable to catalyze the reduction of acids with higher  $\text{p}K_a$  values, starting with *p*-toluenesulfonic acid ( $\text{p}K_a = 8.3$  in  $\text{CH}_3\text{CN}$ ).<sup>26</sup>

Noteworthy, the addition of acid also affects the  $\text{Co}^{\text{III/II}}$  system, which shifts to more positive potentials and partly loses reversibility.  $^1\text{H}$  NMR experiments confirmed that the  $\text{Co}^{\text{III}}$  form of **Cat1** is not protonated under these conditions (Fig. S2 $\ddagger$ ),

neither does *p*-cyanoaniline coordinate to any of the  $\text{Co}^{\text{III}}$ ,  $\text{Co}^{\text{II}}$  and  $\text{Co}^{\text{I}}$  states of **Cat1** (Fig. S3 $\ddagger$ ) in the absence of acid. However, when 5 equivalents of *p*-cyanoanilinium tetrafluoroborate is added to an electrochemically-generated solution of the  $\text{Co}^{\text{II}}$  form of **Cat1**, the EPR signal is significantly changed, from a broad signal centered at  $g_1 = 2.240$ ,  $g_2 = 2.130$  and  $g_3 = 2.004$  to a better resolved spectrum characteristic for a low spin  $d^7$  ( $S = \frac{1}{2}$ ) electronic configuration of  $\text{Co}$  (Fig. 3). It furthermore displays a 5-line superhyperfine structure with an intensity ratio of 1 : 2 : 3 : 2 : 1 and a coupling constant of 45 Hz in line with the coordination of two equivalent nitrogen-based ligands. Of note, a similar behavior was observed when the  $\text{Co}^{\text{II}}$  form of **Cat1** was prepared by chemical reduction with cobaltocene instead of exhaustive bulk electrolysis (Fig. S4 $\ddagger$ ). No such change is observed when *p*-cyanoaniline is added (Fig. S4 $\ddagger$ ). When  $\text{HBF}_4 \cdot \text{Et}_2\text{O}$  is used as proton source instead of *p*-cyanoanilinium tetrafluoroborate, this superhyperfine structure is changed to a 3-line structure with a coupling constant of 40 Hz (Fig. 3), suggesting the coordination of a single nitrogen-based axial ligand,  $\text{CH}_3\text{CN}$  being the only plausible one under these conditions. In the former case, coordination of  $\text{CH}_3\text{CN}$  and *p*-cyanoanilinium (or *p*-cyanoaniline generated *in situ* upon protonation of the complex) can be considered without being possible to discriminate one from the other at the EPR level. Taken all together, these observations suggest (i) protonation of the ligand in **Cat1** occurs upon reduction from the  $\text{Co}^{\text{III}}$  to the  $\text{Co}^{\text{II}}$  state in the presence of acid; (ii) at the same time, chloride axial ligands are displaced for nitrogen ligands; (iii) the nature and number of axial ligands depend on the nature of the acid employed. It should also be underlined that the binding of one vs. two ligands in the cobalt + II oxidation state likely depends on a subtle balance of their donating ability, as previously stated

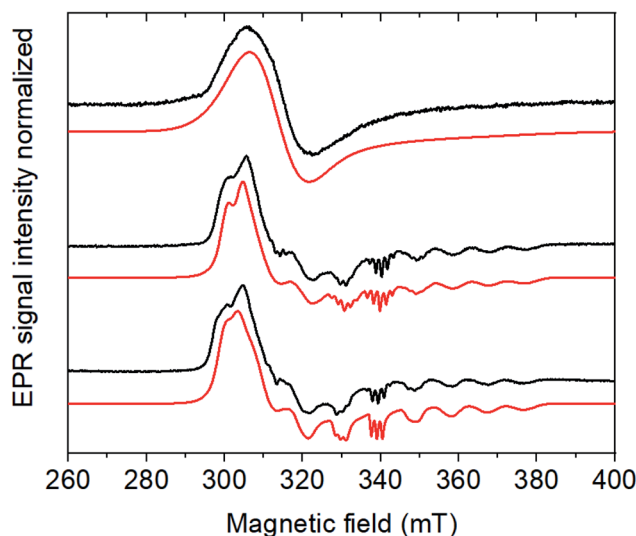


**Fig. 3** CW X-band EPR spectra (9.65 GHz) of the electrochemically generated  $\text{Co}^{\text{II}}$  form of **Cat1** (0.5 mM) as prepared (top), with 5 eq. of the acids *p*-cyanoanilinium tetrafluoroborate (middle),  $\text{HBF}_4$  (bottom) and their respective simulations in red. Experimental conditions: 30 K, 1 mW microwave power, 1600 G field sweep. Simulation parameters are reported in Table S1 $\ddagger$ .





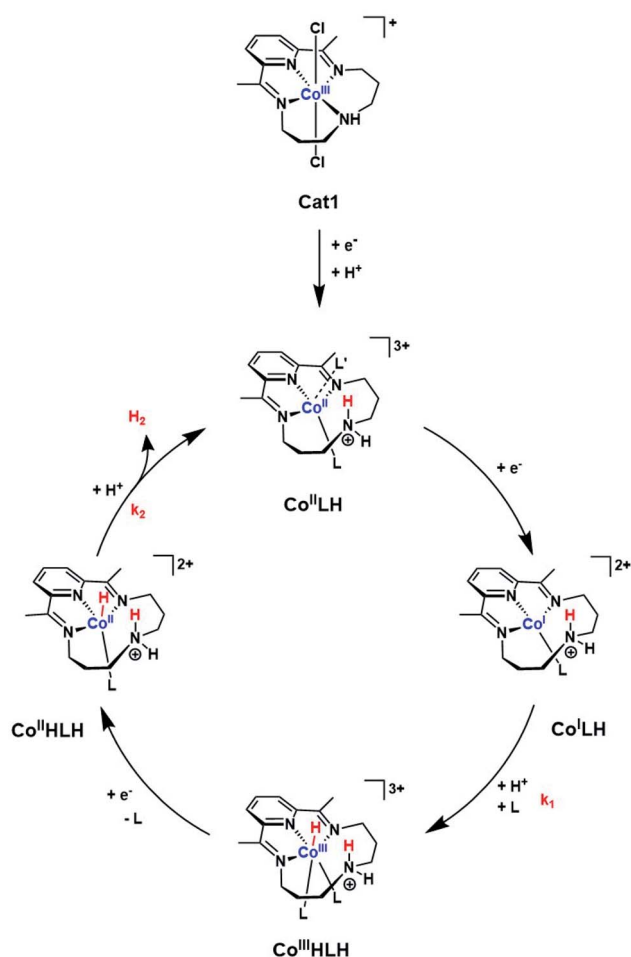
for **Cat1** (ref. 11) and also found for cobaloximes and related cobalt diimine–dioxime complexes.<sup>27–30</sup> A possible structure of **Co<sup>III</sup>LH**, in line with a previous proposition,<sup>13</sup> is shown in Scheme 1.

Although the formation of the protonated **Co<sup>II</sup>** derivative of **Cat1** falls into the proton-coupled electron transfer classification, the cathodic peak potential does not follow the increase of 29 mV per decade of acid concentration expected for an irreversible EC process with a fully displaced protonation equilibrium (e.g. in the pure kinetic KP zone);<sup>31</sup> rather the cathodic peak potential rapidly shifts to a new value upon addition of acid and then keeps this value unchanged upon further addition of acid (Fig. 2). This behavior is characteristic of the extraordinary kinetic (KE) zone,<sup>31</sup> with fast protonation of the **Co<sup>II</sup>** species so that, even with few equivalents of acid added, the new wave is observed at a potential close to the apparent standard potential of the **Co<sup>III</sup>/Co<sup>II</sup>LH** couple, thus with a ~250 mV shift compared to the original **Co<sup>III</sup>/Co<sup>II</sup>** couple. Recording the cyclic voltammograms at a significantly higher scan rate (10 V s<sup>-1</sup>) did not allow approaching the pure kinetic KP zone although a slightly more progressive evolution of the cathodic peak potential was observed with an increase of ~200 mV per decade of acid

concentration (Table S2†). Simulations using the DigiElch software allowed to reproduce the potential shift of such an EC process at both 0.1 and 10 mV s<sup>-1</sup> using a protonation equilibrium constant higher than 10<sup>4</sup> and a bimolecular protonation rate of 10<sup>7</sup> mol<sup>-1</sup> L s<sup>-1</sup>, suggesting that the amine moiety can potentially act as a proton relay during catalysis.<sup>32</sup>

Protonation of the **Co<sup>II</sup>** state should also alter the standard potential of the **Co<sup>II</sup>/Co<sup>I</sup>** couple. At 100 mV s<sup>-1</sup>, this redox process is hidden by the catalytic wave it triggers. However, measuring cyclic voltammograms at 10 V s<sup>-1</sup> enabled the catalysis to be outrun and a reversible wave to be recovered centred at -0.89 V vs. **Fc<sup>+</sup>/Fc** (Fig. 2 bottom) that likely corresponds to the actual **Co<sup>II</sup>LH/Co<sup>I</sup>LH** couple responsible for catalysis. Remarkably, raising acid concentration, we found that catalysis proceeds under pure kinetic conditions, where a catalytic current plateau, independent of the scan rate, is observed (Fig. 4) because substrate consumption is negligible (pure kinetic KS zone).<sup>31,33</sup> Under these conditions, the mid-wave potential of the catalytic process is found at -0.87 V vs. **Fc<sup>+</sup>/Fc**. Varying the catalyst concentration for a given acid concentration showed a linear dependence of the catalytic current with the catalyst concentration (Fig. S6†). The catalytic plateau current also linearly varies with the acid concentration (Fig. S7†).

Together these data are consistent with a mechanism for H<sub>2</sub> evolution catalyzed by **Cat1** following an ECEC reaction scheme (Scheme 1), where E and C stand for electrochemical steps and chemical (i.e. protonation) steps and with the second reduction occurring at a potential more positive to that of the first one: reduction of the protonated **Co<sup>II</sup>** (**Co<sup>II</sup>LH**) state yields **Co<sup>I</sup>LH**, which is further protonated to yield the **Co<sup>III</sup>HLH** species. Further reduction of this derivative then produces the **Co<sup>II</sup>** hydride **Co<sup>II</sup>HLH** species that is further protonated to evolve H<sub>2</sub> and regenerate the starting **Co<sup>II</sup>LH** complex. Some of the



Scheme 1 Proposed ECEC mechanism for H<sub>2</sub> evolution mediated by **Cat1**. L and L' indicate acetonitrile or *p*-cyanoaniline.

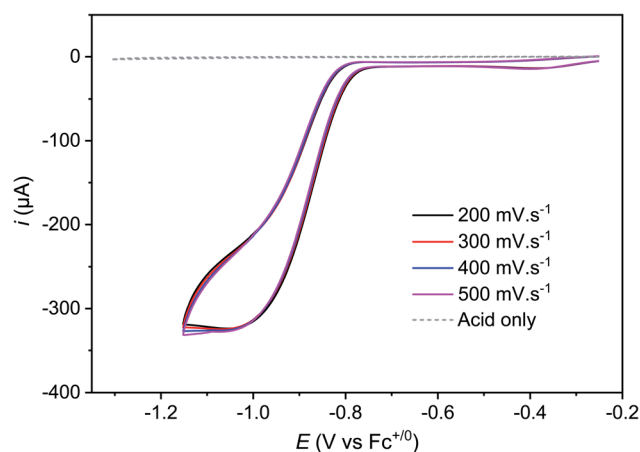


Fig. 4 Cyclic voltammograms of **Cat1** (1.6 mM) in CH<sub>3</sub>CN (+0.1 M <sup>t</sup>Bu<sub>4</sub>NBF<sub>4</sub>) recorded at a glassy carbon electrode (1.6 mm diameter) in the presence of 60 mM *p*-cyanoanilinium tetrafluoroborate at various scan rates, scan rate ranging from 200 to 500 mV s<sup>-1</sup> and with ohmic drop compensation. A control voltammogram of 60 mM *p*-cyanoanilinium tetrafluoroborate without **Cat1** at 100 mV s<sup>-1</sup> is shown for comparison.



distorted geometries displayed in Scheme 1 for transient intermediates involved in the catalytic cycle are approximate and we do realize that they do not correspond to ideal geometries for coordination complexes with corresponding electronic structures. Protonation of the amine residue of the macrocyclic ligand namely generates an ammonium moiety unable to coordinate the cobalt center, though with significant steric hindrance preventing for example the adoption of a perfect square planar (or octahedral) geometry favored by the  $d^8$  (or  $d^6$ ) configuration in the  $\text{Co}^{\text{I}}\text{LH}$  (or  $\text{Co}^{\text{III}}\text{HLH}$ ) species, as demonstrated for the unprotonated  $\text{Co}^{\text{I}}$  (ref. 14) or  $\text{Co}^{\text{III}}$ -hydride species,<sup>34</sup> respectively. Of note this family of cobalt complexes can accommodate various coordination spheres as demonstrated by the heptacoordinated systems recently reported.<sup>35,36</sup>

Eqn (1) gives the plateau current  $i_p$  for such a process, assuming that the two electrons required to complete catalytic turnover are transferred from the electrode to the catalyst.

$$i_{\text{pl}} = 2FS C_{\text{cat}}^0 \sqrt{k_2 D_{\text{cat}} C_{\text{AH}}^0} \quad (1)$$

where  $F$  is the Faraday constant,  $S$  is the geometric electrode surface area,  $C_{\text{cat}}^0$  is the concentration of the catalyst and  $D_{\text{cat}}$  is the diffusion coefficient of the catalyst, determined to be  $10^{-5} \text{ cm}^2 \text{ s}^{-1}$  from the scan-rate dependence of the peak current of the first cathodic wave and the Randles–Sevcik equation (see ESI†).

From plateau currents measured over a range of concentrations for both catalyst and acid (Fig. S6 and S7†), we found a value of  $5.3 \pm 0.1 \times 10^3 \text{ mol}^{-1} \text{ L s}^{-1}$  for the second order rate constant  $k_2$ . The rate constant for the first protonation step  $k_1$  of ECEC processes is accessible from the Foot-of-the-Wave Analysis (FOWA).<sup>37,38</sup> This analysis requires the knowledge of the apparent standard potential of the redox couple involved, *i.e.*  $\text{Co}^{\text{II}}\text{LH}/\text{Co}^{\text{I}}\text{LH}$ , which could be determined to  $-0.89 \text{ V vs. Fc}^+/\text{Fc}$  using high scan rates (Fig. 2 bottom). FOWA was performed at 3 different scan rates (100, 400 and  $1000 \text{ mV s}^{-1}$ ) for two different acid concentrations (5 and 25 mM) and gave a value of  $2.5 \pm 0.4 \times 10^4 \text{ mol}^{-1} \text{ L s}^{-1}$  for the second order rate constant  $k_1$  (Fig. S8†). The higher value of  $k_1$  compared to  $k_2$  is in line with the midwave of the catalytic process being shifted positively compared to the standard potential of the  $\text{Co}^{\text{II}}\text{LH}/\text{Co}^{\text{I}}\text{LH}$  couple.<sup>38</sup> Analysis of this shift using eqn (2) for the data shown in Fig. S6 and S7† also leads to an average value of  $2.5 \times 10^4 \text{ mol}^{-1} \text{ L s}^{-1}$  for the second order rate constant  $k_1$ , although with a much larger error margin.

$$E_{\text{cat}/2} = E_{\text{Co}^{\text{II}}\text{LH}/\text{Co}^{\text{I}}\text{LH}}^0 + \frac{RT}{2F} \ln \frac{k_1}{k_2} \quad (2)$$

The  $k_1$  value can finally be confirmed from the analysis of cyclic voltammograms recorded at low acid concentration where the system belongs to the “total catalysis” regime (Fig. 5).<sup>31,33</sup> In this regime, catalysis is so fast that all the acid present in the diffusion layer is consumed during the sweep of the catalytic wave. As a consequence, the unprotonated  $\text{Co}(\text{II})$  form of **Cat1** is regenerated after catalysis and its reduction is observed at  $-0.96 \text{ V vs. Fc}^+/\text{Fc}$ .

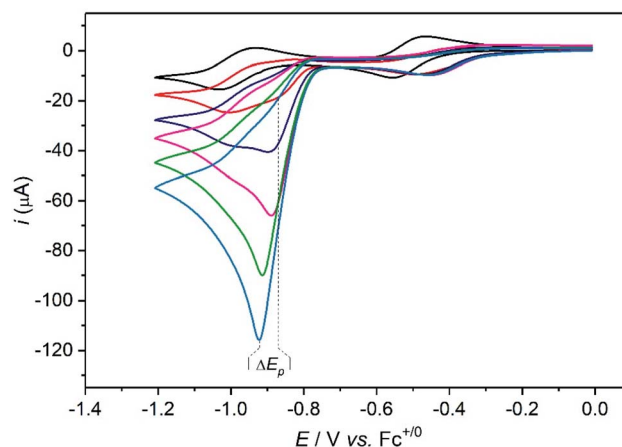


Fig. 5 Cyclic voltammograms of **Cat1** (2 mM) in  $\text{CH}_3\text{CN}$  (+0.1 M  $n\text{Bu}_4\text{NBF}_4$ ) recorded at a glassy carbon electrode (1.6 mm diameter) in the presence of various concentrations of *p*-cyanoanilinium tetrafluoroborate at  $100 \text{ mV s}^{-1}$ : 0 (black), 4 (red), 8 (navy), 12 (magenta), 16 (green), 20 (cyan) mM.

Based on simulations, Dempsey and coworkers could propose eqn (3) to describe the variation of the catalytic peak potential  $E_p$ .<sup>39</sup>

$$E_p = E_p^0 - 0.409 \frac{RT}{F} + \frac{RT}{2F} \ln \left( \frac{RT}{F_v} \frac{D_{\text{cat}}}{D_{\text{AH}}} \frac{k_1 (2C_{\text{cat}}^0)^2}{C_{\text{AH}}^0} \right) \quad (3)$$

As the intensity of the catalytic wave in the “total catalysis” regime is controlled by the diffusion of the acid, the  $D_{\text{cat}}/D_{\text{AH}}$  ratio between the diffusion coefficient of the catalyst and *p*-cyanoanilinium cation can be obtained from the ratio between the catalytic peak current and the current of the monoelectronic  $\text{Co}^{\text{II}}/\text{Co}^{\text{I}}$  wave measured in the absence of acid, according to eqn (4).

$$\frac{i_{\text{peak}}}{i_p^0} = 1.365 \frac{C_{\text{AH}}^0}{C_{\text{cat}}^0} \sqrt{\frac{D_{\text{AH}}}{D_{\text{cat}}}} \quad (4)$$

Applying eqn (3) to the data shown in Fig. 5 yields a  $k_1$  value of  $2.05 \pm 0.30 \times 10^4 \text{ mol}^{-1} \text{ L s}^{-1}$  for the second order rate constant  $k_1$ . This value is in good agreement with the one obtained by FOWA although neither  $k_1$  nor  $k_2$  comply with the condition of being greater than  $10^7 \text{ mol}^{-1} \text{ L s}^{-1}$  required for eqn (3) to be valid.<sup>39</sup>

Interestingly, these data allow ruling out homolytic  $\text{H}_2$  evolution mediated by **Cat1**. In such a mechanism, the first protonation step generating the  $\text{Co}^{\text{III}}\text{-H}$  derivative with the  $k_1$  rate constant still exists but it is followed by reductive elimination of  $\text{H}_2$  from two  $\text{Co}^{\text{III}}\text{-H}$  species with a  $k_d$  second-order rate constant. The linear dependency of the plateau current with the catalyst concentration (Fig. S6†) rules out homolytic  $\text{H}_2$  evolution from this  $\text{Co}^{\text{III}}\text{-H}$  derivative in the non-steady state where the rate-determining step is the reductive elimination step.<sup>38,40</sup> The identification of two distinct rate constants with  $k_1$  being the largest one also allows to rule out steady state



homolytic H<sub>2</sub> evolution with the rate-determining step being the formation of the Co<sup>III</sup>-H derivative, therefore implying that  $k_1 < k_4$ . Finally, while the mechanism proposed in Scheme 1 does not formally exclude that formation of the Co<sup>III</sup>HLH species may proceed through intramolecular protonation of the Co<sup>I</sup> center of Co<sup>I</sup>LH followed by reprotonation of the ligand, we believe that such a possibility is unlikely as Et<sub>3</sub>NH<sup>+</sup>, an acid with a pK<sub>a</sub> similar to that of the protonated N<sub>4</sub>H<sub>2</sub><sup>+</sup> ligand in Co<sup>I</sup>LH, is unable to protonate Co<sup>I</sup> complexes with similar  $E^0_{\text{Co}^{\text{II}}/\text{Co}^{\text{I}}}$  value such as [Co<sup>I</sup>(dmgBF<sub>2</sub>)<sub>2</sub>(CH<sub>3</sub>CN)] (dmgH<sub>2</sub> = dimethylglyoxime) in CH<sub>3</sub>CN.<sup>41</sup>

The mechanism proposed here for H<sub>2</sub> evolution differs from the one proposed by Llobet and Gimbert-Suriñach for aqueous conditions.<sup>13,14</sup> First we clearly evidenced that the Co<sup>II</sup> form of **Cat1** is protonated under the conditions investigated here. Ligand protonation also occurs in aqueous electrolyte, as shown by a 59 mV pH unit<sup>-1</sup> shift of the redox process reported by Peters and coworkers.<sup>19</sup> Second, we propose that H<sub>2</sub> is formed from a Co<sup>II</sup>-H and not a Co<sup>III</sup>-H intermediate. We recognize that the electrochemical responses of ECEC and ECCE sequences, both starting from a Co<sup>II</sup> derivative and implying Co<sup>II</sup>-H and Co<sup>III</sup>-H active species, respectively, are similar. However DFT calculations clearly demonstrated that the standard potential of the Co<sup>III</sup>-H/Co<sup>II</sup>-H is more positive than that of the Co<sup>II</sup>/Co<sup>I</sup> couple,<sup>13</sup> a feature also observed for cobaloximes and cobalt diimine-dioxime complexes for which the ECEC mechanism is now accepted. Importantly, the mechanism shown in Scheme 1 involves the Co<sup>II</sup>HLH species that was proposed by Llobet and Gimbert-Suriñach under photocatalytic conditions,<sup>13</sup> therefore unifying the mechanistic understanding of this catalyst. DFT calculations previously indicated a near-thermoneutral intramolecular H<sub>2</sub> evolution step from this protonated hydride intermediate.<sup>13</sup> Our analysis shows that this step is also the rate-determining one, which explains why catalysis is so fast. Still, the observation that the rate constant of this step is first order in acid concentration suggests that intramolecular H<sub>2</sub> formation is coupled with protonation, either in a concerted manner or through kinetic coupling with the fast reprotonation of the amine group of the ligand.

The maximal turnover frequency (TOF<sub>max</sub>) of **Cat1** therefore approximates  $k_2 \times [\text{acid}]$  and a TOF<sub>max</sub> value of  $5.3 \times 10^3 \text{ s}^{-1}$  can be extrapolated for 1 M *p*-cyanoanilinium tetrafluoroborate concentration. Based on this value and an apparent equilibrium potential of the H<sup>+</sup>/H<sub>2</sub> couple of -0.47 V vs. Fc<sup>+</sup>/Fc at 1 M *p*-cyanoanilinium tetrafluoroborate concentration and taking homoconjugation into account,<sup>26</sup> we could derive the red trace in the catalytic Tafel plot<sup>42,43</sup> shown in Fig. 6. Interestingly, **Cat1** displays significant catalytic activity ( $\log(\text{TOF}/\text{s}^{-1}) > 1$ ) at low overpotential values, a property shared by very few other molecular complexes including cobaloximes,<sup>42,44</sup> DuBois' nickel bisdiphosphine catalysts<sup>42,45</sup> and bis(thiosemicarbazone) cobalt<sup>46</sup> and nickel<sup>47</sup> complexes. Its overpotential requirement, estimated to be ~400 mV at the catalytic half-wave potential (and corresponding to the inflexion point in the red catalytic Tafel plot on Fig. 6) is ~100 mV higher than that of cobaloxime, cobalt diimine-dioxime<sup>48</sup> or DuBois' complexes. Importantly, the high TOF<sub>max</sub> value also places **Cat1** in an intermediate

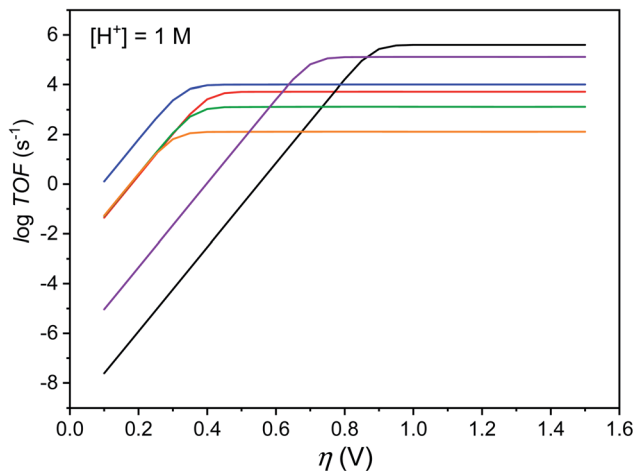


Fig. 6 Catalytic Tafel plots. Comparison of performances for H<sub>2</sub> evolution catalyzed by **Cat1** in CH<sub>3</sub>CN in the presence of 1 M *p*-cyanoanilinium (red line), with other catalysts reported in the literature: black: Fe<sup>II</sup>TPP, DMF, Et<sub>3</sub>NH<sup>+</sup>; <sup>42,49</sup> blue: Co<sup>II</sup>(dmgH)<sub>2</sub>py, DMF, Et<sub>3</sub>NH<sup>+</sup>; <sup>42</sup> green: [Ni<sup>II</sup>(P<sup>Ph</sup><sub>2</sub>N<sub>2</sub>C<sub>6</sub>H<sub>4</sub>X)<sub>2</sub>]<sup>2+</sup>, X = CH<sub>2</sub>P(O)(OEt)<sub>2</sub>, MeCN, DMFH<sup>+</sup>; <sup>42,45</sup> orange: 4-bis(4-(*p*-methoxyphenyl)thiosemicarbazone)-2,3-butane cobalt, DMF, Et<sub>3</sub>NH<sup>+</sup>; <sup>46</sup> purple: [Co<sup>II</sup>(bapbpy)Cl], DMF, Et<sub>3</sub>NH<sup>+</sup>. <sup>23</sup>

position between cobaloximes and DuBois' complexes, the two champion H<sub>2</sub>-evolving molecular catalyst series identified so far in non-aqueous solvents.<sup>42</sup> It is noteworthy that all three catalysts possess proton relays in their second-coordination sphere and the protonation of these relays is coupled with the metal-centered reduction step that sets the potential of the catalytic wave. The same conclusion can be reached with thiosemicarbazone nickel and cobalt complexes, with ligand-centered reduction occurring in these cases at quite positive potentials.<sup>46,47</sup>

## Conclusions

While **Cat1** is becoming more and more popular as a molecular H<sub>2</sub>-evolving catalyst for the design of aqueous systems, it is increasingly important to advance the understanding of its H<sub>2</sub> evolution catalysis mechanism<sup>13</sup> and performance by providing insight into the catalytic steps involved. This is especially the case when considering structural modification<sup>50</sup> or molecular engineering<sup>51</sup> in order to either enhance catalytic activity or stability<sup>16</sup> or immobilise a catalytic centre for integration in photoelectrodes<sup>7-9</sup> or devices. In the societal context, both of these objectives are ultimately necessary to achieve industrial relevancy and technological maturity of hydrogen-producing electrolyzers based on molecular catalysts made from earth-abundant elements.<sup>2,4</sup>

In this study, new EPR evidence for the structure of the Co<sup>II</sup> state of the catalyst and its dependence on the presence and nature of the acid has been presented, as well as NMR and cyclic voltammetry data indicating that fast protonation of the ligand occurs at the Co<sup>II</sup> stage. Carrying on from previous work in the literature,<sup>13,14,22</sup> these results reconcile mechanisms at play under electrochemical and photochemical conditions.



Furthermore, a proper utilisation of the most advanced analytical methods available for molecular catalysis of electrochemical reactions has allowed definitively ruling out a homolytic H<sub>2</sub> evolution mechanism and substantiated the proposed heterolytic ECEC mechanism, for which the rate constants for the two successive protonation steps could be determined. The rate-determining step has been confirmed as the intramolecular H<sub>2</sub> evolution step, surmised to be coupled to the second protonation, thereby regenerating a protonated ligand and thus acting as a proton relay in catalysis,<sup>32</sup> which, interestingly, is at variance with the behaviour of the dioxime bridge in cobalt diimine–dioxime complexes.<sup>48</sup> Catalytic Tafel plots could be derived to enable the benchmarking of the H<sub>2</sub> evolution performance of Cat1 alongside other highly efficient catalysts and confirm its place on the podium.

## Conflicts of interest

There are no conflicts to declare.

## Acknowledgements

This work received funding from the French National Research Agency (Labex ARCANE, CBH-EUR-GS, ANR-17-EURE-0003), the European Research Council and European Commission's Seventh Framework Program (FP7/2007–2013) under grant agreement no. 306398 (project PhotocatH<sub>2</sub>ode), the European Union's Horizon 2020 Research and Innovation program under grant agreement no. 765376 (eSCALED Marie Curie ITN project). C.-B. L. acknowledges support from the Chinese Scientific Council for a post-doctoral scholarship.

## References

- V. Artero, M. Chavarot-Kerlidou and M. Fontecave, *Angew. Chem., Int. Ed.*, 2011, **50**, 7238–7266.
- J. R. McKone, S. C. Marinescu, B. S. Brunschwig, J. R. Winkler and H. B. Gray, *Chem. Sci.*, 2014, **5**, 865–878.
- N. Queyriaux, R. T. Jane, J. Massin, V. Artero and M. Chavarot-Kerlidou, *Coord. Chem. Rev.*, 2015, **304–305**, 3–19.
- L. Tong, L. Duan, A. Zhou and R. P. Thummel, *Coord. Chem. Rev.*, 2020, **402**, 213079.
- V. S. Thoi, Y. J. Sun, J. R. Long and C. J. Chang, *Chem. Soc. Rev.*, 2013, **42**, 2388–2400.
- J. L. Karn and D. H. Busch, *Nature*, 1966, **211**, 160–162.
- S. Bold, J. Massin, E. Giannoudis, M. Koepf, V. Artero, B. Dietzek and M. Chavarot-Kerlidou, *ACS Catal.*, 2021, **11**, 3662–3678.
- C. Nie, W. Ni, L. Gong, J. Jiang, J. Wang and M. Wang, *J. Mater. Chem. A*, 2019, **7**, 27432–27440.
- C. Nie, C. Liu, L. Gong and M. Wang, *J. Mater. Chem. A*, 2021, **9**, 234–238.
- R. Gueret, C. E. Castillo, M. Rebarz, F. Thomas, A. A. Hargrove, J. Pecaout, M. Sliwa, J. Fortage and M. N. Collomb, *J. Photochem. Photobiol., B*, 2015, **152**, 82–94.
- S. Varma, C. E. Castillo, T. Stoll, J. Fortage, A. G. Blackman, F. Molton, A. Deronzier and M. N. Collomb, *Phys. Chem. Chem. Phys.*, 2013, **15**, 17544–17552.
- C. Gimbert-Surinach, J. Albero, T. Stoll, J. Fortage, M. N. Collomb, A. Deronzier, E. Palomares and A. Llobet, *J. Am. Chem. Soc.*, 2014, **136**, 7655–7661.
- S. Grau, M. Schilling, D. Moonshiram, J. Benet-Buchholz, S. Luber, A. Llobet and C. Gimbert-Surinach, *ChemSusChem*, 2020, **13**, 2745–2752.
- D. Moonshiram, C. Gimbert-Surinach, A. Guda, A. Picon, C. S. Lehmann, X. Zhang, G. Doumy, A. M. March, J. Benet-Buchholz, A. Soldatov, A. Llobet and S. H. Southworth, *J. Am. Chem. Soc.*, 2016, **138**, 10586–10596.
- C. H. Lee, D. Villagran, T. R. Cook, J. C. Peters and D. G. Nocera, *ChemSusChem*, 2013, **6**, 1541–1544.
- M. Sandroni, R. Gueret, K. D. Wegner, P. Reiss, J. Fortage, D. Aldakov and M. N. Collomb, *Energy Environ. Sci.*, 2018, **11**, 1752–1761.
- R. Gueret, L. Poulard, M. Oshinowo, J. Chauvin, M. Dahmane, G. Dupeyre, P. P. Laine, J. Fortage and M. N. Collomb, *ACS Catal.*, 2018, **8**, 3792–3802.
- S. Roy, M. Bacchi, G. Berggren and V. Artero, *ChemSusChem*, 2015, **8**, 3632–3638.
- C. C. L. McCrory, C. Uyeda and J. C. Peters, *J. Am. Chem. Soc.*, 2012, **134**, 3164–3170.
- N. Kaeffer, A. Morozan, J. Fize, E. Martinez, L. Guetaz and V. Artero, *ACS Catal.*, 2016, **6**, 3727–3737.
- V. Artero and M. Fontecave, *Chem. Soc. Rev.*, 2013, **42**, 2338–2356.
- C. F. Leung, Y. Z. Chen, H. Q. Yu, S. M. Yiu, C. C. Ko and T. C. Lau, *Int. J. Hydrogen Energy*, 2011, **36**, 11640–11645.
- N. Queyriaux, D. Y. Sun, J. Fize, J. Pecaout, M. J. Field, M. Chavarot-Kerlidou and V. Artero, *J. Am. Chem. Soc.*, 2020, **142**, 274–282.
- C. Römelt, T. Weyhermüller and K. Wieghardt, *Coord. Chem. Rev.*, 2019, **380**, 287–317.
- A. M. Appel, S. J. Lee, J. A. Franz, D. L. DuBois, M. R. DuBois and B. Twamley, *Organometallics*, 2009, **28**, 749–754.
- V. Fourmond, P. A. Jacques, M. Fontecave and V. Artero, *Inorg. Chem.*, 2010, **49**, 10338–10347.
- J. Niklas, K. L. Mardis, R. R. Rakhimov, K. L. Mulfort, D. M. Tiede and O. G. Poluektov, *J. Phys. Chem. B*, 2012, **116**, 2943–2957.
- T. Arcos, B. de Castro, M. J. Ferreira, M. Rangel and J. B. Raynor, *J. Chem. Soc., Dalton Trans.*, 1994, 369–377.
- A. Bakac and J. H. Espenson, *J. Am. Chem. Soc.*, 1984, **106**, 5197–5202.
- A. Bhattacharjee, E. S. Andreiadis, M. Chavarot-Kerlidou, M. Fontecave, M. J. Field and V. Artero, *Chem.–Eur. J.*, 2013, **19**, 15166–15174.
- J. M. Savéant, *Elements of Molecular and Biomolecular Electrochemistry*, Wiley, 2006.
- J. M. Saveant, *Angew. Chem., Int. Ed.*, 2019, **58**, 2125–2128.
- J. M. Saveant and K. B. Su, *J. Electroanal. Chem.*, 1984, **171**, 341–349.
- A. F. M. M. Rahman, W. G. Jackson, A. C. Willis and A. D. Rae, *Chem. Commun.*, 2003, 2748–2749.



- 35 J.-W. Wang, K. Yamauchi, H.-H. Huang, J.-K. Sun, Z.-M. Luo, D.-C. Zhong, T.-B. Lu and K. Sakai, *Angew. Chem., Int. Ed.*, 2019, **58**, 10923–10927.
- 36 R. Gueret, C. E. Castillo, M. Rebarz, F. Thomas, M. Sliwa, J. Chauvin, B. Dautreppe, J. Pécaut, J. Fortage and M.-N. Collomb, *Inorg. Chem.*, 2019, **58**, 9043–9056.
- 37 C. Costentin, S. Drouet, M. Robert and J.-M. Savéant, *J. Am. Chem. Soc.*, 2012, **134**, 11235–11242.
- 38 C. Costentin and J.-M. Savéant, *ChemElectroChem*, 2014, **1**, 1226–1236.
- 39 E. S. Rountree, D. J. Martin, B. D. McCarthy and J. L. Dempsey, *ACS Catal.*, 2016, **6**, 3326–3335.
- 40 C. Costentin, H. Dridi and J.-M. Savéant, *J. Am. Chem. Soc.*, 2014, **136**, 13727–13734.
- 41 C. Baffert, V. Artero and M. Fontecave, *Inorg. Chem.*, 2007, **46**, 1817–1824.
- 42 V. Artero and J.-M. Saveant, *Energy Environ. Sci.*, 2014, **7**, 3808–3814.
- 43 C. Costentin, S. Drouet, M. Robert and J. M. Saveant, *Science*, 2012, **338**, 90–94.
- 44 M. Razavet, V. Artero and M. Fontecave, *Inorg. Chem.*, 2005, **44**, 4786–4795.
- 45 U. J. Kilgore, J. A. S. Roberts, D. H. Pool, A. M. Appel, M. P. Stewart, M. R. DuBois, W. G. Dougherty, W. S. Kassel, R. M. Bullock and D. L. DuBois, *J. Am. Chem. Soc.*, 2011, **133**, 5861–5872.
- 46 T. Straistari, R. Hardre, J. Fize, S. Shova, M. Giorgi, M. Reglier, V. Artero and M. Orio, *Chem.–Eur. J.*, 2018, **24**, 8779–8786.
- 47 T. Straistari, J. Fize, S. Shova, M. Réglier, V. Artero and M. Orio, *ChemCatChem*, 2016, 2262–2268.
- 48 D. Sun, A. K. Harshan, J. Pecaut, S. Hammes-Schiffer, C. Costentin and V. Artero, *Chemelectrochem*, 2021, **8**, 2671–2679.
- 49 I. Bhugun, D. Lexa and J. M. Saveant, *J. Am. Chem. Soc.*, 1996, **118**, 3982–3983.
- 50 W. X. Nie, D. E. Tarnopol and C. C. L. McCrory, *J. Am. Chem. Soc.*, 2021, **143**, 3764–3778.
- 51 N. Coutard, N. Kaeffer and V. Artero, *Chem. Commun.*, 2016, **52**, 13728–13748.



# Molecular engineering of electrocatalytic nanomaterials for hydrogen evolution based on a cobalt tetraazamacrocyclic catalyst

Andrew J. Bagnall,<sup>1,2</sup> Matthieu Haake,<sup>1</sup> Sergi Grau-Abarca,<sup>3</sup> Navid Jameei Moghaddam,<sup>3</sup> Tatiana Straistari,<sup>1</sup> Matthieu Koepf,<sup>1</sup> Carolina Gimbert-Suriñach,<sup>3,4</sup> Antoni Llobet,<sup>4,5</sup> Leif Hammarström,<sup>2</sup> Murielle Chavarot-Kerlidou,<sup>1</sup> Bertrand Reuillard,<sup>1\*</sup> and Vincent Artero<sup>1</sup>

<sup>1</sup>Univ. Grenoble Alpes, CNRS, CEA, IRIG, Laboratoire de Chimie et Biologie des Métaux, 17 rue des Martyrs, F-38054 Grenoble, Cedex, France; [vincent.artero@cea.fr](mailto:vincent.artero@cea.fr)

<sup>2</sup>Ångström Laboratory, Department of Chemistry, Uppsala University, SE75120 Uppsala, Sweden

<sup>3</sup>Universitat Autònoma de Barcelona (UAB), 08193 Barcelona, Catalonia, Spain

<sup>4</sup>Institute of Chemical Research of Catalonia (ICIQ), Barcelona Institute of Science and Technology (BIST) Av. Països Catalans 16, 43007, Tarragona, Spain

<sup>5</sup>Department de Química Universitat Autònoma de Barcelona Cerdanyola del Vallès, 08193 Barcelona, Spain

---

## Abstract (*Abstract Heading*)

Molecular catalysts might represent an interesting alternative to expensive metal cathodes for the production of green hydrogen. In particular, the modularity of their structure allows fine understanding of their catalytic properties. In this work we study the non-covalent integration of two macrocyclic cobalt complexes and their different activity toward the electrocatalytic production of H<sub>2</sub> in aqueous conditions. We show that the nature of the coordinating amine in the macrocycle plays an important role on the activity towards H<sub>2</sub> production but also on the stability of the electrocatalytic response.

Keywords: *hydrogen, electrocatalysis, molecular catalyst, solar fuels, carbon nanotubes*

## Introduction

The necessary global energy transition towards the use of sustainable energy sources is driving a push for the production of clean fuels able to conveniently and efficiently store the harvested renewable but intermittent energy. Currently, Hydrogen ( $H_2$ ) represents one of the most promising potential solar fuels, due to its high energy density per mass, relative simplicity to produce from an abundant resource and re-conversion to electricity when combined with oxygen in fuel cells to produce only water as a by-product.<sup>1</sup> Sustainable and scalable production of  $H_2$  from electrolyzers will require the development of efficient and stable catalysts based on broadly available materials,<sup>2,3</sup> and their effective incorporation into integrated systems.<sup>4,5</sup> Currently however, most electrolyser technology still heavily relies on the use of scarce platinum-group metals (PGMs) as  $H_2$  production and  $H_2O$  oxidation catalysts.<sup>6–11</sup>

The use of molecular catalysts represents a strategy which can enable the replacement of PGMs with earth-abundant first-row transition metals, by binding them within a specifically designed coordination sphere. This field of research has been very active over the past two decades and the development of such catalysts has been thoroughly reported in the literature.<sup>12,13</sup> Through molecular engineering, it is possible to optimise the catalytic activity, selectivity and stability of the metal-centred active site, by tuning the critical steric and electronic effects from the inner and outer coordination spheres.<sup>14–16</sup> From this work, a number of  $H_2$ -producing catalyst families have emerged, which include the DuBois nickel bisdiphosphine catalysts,<sup>17–19</sup> FeFe hydrogenase mimics,<sup>20–24</sup> cobaloximes,<sup>18,25–28</sup> cobalt diimine-dioximes,<sup>28–31</sup> and many others.<sup>32–38</sup>

$[Co(N_4H)Cl_2]^+$  (**1**) is a cobalt tetraazamacrocyclic complex which is an effective catalyst for the hydrogen evolution reaction (HER) in organic solvents, as well as in fully aqueous conditions.<sup>30,39–42</sup> Although it structurally bears much similarity to other cobalt tetraazamacrocyclic HER catalysts,<sup>28</sup> the performances of **1** match those of the best reported molecular catalysts, such as the DuBois catalyst in organic homogeneous conditions, with a maximal turnover frequency ( $TOF_{max}$ ) of  $5.3 \times 10^3 \text{ s}^{-1}$  in MeCN,<sup>39</sup> with reasonable stability: **1** has been reported to reach turnover numbers (TONs) of up to 7700 in aqueous photocatalytic conditions,<sup>43</sup> all at a moderate overpotential requirement.

It was postulated that the specific structure of the macrocyclic ligand, based on the pyridyldiimine (PDI) redox active core, plays a key role in the catalyst's stability against decomposition.<sup>40,41</sup> Specifically, it prevents potential hydrolysis, which often occurs in acidic conditions, and the decoordination of the cobalt centre at low oxidation states, observed for more simple bidentate ligands systems.<sup>13</sup> The latter point is an important feature as the lower coordination number in the formal Co(I) oxidation state is key to enable the binding of one substrate proton to generate a reactive hydride ligand. Furthermore, it has been proposed that the macrocycle's amine moiety can act as a proton relay, increasing the rate of key catalytic steps by controlled shuttling of protons.<sup>39,44</sup> In addition, **1** has previously shown reasonable tolerance to  $O_2$ , an important factor for stability in water splitting devices.<sup>45</sup>

Recently **1** has received a lot of interest because of its potential for structural modification to optimise its catalytic properties for the HER<sup>44,46</sup> and the related carbon dioxide reduction reaction ( $CO_2RR$ ),<sup>47</sup> and to immobilise it on photosensitisers to construct photocatalytic systems.<sup>48–51</sup> So far however, immobilisation of derivatives of **1** onto electrodes for direct electrocatalytic production of  $H_2$  in water have not yet been reported. Integration of such molecular catalysts at cathode surfaces represents a major practical requirement to develop useful, stable and scalable molecular materials for electrolyzers.<sup>12,52,53</sup> In addition, the selection of appropriate electrode materials is important for the integration of the  $H_2$ -evolving catalysts into devices. Multiwalled carbon nanotubes (MWCNTs) represent a very convenient choice of electrode material for molecular electrocatalysis applications due to their very highly developed surfaces and excellent conductivity which allow a high surface loading of active centres to be achieved without loss of electron transfer efficiency between the pi-conjugated surface and the catalyst.<sup>54,55</sup> Moreover, their surface can be chemically modified by numerous covalent or non-covalent strategies them versatile nanoplatforms for molecular catalyst integration.<sup>56</sup> In particular, in recent years, non-covalent modification of MWCNTs with pyrene group-bearing molecular catalysts has been widely employed as a smooth and efficient approach to

carry out numerous electrocatalytic processes such as H<sub>2</sub> evolution<sup>57,58</sup> and oxidation,<sup>59,60</sup> CO<sub>2</sub> reduction<sup>61–63</sup> and even water oxidation.<sup>64–66</sup>

An additional consideration for device engineering is scalability and mass production. For larger-scale manufacturing, carbon-based printed electronics utilising printing techniques that can eventually be scaled up by being adapted to e.g. roll-to-roll processing may represent a promising strategy for the construction of electrodes for a device.<sup>67</sup>

In this work we describe the development of original derivatives of **1**, functionalised with pyrene anchoring groups to allow their immobilisation at the surface of MWCNTs based electrodes (**2** and **3**, Figure 1).

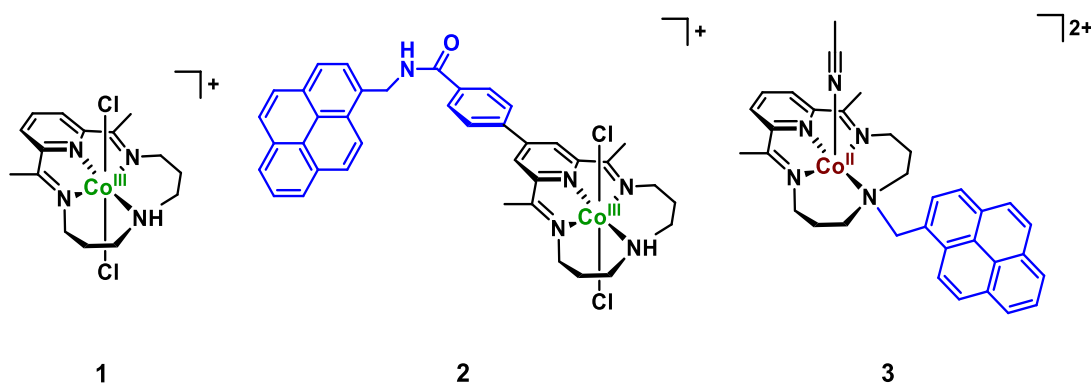


Figure 1: Chemical structures of **1**, **2** and **3** in their air-stable oxidation states when isolated as solids.

**2** was functionalised with a pyrene moiety through a rigid benzamidomethyl bridge bound to the *para*-position of the macrocycle pyridine, whereas **3** was functionalised analogously through a methylene bridge bound to the amine on the opposite side of the macrocycle. This key distinction between the complexes allows one to study the impact of the incorporation of the anchoring group in the ligand scaffold upon the catalytic activity. More specifically, it enables one to draw further conclusions on the role of the proton at the cyclic amine on the protonation of the reduced metal and the Co-hydride intermediate. Moreover, this underscores rational design principles regarding the significance of carefully selecting the positions for appendage of additional moieties on the basis of which functional groups play critical roles in the catalytic mechanism, while also considering the length and rigidity of bridge to the anchoring group, which can potentially affect the mobility of the catalyst bound on the surface and the accessibility of its coordination sites, as well as the strength of electronic coupling of the metal to the carbon electrode surface, which may be an important factor.<sup>68–70</sup>

## Results and Discussion

**Synthesis and characterisation of complexes 2 and 3.** Complex **2** was synthesised in 6 consecutive steps, starting from commercial chelidamic acid, with an overall yield of 30% (see experimental part for synthetic details). Functionalisation at the *para* position of the pyridine ring was achieved by a palladium-catalysed cross-coupling reaction prior to the templated synthesis of the catalytic core, followed by an amide coupling with 1-pyrenemethylamine to yield the pyrene-appended catalyst **2**. The synthetic route to pyrene-appended complex **3** involved preparing the triamine with a 1-pyrenemethyl group on the central amine, before templated macrocyclisation. Both complexes were fully characterised, where possible, using NMR/EPR, UV-vis and IR spectroscopy techniques as well as high resolution mass spectrometry. Full synthetic details and characterisations are provided in the Supporting Information.

Prior to electrode integration, the electrochemical properties of the new complexes **2** and **3** were first characterised in organic solvent to evaluate the impact of the integration of the pyrene anchors on the redox properties of the Co centre and the ligand. Cyclic voltammetry (CV) experiments were performed in dry and degassed *N,N*-dimethylformamide (DMF) (Figure 2, Table S1).



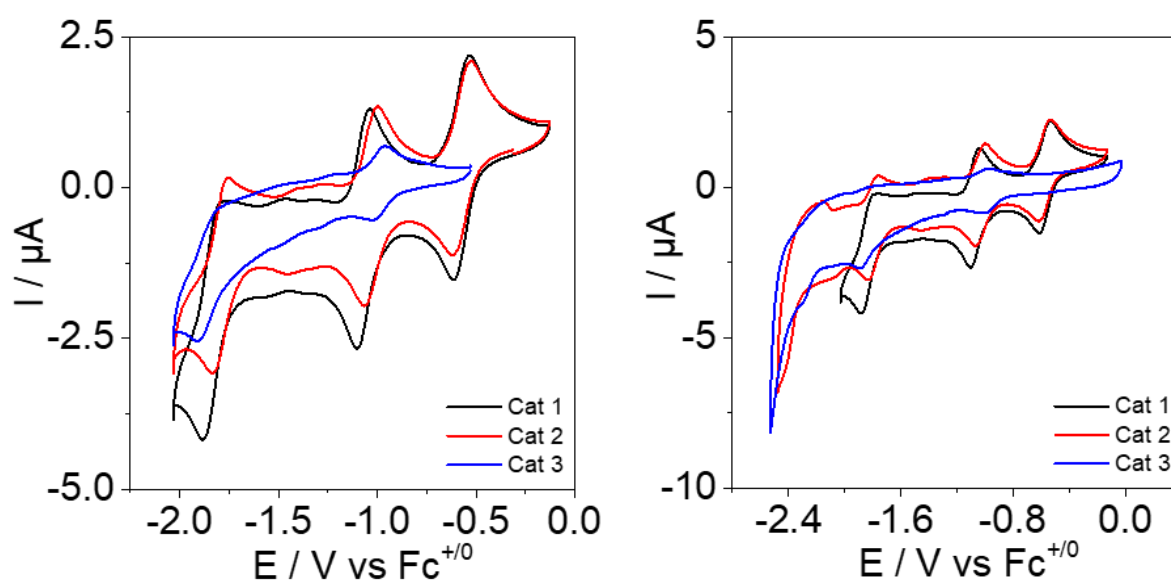


Figure 2: Voltammograms of each catalyst dissolved in degassed DMF.

CV of the complex **1** allows to observe two reversible redox events at  $E_{1/2} = -0.57$  and  $-1.07$  V vs  $\text{Fc}^{+/0}$  which were attributed to the  $\text{Co}^{3+/2+}$  and  $\text{Co}^{2+/+}$  redox couple, respectively, followed by a third quasi reversible redox process at  $E_{1/2} = -1.83$  V vs  $\text{Fc}^{+/0}$  which was attributed to the PDI redox active ligand, close to the previously reported potential for the similar dibromide complex in acetonitrile.<sup>71</sup> CV of complex **2** showcases a very similar redox signature with redox processes at  $E_{1/2} = -0.57$  and  $-1.03$  V vs  $\text{Fc}^{+/0}$  attributed to the  $\text{Co}^{3+/2+}$  and  $\text{Co}^{2+/+}$  redox couple, respectively, as well as a third quasi reversible system at  $E_{1/2} = -1.79$  V vs  $\text{Fc}^{+/0}$  of the modified PDI moiety. The slight anodic shift of the redox potential of the  $\text{Co}^{2+/+}$  and PDI/PDI<sup>-</sup> redox couples observed between complex **1** and **2** can be explained by the change of electronic density at the PDI moiety and at the metal stemming from the *para* substitution of the pyridine ligand with the phenyl group bearing the anchoring unit. This trend was observed recently on parent Co complexes.<sup>47</sup> Complex **3** showed only one Co-centred redox process, at  $E_{1/2} = -0.98$  V vs  $\text{Fc}^{+/0}$ , assigned to the  $\text{Co}^{2+/+}$  redox couple while the redox system at  $E_{1/2} = -1.86$  V vs  $\text{Fc}^{+/0}$  is attributed to the PDI/PDI<sup>-</sup>, very close to the potentials described for the same complex without the pyrene anchor.<sup>44</sup> The catalytic properties of the three complexes were then investigated in the presence of trifluoroacetic acid (TFA, 10 mM), using CV (Figure S2). In the presence of a strong  $\text{H}^+$  source, all complexes exhibit a strong catalytic wave which is attributed to the electrocatalytic reduction of protons to  $\text{H}_2$  as previously shown for this family of complexes. Similar “plateau” currents, around 30  $\mu\text{A}$ , are obtained for all three complexes with half wave potentials of  $E_{\text{cat}/2} = -1.77$ ,  $-1.78$  and  $-1.85$  V vs  $\text{Fc}^{+/0}$  for complexes **1**, **2** and **3**, respectively. These observations indicate that the structural modifications of the ligand, whether on the PDI moiety or on the cyclic amine, following the integration of the pyrene anchors only moderately modify the catalytic properties of the catalyst in homogeneous conditions and in presence of a strong acid.

To further investigate the behaviour of the catalysts once immobilised onto MWCNTs (Figure 3a), modified electrodes were prepared by dropcasting a standard 3 mg/mL dispersion of MWCNTs in EtOH onto 1.6 mm diameter glassy carbon (GC) discs (full head-surface diameter: 6.0 mm). After drying of the MWCNTs deposit, the electrode was immersed in 10 mM solutions of the catalysts in DMF. The modified electrode was then rinsed with DMF to remove unbound catalyst and then with  $\text{H}_2\text{O}$  to remove traces of DMF (Figure S3). The redox properties of the surface bound complexes were first studied using CV in aqueous media in 0.1 M potassium phosphate buffer at pH 7 (Figure 3b, Figure S4-S7).

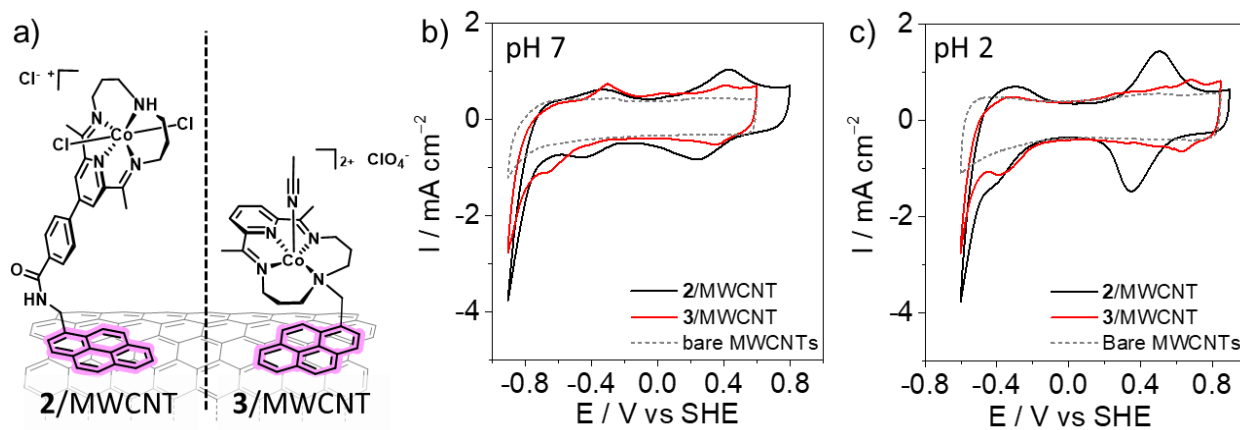


Figure 3 : a) Schematic representation of the complex **2** (left) and **3** (right) immobilised onto MWCNTs b) CVs of **2**/MWCNTs (black line) and **3**/MWCNTs (red line) modified electrodes in potassium phosphate buffer 0.1 M pH 7 and c) CVs of **2**/MWCNTs (black line) and **3**/MWCNTs (red line) modified electrodes in KCl/HCl 0.1 M pH 2, under argon and at 25°C ( $v = 0.1 \text{ mV s}^{-1}$ )

For both modified electrodes, CV measurements showed one well-defined reversible peak system corresponding to the  $\text{Co}^{3+/2+}$  redox process at  $E_{1/2} = 0.31 \text{ V vs SHE}$  ( $\Delta E_p = 180 \text{ mV}$ ) and  $E_{1/2} = 0.39 \text{ V vs SHE}$  ( $\Delta E_p = 50 \text{ mV}$ ), **2**/MWCNT and **3**/MWCNT, respectively (Figure 3b). Analogously to the solution study, the CVs of complex **3**/MWCNT showed much lower peak intensity. The larger peak-to-peak separation observed with complex **2** could be rationalised by the potential decoordination of a  $\text{Cl}^-$  ligand. For both complexes, linear dependency of the peak current with the scan rate could be observed at least until  $0.2 \text{ V s}^{-1}$ , as expected from surface confined redox processes (Figures S4 and S5). The integration of the  $\text{Co}^{2+}$  to  $\text{Co}^{3+}$  oxidation wave typically allows the quantification of the amount of electrochemically active complex grafted at the electrode surface through the conversion of the charged passed into a surface loading, according to equation (1):

$$\Gamma_{\text{Co}} = \frac{q}{nFS} \quad (1)$$

Where  $\Gamma_{\text{Co}}$  is the amount of complex grafted at the surface of the electrode ( $\text{mol cm}^{-2}$ ),  $q$  is the charged passed during the oxidation process (C),  $n$  is the number of electrons involved (one, here),  $F$  is the Faraday constant ( $96485 \text{ C mol}^{-1}$ ) and  $S$  is the geometrical surface of the electrode ( $\text{cm}^2$ ). From this, the surface concentration of complex **2** was calculated to be  $17.0 \pm 1 \text{ nmol cm}^{-2}$ , while a much lower coverage of  $1.2 \pm 0.4 \text{ nmol cm}^{-2}$  was obtained for complex **3**.

When scanning **2**/MWCNT at more negative potentials an additional reversible redox process could be observed at  $E_{1/2} = -0.39 \text{ V vs SHE}$  ( $\Delta E_p = 120 \text{ mV}$ ) which was attributed to the  $\text{Co}^{2+/+}$  redox couple. For **3**/MWCNT a poorly reversible redox system could be observed at  $E_{1/2} = -0.48 \text{ V vs SHE}$  ( $\Delta E_p = 360 \text{ mV}$ ), also assigned to the reduction of  $\text{Co}^{2+}$  to  $\text{Co}^+$  (Figure 3b). Below these potentials, a sharp current increase could be observed, larger for **2**/MWCNT, which was postulated to arise from the electrocatalytic proton reduction by the grafted catalysts (Figure 3b). As a reference, the same non-functionalised MWCNT electrode showed only a very small current increase.

From previous work performed in homogeneous conditions, it is expected that the core ligand system of **1** tolerates acidic conditions while allowing improved hydrogen evolution activity.<sup>30,42,44</sup> Thus, similar CVs experiments were therefore performed on **2**/MWCNTs and **3**/MWCNTs at more acidic pH to probe the potential changes in behaviour of the Co-centred redox activity as well as the activity towards proton reduction (Figure 3c). In these more acidic conditions (pH 2),  $\text{Co}^{3+/2+}$  redox couples of both complex **2** and **3** shifted towards more anodic potentials, to  $E_{1/2} = 0.43 \text{ V vs SHE}$  ( $\Delta E_p = 150 \text{ mV}$ ) and  $E_{1/2} = 0.67 \text{ V vs SHE}$  ( $\Delta E_p = 60 \text{ mV}$ ), respectively. As observed at neutral pH, the peak-to-peak separation is larger for **2**. As expected, the peak current intensity measured at pH 2 also varied linearly with the scan rate for both **2**/MWCNT and **3**/MWCNT up to  $0.2 \text{ V s}^{-1}$  (Figure S6 and S7). Interestingly, the potential shift observed for complex **3** follows a  $56 \text{ mV/pH}$  slope, indicating a proton-coupled electron transfer, while the shift is

only of 20 mV/pH for complex **2** (Figure S8). Another striking difference is the peak intensity change between measurements at pH 2 and pH 7 for complex **2**. At pH 2, the apparent electrochemically measured loading rises to  $24.0 \pm 2.0 \text{ nmol cm}^{-2}$  for complex **2**, corresponding to a 41% increase compared to what was observed at pH 7. By comparison, surface loadings of  $1.4 \pm 0.1 \text{ nmol cm}^{-2}$  were measured for complex **3**, with only a modest increase compared to the values obtained at pH 7. The  $\text{Co}^{2+/+}$  redox couples are only moderately affected by the change in pH, with anodic shifts of 50 mV and 120 mV for **2** and **3**, respectively, hinting that this redox event does not involve an associated proton transfer (Figure S8). At pH 2, a catalytic wave attributed to the electrocatalytic reduction can also be observed at about  $-0.45 \text{ V vs SHE}$ , for both **2**/MWCNT and **3**/MWCNT. Interestingly, for both complexes, at neutral or acidic pH, this catalytic wave occurs beyond the  $\text{Co}^{2+/+}$  redox couples, whereas previous literature described the  $\text{Co}^+$  state as sufficiently reducing  $\text{H}^+$  in acidic organic media.<sup>39,44</sup> This hints that an extra electron is necessary to initiate catalysis in aqueous media, thereby forming a formal  $\text{Co}^0$  complex, with the electron located either at the metal or the redox active PDI ligand, similarly to previously described molecular systems.<sup>72,73</sup> Previous attempts by Lacy et al. to isolate  $\text{Co}^0$  forms of **1** after chemical reduction in organic medium showed that it reverts to a  $\text{Co}^+$  form by deprotonation of the macrocycle amine to an inorganic amide.<sup>71</sup> This would indicate that a  $\text{Co}^0$  intermediate would be unstable but highly catalytically active for the HER. In general, the CV responses for immobilised **3** tend to be more complicated than those obtained with **2**. This may be expected, as it is known for similar complexes that modifications at the amine position impact the electrochemical and catalytic behaviour of the active site.<sup>44</sup>

In order to confirm the nature of the catalytic wave observed and benchmark the activity of **2**/MWCNT and **3**/MWCNT towards the electrocatalytic production of  $\text{H}_2$ , controlled potential electrolysis (CPE) was performed using a two-compartment cell, in both neutral and acidic conditions at potentials where the catalytic wave can be observed (Figure 4).

At pH 2 and at  $E_{\text{app}} = -0.6 \text{ V vs SHE}$ , a drastically different current response can be observed for **2**/MWCNT and **3**/MWCNT (Figure 4a, Figure S9). **2**/MWCNT shows initial currents of about  $-2.5 \text{ mA cm}^{-2}$  steadily decreasing to  $-1.0 \pm 0.2 \text{ mA cm}^{-2}$  over the course of an hour, while **3**/MWCNT displays lower initial currents of about  $-1.5 \text{ mA cm}^{-2}$  sharply decaying to below  $-0.5 \text{ mA cm}^{-2}$  within few minutes and reaching the same current value as a bare MWCNT electrode ( $-0.2 \pm 0.1 \text{ mA cm}^{-2}$ ) after one hour. Sampling the headspace of the working electrode compartment,  $\text{H}_2$  could be quantified using gas chromatography (Figure 4b). In these conditions (pH 2), a relatively stable  $\text{H}_2$  production rate could be observed with  $23.9 \pm 5.3 \mu\text{mol cm}^{-2}$  of  $\text{H}_2$  produced after 1h CPE with **2**/MWCNT, with a faradaic efficiency ( $\text{FE}_{\text{H}_2}$ ) of  $97.7 \pm 2.1\%$  (Figure S11, Table S2). This corresponds to  $\text{TON}_{\text{H}_2}$  of  $1 \pm 0.3 \times 10^3$  for **2**/MWCNT after 1h of CPE (Table S2). In contrast, the production of  $\text{H}_2$  with **3**/MWCNT quickly levelled off to reach  $5.3 \pm 1.0 \mu\text{mol cm}^{-2}$  after 1 h with a lower  $\text{FE}_{\text{H}_2}$  of  $90.4 \pm 3.3\%$ , hinting at a faster deactivation of **3** at the electrode surface and putting a high degree of uncertainty on the  $\text{TON}_{\text{H}_2}$  displayed in Table S2.

Performing the same series of experiments in neutral pH conditions enabled the observation of a much more sustained current response for **2**/MWCNT (Figure 4c, Figure S10). After 1h CPE, about  $-1.8 \pm 0.2 \text{ mA cm}^{-2}$  at  $E_{\text{app}} = -0.9 \text{ V vs SHE}$  could be measured, corresponding to more than 80% of the initial current density. Less stable current responses were obtained with **3**/MWCNT, where currents decreased relatively quickly from  $-1.8$  to  $-1.0 \pm 0.2 \text{ mA cm}^{-2}$  within 1 h, thus retaining around 60% of catalytic activity. Importantly, the production of  $\text{H}_2$  remained stable over the course of the electrolysis for both **2**/MWCNT and **3**/MWCNT, reaching  $35.0 \pm 5.0 \mu\text{mol cm}^{-2}$  and  $23.2 \pm 0.9 \mu\text{mol cm}^{-2}$  of  $\text{H}_2$ , respectively, with  $\text{FE}_{\text{H}_2}$  of 100% (Figure S11, Table S2).  $\text{TON}_{\text{H}_2}$  calculated for **2**/MWCNT and **3**/MWCNT could reach  $2 \pm 0.3 \times 10^3$  and  $20 \pm 5 \times 10^3$ , respectively, after 1 h CPE. The much higher TONs obtained with **3**/MWCNT need to be put in perspective with the much lower surface loading, quantified using CV. Importantly, MWCNT control electrodes only generated small amount of  $\text{H}_2$ , 1.8 and  $0.3 \mu\text{mol cm}^{-2}$ , at pH 2 and 7, respectively, indicating that the  $\text{H}_2$  evolution activity is due to the presence of the Co complexes (Figure 4).

CV measurements were performed post-electrolysis in order to gain more insight on the molecular integrity of the molecular catalyst at the electrode surface, *post-operando* (Figure S12 and S13). At pH 2, the CV response of **2**/MWCNT apparently showcases a drastic decrease in surface loading of **2**, with only  $14.3 \pm 5.7 \text{ nmol cm}^{-2}$  of electrochemically active complex after 1 h, less than 60% of the initial surface concentration (Table S2). In parallel, the  $\text{Co}^{3+/2+}$  redox response was also shifted towards more negative

potentials, hinting at a change in the coordination environment of the Co centre. The  $\text{Co}^{2+/+}$  couple was not visible in the same potential window and the catalytic wave was notably smaller, in broad agreement with the CPE results where the electrocatalytic response dropped by about 60%. *Post-operando*, the **3**/MWCNT modified electrode did not display noticeable redox activity, if not for a sharp irreversible process at  $E_{\text{ox}} = 0.35$  V vs SHE (Figure S12b), which could indicate a degradation of the catalyst but most likely stems from a polluting source in the electrolyte as it can be observed on the base MWCNT electrode control (Figure S14). Degradation of **3** is, however, highly likely as the catalytic current drops to the control value, producing only traces of  $\text{H}_2$  (Figure 4a and b).

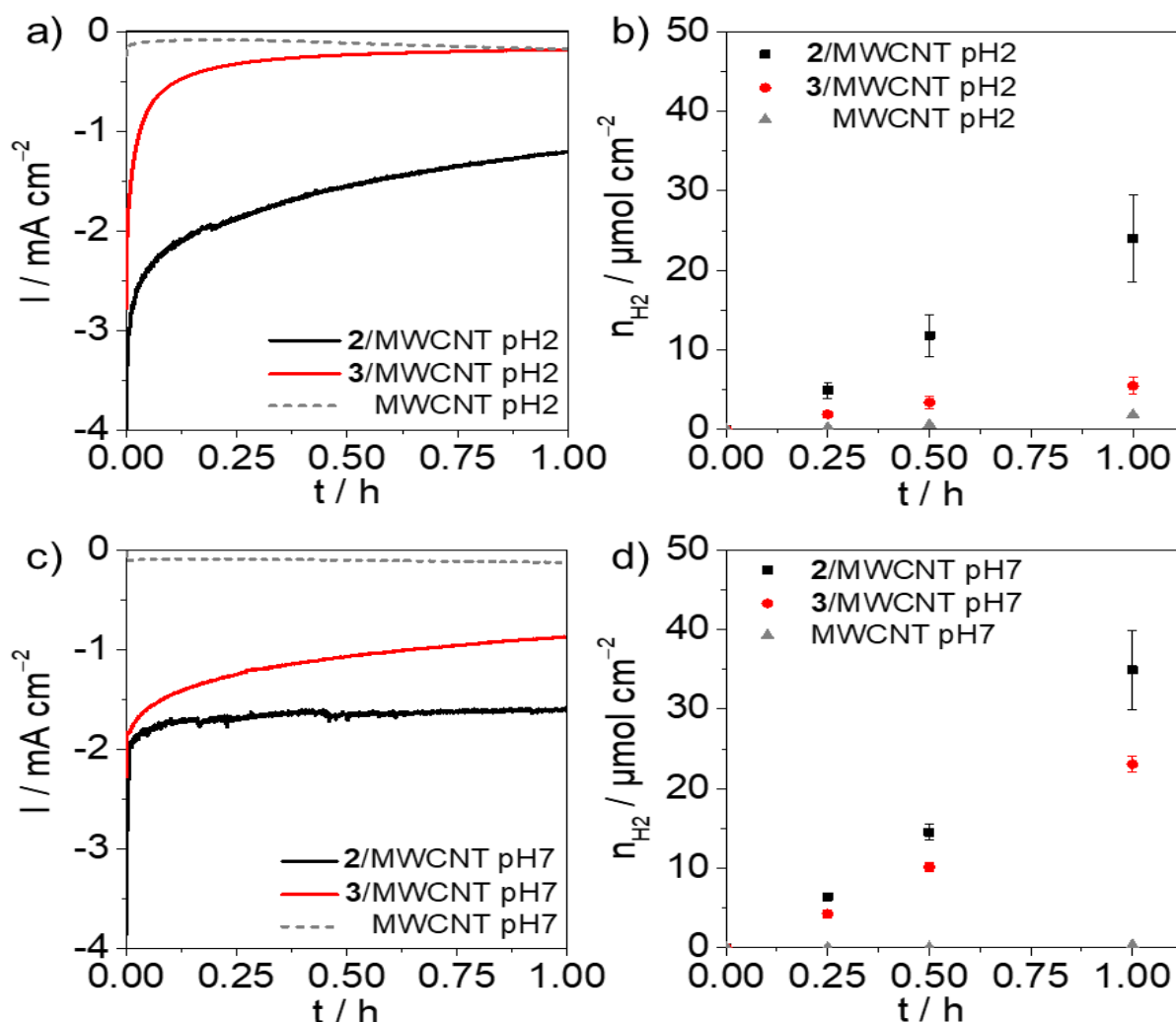


Figure 4 : CPE traces of **2**/MWCNT (black traces), **3**/MWCNT (red traces) and bare MWCNT (black dotted traces) modified electrodes at a)  $-0.6$  V vs SHE in KCl/HCl 0.1 M pH 2 and b)  $-0.9$  V vs SHE in 0.1 M phosphate buffer at pH 7. Production of  $\text{H}_2$  as function of time with **2**/MWCNT (black traces), **3**/MWCNT (red traces) and bare MWCNT modified electrodes at c)  $-0.6$  V vs SHE in KCl/HCl 0.1 M pH 2 and d)  $-0.9$  V vs SHE in 0.1 M phosphate buffer at pH 7. All measurements were performed under  $\text{N}_2$ .

By contrast, the CV performed on **2**/MWCNT post CPE in neutral conditions shows a retention of nearly 80% of the initial surface concentration, in line with the CPE results (Figure S13a, Table S2). Again, a slight negative potential shift of the  $\text{Co}^{3+/2+}$  redox couple ( $E_{1/2} = 0.34$  V vs SHE) was observed along with the disappearance of the  $\text{Co}^{2+/+}$  reduction process, as observed at pH 2 and tentatively attributed to a change of coordination environment of the Co complex. The  $\text{H}_2$  production activity being maintained hints that this new species remains catalytically active. CV post operando performed on **3**/MWCNT show almost no initial redox signature of **3** (Figure S13b). This is in contrast to the electrocatalytic response of **3**/MWCNT for  $\text{H}_2$  evolution which, despite decreasing overtime, still shows activity after 1 h of CPE (Figure 4c and d). This questions the nature of the catalytically active species, as well as the relevance of the electrochemical quantification of the adsorbed complexes, especially for **3**.

On the basis of data obtained from CPE and CV measurements it is evident that **2** achieves the better activity and performance for the HER in both acidic and neutral pH conditions. Importantly, in both conditions **2**/MWCNT maintains higher and more stable catalytic currents than **3**/MWCNT along with improved faradaic efficiency at pH 2. Firstly, the appendage of the pyrene anchor to the amine may be hindering its availability as a proton relay, which may have an effect if this indeed plays a key role in the catalytic mechanism under heterogeneous conditions at the aqueous interface. Secondly, the relative mobility of the pyrene anchor attached by the methylene bridge may enable undesired interactions with the cobalt centre, both affecting its electronics and sterically blocking one of the axial positions where the hydride could bind. It may be hypothesised that a tight interaction of the cobalt atom with the pyrene anchored on the MWCNTs could pull the cobalt deep enough within the electrochemical double layer (EDL) at many sites, causing electronic coupling with the electrode band structure, replacing OSET with ISET mechanisms and coupled proton transfers, convoluting CV responses.<sup>68,69</sup>

For derivative **2**, the structural modification at the *para* position of the macrocycle pyridine does not seem to adversely affect its catalytic activity, as it retains similar redox responses to those of the parent complex **1**, suggesting an analogous mechanism for HER. In recent work, this modification strategy has been used successfully to either improve catalytic activities of the Co centre of **1**<sup>46,47</sup> or to anchor it onto light-harvesting materials.<sup>48-51</sup> In the case of **2**, the conjugated benzamide linker is assumed to be quite rigid, which is likely to prevent direct interactions between the active site and the pyrene anchor while simplifying its redox interactions with the MWCNT electrode surface.

This serves to highlight some rational design principles for modifying molecular catalysts for heterogenisation. Ideally, when appending anchoring groups, any negative impact on the active site's efficiency or ability to turn over should be avoided or minimised. Therefore, it may be important to have sufficient mechanistic insight, at the relevant conditions, into which parts of the active site play crucial roles in optimising the sterics or electronics of the system or which function as proton or electron relays for catalysing the reaction in question. Considering the effects of substitution of certain atoms or functional groups, which may be revealed by synthesising analogous control systems, may help to predict and understand changes in behaviour or performance upon modification and immobilisation, and avoid substitutions that are detrimental to catalytic activity.

Additionally, the flexibility, size and nature of the linker to an anchoring group or directly to a material should be anticipated to also play a role in controlling which ways and how closely the active site will be able to interact with the material's surface, which can be pivotal in determining the mechanisms and efficiencies of electron and proton transfers to an active site.

## Conclusions

In this work, we described the synthesis and full characterisation of novel derivatives, **2** and **3**, of the hydrogen evolving complex  $[\text{Co}(\text{N}_4\text{H})\text{Cl}_2]^+$  (**1**) functionalised with a pyrene moiety at two different positions on the macrocycle. Following their integration into MWCNTs-based electrodes through non-covalent pi-interactions, the electrocatalytic properties of the two molecular cathodes towards the production of  $\text{H}_2$  were tested in aqueous conditions – notably, at both acidic and neutral pHs.

The comparisons of **2**/MWCNT and **3**/MWCNT in acidic and neutral conditions showed that notable differences could be observed for the electrochemically determined surface loading, as well as substantial variations in the redox response, depending on the pH of the electrolyte. The electrocatalytic performances of the two molecular electrodes demonstrated that reasonably stable catalytic responses could be obtained in neutral conditions. In particular **2**/MWCNT retained about 80% of catalytic activity after 1 h CPE ( $-1.8 \pm 0.2 \text{ mA cm}^{-2}$ ), while reaching a  $\text{TON}_{\text{H}_2}$  of  $2 \pm 0.3 \times 10^3$  with 100% faradaic efficiency at 0.53 V overpotential. Post-operando CV measurements seemed to indicate that **2**/MWCNT retained its molecular integrity while it was not possible to draw such conclusion for **3**/MWCNT. Under acidic conditions (pH 2), both complexes showed much lower stability. In fact, after 1 h CPE, **3**/MWCNT showed the same currents as a bare MWCNT electrode indicating a rather fast deactivation of the adsorbed molecular active site. **2**/MWCNT showed better stability also in acidic media.

Overall, in this particular case, the modification of the PDI ligand to integrate a surface-anchoring function at the *para* position of the macrocycle pyridine allowed to reach much more stable and higher catalytic currents than the one modified with a methylene linker at the macrocycle amine. The latter more strongly impacted the geometry and accessibility of the Co centre, thereby directly impacting the catalytic response. Importantly, this work underlines the importance of the rational ligand design to take into consideration the effects of structurally altering and appending anchoring groups to catalytic active sites. The observed sustained electrocatalytic H<sub>2</sub> evolution activity should be expected to be significantly improved by future immobilisation onto more advanced conducting materials and, with optimised anchoring strategies, making anchorable derivatives of [Co(N<sub>4</sub>H)Cl<sub>2</sub>]<sup>+</sup> exciting early candidates as oxygen-tolerant, platinum group metal-free molecular catalysts for testing on the cathodes of scalable PEM electrolyzers.

## Acknowledgements:

This work received funding from the European Union's Horizon 2020 Research and Innovation program under grant agreement no. 765376 (eSCALED Marie Curie ITN project).

## References:

- 1 T. Faunce, S. Styring, M. R. Wasielewski, G. W. Brudvig, A. W. Rutherford, J. Messinger, A. F. Lee, C. L. Hill, H. deGroot, M. Fontecave, D. R. MacFarlane, B. Hankamer, D. G. Nocera, D. M. Tiede, H. Dau, W. Hillier, L. Wang and R. Amal, *Energy Environ. Sci.*, 2013, **6**, 1074.
- 2 A. M. Oliveira, R. R. Beswick and Y. Yan, *Current Opinion in Chemical Engineering*, 2021, **33**, 100701.
- 3 A. Velazquez Abad and P. E. Dodds, *Energy Policy*, 2020, **138**, 111300.
- 4 A. K. Ringsmuth, M. J. Landsberg and B. Hankamer, *Renewable and Sustainable Energy Reviews*, 2016, **62**, 134–163.
- 5 J. H. Montoya, L. C. Seitz, P. Chakthranont, A. Vojvodic, T. F. Jaramillo and J. K. Nørskov, *Nature Mater*, 2017, **16**, 70–81.
- 6 P. C. K. Vesborg and T. F. Jaramillo, *RSC Adv.*, 2012, **2**, 7933–7947.
- 7 S. Ardo, D. Fernandez Rivas, M. A. Modestino, V. Schulze Greiving, F. F. Abdi, E. Alarcon Llado, V. Artero, K. Ayers, C. Battaglia, J.-P. Becker, D. Bederak, A. Berger, F. Buda, E. Chinello, B. Dam, V. Di Palma, T. Edvinsson, K. Fujii, H. Gardeniers, H. Geerlings, S. M. H. Hashemi, S. Haussener, F. Houle, J. Huskens, B. D. James, K. Konrad, A. Kudo, P. P. Kunturu, D. Lohse, B. Mei, E. L. Miller, G. F. Moore, J. Muller, K. L. Orchard, T. E. Rosser, F. H. Saadi, J.-W. Schüttauf, B. Seger, S. W. Sheehan, W. A. Smith, J. Spurgeon, M. H. Tang, R. van de Krol, P. C. K. Vesborg and P. Westerik, *Energy Environ. Sci.*, 2018, **11**, 2768–2783.
- 8 C. R. Cox, J. Z. Lee, D. G. Nocera and T. Buonassisi, *Proc. Natl. Acad. Sci. U.S.A.*, 2014, **111**, 14057–14061.
- 9 C. C. Pavel, F. Cecconi, C. Emiliani, S. Santiccioli, A. Scaffidi, S. Catanorchi and M. Comotti, *Angew. Chem. Int. Ed.*, 2014, **53**, 1378–1381.
- 10 S. Lu, J. Pan, A. Huang, L. Zhuang and J. Lu, *Proc. Natl. Acad. Sci. U.S.A.*, 2008, **105**, 20611–20614.
- 11 R. M. Bullock, J. G. Chen, L. Gagliardi, P. J. Chirik, O. K. Farha, C. H. Hendon, C. W. Jones, J. A. Keith, J. Klosin, S. D. Minter, R. H. Morris, A. T. Radosevich, T. B. Rauchfuss, N. A. Strotman, A. Vojvodic, T. R. Ward, J. Y. Yang and Y. Surendranath, *Science*, 2020, **369**, eabc3183.
- 12 N. Coutard, N. Kaefffer and V. Artero, *Chem. Commun.*, 2016, **52**, 13728–13748.
- 13 V. Artero, M. Chavarot-Kerlidou and M. Fontecave, *Angew. Chem. Int. Ed.*, 2011, **50**, 7238–7266.
- 14 N. Queyriaux, N. Kaefffer, A. Morozan, M. Chavarot-Kerlidou and V. Artero, *Journal of Photochemistry and Photobiology C: Photochemistry Reviews*, 2015, **25**, 90–105.
- 15 V. Artero, *Nat Energy*, 2017, **2**, 17131.
- 16 E. S. Andreiadis, M. Chavarot-Kerlidou, M. Fontecave and V. Artero, *Photochemistry and Photobiology*, 2011, **87**, 946–964.
- 17 U. J. Kilgore, J. A. S. Roberts, D. H. Pool, A. M. Appel, M. P. Stewart, M. R. DuBois, W. G. Dougherty, W. S. Kassel, R. M. Bullock and D. L. DuBois, *J. Am. Chem. Soc.*, 2011, **133**, 5861–5872.
- 18 V. Artero and J.-M. Saveant, *Energy Environ. Sci.*, 2014, **7**, 3808–3814.
- 19 M. L. Helm, M. P. Stewart, R. M. Bullock, M. R. DuBois and D. L. DuBois, *Science*, 2011, **333**, 863–866.
- 20 D. Schilter, J. M. Camara, M. T. Huynh, S. Hammes-Schiffer and T. B. Rauchfuss, *Chem. Rev.*, 2016, **116**, 8693–8749.
- 21 A. C. Ghosh, C. Duboc and M. Gennari, *Coordination Chemistry Reviews*, 2021, **428**, 213606.
- 22 S. Ott, M. Kritikos, B. Åkermark, L. Sun and R. Lomoth, *Angew. Chem.*, 2004, **116**, 1024–1027.
- 23 F. Wang, W.-G. Wang, H.-Y. Wang, G. Si, C.-H. Tung and L.-Z. Wu, *ACS Catal.*, 2012, **2**, 407–416.
- 24 D. Streich, Y. Astuti, M. Orlandi, L. Schwartz, R. Lomoth, L. Hammarström and S. Ott, *Chem. Eur. J.*, 2010, **16**, 60–63.

- 25 D. W. Wakerley and E. Reisner, *Phys. Chem. Chem. Phys.*, 2014, **16**, 5739–5746.
- 26 J. L. Dempsey, B. S. Brunschwig, J. R. Winkler and H. B. Gray, *Acc. Chem. Res.*, 2009, **42**, 1995–2004.
- 27 M. Razavet, V. Artero and M. Fontecave, *Inorg. Chem.*, 2005, **44**, 4786–4795.
- 28 N. Kaefffer, M. Chavarot-Kerlidou and V. Artero, *Acc. Chem. Res.*, 2015, **48**, 1286–1295.
- 29 P.-A. Jacques, V. Artero, J. Pécaut and M. Fontecave, *Proc. Natl. Acad. Sci. U.S.A.*, 2009, **106**, 20627–20632.
- 30 C. C. L. McCrory, C. Uyeda and J. C. Peters, *J. Am. Chem. Soc.*, 2012, **134**, 3164–3170.
- 31 D. Sun, A. Karippara Harshan, J. Pécaut, S. Hammes-Schiffer, C. Costentin and V. Artero, *ChemElectroChem*, 2021, **8**, 2671–2679.
- 32 L. Chen, R. U. R. Sagar, J. Chen, J. Liu, S. Aslam, F. Nosheen, T. Anwar, N. Hussain, X. Hou and T. Liang, *International Journal of Hydrogen Energy*, 2021, **46**, 19338–19346.
- 33 B. Mondal, K. Sengupta, A. Rana, A. Mahammed, M. Botoshansky, S. G. Dey, Z. Gross and A. Dey, *Inorg. Chem.*, 2013, **52**, 3381–3387.
- 34 R. M. Kellett and T. G. Spiro, *Inorg. Chem.*, 1985, **24**, 2373–2377.
- 35 N. Queyriaux, R. T. Jane, J. Massin, V. Artero and M. Chavarot-Kerlidou, *Coordination Chemistry Reviews*, 2015, **304–305**, 3–19.
- 36 N. Queyriaux, D. Sun, J. Fize, J. Pécaut, M. J. Field, M. Chavarot-Kerlidou and V. Artero, *J. Am. Chem. Soc.*, 2020, **142**, 274–282.
- 37 L. Tong, L. Duan, A. Zhou and R. P. Thummel, *Coordination Chemistry Reviews*, 2020, **402**, 213079.
- 38 F. Lucarini, D. Bongni, P. Schiel, G. Bevini, E. Benazzi, E. Solari, F. Fadaei-Tirani, R. Scopelliti, M. Marazzi, M. Natali, M. Pastore and A. Ruggi, *ChemSusChem*, 2021, **14**, 1874–1885.
- 39 C.-B. Li, A. J. Bagnall, D. Sun, J. Rendon, M. Koepf, S. Gambarelli, J.-M. Mouesca, M. Chavarot-Kerlidou and V. Artero, *Sustainable Energy Fuels*, 2022, **6**, 143–149.
- 40 S. Varma, C. E. Castillo, T. Stoll, J. Fortage, A. G. Blackman, F. Molton, A. Deronzier and M.-N. Collomb, *Phys. Chem. Chem. Phys.*, 2013, **15**, 17544.
- 41 R. Gueret, C. E. Castillo, M. Rebarz, F. Thomas, A.-A. Hargrove, J. Pécaut, M. Sliwa, J. Fortage and M.-N. Collomb, *Journal of Photochemistry and Photobiology B: Biology*, 2015, **152**, 82–94.
- 42 S. Roy, M. Bacchi, G. Berggren and V. Artero, *ChemSusChem*, 2015, **8**, 3632–3638.
- 43 M. Sandroni, R. Gueret, K. D. Wegner, P. Reiss, J. Fortage, D. Aldakov and M.-N. Collomb, *Energy Environ. Sci.*, 2018, **11**, 1752–1761.
- 44 S. Grau Abarca, M. Schilling, D. Moonshiram, J. Benet-Buchholz, S. Lubber, A. Llobet and C. Gimbert-Suriñach, *ChemSusChem*, 2020, **13**, 2745–2752.
- 45 J. Wang, K. Yamauchi, H. Huang, J. Sun, Z. Luo, D. Zhong, T. Lu and K. Sakai, *Angew. Chem. Int. Ed.*, 2019, **58**, 10923–10927.
- 46 C. H. Lee, D. Villágran, T. R. Cook, J. C. Peters and D. G. Nocera, *ChemSusChem*, 2013, **6**, 1541–1544.
- 47 W. Nie, D. E. Tarnopol and C. C. L. McCrory, *J. Am. Chem. Soc.*, 2021, **143**, 3764–3778.
- 48 S. Bold, J. Massin, E. Giannoudis, M. Koepf, V. Artero, B. Dietzek and M. Chavarot-Kerlidou, *ACS Catal.*, 2021, **11**, 3662–3678.
- 49 S. Bold, T. Straistari, A. B. Muñoz-García, M. Pavone, V. Artero, M. Chavarot-Kerlidou and B. Dietzek, *Catalysts*, 2020, **10**, 1340.
- 50 C. Nie, C. Liu, L. Gong and M. Wang, *J. Mater. Chem. A*, 2021, **9**, 234–238.
- 51 C. Nie, W. Ni, L. Gong, J. Jiang, J. Wang and M. Wang, *J. Mater. Chem. A*, 2019, **7**, 27432–27440.
- 52 R. M. Bullock, A. K. Das and A. M. Appel, *Chem. Eur. J.*, 2017, **23**, 7626–7641.
- 53 K. E. Dalle, J. Warnan, J. J. Leung, B. Reuillard, I. S. Karmel and E. Reisner, *Chem. Rev.*, 2019, **119**, 2752–2875.
- 54 J. M. Schnorr and T. M. Swager, *Chem. Mater.*, 2011, **23**, 646–657.
- 55 M. F. L. De Volder, S. H. Tawfick, R. H. Baughman and A. J. Hart, *Science*, 2013, **339**, 535–539.
- 56 N. Karousis, N. Tagmatarchis and D. Tasis, *Chem. Rev.*, 2010, **110**, 5366–5397.
- 57 X. Li, H. Lei, X. Guo, X. Zhao, S. Ding, X. Gao, W. Zhang and R. Cao, *ChemSusChem*, 2017, **10**, 4632–4641.
- 58 B. Reuillard, J. Warnan, J. J. Leung, D. W. Wakerley and E. Reisner, *Angew. Chem. Int. Ed.*, 2016, **55**, 3952–3957.
- 59 P. D. Tran, A. Le Goff, J. Heidkamp, B. Jousselme, N. Guillet, S. Palacin, H. Dau, M. Fontecave and V. Artero, *Angew. Chem. Int. Ed.*, 2011, **50**, 1371–1374.
- 60 J. Schild, B. Reuillard, A. Morozan, P. Chenevier, E. Gravel, E. Doris and V. Artero, *J. Am. Chem. Soc.*, 2021, jacs.1c07093.
- 61 A. Maurin and M. Robert, *J. Am. Chem. Soc.*, 2016, **138**, 2492–2495.
- 62 B. Reuillard, K. H. Ly, T. E. Rosser, M. F. Kuehnel, I. Zebger and E. Reisner, *J. Am. Chem. Soc.*, 2017, **139**, 14425–14435.
- 63 S. Pugliese, N. T. Huan, J. Forte, D. Grammatico, S. Zanna, B. Su, Y. Li and M. Fontecave, *ChemSusChem*, 2020, cssc.202002092.
- 64 S. Rajabi, F. Ebrahimi, G. Lole, J. Odrobina, S. Dechert, C. Jooss and F. Meyer, *ACS Catal.*, 2020, **10**, 10614–10626.

- 65 J. Creus, R. Matheu, I. Peñafiel, D. Moonshiram, P. Blondeau, J. Benet-Buchholz, J. García-Antón, X. Sala, C. Godard and A. Llobet, *Angew. Chem. Int. Ed.*, 2016, **55**, 15382–15386.
- 66 F. Li, B. Zhang, X. Li, Y. Jiang, L. Chen, Y. Li and L. Sun, *Angew. Chem. Int. Ed.*, 2011, **50**, 12276–12279.
- 67 R. N. Dürr, S. Chasvised, M. Gil-Sepulcre, A. Howe, M. A. Hoque, V. N’Guyen, S. Sadeghi, S. Reynaud, C. Cugnet, L. Authier, C. Gimbert-Suriñach, A. Bousquet, A. Llobet and L. Billon, *ACS Appl. Energy Mater.*, 2021, **4**, 10534–10541.
- 68 M. N. Jackson and Y. Surendranath, *Acc. Chem. Res.*, 2019, **52**, 3432–3441.
- 69 C. J. Kaminsky, S. Weng, J. Wright and Y. Surendranath, *Nat Catal*, 2022, **5**, 430–442.
- 70 D. Dhar, C. G. McKenas, C.-W. Huang, J. M. Atkin, J. L. Dempsey and M. R. Lockett, *ACS Appl. Energy Mater.*, 2020, **3**, 8038–8047.
- 71 D. C. Lacy, C. C. L. McCrory and J. C. Peters, *Inorg. Chem.*, 2014, **53**, 4980–4988.
- 72 M. Ghosh, T. Weyhermüller and K. Wieghardt, *Dalton Trans.*, 2010, **39**, 1996.
- 73 N. Queyriaux, *ACS Catal.*, 2021, **11**, 4024–4035.



# Ultrafast Electron Transfer from CuInS<sub>2</sub> Quantum Dots to a Molecular Catalyst for Hydrogen Production: *Rethinking the Binding Models*

Andrew J. Bagnall,<sup># 1,2</sup> Nora Eliasson,<sup># 1</sup>  
Murielle Chavarot-Kerlidou,<sup>2</sup> Vincent Artero<sup>2</sup>, Haining Tian,<sup>1</sup> Leif Hammarström\*<sup>1</sup>

<sup>1</sup>Ångström Laboratory, Department of Chemistry, Uppsala University, SE75120 Uppsala, Sweden;  
leif.hammarstrom@kemi.uu.se

<sup>2</sup>Univ. Grenoble Alpes, CNRS, CEA, IRIG, Laboratoire de Chimie et Biologie des Métaux, 17 rue des Martyrs, F-38054  
Grenoble, Cedex, France

---

## Abstract

Quantum dots with molecular catalysts attract increasing attention for studies of the photocatalytic hydrogen evolution reaction (HER). CuInS<sub>2</sub> (CIS) QDs have relatively reducing conduction bands, but their electronic structure and defect states often lead to poor performance, prompting many researchers to use a core-shell structure. Molecular cobalt HER catalysts on the other hand often suffer from poor stability. Here we combined CIS QDs, synthesised in an aqueous process and passivated by *L*-cysteine and iodide, with two tetraazamacrocyclic cobalt complexes and demonstrate very high HER turnover numbers (up to TON ~8000 per catalyst) with ascorbate as donor (pH = 4.5). Photoluminescence quenching data showed very strong binding of the catalyst to the QDs even at only 1 μM catalyst, and an entirely static quenching. The data was fitted with a Poissonian distribution of catalysts over the QDs, from which binding and concentration of QDs could be evaluated. Surprisingly, there was no important difference between catalysts with and without carboxylate as a potential binding group. Transient absorption spectroscopy confirmed ultrafast quenching of the QDs and formation of the reduced catalyst (Co<sup>2+</sup>) for both complexes ( $t \approx 4$  ps). The favorable results show that the tetraazamacrocyclic cobalt complex is an unusually stable catalyst under photochemical conditions. They also suggest that CIS without an inorganic passivating shell can be a useful photosensitiser, whose small size may be favorable for e.g. sensitization of mesoporous electrodes.

*Keywords:* hydrogen, photocatalysis, copper indium sulfide, quantum dots, molecular catalyst, transient absorption, artificial photosynthesis

## Introduction

In recent years there has been a growing interest in combining the strong and independently tunable light harvesting properties of colloidal quantum dots (QDs) with the potentially fast and selective catalysis provided by molecular catalysts via interfacial charge transfer (CT), allowing the precise making and breaking of chemical bonds from photogenerated charge carriers with sufficient potentials. Some advantages of QD photosensitisers over molecular dyes is their exceeding photostability, long exciton lifetimes and their broad absorption spectral coverage across the solar spectrum, which are pivotal properties in the design of efficient photocatalytic systems.

Ternary I-III-VI metal chalcogenide QDs, e.g. CuInS<sub>2</sub> (CIS) and AgInS<sub>2</sub> (AIS), have gained increasing attention in the last decade as alternatives to the commonly used Cd- and Pb binary chalcogenides. Their high-energy conduction bands are beneficial for reductive photochemistry, such as proton and CO<sub>2</sub> reduction. As a result of their composition, the ternary QDs often suffer from a large number of lattice imperfections with potential fluctuations that result in carrier localisation and complex photophysical behaviour. Moreover, neat CIS QDs and nanorods have been reported to show very poor photocatalytic H<sub>2</sub> performance with added co-catalysts, and CIS/ZnS core-shell structures have often been preferred for photocatalytic reactions.<sup>1-4</sup>

The resistance, however, of CIS QDs to off-stoichiometry offers additional degrees of freedom to tune photophysical and electronic properties. In CIS, higher photocatalytic activities (towards the HER) have been reported for Cu-deficient structures, attributed to more efficient hole transfer, provided by the lower VB-edge, despite accelerated electron trapping rates,<sup>2,5</sup> and even neat, Cu-deficient CIS QDs showed high H<sub>2</sub> production activities with simple metal salts as co-catalysts.<sup>5</sup>

Molecular catalysts on the other hand represent an interesting method for enhancing the catalytic activity of more Earth-abundant first-row transition metals.<sup>6</sup> Often inspired by biology, the coordination sphere around the metal can be tuned to improve activity, selectivity and stability for the desired reaction, and anchoring groups can be included in the molecular structure to enable integration onto materials.<sup>7-9</sup>

One such catalyst is the cobalt tetraazamacrocyclic complex, [Co(N<sub>4</sub>H)Cl<sub>2</sub>]<sup>+</sup> (**CAT1**), which is an effective and robust, oxygen-tolerant catalyst for the hydrogen evolution reaction (HER) in both organic and aqueous conditions. CAT1 is reported to display notable activity, efficiency and stability in both electrocatalytic and photocatalytic conditions.<sup>10-15</sup> Indeed, this catalyst has been successfully used with a diverse range of photosensitisers, including [Ru<sup>II</sup>(bpy)<sub>3</sub>]<sup>2+</sup>,<sup>15-18</sup> the triazatriangulenium derivative organic dye (TATA<sup>+</sup>),<sup>19,20</sup> and CdTe QDs,<sup>21</sup> as well as in dye-catalyst assembly systems.<sup>22,23</sup> However, the excellent performances of CAT1 and its anchorable derivatives with CIS/ZnS-GSH QDs (GSH: glutathione), reported by the Wang and Collomb groups, are particularly noteworthy.<sup>3,24,25</sup> This combination of PS and molecular catalyst has remarkable reported turn-over numbers (TON) of up to 7700 at pH 5.0, with electron transfer (ET) rates on the nanosecond time scale or apparently even below, in the case of an anchored derivative.

Despite the large number of reports on photocatalytic activities in QD-molecular systems and an increasing interest in QDs as photosensitisers for electron and hole acceptors, there are limited spectroscopic studies on CT rates involving molecular catalysts. For the present catalyst, Sandroni *et al.* reported TON of 4580 and 900 (pH 4.5) with respect to CAT1 and CIS/ZnS QDs, respectively, but no photophysics or CT rates were reported.<sup>3</sup> Nie *et al.* introduced a 2',6'-dicarboxypyridin-4'-yl anchoring group on the macrocyclic ligand of CAT1 for covalent attachment to the CIS/ZnS QD surface.<sup>24</sup> They reported TON of 2670 and 1360 with respect to the functionalised and unfunctionalised CAT1, respectively. For the covalently attached CAT1, ET rates ( $\tau_{ET}$ ) were determined through TCSPC for the Co<sup>3+</sup> to Co<sup>2+</sup> (0.61 ns, 84.4 %) and Co<sup>2+</sup> to Co<sup>+</sup> (0.78 ns, 74.9 %) reduction steps – approximately twice as fast when compared to freely diffusing CAT1. They also reported ET rates obtained from femtosecond transient absorption (fs-TA) experiments of 1.2 ns for surface bound CAT1, but it is unclear whether the first or second reduction step was monitored since the absorption band from the reduced catalyst was not observed.

The direct observation of reduced/oxidised species in TA has many advantages compared to indirect determinations of CT rates relying on changes in the QD signal response in the presence of the acceptor/donor, *e.g.* accelerated excitonic bleach recovery dynamics or a lowering of the initial ( $t_0$ )  $\Delta$ Abs magnitude upon interfacial transfer of CB electrons, as such observations can reflect changes in the QD-environment interface not directly related to CT rates. Yet, studies in the literature remain very scarce in this regard. More solid spectroscopic investigations could be beneficial in order to understand the underlying charge separation dynamics following photoexcitation. In the MIR region, CT rates can be determined directly via spectral shifts in molecular signatures superimposed upon the positive transient(s) from intraband transitions commonly observed in bulk- and nano- semiconducting materials, *e.g.* as reported in Huang *et al.*<sup>26</sup> and Eliasson *et al.*<sup>27</sup> Probing the direct formation of the reduced catalyst in the UV-Vis (*e.g.* Eliasson *et al.*<sup>27</sup>) can be more feasible in cases where IR resonances are weak, but this suffers from the breadth of electronic absorption bands and spectral overlap.

Earlier reports of ternary QD photosensitisers have largely relied on organic solvents using organic acids as proton sources, and there still remains a number of challenges to produce high quality QDs in aqueous conditions. Herein, we rely on a facile water-based synthesis of Cu-deficient CIS QDs with a hybrid-passivation layer developed by Huang *et al.*,<sup>28</sup> based on a core/shell procedure reported by Chen *et al.*<sup>29</sup> The hybrid passivation<sup>30</sup> layer consists of shorter organic ligands (L-cysteine) and halide anions (iodide), where the latter can passivate surface sites inaccessible to the ligand.

Alongside CAT1, a novel derivative incorporating a benzoic acid moiety was prepared: CAT1-CO<sub>2</sub>H (Figure 1). It was intended that this moiety function as an anchoring group, via electrostatic or other interactions, in order to bind the catalyst to the PS, analogous to previous studies by Nie *et al.* and also to similar systems with different catalysts.<sup>24,27</sup>

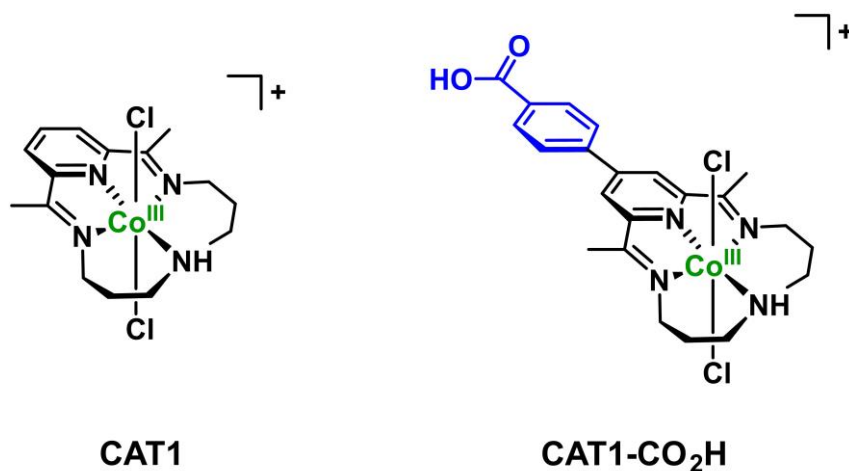


**Figure 1.** Chemical structures of the molecular catalyst, CAT1, and its novel derivative, CAT1-CO<sub>2</sub>H, functionalised with a benzoic acid moiety (in blue), both in the Co<sup>3+</sup> oxidation state.

We combine the QDs together with CAT1 and CAT1-CO<sub>2</sub>H in an efficient hydrogen-evolving system with ascorbate as the sacrificial donor. We investigate the role of the anchoring group (-CO<sub>2</sub>H) in varying conditions through steady-state and time-resolved quenching experiments, reporting remarkably efficient quenching for both catalysts. A static quenching model based on a Poisson distribution of QD bound catalysts was applied, emphasising high binding affinities as well as providing an indirect estimation of the QD concentration. Through fs-TA measurements, we provide direct (UV-Vis) and indirect (MIR) evidence of ultrafast (< 10 ps) reduction of CAT1 with/without anchoring group (-CO<sub>2</sub>H) – two orders of magnitudes faster than reported by Nie *et al.* using CIS/ZnS.<sup>24</sup>

There is currently insufficient understanding, investigation and modelling as to the underlying factors for the high TON in these inorganic-organic hybrid systems. It is hoped that this study can reveal some of the underlying behaviour through investigating this interesting system.

## Results and Discussion

### *Quantum Dot Synthesis and Characterisation*

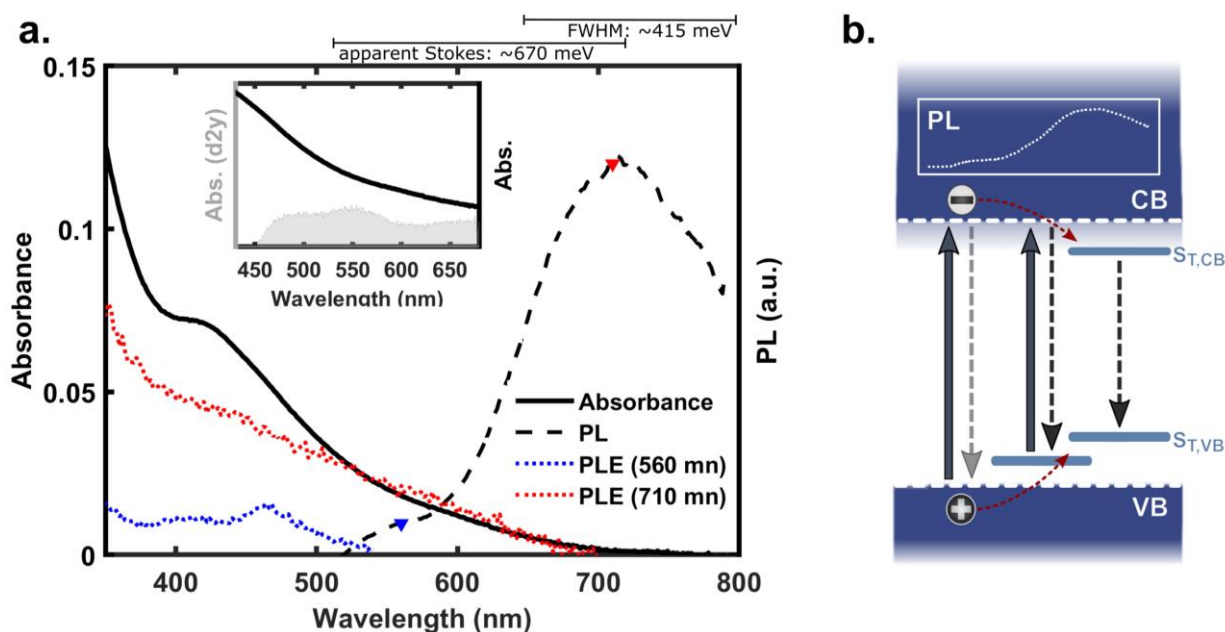
The hybrid (L-cysteine/iodide) passivation layer, that provides a compact surface protection, is introduced during synthesis so that no ligand or solvent exchange is required. The reduced size profile of the L-cysteine coated particles can be beneficial for their utilisation in a PEC, allowing sensitisation of photoelectrode materials with limited pore size. This was demonstrated by Huang *et al.* with CIS-sensitised photocathodes of mesoporous nickel oxide (NiO) printed onto fluorine-doped tin oxide (FTO), used in PEC without the use of sacrificial donors.<sup>28</sup> Small sized capping ligands are likely beneficial for interfacial CT rates compared to thick insulating layers that could lower electron tunnelling probabilities, which could contribute to the sub-ps ET rates between hybrid passivated CIS QDs (Cu:In, ~1:5) and a FeFe-hydrogenase mimic reported previously.<sup>27</sup> The synthesis resulted in CIS QDs (~4 nm) with a ratio of approximately 1:3.5 copper to indium (*i.e.* Cu-deficient) in a chalcopyrite crystal phase according to inductively coupled plasma (ICP) measurements and powder X-ray diffraction (Table S1, Figure S1).<sup>28</sup>

Figure 2 shows a representative ensemble absorption and PL spectra from the CIS QDs (see Figure S2 for more batches). The broad and featureless absorption spectrum is typical for the ternary species due to the variable nature of allowed optical transitions. The band-edge exciton results in an absorption band centred at approximately 515 nm (~2.4 eV), estimated from the 2<sup>nd</sup> derivative of the absorption spectrum and by

plotting  $(ah\nu)^2$  against  $h\nu$  (Figure S3). We associate the more distinct absorption feature at  $\sim 430$  nm with a higher excitonic state which, based on our previous investigation of  $\text{Cu}_{0.2}\text{In}_1\text{S}_x$  QDs ( $\sim 2\text{-}3$  nm), most likely involves a deeper hole state that obtains more band-edge character if the VB edge is further depleted from Cu-states by decreasing Cu-content.<sup>27</sup>

The absorption tail at lower energies ( $\sim 550\text{--}700$  nm) corresponds to sub-bandgap transitions, mainly dominated by  $\text{Cu}^+$  states in proximity to the VB edge. The presence of sub-bandgap optical transitions which superimpose on the lowest energy band-edge transition is suggested in CIS QDs. Jara *et al.* (2016), for example, showed that the tail absorption decreases with increasing Cu-deficiency, revealing a more distinct excitonic feature.<sup>31</sup> An alternative interpretation is that the low-energy tail is due to a symmetry-forbidden bandgap transition.<sup>32</sup> The broad bandwidth of the main PL band (FWHM:  $\sim 415$  meV) and the large apparent Stokes shift ( $E_{\text{VB-CB}} - E_{\text{PL},715\text{nm}}$ :  $\sim 670$  meV) may indicate that the dominating band centred at  $\sim 715$  nm involves trapped carriers (electrons and/or holes), although a model with large electron-phonon coupling has been proposed to explain these characteristics.<sup>32</sup>

The PL excitation (PLE) spectrum monitored at 710 nm shows contributions from excitation above and below the lowest energy band-edge transition whereas the higher energy PL tail ( $< 600$  nm) follows only from excitation above or similar to the band-edge transition energy ( $\geq 2.4$  eV). The PL decay is multiexponential and wavelength-dependent (Table S3), as is typical for CIS QDs, supporting that intra-bandgap trap states of varying nature can mediate radiative recombination. A tentative model that is consistent with data (see PL quenching studies) is depicted in Figure 2b.



**Figure 2.** a) Absorbance, photoluminescence (PL) and photoluminescence excitation (PLE) spectra for a CIS QD sample (ca.  $1\ \mu\text{M}$ ) dispersed in water. The blue/red triangles on the PL spectrum indicate the wavelengths where the PLE was monitored (560/710 nm). The 560 nm PLE is presented with a scale factor of 5:1. Inset: close-up showing absorption spectrum (black) and its second derivative ( $d^2y$ , shaded grey). The  $d^2y$  has been smoothed with a moving average filter and scaled for clarity. b) Schematic diagram of the involved transitions. Absorption is shown in solid arrows and PL in dashed arrows (tentative assignment).

### Photocatalytic Studies

CAT1 catalyses the HER by a heterolytic ECEC-type mechanism. Under homogeneous organic conditions, this was previously reported to involve the protonation and decoordination of the macrocycle amine at the  $\text{Co}^{2+}$  state, in effect potentially acting as a proton relay, followed by a one electron reduction before the rate-determining second protonation step.<sup>11</sup> Under homogeneous aqueous conditions, however, it has also been proposed that the protonation of the macrocycle amine does not necessarily play a role and that the  $\text{Co}^+$ -hydride may instead directly receive a proton from solution.<sup>18</sup> In either case, it is necessary to reduce the cobalt centre to the  $\text{Co}^+$  state in order to initiate HER catalytic turnover.

The photocatalytic system consisted of the hybrid-passivated CIS QDs as the photosensitiser with either CAT1 or CAT1-CO<sub>2</sub>H, in a solution of 0.5 M ascorbic acid/sodium ascorbate (H<sub>2</sub>Asc/NaHAsc) buffer in water at pH 4.5 to maintain a constant concentration of protons (Figure 3). Ascorbate also acts as the sacrificial electron donor (or QD hole scavenger), replacing the electrons donated by the photoexcited QDs to the catalyst and thereby reduces electron-hole recombination processes.<sup>24</sup>

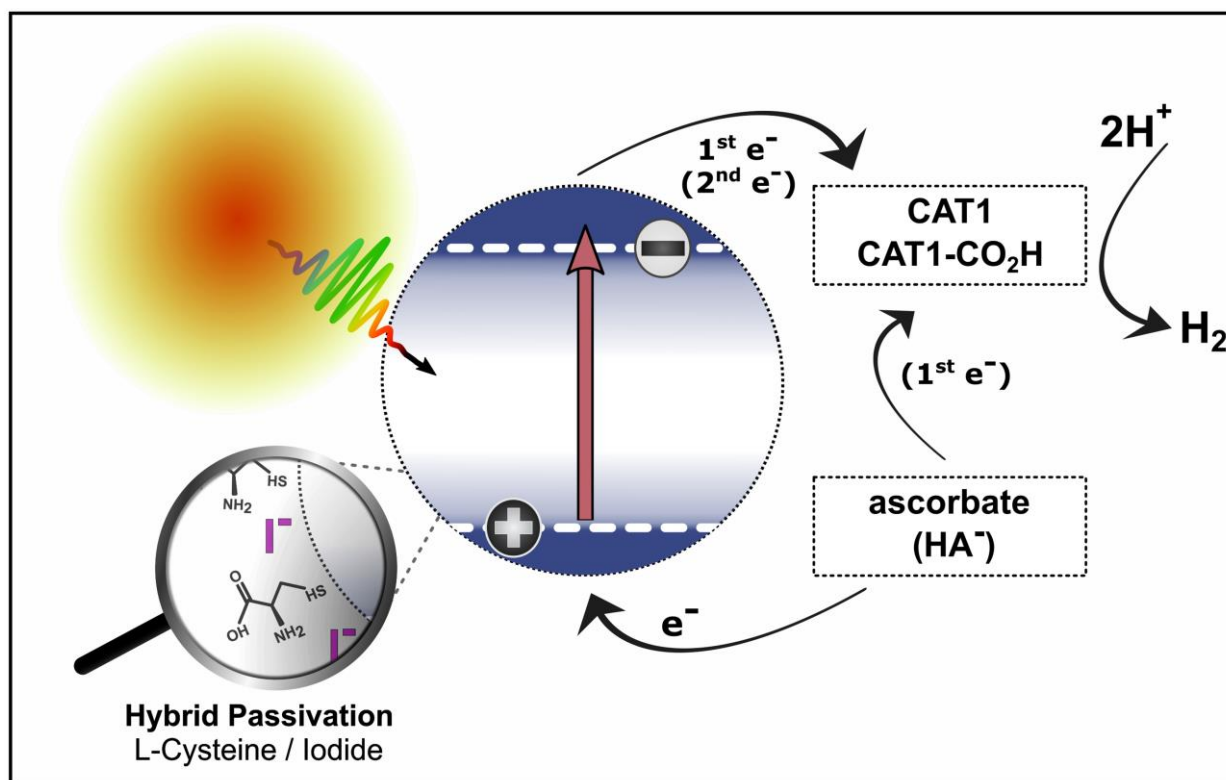


**Figure 3.** Illustration of the investigated photocatalytic system in aqueous solution with hybrid-passivated CIS QDs as photosensitiser, CAT1 or CAT1-CO<sub>2</sub>H as molecular HER catalysts and ascorbate as sacrificial electron donor.

These conditions for pH and buffer concentration were already previously established as appropriate and effective for the closely related CIS/ZnS QD + CAT1 photosystems in literature.<sup>3,24</sup> The pH of 4.5 resulted in higher initial TOFs than at pH 5.0 and pH 5.5, although similar behaviour with somewhat higher lifetime TONs per QD and catalyst were reported at the latter pH values. The catalyst system is known to be active in this pH range and reported to be stable down to pH 2 or below.<sup>10,13</sup> More acidic conditions at pHs below the pK<sub>a1</sub> of ascorbic acid should sharply reduce the concentration of ascorbate, as per the Henderson-Hasselbalch equation,<sup>33</sup> so pH 4.5 represents a good balance of sufficient proton concentration for the HER and system stability.

In order to investigate if the CIS QDs with the hybrid passivation ligand system would still behave similarly to those with a ZnS outer shell used in previous studies and whether the addition of the carboxylic acid anchoring group to the catalyst would have any effect, photocatalytic experiments with H<sub>2</sub> gas measurements by gas chromatography at 2, 4, 8 and 24 hours of irradiation were carried out (Figure 4). As the default illumination condition, a 57 mW/cm<sup>2</sup> light intensity from an LED light source (420-750 nm), roughly similar to one sun, was applied to the samples. For comparison, the studies of Sandroni *et al.* and Nie *et al.* used a 150 W Xe-lamp for irradiation, but the details on the intensity reaching the sample were not fully elaborated.<sup>3,24</sup>

It is known for the related systems that the rate of H<sub>2</sub> production increasingly slows down after one day, which is attributed in the literature to either the degradation of catalyst or the build-up of oxidised ascorbate in the form of dehydroascorbic acid, which traps electrons and hinders ET to the catalyst. Longer time periods were therefore not investigated for the system reported herein.<sup>3,34</sup>

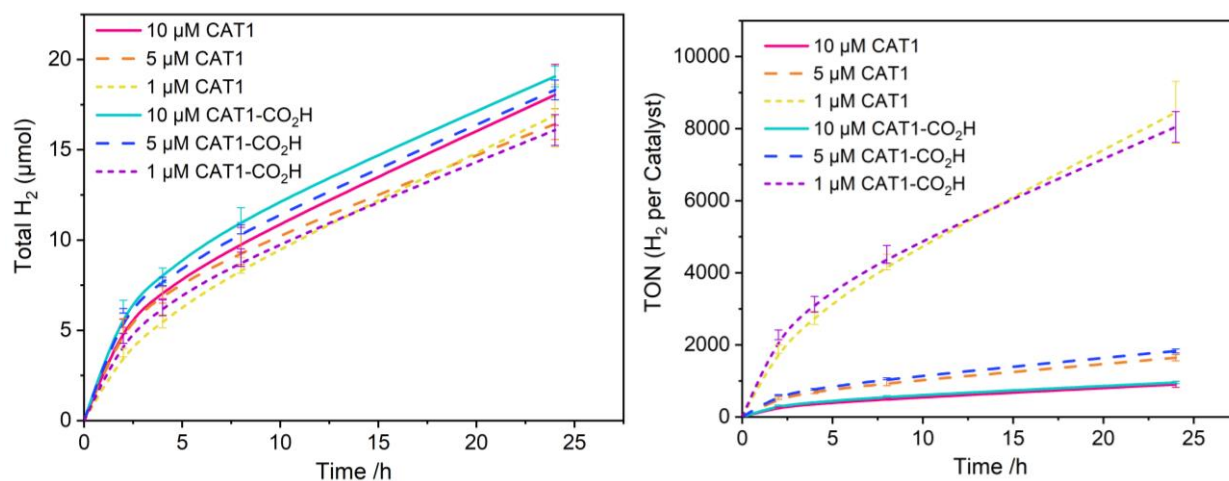


**Figure 4.** H<sub>2</sub> (Left) and TON of H<sub>2</sub> produced per catalyst (Right) measured by gas chromatography against time of irradiation for different concentrations of CAT1 and CAT1-CO<sub>2</sub>H (2 mL solution, 7 mL headspace). Constant visible light irradiation intensity (57 mW/cm<sup>2</sup>) and CIS QD concentration (QD absorbance at 405 nm of 0.35 with a 1 cm pathlength, corresponding to ca. 5 μM QDs; see text). Buffer solution: 0.5 M H<sub>2</sub>Asc/NaHAsc, pH 4.5.

From the H<sub>2</sub> measurements it was observed that, under these conditions and with these concentrations of QDs (ca. 5 μM) and catalyst (1-10 μM), the concentration of catalyst has only a small effect on the amount of H<sub>2</sub> produced over 24 hours: a decrease in concentration of either catalyst by one order of magnitude (from 10 μM to 1 μM) resulted in a decrease in hydrogen production of only about 10%. This results in the TON per catalyst decreasing sharply with increasing catalyst concentration over this range.

Although the amount of H<sub>2</sub> produced over one day by this system is on the same order of magnitude as that reported in literature for CIS/ZnS QDs, the behaviour of the present CIS system differs somewhat: for QDs with the ZnS shell, increasing catalyst concentration resulted in notable – but not proportional – increases in hydrogen production, although with some loss of TON per catalyst. The TON in 24 h obtained with 1 μM catalyst (TON ~ 8000) is very similar to what was reported in Sandroni *et al.* The ten-fold lower QD concentration employed here may be at least partially compensated by stronger light irradiation; the irradiation intensity is not possible to compare based on the published data. Nevertheless, it seems likely that the quantum yield for H<sub>2</sub> production is at least similar, if not better, in the present system. It is important to note that the observed rate of H<sub>2</sub> evolution is given by the rate of photon absorption multiplied by the H<sub>2</sub> quantum yield. The latter is determined by the relative rates of several productive ET and PT steps and the competing charge trapping recombination reactions. It is interesting that the present CIS QDs appear to give similar quantum yields to the core-shell QDs, given that the shell is expected to retard in particular trapping and recombination reactions.<sup>3</sup>

Furthermore, the effect of the presence of the anchoring group on CAT1-CO<sub>2</sub>H versus CAT1 with no specific anchoring group seems to be practically negligible, giving only a 4% improvement over 24 hours on average over the three concentrations. This is surprising and would seem to imply that, with the hybrid-passivated CIS QDs under these conditions, the limiting factor in H<sub>2</sub> production is not the proximity of catalyst to facilitate ET. An alternative interpretation is that the anchoring group is not necessary to obtain a high affinity between QDs and catalysts. To investigate this possibility, we undertook a photo-physical study of the system.

#### Photoluminescence Quenching by Ascorbate Buffer

We first investigated the effect of ascorbate on the QD PL. PL intensity quenching and TCSPC experiments were carried out with increasing concentration of ascorbate buffer at pH 4.5 (Figure S4), without catalyst. Increasing concentrations of ascorbate resulted in a linear increase in  $F_0/F$  ( $\tau_0/\tau$ ) up to circa 0.5 M with a  $K_{sv}$  of  $6.2 \pm 0.4 \text{ M}^{-1}$ , attributed to hole transfer processes from the QDs to ascorbate. It is concluded that ascorbate is predominantly acting as a dynamic quencher of the QDs' photoluminescence. Thus, its reductive quenching effect should be dependent on its local concentration and be generally slower than the oxidative quenching involving ET to catalyst species. It should be noted as well that addition of ascorbate

induces a moderate redshift of the PL emission peak; this is the opposite effect to that of the catalysts (*vide infra*).

### Photoluminescence Quenching by Catalysts

The observations from photocatalytic studies may imply that the mechanism of electron transfer from the CIS QD photosensitisers to the catalyst may be largely independent of diffusion. Therefore, a series of PL quenching experiments were carried out, combining the CIS QDs with each catalyst in different concentrations, with and without ascorbate buffer, to investigate oxidative and reductive electron transfer processes.

Samples were prepared with specific relative concentrations of QDs by diluting to control their absorbance at the shoulder at 405 nm. Measurements were taken both in water only and also in 0.1 M or 0.5 M ascorbate buffer at pH 4.5 for certain QD concentrations, to emulate the conditions used in the photocatalysis experiments. The plots of PL quenching spectra from the conditions investigated are shown in Figure 5 and the Supporting Information (Figures S5-S6). For the highest QD concentrations, a 1 mm cuvette was used in a front-face collection geometry to minimise inner filter effects whilst enabling monitoring of PL quenching at the higher QD concentrations required for photocatalysis and TA spectroscopy.

By monitoring the steady-state PL intensity from the QDs in the presence of CAT1 and CAT1-CO<sub>2</sub>H, highly efficient quenching was observed even at low catalyst concentrations. The PL intensity was reduced by 56% with the addition of only 1.1  $\mu$ M CAT1 to QDs with an absorbance of 0.07 at 405 nm in a 1 cm cuvette, estimated to be around 1.0-1.5  $\mu$ M (*vide infra*); for CAT1-CO<sub>2</sub>H the decrease in PL under the same conditions was 50%. Because the unquenched PL lifetime is < 1  $\mu$ s, the strong quenching at only 1.1  $\mu$ M catalyst is inconsistent with diffusional quenching. Whenever the concentration of either catalyst was increased ([QD] was kept constant), there was a drop in PL intensity accompanied by a small blueshift of the main emission peak at 700–730 nm (see Figure S5).

Despite lacking the intended anchoring group, CAT1 generally proves to be the more effective quencher, with more rapid loss of QD PL intensity per catalyst concentration, implying that a specific anchoring group is not necessary in this system for the molecular catalyst to already interact strongly with the QD. Nonetheless, for photocatalysis, the modification at the pyridine position of the macrocycle did not adversely affect the catalyst's comparative performance, implying that such modification is acceptable for appending groups to CAT1 without hindering the catalytic mechanism.

Furthermore, from Figure 5a it is clear that the relationship of quenching efficiency against concentration of either catalyst was found to deviate significantly from the linear trend of  $F_0/F$  vs. [quencher] typical of the Stern-Volmer relationship which pertains to either dynamic (collisional) quenching processes or static quenching processes in the low association regime.<sup>35</sup> Rather, the plots show a very strong upward curvature: when a logarithmic scale is applied to the y-axis (Figure 5, b-d), the data sets show a clear linear behaviour, implying that the quenching efficiency grows exponentially with concentration of the catalysts at [cat.] < 50  $\mu$ M. This indicates that the application of the modified Stern-Volmer equation for cooperative dynamic and static quenching cannot provide a satisfying fit for the data, as this would lead to a quadratic curvature.<sup>36</sup>

Moreover, TCSPC experiments do not support a dynamic contribution from the catalysts. When the catalysts acted as quenchers, the lifetimes retrieved from applying triexponential fits to the PL decay profiles remain largely unperturbed ( $\tau_1 = 20 \pm 3$  ns [ $\sim 65$  %],  $\tau_2 = 110 \pm 10$  ns [ $\sim 25$  %], with a minor [ $\sim 7$  %]  $\tau_3 =$  ca. 380 ns at 700 nm; see Figure S8, Table S3). Therefore, a different quenching model is judged to be necessary to appropriately interpret the data (*vide infra*).

We note that quenching by the catalyst leads to a blue shift of the remaining PL, opposite to the effect with ascorbate. This can be rationalised by the catalyst preferentially accepting electrons from intra-bandgap states in proximity to the CB edge, likely surface trap states, while transitions involving deeper hole states are more efficiently quenched by ascorbate. Note that an explanation based on a QD size distribution would require that the catalyst preferentially quenches the subset of larger QDs, which is unintuitive from the

smaller driving force for ET. This, however, could be rationalised with the higher surface area of larger QDs, meaning that the probability for a catalyst to adsorb is higher.

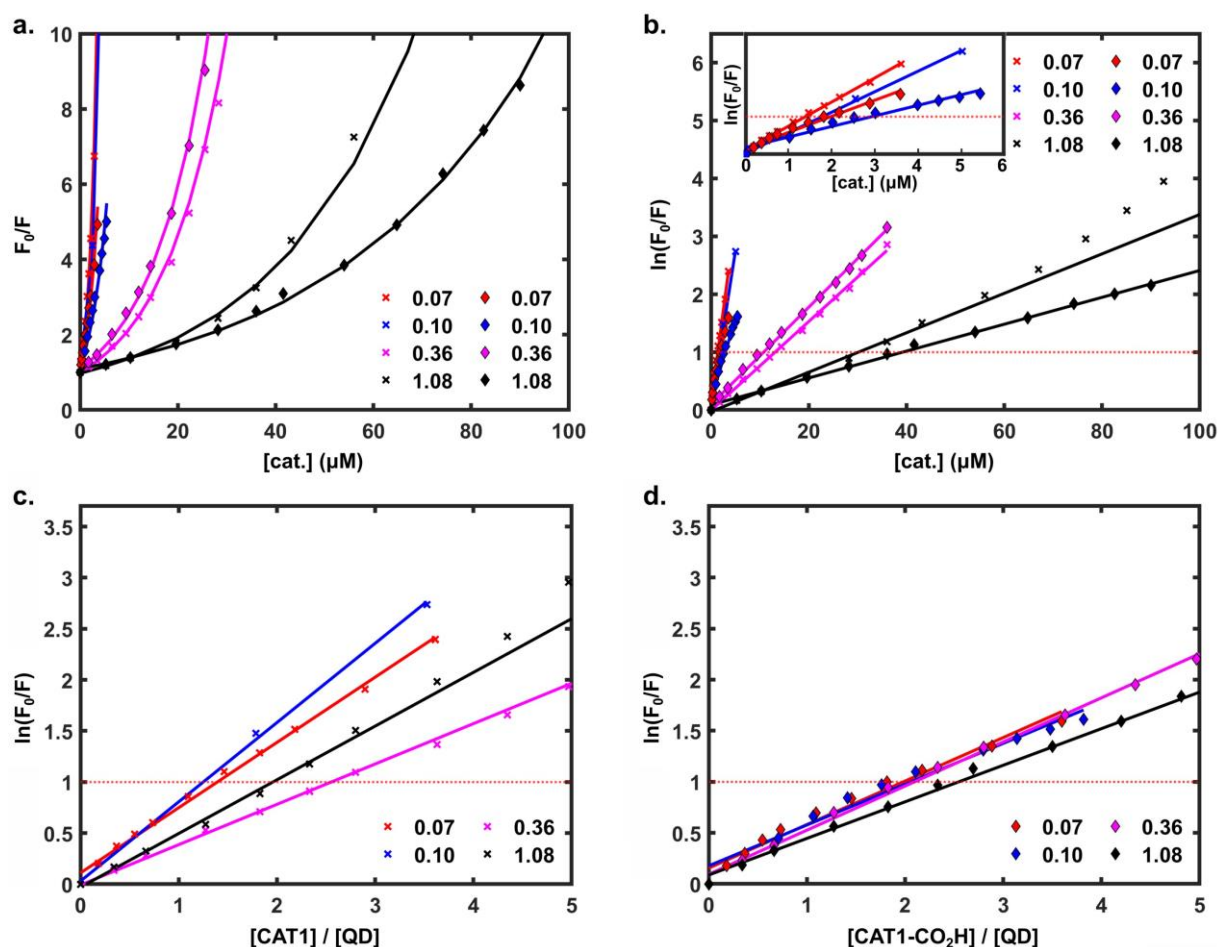


Figure 5. Photoluminescence quenching of the CIS QD system with CAT1 ( $\times$ ) or CAT1-CO<sub>2</sub>H ( $\blacklozenge$ ) for different QD concentrations represented by the absorbance at 405 nm in a 1 cm cuvette (rel.[QD]), as indicated in the insets. The plots show a)  $F_0/F$  against catalyst concentration, b)  $\ln(F_0/F)$  against catalyst concentration with an inset at lower rel.[QD], c)  $\ln(F_0/F)$  against  $[CAT1] / \text{rel.}[QD]$  and d)  $\ln(F_0/F)$  against  $[CAT1-CO_2H] / \text{rel.}[QD]$ . Solid lines represent fits over the linear regions (exponential trend for  $F_0/F$ ). The dashed red line in b-d indicates where  $\ln F_0/F = \lambda = 1$ .

Finally, we do not observe any evidence for build-up of a steady-state concentration  $Co^{2+}$  with ascorbate when the solutions are exposed to air, *i.e.* we consider  $Co^{3+}$  as the initial state before excitation of the QDs (*vide infra*).

### Modelling of Oxidative PL Quenching by the Catalysts

The very low concentrations of catalysts required for almost complete quenching together with the unperturbed TCSPC lifetimes infer that the QDs and catalysts have to be pre-associated (static quenching,  $< 100$  ps timescale). Additionally, when adjusted for the QD concentrations represented by the absorbance at 405 nm in a 1 cm cuvette ( $F_0/F$  against  $[\text{cat.}]/[\text{QD}]$ ), the datasets for each sample without buffer show good agreement for a three-fold variation in catalyst concentration (Figures 4c & d), particularly for CAT1-CO<sub>2</sub>H. This agreement across concentrations suggests that the relative concentrations of  $[\text{cat.}]/[\text{QD}]$  are important, as opposed to the total or free catalyst concentration, which implies a strong binding and highly efficient quenching. To account for the observed exponential increase in intensity ratio ( $F_0/F$ ) with catalyst concentration, we have applied a model assuming a random (Poissonian) distribution of adsorbed catalyst over the QDs in order to explain the efficiency and rate of electron transfer in solution. The Poisson model is analogous to previous treatments of fluorescence quenching in micelles<sup>37</sup> or the “quenching sphere of action” at high concentrations of quenchers in solution,<sup>35,38</sup> and has been applied to determine adsorption constants in e.g. CdS QD-Viologen complexes by Morris-Cohen et al (2011).<sup>39</sup>



In this model, we assume very favourable QD-catalyst interactions, regardless of the presence of an intended anchoring group, such that the equilibrium constant (or affinity constant,  $K_a$ ) of binding for a catalyst molecule with a QD particle is high enough that the majority of catalyst molecules will adsorb, leaving negligible free catalyst dissolved in solution. We furthermore assume that the quenching is ideal; the efficiency of ET from the photoexcited QD particle to an adsorbed catalyst can be approximated as unity, so that the QD contribution to the observed PL intensity is negligible when at least one catalyst is bound. In terms of quenching (the effect on the  $F_0/F$  ratio), this assumes therefore that if the number of quenchers (catalysts) bound to a QD ( $n$ ) is higher than 0 ( $n \geq 1$ ), then the quenching probability is  $\sim 100\%$ . Therefore, the ratio of the initial peak PL intensity to the quenched peak PL intensity is equivalent to the ratio of the total number of QDs to the number of QDs with no adsorbed quencher (Equation 1).

$$F_0/F = [\text{QD}]_{\text{total}} / [\text{QD}]_{n=0} \quad (1)$$

i.e.  $F_0/F$  is the inverse of the proportion of the PL that is not quenched. In the Poisson distribution model, the probability of there being no quencher bound to a QD (or proportion of QDs without bound quencher:  $[\text{QD}]_{n=0} / [\text{QD}]_{\text{total}}$ ) is  $P(0)$ , defined in Equation 2.

$$P(0) = e^{-\lambda} \quad (2)$$

where  $\lambda$  is the mean number of quenchers per QD, assuming that the catalysts bind independently to the QDs so that the presence of a catalyst does not affect the probability of binding a second one. We expect this to be valid for the range of  $\lambda$  values investigated herein, considering that the number of available surface sites should be significantly larger than for e.g. molecular catalysts. It follows from eqs. 1-2 that

$$F_0/F = e^{\lambda} \quad (3)$$

The value of  $P(0)$  decreases as [quencher] increases and  $\lambda$  increases, i.e.  $F_0/F$  increases. Plotting  $F_0/F$  on a logarithmic scale against the total added concentration of quenchers gives a linear trend over moderate concentrations of either of the catalysts. The data can be fitted with an exponential equation, the exponent of which is  $\lambda$ . Hence, exponent variables can be extracted from the exponential fitting of PL quenching plots, analogous to the quenching sphere of action model.<sup>35</sup>

The model fits the data quite well, even up to  $F_0/F = 10$  or more. The good agreement between data for a three-fold variation in QD concentration (Figure 5c-d), especially with CAT1-CO<sub>2</sub>H, suggests that the amount of unbound catalyst is rather small under the present conditions. Lower binding affinities could be accounted for by adding a coefficient before  $\lambda$ . The data can be used to estimate the concentration of QDs (Table S4) from the known concentration of the catalyst and the value of  $\lambda$ . In Figure 5b, the horizontal dotted red line marks the value of  $\ln(F_0/F)$  which in the model is when the concentration of bound catalyst is equal to the concentration of QDs. For the experiment with CAT1 and the lowest [QD] ( $Ab_{S_{405}} = 0.07$  in a 1 cm cell), this gives approximately 1  $\mu\text{M}$  QDs. If the fraction of unbound catalyst is not negligible, this estimate will overestimate the true QD concentration. CAT1 quenches ca. 50% more efficiently than CAT1-CO<sub>2</sub>H at low QD concentrations, while the difference at higher QD concentrations is smaller. This probably reflects better binding of CAT1 to the QDs. The presence of ascorbate increases  $\lambda$  of the catalyst. Thus, the experiments with CAT1 and ascorbate should probably give the best estimates of  $\lambda$  and thus the concentration of QDs. The obtained concentrations are in relatively good agreement with our calculations (see Calculation S1) based on the average QD diameter and amount of cationic ( $\text{In}^{3+}$ ) precursor, supporting the accuracy of these assumptions. We can only speculate on the reason for increased catalyst binding due to ascorbate, if this is e.g. due to ascorbate either binding to the QDs or affecting the solution ionic strength. In any case, it is clear that ascorbate itself quenches the QD PL much slower than the catalyst does, so that the primary reaction of the QDs is with the catalyst.

It is intriguing that both catalysts bind so strongly to the QDs. Ultrafast quenching by metal complex catalysts has been inferred before<sup>4,40,41</sup>, and electron transfer demonstrated on even sub-ps time scale,<sup>26,27</sup> but only in presence of excess catalyst. Here we show that catalysts are predominantly bound to the QDs even at concentrations as low as 1  $\mu\text{M}$  of each species, meaning that the fraction of unbound catalyst is surprisingly small, and that a single catalyst is sufficient to completely quench the PL. The catalysts' reduction

potentials suggest that ET from the CIS QDs to the catalyst is thermodynamically favourable, and the lack of a spectral overlap between the QD PL and catalysts' absorption spectra rules out significant contributions from energy transfer (EnT) processes. PL quenching experiments therefore suggest efficient oxidative quenching by surface adsorbed CAT1 and CAT1-CO<sub>2</sub>H with high association constants, inferring electron transfer rates faster than the time-resolution of the TCSPC experiments (< 100 ps). Ultrafast fs-TA was therefore employed to follow the formation of charge separation products.

### *Femtosecond Transient Absorption*

The fs-TA spectra of CIS QDs in water after 400 nm excitation (Figure 6a) show long-lived (> 8 ns) negative bands at ~430 nm (B0), ~520 nm (B1) and 610 nm (B2) as well as broad positive signals (< 400 nm, > 525 nm) extending into the NIR and MIR regions (Figure S9). Similar features are observed for pump wavelengths between ~390-520 nm, with negative bands corresponding to the 2<sup>nd</sup> derivative of the ground state absorption spectrum (inset Figure 6a, S9c). This supports the claim that these excitation energies correspond to transitions above or similar to the optical bandgap and that the fate of the carriers remains indifferent after initial relaxation of excess energies. Based on our previous study on similar QDs (albeit with smaller size and higher Cu-deficiency, see Ref. 27, Eliasson *et al.*), we attribute the main negative bands (B1 and B2) to the bleaching of two independent optical transitions dominated by state filling effects involving VB-CB (B1) interband and S<sub>T</sub>,VB-CB (B2) sub-bandgap optical transitions, as illustrated in Figure 6b.<sup>27</sup>

The bleaching of optical transitions results from the reduced oscillator strength experienced by the probe pulse due to pump-generated carriers occupying the involved states, effectively lowering the probability of probe absorption in those spectral regions. The recovery of the bleach band associated with VB-CB excitonic transitions (B1) is usually considered to be dominated by the CB-edge population due to the higher density and degeneracy of the VB as well as fast hole trapping events.<sup>42</sup>

The latter is likely responsible for the few hundred femtosecond ingrowth observed for the B2 band (Figure 6d, bottom), which is consistent with the concomitant bleaching of *e.g.* Cu<sup>+</sup>-CB transitions due to hole localisation events converting optically active Cu<sup>+</sup> to inactive Cu<sup>2+</sup>. The broad and featureless nature of the positive signals in the visible and NIR region are indicative of transitions involving electron and hole trap states, but their origin will not be discussed further herein. In the MIR, we associate the probe pulse absorption induced by the pump pulse to intra(sub)band transitions dominated by CB electrons (Figure 6b, gray arrow), with possible contributions from shallow trap states.

In the presence of the ascorbate buffer (H<sub>2</sub>Asc/NaHAsc, pH 4.5), the QD signals in all probe regions (UV-Vis/NIR/MIR) are subject to both static (within IRF, relative ΔAbs. ratio of B1/B2 at t<sub>0</sub>) and dynamic (t > t<sub>0</sub>) changes compared to neutral pH (Figure 6a vs. 6c). Control experiments using an acetate buffer (NaOAc/HAc, pH 4.5) indicate that these differences are pH-related and not the result of ultrafast hole scavenging by HA<sup>-</sup> (Figure 6d, Figure S10), consistent with TCSPC experiments of reductive quenching by HA<sup>-</sup> occurring on slower timescales. These observations highlight the necessity of careful pH control when relying on indirect support (*e.g.* accelerated bleach band recovery) of CT between QDs and electron/hole acceptors in order to facilitate interpretation of QD optical response in TA measurements.

The addition of CAT1 and CAT1-CO<sub>2</sub>H to CIS (H<sub>2</sub>Asc/NaHAsc, pH 4.5) results in significant changes to the fs-TA spectra in the MIR and UV/Vis probe regions (Figure 7, Figure S12-S13). Firstly, the broad positive QD feature in the MIR shows a significantly accelerated decay in the presence of both catalysts, consistent with the depletion of pump-generated CB electrons due to ET events to the catalysts on the time scale of 1 ps and above (see Figure 7b). Secondly, in the UV-Vis probe region, the presence of either catalyst leads to a significantly enhanced recovery of the B1 band whereas the B2 band remains relatively unperturbed. Furthermore, we observe the formation of a long-lived CT product visible as a positive transient at ~530 nm superimposed on the B1 bleach band (Figure 7c, d).

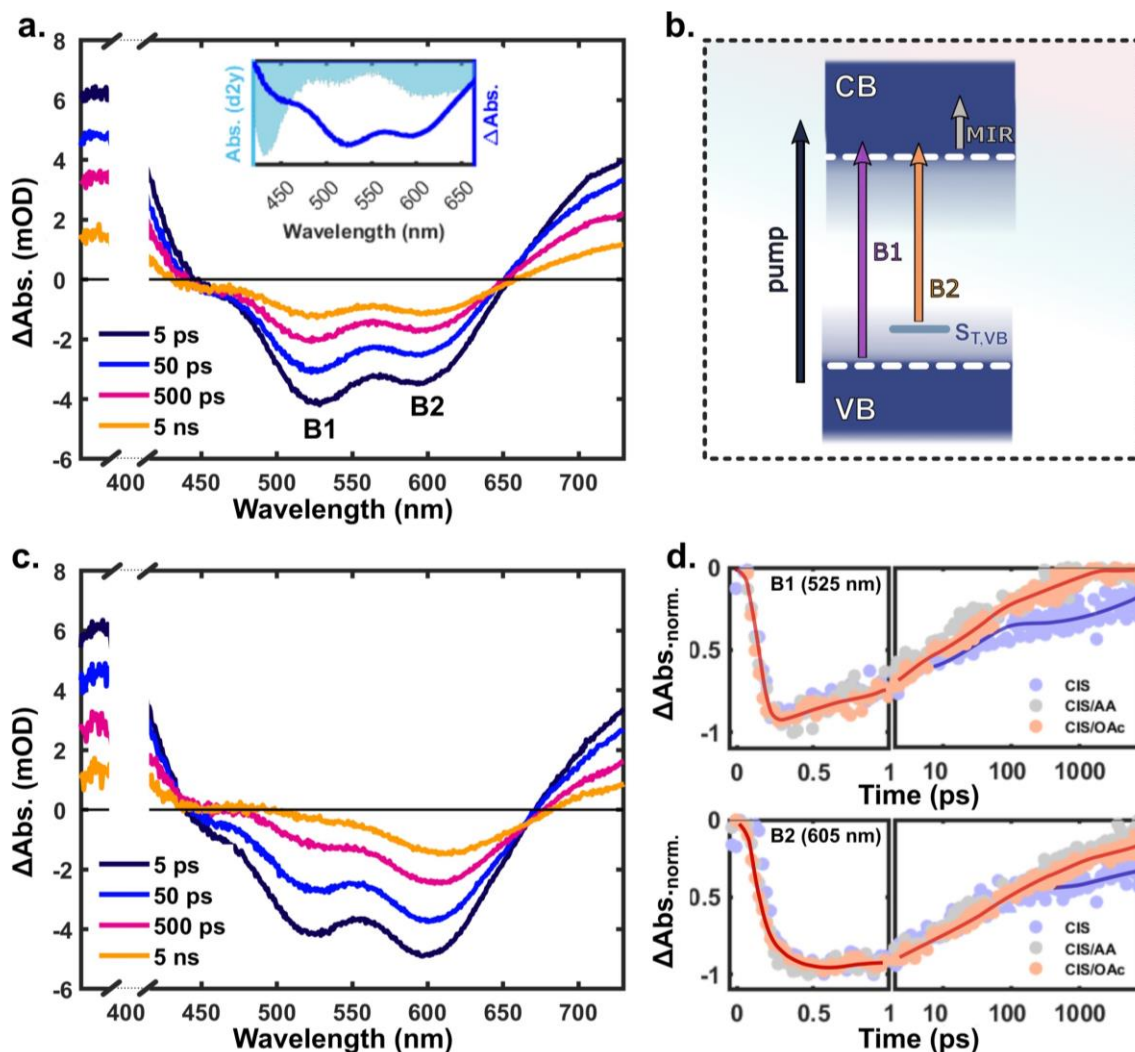


**Figure 6.** fs-TA measurements using a 400 nm pump. **a)** Fs-TA spectra of CIS QDs in H<sub>2</sub>O at indicated time-delays. The inset shows the second derivative of the QD ground state absorption spectrum (light blue) together with the fs-TA spectrum at 50 ps pump-probe time delay (dark blue). **b)** Schematic of the pump-induced optical transitions monitored in the UV-Vis (B1/B2 bleach bands) and MIR (PIA). **c)** fs-TA spectra of CIS QDs in H<sub>2</sub>Asc/NaHAsc buffer (pH 4.5, 0.1 M). **d)** Normalised fs-TA kinetics comparing CIS QDs in H<sub>2</sub>O at neutral pH (CIS, blue) with CIS in H<sub>2</sub>Asc/NaHAsc (grey) and NaOAc/HAc (red) buffer at a pH of ~4.5.

Previous studies have suggested that HA<sup>-</sup> will reduce CAT1 (Co<sup>3+</sup> to Co<sup>2+</sup>) in the dark,<sup>17,21,24</sup> consistent with our observations of significant changes in the ground state absorption spectrum of the Co<sup>3+</sup> species in the presence of ascorbate, if the solution is free from oxygen (Figure S14b). By performing fs-TA measurements in the presence and absence of H<sub>2</sub>Asc/NaHAsc buffer (pH 4.5, no purging), we can conclude that the spectral signature of the formed species is nearly identical in both cases (Figure S15.), suggesting that the dominating CT product probed in both cases corresponds to the singly reduced Co<sup>2+</sup> forms of CAT1 and CAT1-CO<sub>2</sub>H, *i.e.* that the initial state before excitation of the QDs is Co<sup>3+</sup>. The absorption band from the Co<sup>2+</sup> on the QD surface is redshifted relative to the freely diffusing Co<sup>2+</sup>, similar to the shift in the absorption spectra of the Co<sup>3+</sup> species resulting from the different dielectric environment experienced by the surface adsorbed catalysts, see inset Figure S14a and S16. Furthermore, the good agreement between the observed positive transient (~530 nm) and the expected contribution from the catalyst based on Co<sup>2+</sup> and Co<sup>3+</sup> reference spectra (Figure S16) strongly suggest catalyst reduction, rather than Stark effects, as its origin. We therefore conclude that the positive transient at ~530 nm corresponds to the absorption band of the catalysts in the Co<sup>2+</sup> state, with an electronic distribution that remains indifferent to the presence of the anchoring group (-CO<sub>2</sub>H). By subtracting the catalyst-free TA surface from each surface with catalyst present, we fit the formation of the reduced catalysts (Co<sup>2+</sup>) to a monoexponential with  $\tau_{ET}$  of ~3.5 ps and ~4.8 ps for CAT1 and CAT1-CO<sub>2</sub>H, respectively, with corresponding decays on the order of 10<sup>4</sup> ps, *i.e.* larger than the experimental time-window (Figure S17). See Supporting Information for further details and fitting parameters (Table S6).

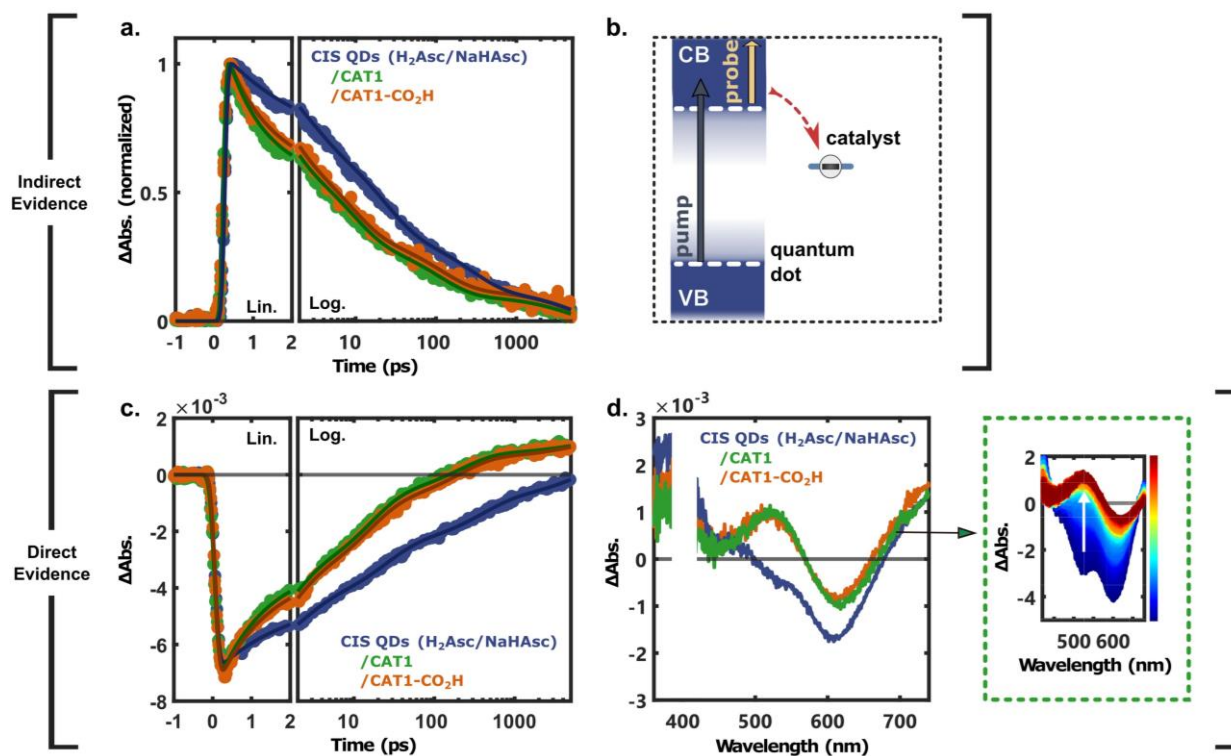


**Figure 7.** Fs-TA spectra ( $\lambda_{\text{pump}}$ : 400 nm) of CIS QDs (blue) mixed with CAT1 (green) or CAT1-CO<sub>2</sub>H (orange) in 0.1 M H<sub>2</sub>Asc/NaHAsc buffer (pH 4.5). **a)** MIR kinetics averaged between 3600-4000 nm and normalised. **b)** Schematic representation of pump and probe in the MIR together with the transfer of electrons from the CB of photoexcited QDs to the catalysts. **c)** UV-Vis kinetics extracted at 530 nm corresponding to the PIA of the reduced catalysts. **d)** Transient spectra at t(2 ns) with a close-up of the CIS/CAT1 spectral evolution from 3 ps (dark blue) to 8 ns (dark red).

## General Discussion

The present study shows a high catalytic activity for photochemical H<sub>2</sub> evolution, comparable to the that reported with core-shell CIS/ZnS QDs and CAT1.<sup>3,24</sup> The novel derivative of CAT1, CAT-CO<sub>2</sub>H, also works similarly well to produce H<sub>2</sub> under these conditions, but its anchoring group is not providing any important improvement in these experiments. Nevertheless, it shows that the pyridine position can be functionalised without impeding catalysis, which supports modifications at this position for improvements of this catalyst following rational design principles.

We seem to have similar quantum yields and TONs as reported for CIS/ZnS, in spite of using hybrid passivation. This is interesting, as the shell is expected to reduce charge recombination and unproductive trapping. Quantum yields were not determined in Sandroni *et al.*,<sup>3</sup> but Nie *et al.*<sup>24</sup> reported a quantum yield of 5.35%. In this respect, it is interesting to note that L.-Z. Wu and co-workers reported a quantum yield of 20% for CIS QDs with Glu ligands and nickel(II) ions assumed to form a co-catalyst *in situ*, although the very high light intensity (3 W LED light at 470 nm) may complicate direct comparison.<sup>5</sup>

We further note that direct comparison with literature reports is difficult not only because of quite different and not well-defined irradiation intensities at the sample, but also large uncertainties in [QD]. The previous papers gave a QD concentration of ca. 110  $\mu\text{M}$  in most experiments, but the reported absorbance at 420 nm in a 1 cm cuvette (0.366) of Sandroni *et al.*<sup>3</sup> is at least one order of magnitude too small to agree with the concentration and extinction coefficient given. Nie *et al.*<sup>24</sup> reported up to 90% PL quenching of 110  $\mu\text{M}$  QDs by only 10  $\mu\text{M}$  catalyst, which is not possible with the short QD PL lifetimes. We thus believe that their QD concentrations could be at least one order of magnitude smaller than the values given. This will obviously affect comparisons of H<sub>2</sub> production.

The investigated system is particularly interesting in that practically all QDs bind at least one catalyst, even at only a few equivalents of catalyst to QD and in the absence of a designed binding motif. This may also

explain why this catalyst is reported in literature to perform surprisingly well with these QDs under conditions at which many other molecular catalysts do not work well (not a large excess of photosensitisers, relatively high catalyst concentration).<sup>3</sup> The origin of this favourable binding interaction is not clear; we note that CAT1 is soluble in water and its electrocatalytic reactions have been investigated in aqueous solution, so association to the QDs should not be simply due to a hydrophobic effect. It would be interesting to see if this behaviour is general for other QDs with molecular catalysts.

The present study investigated the photoinduced electron transfer leading to  $\text{Co}^{3+}$ -to- $\text{Co}^{2+}$  reduction to complete the catalytic cycle, at least one further reduction step and two protonations are required. Investigation of further reduction of the  $\text{Co}^{2+}$  catalyst, by PL quenching and fs-TA with ascorbate under argon atmosphere, is in progress. Similar experiments by Wang and co-workers showed that the rate of electron transfer from the QD to  $\text{Co}^{2+}$  and  $\text{Co}^{3+}$  were very similar ( $\tau$  ca. 1 ns).<sup>24</sup>

This can be understood from a larger reorganisation energy in the first reduction that counteracts its larger driving force. Although electron transfer is much slower in their core-shell system than what we observe here (ca. 4 ps), it is clearly too fast for a diffusional reaction. While not discussed in the paper, their results suggest that the catalyst remains bound to a large extent also in the  $\text{Co}^{2+}$  state, even at very small cat./QD ratios. We propose that the same is true in our system, so that the catalyst remains largely bound to the QDs throughout the photocatalytic cycle. This gives a very different picture of the catalytic cycle than what is generally assumed, in that catalyst diffusion is not needed. For example, in a recent paper, it was claimed that the rate of electron transfer to the catalyst at the QD surface is not relevant for catalysis, as the catalyst needs to diffuse to interact with the QD.<sup>43</sup>

In the present systems, this is clearly not correct. Moreover, mass transport of water substrate (55 M) and ascorbate (0.5 M) is also not rate limiting. What is rate limiting here, as well as in systems where the catalyst needs to diffuse, is the limited rate of photon absorption, which is at best on the order of  $10 \text{ s}^{-1}$  per QD under ca. 1 sun irradiation, and the quantum yield that is typically ~10% or lower. The low quantum yield is a consequence of different charge recombination, trapping and side reactions. It is important to note that the rate of photogenerated  $\text{H}_2$  in general photocatalytic systems is given by the rate of photon absorption multiplied with the quantum yield. Thus, increasing the QD-catalyst electron transfer rate may not lead to increased efficiency, if the rate is already large enough compared to other exciton decay pathways. Similarly, an intrinsically high catalyst turnover frequency may not help if this step is not limiting the overall photocycle. Instead, good catalyst stability while waiting for the second electron and/or substrate proton may be key. If that is the case, we want more stable catalysts rather than faster ones, in order to cope with the amount of time spent in a reduced, intermediate state waiting to be able to complete the cycle. In this context, CAT1 is a logical choice vs. other cobalt tetraazamacrocycles, and this may at least partially explain its excellent performance with CIS and CIS/ZnS QDs.

The strong binding and rapid photoreduction of the catalyst explain why the photochemical  $\text{H}_2$  production rate hardly increases with increasing catalyst concentration in our experiment. Already at low concentrations, most QDs has one catalyst bound, and this is sufficient to harvest the photogenerated charges. Higher catalyst concentrations may instead lead to competition for redox equivalents and increase recombination losses, even if we did not reach that regime at catalyst concentrations up to 10  $\mu\text{M}$ .

While the present experiments suggested that the catalysts were predominantly bound, and were not able to register an important difference in either electron transfer rate or photocatalysis with or without a potential binding group, stronger binding may be more important in heterogenised systems. For example, with QDs and catalysts on an electrode for photoelectrochemical water splitting, a strong binding may prevent gradual leakage of the catalysts from the electrode surface. For CIS and other chalcogenide QDs, better binding groups than carboxylate would be preferred, *e.g.* softer ligands.

It is encouraging that good photocatalytic results are obtained with the hybrid-passivated CIS QDs, as their small size is favourable for sensitisation of mesoporous photocathode materials, such as NiO, while also avoiding damaging the NiO layer.<sup>28</sup> This may open the way to more photoelectrochemical designs with this QD-catalyst system.

## Conclusions

To summarise, the effectiveness of CIS QDs with hybrid passivation under photocatalytic conditions is demonstrated for the timescales studied (24 h), giving up to TON ~8000 at low catalyst concentration. A novel, catalytically active derivative of the hydrogen-evolving catalyst  $[\text{Co}(\text{N}_4\text{H})\text{Cl}_2]^+$  is also reported. We report that the remarkable performances reported for many quantum dot-molecular catalyst combinations used for photocatalysis to produce solar fuels can in some cases be attributed to the unanticipated formation of tightly-bound complexes in solution, resulting in very strong static quenching of photosensitisers' photoluminescence, even in the absence of specifically designed anchoring groups on either species. Femto-second TAS confirms the reduction of either catalyst, by direct observation of the reduced catalyst, on ultrafast timescales (~3.5 ps and ~4.8 ps for CAT1 and CAT1-CO<sub>2</sub>H, respectively) upon photoexcitation of the CIS QDs. The fact that this reduction occurs faster than the diffusion limit confirms the catalyst's adsorption onto the QDs and static quenching, with or without the carboxylic acid group, similar to previous results for other molecular hydrogen evolution and CO<sub>2</sub> reduction catalysts investigated.<sup>4,26,27</sup>

To describe this phenomenon, a full PL quenching study was made, varying both the catalyst and QD concentrations, in the presence and absence of ascorbate. A Poissonian distribution model for the adsorption of molecular catalysts to quantum dots has been proposed and fitted to photoluminescence quenching data under a range of conditions. This supports the strong association of catalyst and QDs down to concentrations of 1 μM each; this is intriguing and may be a more general phenomenon that would facilitate exploration of QD-catalyst combinations. The origin of the favourable interaction for such diverse catalyst structures, however, remains to be clarified.

## Experimental Procedures

### *Quantum Dot Sample Preparation and Characterisation*

The CIS QDs were synthesised according to a literature method.<sup>28,29</sup> Briefly, the capping ligand L-cysteine (17 mL, 2.4 mg, 0.02 mmol) was mixed with CuCl<sub>2</sub> (6 mL, 0.006 mmol), sodium citrate (0.40 mL, 0.16 mmol), and InCl<sub>3</sub> (0.04 mL, 0.04 mmol). Na<sub>2</sub>S (0.062 mL, 0.062 mmol) was injected under magnetic stirring (300 rpm) and the reactant system was heated to ~95 °C and kept for 40 min before the reaction was stopped using a cold water bath. TBAI (1 mL) was subsequently added (dropwise) during stirring. The solution was left stirring at room temperature (30 min) before the QDs were isolated by precipitation through the addition of ethanol and centrifugation (15 min, 9600 rpm). The QDs were redispersed in water (typically 1.4 mL, ~150-250 μM). The relative Cu and In content quantified by inductively coupled plasma optical emission spectroscopy (ICP-OES, Avio 200, PerkinElmer, Inc.). The samples were digested in a 1:1 HNO<sub>3</sub>/H<sub>2</sub>O<sub>2</sub> mixture and subsequently diluted to ~4% (v/v) HNO<sub>3</sub> with ICP grade water before filtering (25 μm). Commercial Cu and In (2% HNO<sub>3</sub>) calibration standards (PerkinElmer, Inc.) were used for calibration curves. Powder X-ray diffraction (P-XRD) was measured using a Simons D5000 diffractometer ( $\lambda = 1.5418 \text{ \AA}$ , 45 kV, 40 mA) with a step size of 0.02° in a 20–80 2θ scan range.

### *Photocatalysis*

For each sample 2 mL aqueous solution of 0.5 M ascorbate buffer at pH 4.5 was made up with the appropriate concentrations of CuInS QDs and catalyst in a reaction vessel of total volume 9 mL, leaving a headspace of 7 mL. Once the reagents were all combined in each reaction vessel, it was kept in the dark, crimp-sealed with an airtight septum and purged with argon (the carrier gas for the gas chromatograph) for half an hour. Once purged, the vessels were placed in the photoreactor box and illuminated with 57 mW/cm<sup>2</sup> light intensity from an LED light source (measured at 500 nm, roughly similar to one sun). Stirring was applied at 300 rpm with identical stirring bars to maintain the consistency of the samples. The temperature inside the box was controlled by its cooling system to keep it at room temperature (20 °C). The samples were removed from the photoreactor box and kept in the dark at the selected time points for gas injections to measure the hydrogen produced, then placed back in the same positions. Injections were made using a 100 μL Hamilton gas syringe, and each sample composition was repeated in triplicate to calculate average values and the standard deviation.

## *Optical Characterization and Photoluminescence Quenching*

Absorption spectra (Varian Cary 50, Agilent Technologies) were obtained using a 1- or 10-mm quartz cuvette. Photoluminescence (PL) and PL excitation (PLE) spectra were recorded on an Edinburgh Instruments fluorimeter in a right-angle (pathlength: 1 cm) or front-face (pathlength: 1 mm) collection geometry. All PL intensity quenching experiments were performed at a constant CIS QD concentration.

Time correlated single photon counting (TCSPC) histograms were recorded using a pulsed diode laser source (Edinburgh Instruments EPL404) operating at 404.7 nm. The time-to-amplitude converter (TAC) was set to a 1 or 5  $\mu$ s time range over 100000 channels. Colloidal Ludox (IRF) and samples were measured in 1- or 10-mm quartz cuvettes in the forward mode under magic angle polarization. Fluorescence decays were fitted to a sum of three exponentials reconvoluted with the IRF.

## *Transient Absorption Spectroscopy*

The femtosecond transient absorption (fs-TA) experiments were performed using the output from a Ti:sapphire based regenerative amplifier with integrated oscillator and pump lasers (Libra, Coherent). The details of the system are described elsewhere.<sup>27</sup>

Briefly, the Libra output was split into a pump and probe which were directed toward the UV–vis–NIR/MIR sample chambers (TAS, Newport Corp./Helios IR, Ultrafast Systems). Pump pulses at  $\sim$ 400 nm were obtained by frequency doubling the fundamental output. Prior to the sample cell, the pump was attenuated using a neutral density filter ( $\sim$ 167/233 nJ/pulse) and passed through a chopper to a 1.5 kHz repetition rate. In the UV-Vis/NIR probe regions, the broadband probe was generated from a calcium fluoride/yttrium aluminium garnet (CaF<sub>2</sub>/YAG) and was recorded on a silicon diode array (Newport custom-made). The samples were placed in quartz cuvettes (1 mm path length) and adjusted to a QD absorbance of 0.4 at the excitation wavelength. To generate the MIR probe, a part of the Libra output was passed through an optical parametric amplifier (TOPAS-prime, Light Conversion) coupled with frequency mixers. A sample cell with a 100  $\mu$ m Teflon spacer between two CaF<sub>2</sub> windows was used for all MIR measurements with a QD absorbance of 0.1 at 400 nm. Samples with catalyst and/or buffer were prepared fresh prior to measurement. All data sets were treated using SurfaceXplorer and individual scans were analysed carefully for inconsistencies, showing no indication of photodamage to the QDs. A power dependent study was performed to determine the regime of per-pulse photon fluence where the kinetics remained power independent.

## **Acknowledgements**

This work received funding from the European Union's Horizon 2020 Research and Innovation program under grant agreement no. 765376 (eSCALED Marie Curie ITN project) as well as the Swedish Energy Agency (grant no. 48572-1). The authors thank M. Pavliuk for kind help in conducting powder X-ray diffraction measurements and for valuable input regarding photocatalytic experiments.

## **References**

- 1 M. D. Regulacio and M.-Y. Han, *Acc. Chem. Res.*, 2016, **49**, 511–519.
- 2 W. Hu, S. Yang and J. Huang, *J. Chem. Phys.*, 2019, **151**, 214705.
- 3 M. Sandroni, R. Gueret, K. D. Wegner, P. Reiss, J. Fortage, D. Aldakov and M.-N. Collomb, *Energy Environ. Sci.*, 2018, **11**, 1752–1761.
- 4 F. Arcudi, L. Đorđević, B. Nagasing, S. I. Stupp and E. A. Weiss, *J. Am. Chem. Soc.*, 2021, **143**, 18131–18138.
- 5 X.-B. Fan, S. Yu, F. Zhan, Z.-J. Li, Y.-J. Gao, X.-B. Li, L.-P. Zhang, Y. Tao, C.-H. Tung and L.-Z. Wu, *ChemSusChem*, 2017, **10**, 4833–4838.
- 6 K. E. Dalle, J. Warnan, J. J. Leung, B. Reuillard, I. S. Karmel and E. Reisner, *Chem. Rev.*, 2019, **119**, 2752–2875.
- 7 N. Coutard, N. Kaeffer and V. Artero, *Chem. Commun.*, 2016, **52**, 13728–13748.
- 8 N. Queyriaux, N. Kaeffer, A. Morozan, M. Chavarot-Kerlidou and V. Artero, *Journal of Photochemistry and Photobiology C: Photochemistry Reviews*, 2015, **25**, 90–105.

- 9 E. S. Andreiadis, M. Chavarot-Kerlidou, M. Fontecave and V. Artero, *Photochemistry and Photobiology*, 2011, **87**, 946–964.
- 10 C. C. L. McCrory, C. Uyeda and J. C. Peters, *J. Am. Chem. Soc.*, 2012, **134**, 3164–3170.
- 11 C.-B. Li, A. J. Bagnall, D. Sun, J. Rendon, M. Koepf, S. Gambarelli, J.-M. Mouesca, M. Chavarot-Kerlidou and V. Artero, *Sustainable Energy Fuels*, 2022, **6**, 143–149.
- 12 S. Varma, C. E. Castillo, T. Stoll, J. Fortage, A. G. Blackman, F. Molton, A. Deronzier and M.-N. Collomb, *Phys. Chem. Chem. Phys.*, 2013, **15**, 17544.
- 13 S. Roy, M. Bacchi, G. Berggren and V. Artero, *ChemSusChem*, 2015, **8**, 3632–3638.
- 14 J. Wang, K. Yamauchi, H. Huang, J. Sun, Z. Luo, D. Zhong, T. Lu and K. Sakai, *Angew. Chem. Int. Ed.*, 2019, **58**, 10923–10927.
- 15 R. Gueret, C. E. Castillo, M. Rebarz, F. Thomas, A.-A. Hargrove, J. Pécaut, M. Sliwa, J. Fortage and M.-N. Collomb, *Journal of Photochemistry and Photobiology B: Biology*, 2015, **152**, 82–94.
- 16 R. Gueret, C. E. Castillo, M. Rebarz, F. Thomas, M. Sliwa, J. Chauvin, B. Dautreppe, J. Pécaut, J. Fortage and M.-N. Collomb, *Inorg. Chem.*, 2019, **58**, 9043–9056.
- 17 D. Moonshiram, C. Gimbert-Suriñach, A. Guda, A. Picon, C. S. Lehmann, X. Zhang, G. Doumy, A. M. March, J. Benet-Buchholz, A. Soldatov, A. Llobet and S. H. Southworth, *J. Am. Chem. Soc.*, 2016, **138**, 10586–10596.
- 18 S. Grau Abarca, M. Schilling, D. Moonshiram, J. Benet-Buchholz, S. Lubert, A. Llobet and C. Gimbert-Suriñach, *ChemSusChem*, 2020, **13**, 2745–2752.
- 19 R. Gueret, L. Poulard, M. Oshinowo, J. Chauvin, M. Dahmane, G. Dupeyre, P. P. Lainé, J. Fortage and M.-N. Collomb, *ACS Catal.*, 2018, **8**, 3792–3802.
- 20 C. Costentin, F. Camara, J. Fortage and M.-N. Collomb, *ACS Catal.*, 2022, 6246–6254.
- 21 C. Gimbert-Suriñach, J. Albero, T. Stoll, J. Fortage, M.-N. Collomb, A. Deronzier, E. Palomares and A. Llobet, *J. Am. Chem. Soc.*, 2014, **136**, 7655–7661.
- 22 S. Bold, T. Straistari, A. B. Muñoz-García, M. Pavone, V. Artero, M. Chavarot-Kerlidou and B. Dietzek, *Catalysts*, 2020, **10**, 1340.
- 23 S. Bold, J. Massin, E. Giannoudis, M. Koepf, V. Artero, B. Dietzek and M. Chavarot-Kerlidou, *ACS Catal.*, 2021, **11**, 3662–3678.
- 24 C. Nie, W. Ni, L. Gong, J. Jiang, J. Wang and M. Wang, *J. Mater. Chem. A*, 2019, **7**, 27432–27440.
- 25 C. Nie, C. Liu, L. Gong and M. Wang, *J. Mater. Chem. A*, 2021, **9**, 234–238.
- 26 J. Huang, M. G. Gatty, B. Xu, P. B. Pati, A. S. Etman, L. Tian, J. Sun, L. Hammarström and H. Tian, *Dalton Trans.*, 2018, **47**, 10775–10783.
- 27 N. Eliasson, B. P. Rimgard, A. Castner, C.-W. Tai, S. Ott, H. Tian and L. Hammarström, *J. Phys. Chem. C*, 2021, **125**, 14751–14764.
- 28 J. Huang, B. Xu, L. Tian, P. B. Pati, A. S. Etman, J. Sun, L. Hammarström and H. Tian, *Chem. Commun.*, 2019, **55**, 7918–7921.
- 29 Y. Chen, S. Li, L. Huang and D. Pan, *Inorg. Chem.*, 2013, **52**, 7819–7821.
- 30 A. H. Ip, S. M. Thon, S. Hoogland, O. Voznyy, D. Zhitomirsky, R. Debnath, L. Levina, L. R. Rollny, G. H. Carey, A. Fischer, K. W. Kemp, I. J. Kramer, Z. Ning, A. J. Labelle, K. W. Chou, A. Amassian and E. H. Sargent, *Nature Nanotech.*, 2012, **7**, 577–582.
- 31 D. H. Jara, K. G. Stamplecoskie and P. V. Kamat, *J. Phys. Chem. Lett.*, 2016, **7**, 1452–1459.
- 32 S. Jeong, M. Ko, S. Jeong, S. Y. Shin, S. M. Park, Y. R. Do and J. K. Song, *J. Phys. Chem. C*, 2020, **124**, 14400–14408.
- 33 H. N. Po and N. M. Senozan, *J. Chem. Educ.*, 2001, **78**, 1499.
- 34 E. Deponti, A. Luisa, M. Natali, E. Iengo and F. Scandola, *Dalton Trans.*, 2014, **43**, 16345–16353.
- 35 J. R. Lakowicz, *Principles of fluorescence spectroscopy*, Springer, New York, 3rd ed., 2006.
- 36 D. Genovese, M. Cingolani, E. Rampazzo, L. Prodi and N. Zeccheroni, *Chem. Soc. Rev.*, 2021, **50**, 8414–8427.
- 37 P. P. Infelta, M. Gratzel and J. K. Thomas, *J. Phys. Chem.*, 1974, **78**, 190–195.
- 38 J. M. Frank and S. J. Wawilow, *Z. Physik*, 1931, **69**, 100–110.
- 39 A. J. Morris-Cohen, M. T. Frederick, L. C. Cass and E. A. Weiss, *J. Am. Chem. Soc.*, 2011, **133**, 10146–10154.
- 40 S. Lian, M. S. Kodaimati and E. A. Weiss, *ACS Nano*, 2018, **12**, 568–575.
- 41 S. Lian, M. S. Kodaimati, D. S. Dolzhenkov, R. Calzada and E. A. Weiss, *J. Am. Chem. Soc.*, 2017, **139**, 8931–8938.
- 42 L. Li, A. Pandey, D. J. Werder, B. P. Khanal, J. M. Pietryga and V. I. Klimov, *J. Am. Chem. Soc.*, 2011, **133**, 1176–1179.
- 43 M. K. Homer, D.-Y. Kuo, F. Y. Dou and B. M. Cossairt, *J. Am. Chem. Soc.*, 2022, jacs.2c04991.